

RD-A138 094 ELECTRICAL LUMINESCENCE AND SIMS (SECONDARY ION MASS
SPECTROSCOPY) CHARAC. (U) AIR FORCE INST OF TECH

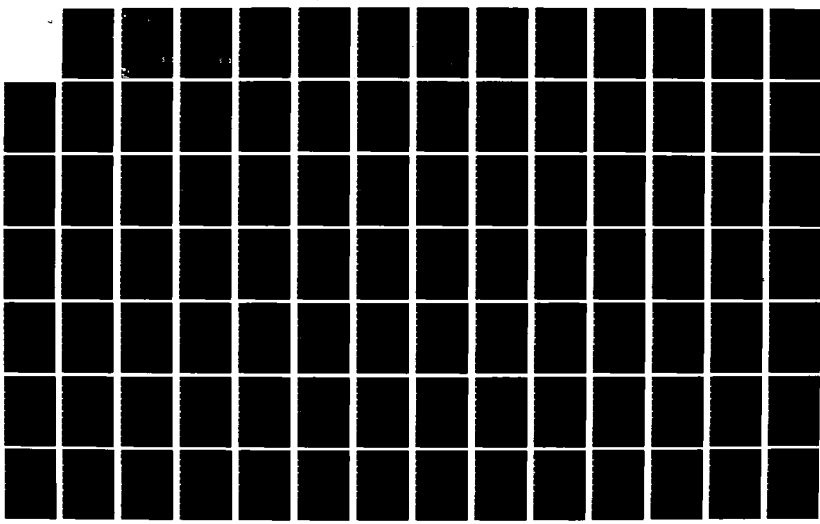
1/4

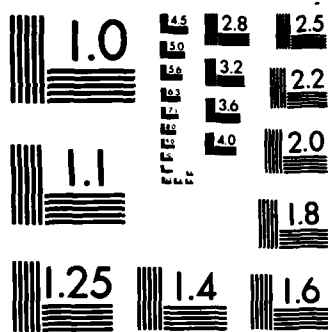
WRIGHT-PATTERSON AFB OH SCHOOL OF ENGI.

UNCLASSIFIED R M SYDENSTRICKER DEC 83 AFIT/DS/PH/83-4

F/G 20/12

NL





MICROCOPY RESOLUTION TEST CHART
NATIONAL BUREAU OF STANDARDS-1963-A

ADA138094



1

ELECTRICAL, LUMINESCENCE AND SIMS
CHARACTERIZATION OF CARBON IMPLANTED
VAPOR PHASE EPITAXIAL GALLIUM ARSENIDE

DISSERTATION

Robert M. Sydenstricker
Major USAF

AFIT/DS/PH/83-4

DISTRIBUTION STATEMENT A

Approved for public release
Distribution Unlimited

DTIC
ELECTE
FEB 22 1984
S B

DEPARTMENT OF THE AIR FORCE
AIR UNIVERSITY (ATC)

AIR FORCE INSTITUTE OF TECHNOLOGY

DTIC FILE COPY

Wright-Patterson Air Force Base, Ohio

84 02 21 185

AFIT/DS/PH/83-4

ELECTRICAL, LUMINESCENCE AND SIMS
CHARACTERIZATION OF CARBON IMPLANTED
VAPOR PHASE EPITAXIAL GALLIUM ARSENIDE

DISSERTATION

Robert M. Sydenstricker
Major USAF

AFIT/DS/PH/83-4

12 DTIC
S ELECTE
FEB 22 1984
D
B

Approved for Public Release; Distribution Unlimited

ELECTRICAL, LUMINESCENCE AND SIMS
CHARACTERIZATION OF CARBON IMPLANTED
VAPOR PHASE EPITAXIAL GALLIUM ARSENIDE

by

Robert M. Sydenstricker, B.S., M.S.

Major USAF

Approved:

Robert D. Hengelholt 12/8/83
Chairman

Gordon S. Stark 12/8/83

Donald C. Taylor 12/8/83

William J. Sutter 12/8/83

Theodore E. Parker 12/8/83

Accepted:

J. S. Przeniawski 9 Dec. 1983
Dean, School of Engineering

ELECTRICAL, LUMINESCENCE AND SIMS
CHARACTERIZATION OF CARBON IMPLANTED
VAPOR PHASE EPITAXIAL GALLIUM ARSENIDE

DISSERTATION

Presented to the Faculty of the School of Engineering
of the Air Force Institute of Technology
Air University
in Partial Fulfillment of the
Requirements for the Degree of
Doctor of Philosophy

Robert M. Sydenstricker, B.S., M.S.
Major, USAF

December 1983

Approved for Public Release; Distribution Unlimited

Acknowledgements

This dissertation was completed with the support and encouragement of many people, too numerous to list here. However, I would like to recognize those who were particularly instrumental in the success of this effort.

First, I would like to thank my advisor, Dr. R.L. Hengehold, who helped identify the problem to analyze.

Dr. Y.S. Park sponsored this research as an Avionics Laboratory project and was very generous with material support. He provided all GaAs substrates, arranged all implantations and provided the SIMS analysis. He also provided helpful discussions.

G. McCoy and R. Ford generously provided the vapor phase epitaxial GaAs material, grown to my particular specifications for this experiment.

J. Miskimen, R. Gabriel and G. Gergal of the AFIT Physics Department staff provided valuable assistance in the luminescence experiments.

Dr. Y.K. Yeo and Dr. F.L. Pedrotti provided both encouragement and technical training on the Avionics Laboratory electrical measurement system.

Captain G. Pomerenke was very helpful during the photoluminescence etch experiments.

J. Ehret provided very timely ion implantations. C. Gessner and R. Patton provided equally timely sample encapsulations following ion implantation.

Dr. D. Look provided temperature dependent electrical measurements on VPE GaAs, along with very helpful discussions.

Dr. Wm. Theis kindly provided discussions of his results of localized vibrational mode studies of carbon in GaAs.

My special thanks to fellow doctoral student, Major O. Swenson, for his support and encouragement.

And, finally, a very special thanks is due my wife, Jeanne, who sacrificed and suffered along with me and without whom this dissertation would never have been completed.

ROBERT M. SYDENSTRICKER

| | |
|---------------------|--------------------------|
| Accession For | |
| NTIS | GRA&I |
| DTIC TAB | <input type="checkbox"/> |
| Unannounced | <input type="checkbox"/> |
| Justification | |
| By _____ | |
| Distribution/ _____ | |
| Availability Codes | |
| Dist | Avail and/or Special |
| A1 | |

(This dissertation was typed by Sharon A. Gabriel)



TABLE OF CONTENTS

| | <u>Page</u> |
|--|-------------|
| Acknowledgements----- | iii |
| List of Figures----- | vii |
| List of Tables----- | xii |
| Abstract----- | xiii |
| I. Introduction----- | I-1 |
| II. Theory and Previous Work----- | II-1 |
| A. Ion Implantation----- | II-1 |
| 1. Range Statistics----- | II-1 |
| 2. Calculation of Implant Profiles----- | II-4 |
| 3. Defect Production by Ion Implantation----- | II-8 |
| 4. Previous Carbon Implants in GaAs----- | II-11 |
| B. Electrical Properties of GaAs----- | II-13 |
| 1. Electrical Carrier Concentration----- | II-14 |
| 2. Electromagnetic Transport Properties----- | II-17 |
| 3. Van der Pauw Equations----- | II-24 |
| 4. Layer Removal Equations----- | II-26 |
| 5. Previous Electrical Measurements on Carbon Implants in GaAs----- | II-29 |
| C. Luminescence Properties of GaAs----- | II-31 |
| 1. Excitation Theory----- | II-31 |
| 2. Luminescence of GaAs----- | II-35 |
| 3. Doping Concentration Effects on Luminescence----- | II-42 |
| 4. Previous Luminescence Results for Carbon Implanted GaAs----- | II-45 |
| D. Secondary Ion Mass Spectroscopy----- | II-46 |
| 1. SIMS Techniques----- | II-46 |
| 2. SIMS Data Calibration----- | II-48 |
| 3. Previous SIMS Results for Carbon Implanted GaAs-- | II-50 |
| III. Description of Experiment----- | III-1 |
| A. Sample Preparation----- | III-1 |
| B. Electrical Measurements - System and Procedures----- | III-7 |
| C. Luminescence Measurements - System and Procedures----- | III-15 |
| IV. Results and Discussion----- | IV-1 |
| A. Characterization of Control Samples----- | IV-1 |
| 1. High Purity VPE GaAs----- | IV-2 |
| a. Electrical Measurements: VPE GaAs----- | IV-2 |
| b. Luminescence Measurements: VPE GaAs----- | IV-7 |
| c. SIMS Measurements: VPE GaAs----- | IV-10 |

| | <u>Page</u> |
|---|-------------|
| 2. Capped and Annealed VPE GaAs----- | IV-13 |
| a. Electrical Measurements: C/A VPE GaAs----- | IV-14 |
| b. Luminescence Measurements: C/A VPE GaAs----- | IV-17 |
| 3. Neon Implanted VPE GaAs----- | IV-30 |
| a. Electrical Measurements: Neon Implanted VPE GaAs----- | IV-31 |
| b. Luminescence Measurements: Neon Implanted VPE GaAs----- | IV-36 |
| B. Characterization of Carbon Implanted GaAs----- | IV-43 |
| 1. Electrical Measurements: Carbon Implanted VPE GaAs----- | IV-43 |
| 2. Luminescence Measurements: Carbon Implanted VPE GaAs----- | IV-62 |
| 3. SIMS Measurements: Carbon Implanted VPE GaAs----- | IV-93 |
| a. SIMS for Carbon----- | IV-94 |
| b. SIMS for Si, Cr and Mn----- | IV-102 |
| V. Conclusions and Recommendations----- | V-1 |
| Bibliography----- | BIB-1 |
| Appendix A: Sheet Resistivity Plateau----- | A-1 |
| Appendix B: Carbon Bonding in GaAs----- | B-1 |
| Appendix C: Si_3N_4 Edge Accumulation----- | C-1 |
| Vita----- | Vita-1 |

LIST OF FIGURES

| <u>FIGURE</u> | | <u>Page</u> |
|---------------|---|-------------|
| II-1 | Comparison of joined half-Gaussian and single Gaussian for a $1 \times 10^{14} \text{ cm}^{-2}$, 120 keV carbon implant into GaAs----- | II-7 |
| II-2 | Ratio of average range and damage distribution as function of mass ratio----- | II-9 |
| II-3 | Calculated range and disorder depth profiles for two implant and substrate mass ratios----- | II-10 |
| II-4 | Theoretical temperature dependence of Hall factor for n-type GaAs----- | II-20 |
| II-5 | 300° K Hall and drift mobilities vs electron concentration in GaAs----- | II-23 |
| II-6 | 300° K Hall mobility vs hole concentration in GaAs----- | II-23 |
| II-7 | Luminescence transitions in GaAs----- | II-36 |
| II-8 | GaAs luminescence spectra changes with doping level----- | II-43 |
| III-1 | Schematic diagram of ion-implantation machine----- | III-4 |
| III-2 | Current flow and voltage contacts for square van der Pauw sample----- | III-9 |
| III-3 | Rotary switch connections from van der Pauw sample to measuring electronics----- | III-11 |
| III-4 | Electrical measurement system diagram----- | III-13 |
| III-5 | Luminescence measurements system diagram----- | III-16 |
| IV-1 | Typical CV measurement of electrical carrier concentration profile in high purity VPE GaAs----- | IV-5 |
| IV-2 | Electrical profiling data for VPE GaAs, Sample 23-3--- | IV-6 |
| IV-3 | PL spectra at 10° K of high purity VPE GaAs----- | IV-8 |
| IV-4 | PL spectra of two high purity VPE GaAs samples----- | IV-11 |
| IV-5 | SIMS data for carbon in VPE GaAs, Sample 13-23----- | IV-12 |
| IV-6 | Electrical profile for capped and annealed control sample 23-4, VPE GaAs----- | IV-16 |

FIGUREPAGE

| | | |
|-------|--|-------|
| IV-7 | PL of VPE GaAs after 850° C anneal with Si_3N_4 encapsulant ----- | IV-19 |
| IV-8 | PL spectra of VPE GaAs sample annealed at 850° C ----- | IV-20 |
| IV-9 | Photoluminescence spectra from unimplanted VPE GaAs control samples which were encapsulated with Si_3N_4 and annealed at three temperatures for the same conditions as the carbon implants ----- | IV-22 |
| IV-10 | PL etch spectra for 950° C C/A control sample etched from original surface to approximately one μ in depth ----- | IV-24 |
| IV-11 | PL etch spectra for 950° C C/A control sample showing exciton and shallow acceptor bands for deep etches----- | IV-25 |
| IV-12 | PL etch data for near surface region of 950° C C/A control sample of VPE GaAs ----- | IV-26 |
| IV-13 | PL etch data for 950° C C/A control sample of VPE GaAs ----- | IV-27 |
| IV-14 | One phonon to zero phonon ratio vs etch depth for the 1.4855 eV (silicon) line from 950° C C/A control sample ----- | IV-29 |
| IV-15 | Theoretical LSS implant profiles for 120 keV carbon and neon with a dose of $1 \times 10^{14} \text{ cm}^{-2}$ ----- | IV-32 |
| IV-16 | Sheet resistivity and sheet Hall coefficient vs depth for 120 keV neon implanted VPE GaAs for doses of $1 \times 10^{13} \text{ cm}^{-2}$ and $1 \times 10^{15} \text{ cm}^{-2}$ ----- | IV-34 |
| IV-17 | Electrical profile results for $1 \times 10^{13} \text{ cm}^{-2}$ dose of 120 keV neon implanted in VPE GaAs, annealed at 850° C for 15 min. in H_2 ----- | IV-35 |
| IV-18 | Comparison of PL spectra from three neon implanted VPE GaAs samples along with the C/A control and the unannealed VPE GaAs spectra----- | IV-37 |
| IV-19 | PL etch spectra from a $1 \times 10^{13} \text{ cm}^{-2}$ dose neon implanted VPE GaAs sample, annealed at 850° C----- | IV-39 |
| IV-20 | PL etch spectra from $1 \times 10^{13} \text{ cm}^{-2}$ dose neon implant in VPE GaAs----- | IV-40 |
| IV-21 | PL etch data for $1 \times 10^{13} \text{ cm}^{-2}$ dose neon implant into VPE GaAs, annealed at 850° C----- | IV-41 |

| <u>FIGURE</u> | <u>PAGE</u> |
|--|-------------|
| IV-22 Electrical profiles for $1 \times 10^{13} \text{ cm}^{-2}$ and $1 \times 10^{14} \text{ cm}^{-2}$ carbon implant dose in VPE GaAs, annealed at 850° C for 15 min. in H_2 ----- | IV-45 |
| IV-23 Electrical profiles for $3 \times 10^{14} \text{ cm}^{-2}$ and $1 \times 10^{15} \text{ cm}^{-2}$ carbon implant dose in VPE GaAs, annealed at 850° C for 15 min. in H_2 ----- | IV-46 |
| IV-24 Electrical profile data vs depth for three implant doses of carbon in VPE GaAs, annealed at 850° C for 15 min. in H_2 ----- | IV-50 |
| IV-25 Electrical profiles of $3 \times 10^{14} \text{ cm}^{-2}$ dose carbon implant dose in VPE GaAs, annealed at three temperatures for 15 min. in H_2 ----- | IV-52 |
| IV-26 Electrical profiles of $1 \times 10^{15} \text{ cm}^{-2}$ carbon implant dose in VPE GaAs, annealed at three temperatures for 15 min. in H_2 ----- | . -53 |
| IV-27 Measured Hall mobility vs. electrical carrier concentration for neon and carbon implanted VPE GaAs----- | IV-58 |
| IV-28 Results of ionized impurity calculations from the measured electrical carrier concentration and Hall mobility----- | IV-60 |
| IV-29 Photoluminescence spectra from VPE GaAs samples implanted with 120 keV carbon at four doses and annealed at 850° C for 15 min. in H_2 ----- | IV-63 |
| IV-30 Comparison of PL spectra for carbon implants into GaAs:Cr (Plot A) and VPE GaAs (Plots B, C)----- | IV-65 |
| IV-31 Photoluminescence spectra from VPE GaAs samples implanted with 120 keV carbon at $3 \times 10^{14} \text{ cm}^{-2}$ dose and annealed at three temperatures for 15 min. in H_2 ----- | IV-67 |
| IV-32 Photoluminescence spectra from VPE GaAs samples implanted with 120 keV carbon at $1 \times 10^{15} \text{ cm}^{-2}$ dose and annealed at three temperatures for 15 min.--- | IV-68 |
| IV-33 PL peak heights vs implanted carbon dose----- | IV-69 |
| IV-34 PL peak heights vs anneal temperatures----- | IV-70 |
| IV-35 PL etch spectra for $1 \times 10^{13} \text{ cm}^{-2}$ dose carbon implant in VPE GaAs----- | IV-73 |

| <u>FIGURE</u> | <u>PAGE</u> |
|---|-------------|
| IV-36 Expanded PL etch spectra for $1 \times 10^{13} \text{ cm}^{-2}$ dose carbon implant in VPE GaAs----- | IV-74 |
| IV-37 PL etch data for $1 \times 10^{13} \text{ cm}^{-2}$ dose carbon implant into VPE GaAs, annealed at 850° C ----- | IV-75 |
| IV-38 Near surface PL etch spectra for $1 \times 10^{15} \text{ cm}^{-2}$ dose carbon implant in VPE GaAs----- | IV-79 |
| IV-39 Expanded PL etch spectra of near surface region of $1 \times 10^{15} \text{ cm}^{-2}$ dose carbon implant in VPE GaAs ----- | IV-80 |
| IV-40 Shallow level PL etch spectra for $1 \times 10^{15} \text{ cm}^{-2}$ dose carbon implant in VPE GaAs, annealed at 950° C ----- | IV-81 |
| IV-41 Deep level PL etch spectra for $1 \times 10^{15} \text{ cm}^{-2}$ dose carbon implant in VPE GaAs, annealed at 950° C ----- | IV-82 |
| IV-42 PL etch spectra for $1 \times 10^{15} \text{ cm}^{-2}$ dose carbon implant in VPE GaAs for depth of 5000 \AA and greater----- | IV-83 |
| IV-43 Expanded PL etch spectra for $1 \times 10^{15} \text{ cm}^{-2}$ dose carbon implant in VPE GaAs for depths of 5000 \AA and greater----- | IV-84 |
| IV-44 PL etch data for near surface region of $1 \times 10^{15} \text{ cm}^{-2}$ dose carbon implant in VPE GaAs, annealed at 950° C ----- | IV-85 |
| IV-45 PL etch data for $1 \times 10^{15} \text{ cm}^{-2}$ dose carbon implant in VPE GaAs, annealed at 950° C ----- | IV-86 |
| IV-46 Comparative PL etch spectra for deep etches of carbon implanted VPE GaAs and control samples----- | IV-90 |
| IV-47 Comparative PL etch spectra for deep etches of carbon implanted VPE GaAs and control samples----- | IV-91 |
| IV-48 One phonon to zero phonon line intensity ratios for $1 \times 10^{13} \text{ cm}^{-2}$ dose carbon implant (Plot A) and $1 \times 10^{15} \text{ cm}^{-2}$ dose carbon implant (Plot B)----- | IV-92 |
| IV-49 Comparison of SIMS data for carbon for unannealed (Plot A) and 850° C , 15 min. anneals (Plot B)----- | IV-96 |
| IV-50 Comparison of SIMS data for carbon concentration and the 1.4935 eV carbon acceptor line intensity for two carbon implant doses----- | IV-98 |

| <u>FIGURE</u> | | <u>PAGE</u> |
|---------------|--|-------------|
| IV-51 | 1.4935 eV PL line intensity versus carbon concentration----- | IV-101 |
| IV-52 | SIMS data from a $1 \times 10^{15} \text{ cm}^{-2}$ dose carbon implanted VPE GaAs sample, annealed at 850° C for 15 min----- | IV-104 |
| A-1 | Results of bulk resistivity calculation for $3 \times 10^{14} \text{ cm}^{-2}$ and $1 \times 10^{15} \text{ cm}^{-2}$ dose of 120 keV carbon implants in VPE GaAs, annealed at 850° C ----- | A-5 |

LIST OF TABLES

| <u>TABLE</u> | | <u>PAGE</u> |
|--------------|---|-------------|
| II-1 | Carbon implanted gallium arsenide, parameter summary----- | II-12 |
| II-2 | Absorption depths in GaAs at 21° K----- | II-33 |
| III-1 | Summary of experimental samples----- | III-8 |
| IV-1 | Surface electrical measurements, VPE GaAs screening--- | IV-3 |
| IV-2 | Sample numbering system----- | IV-4 |
| IV-3 | Surface electrical measurements, capped and annealed VPE GaAs----- | IV-15 |
| IV-4 | Surface electrical measurements for 120 keV neon implants in VPE GaAs (annealed at 850° C for 15 min. in H ₂)----- | IV-31 |
| IV-5 | Surface electrical measurements for 120 keV carbon implanted VPE GaAs, annealed at 850° C for 15 min. in H ₂ ----- | IV-43 |
| IV-6 | Comparison of single measurement sheet carrier concentration results and integrated carrier concentration through the thermal conversion layer----- | IV-48 |
| IV-7 | Surface electrical measurements for high temperature anneals----- | IV-51 |
| IV-8 | Summary of carbon implanted samples analyzed with SIMS----- | IV-94 |
| IV-9 | Relationship of carbon concentration and 1.4935 eV line strength----- | IV-99 |

Abstract

The electrical, luminescence and mass distribution properties of carbon implanted VPE GaAs have been analyzed. Room temperature Hall measurements and low temperature photoluminescence, each combined with chemical etching, and SIMS experiments were performed on VPE GaAs which had been implanted with 120 keV carbon atoms in doses ranging from 1×10^{13} cm $^{-2}$ to 1×10^{15} cm $^{-2}$. These samples were subsequently encapsulated with chemical vapor deposition Si 3 N 4 and annealed at 850° C to 950° C for 15 minutes in flowing H $_2$. Unimplanted and neon implanted control samples were also analyzed.

The electrical and photoluminescence etch data independently identify a saturation effect for substitutional carbon acceptors at a concentration of approximately 3×10^{17} cm $^{-3}$. For lower concentrations, the carbon goes strongly to As sites and acts as an acceptor, while for higher concentrations the carbon goes to electrically and optically inactive sites, identified as precipitated carbon clusters.

A relative minimum is observed in the electrical carrier concentration profiles for the higher dose carbon implants which is very similar to that reported for high dose Si implants. However, this study leads to the conclusion that this dip in the electrical carrier concentration profile is due to a combination of precipitated carbon and implant damage, rather than electrical self-compensation of substitutional carbon.

A strongly p-type surface thermal conversion layer is formed when the n-type VPE GaAs is annealed. In this experiment, the effect of the relatively shallow conversion layer could be separated

from the majority of the carbon implanted layer. The thermal conversion layer is unrelated to carbon and may be related to indiffused Si, outdiffused Cr, residual Zn or Mn from an unknown source, all of which exhibited some near surface accumulation in the processed samples.

The successful correlation of the PL etch data for the intensity of the clearly resolved 1.4935 eV conduction band to carbon acceptor transition to the rapidly varying carbon concentration implant profile indicates that the electron diffusion length in these samples was 0.2 microns or less, a significantly lower value than is usually assumed. The 1.4935 eV line intensity was found to be proportional to the one-third power of the carbon concentration for concentrations of $1 \times 10^{16} \text{ cm}^{-3}$ up to the saturation value of $3 \times 10^{17} \text{ cm}^{-3}$. Thereafter, the 1.4935 eV line intensity decreased proportional to the minus one-half power of the carbon concentration up a carbon concentration of $3 \times 10^{19} \text{ cm}^{-3}$.

The SIMS data for carbon revealed a dose dependent asymmetric behavior for the carbon profiles which is not adequately described by LSS theory.

Several new luminescence lines are reported. Defect related excitons appear at 1.5102, 1.5083 and 1.5020 eV and their intensities are strongly enhanced by the presence of carbon. A new vacancy complex has been identified at 1.384 eV which has tentatively been associated with Si acceptors.

This experiment verifies that thermal diffusion of carbon in GaAs is not due to a single, simple mechanism. The most plausible explanation of the observed carbon diffusion is that the precipitated

Exi6 tota. (F-5 power/ce)

carbon clusters at high concentrations inhibit thermal diffusion, while at low concentrations individual carbon atoms diffuse rapidly through the GaAs lattice.

The overall conclusion is that for carbon concentrations above approximately $3 \times 10^{17} \text{ cm}^{-3}$ the excess carbon will not go substitutional and that for carbon concentrations less than $3 \times 10^{17} \text{ cm}^{-3}$, the carbon will reside predominately on As sites as an acceptor. Thus, despite the fact that carbon is a Group IVA impurity in GaAs, it is not likely to demonstrate amphoteric behavior as have other Group IVA dopants.

ELECTRICAL, LUMINESCENCE AND SIMS
CHARACTERIZATION OF CARBON IMPLANTED
VAPOR PHASE EPITAXIAL GALLIUM ARSENIDE

I. Introduction

Gallium Arsenide (GaAs) is a semiconductor whose electrical properties make it attractive for use in solid state electronic devices. Presently, silicon is the most widely used semiconductor material, and a large technology base has been built on silicon devices. However, GaAs offers some advantages over silicon, especially in applications which require higher speed operation.

The characteristics of GaAs which make it attractive for high speed devices include the electrical carrier mobility and the energy band structure. The electron mobility in GaAs is approximately four times larger than the electron mobility in silicon, the main reason that GaAs devices are faster. The energy gap in GaAs is also larger. This provides for higher temperature operation since thermally generated noise carriers are less than in silicon at the same temperature. And, due to certain valleys in the GaAs conduction band, GaAs can sustain electrical oscillations at microwave frequencies when a constant voltage is applied. It is the combination of these characteristics that make GaAs very attractive for high speed devices (see, for example, Refs 1, 2, 3).

The US Air Force has an interest in GaAs for high speed digital devices, as well as for microwave communication and radar components. In these areas, the upper limit of 2 Ghz for silicon devices may be increased to 20 Ghz with GaAs devices. The Avionics Laboratory at

Wright-Patterson Air Force Base has a major exploratory development thrust in the area of high speed GaAs integrated circuit technology. Part of this effort is the research done by the Electronic Research Branch of the Laboratory's Electronic Technology Division. This Branch of the Laboratory is addressing the potential and limitations of ion-implantation of GaAs as a semiconductor doping technique for device fabrication.

Ion-implantation offers some advantages over conventional thermal diffusion as a doping technique for semiconductors. Among these are a wider choice of possible doping atoms, along with the precise control over the amount of ions implanted and increased control over the volume of the semiconductor which is doped with ions. Device fabrication with ion-implantation has the potential for improved device yields and increased speed of device production. (A good presentation of ion-implantation as a semiconductor doping technique can be found in Reference 4.)

However, ion-implantation techniques still require research. Optimum results have been found to depend on such things as the choice of dopant atom and the processing parameters that accompany ion-implantation. Implantation into GaAs also brings along a unique set of problems. For example, the post-implantation thermal annealing step requires some method to control the unequal vaporization of Ga and As. Thus, an encapsulant such as a layer of silicon nitride (Si_3N_4) is often deposited before the anneal step. GaAs has been observed to change from n-type to p-type electrical activity simply by heat treating the sample. This long recognized thermal conversion phenomenon (Refs 5, 6, 7) has not been completely solved to date, though techniques to reduce or remove the effect are known (Refs 8,9). In summary, the approach to ion-implantation into GaAs often remains an empirical effort towards optimum results with considerable work

remaining before the basic physics of the technique are fully understood.

This dissertation addresses the effects of carbon implanted into GaAs. Carbon is one of the Group IVA elements of the periodic table (C, Si, Ge, Sn, Pb) which can be either donors or acceptors in GaAs depending on whether they reside at Ga or As sites, respectively, in the GaAs crystal lattice. The physical mechanisms which govern this amphoteric behavior are not fully understood. However, despite the fact that there is not a firm theoretical basis for predicting the amphoteric role of Group IVA dopants in GaAs, this dual role as a dopant has been used to fabricate p-n junctions using Si as a dopant (Refs 10, 11). Also, implantation with Ge and Sn has demonstrated amphoteric behavior when implantation or annealing parameters are changed (Refs 12, 13, 14, 15).

Implantation of carbon into GaAs is a particularly attractive technique because conventional doping methods do not work well with carbon. Attempts to introduce controlled amounts of carbon into epitaxial layers of GaAs have met with difficulty (Refs 16, 17, 18). Through ion implantation, a controlled range of carbon concentrations can be introduced.

Though carbon has been difficult to introduce intentionally in a controlled fashion, it is also, paradoxically, often a residual impurity in high purity GaAs (Ref 17). Hence, there is a continuing interest in ways to monitor the presence and effect of carbon in GaAs. One study (Ref 19) has postulated that residual carbon is the cause of the bothersome thermal conversion which can have disastrous effects on GaAs electrical devices such as field effect transistors (Ref 8). Carbon is also identified as one of the governing mechanisms for producing undoped semi-

insulating GaAs grown by the liquid encapsulated Czochralski technique (Ref 20).

Intuitively, carbon would appear to be a good choice for implantation doping for GaAs devices because of its relatively small mass and its apparently low thermal diffusion coefficient. Implanted carbon should cause much less lattice damage than ions which approach or exceed the mass of Ga or As. While there is limited thermal diffusion data on carbon, one published depth profiling measurement of a carbon implant demonstrated that up to 900° C carbon exhibited very little thermal diffusion (Ref 21). The difficulty reported in using thermal diffusion doping with carbon (mentioned above) also indicates that carbon does not move readily through the GaAs lattice. Thus, carbon's small mass and low thermal diffusion make it an attractive implant candidate for GaAs.

This dissertation addresses the general problem of carbon's effect on the material properties of GaAs with the particular goal of clarifying the reasons for the low electrical activation of carbon implants in GaAs. There is a relative scarcity of data on carbon implants in general (see Section II.A.4), particularly in comparison to other Group IVA atoms, thus any new data should contribute to the understanding of Group IVA as dopants in GaAs. The approach taken in this experiment was to combine layer removal data collection techniques to collect electrical transport data, induced photoluminescence spectra and secondary ion mass spectroscopy (SIMS) data throughout the carbon implanted layer in high purity vapor phase epitaxial (VPE) GaAs. This particular combination of experimental techniques with attempts at data correlation had not previously been tried on a common set of samples. Also, the use of high purity VPE GaAs as an implant substrate is new. One other distinctive approach was the

detailed characterization of a set of control samples, which were found to be essential to separating the effects due to processing steps (such as annealing) from the effects due to carbon in GaAs. The motivation for the control samples was the strong possibility that previous electrical measurements on carbon implants in GaAs had been obscured by thermal conversion effects from the annealing process. As a result of this experimental approach, a new model has been developed for the concentration dependent behavior of carbon in GaAs. This model explains the observed electrical, luminescence and SIMS profiling data and explains why high dose carbon implants in GaAs have low electrical activation efficiencies.

II. Theory and Previous Work

In this section, the relevant theoretical background necessary to understand the experimental results will be presented. These include a description of ion implantation into solids, a review of the electrical and luminescence properties of GaAs, and a description of secondary ion mass spectroscopy. At the end of each of these presentations, the previous results for carbon implanted GaAs samples will be summarized.

A. Ion Implantation

The technique of ion implantation is described below. The discussion shows how the ion implantation beam parameters of total implanted dose and ion energy are converted into the implanted ion concentration profile. Also, the theory of defect production will be presented, since defect production can be an important factor in the successful doping of semiconductors by ion implantation.

1. Range Statistics. Ion implantation was first proposed as a technique for introducing impurity atoms into semiconductors in the 1950s (Ref 22). However, most work on ion implantation as a technique for fabricating semiconductor devices did not begin until about 1965. One of the major theoretical milestones was the work of Lindhard, Scharff and Shiott, often abbreviated as LSS (Ref 23). Their work produced a unified range theory which could predict ion ranges in amorphous solids. This theory continues to be refined and expanded today, due in large part to the use of ion implantation for semiconductor devices.

Although an ion beam is usually designed to have ions of a particular mass and energy, the entry points of the ions into the solid are random variables. Thus, each ion undergoes a different scattering path through

the solid where the number of collisions and energy transferred per collision are random variables. As a result, the stopping points for the ions can be described statistically, i.e., described the average range and moments of the distribution.

The original LSS theory developed a set of formulas, graphs and tables from which the range distribution of any ion and substrate combination could be found. These procedures could be quite lengthy and often were not accurate enough for semiconductor device fabrication work. Several computer based techniques have since been developed. One of these (Ref 24) outputs a tabular format of range statistics for various ion and substrate combinations over a set of ion energies from 10 keV to 1 MeV. From these range statistics, one can calculate the expected range distribution for given implantation conditions (as described in the following section). What follows is a brief overview of some of the key features of the calculation of the range statistics. Then, in the following section, these statistics are applied to the particular cases of carbon and neon implantation into GaAs. These were the two implant species used in the experiment.

For energies up to several MeV, there are two main energy loss mechanisms for ion implantation into amorphous targets. These are the nuclei-ion and electron-ion collisions. If a stopping power can be derived for each of these two processes, then the energy loss with distance is given by

$$- \frac{dE}{dx} = N[S_n(E) + S_e(E)] \quad (1)$$

where N is the atomic density and $S_n(E)$ and $S_e(E)$ are the nuclear

and electronic stopping powers, respectively. If the stopping powers are known, then simply integrating Eq (1) gives the average total range as

$$\langle R(E) \rangle = \frac{1}{N} \int_0^{E_0} \frac{dE}{[S_n(E) + S_e(E)]} \quad (2)$$

with E_0 being the initial energy of the incident ion.

However, in most experiments it is the depth of penetration below the surface which is of interest, rather than the total along track path length. Hence, the component of range along the direction of the ion beam, R_p , is of interest, and angular deviations of a particle as well as the energy loss must be accounted for. A development of LSS theory by Sanders (Ref 25) using spherical coordinates allows the calculation of R_p from nuclear scattering, and Gibbons et al (Ref 24) have added the contribution of electron scattering to R_p .

Sanders develops an LSS type integro-differential equation to solve for $P(r, n, E)$ which is the probability density function such that a particle with initial energy E and direction of motion n will come to rest at location r from the origin (the point where the ion enters the solid). Expansion in Legendre polynomials leads to recurrence relations for the moments of $P(r, n, E)$. The relationship of these moments to the projected range moments is given by

$$\langle r_p^n \rangle = \int_{\text{all space}} (r \cos \theta)^n P(r, E, \cos \theta) dV \quad (3)$$

Sanders also gives the generalization of this approach for a binary compound, such as GaAs. The electronic stopping power $S_e(E)$ can be included in this approach as an additive term in the Sanders recurrence

relations such that Se is proportional to the square root of the ion's energy (see Ref 24). This is valid because the ion's velocity is less than the velocity of electrons with Fermi energy E_f in the free electron gas.

In the notation of Eq (3), we have the projected range, R_p ; the second moment, σ_p^2 ; and the third central moment written as

$$R_p = \langle r_p \rangle \quad (4)$$

$$\sigma_p = \langle r_p^2 \rangle - \langle r_p \rangle^2 \quad (5)$$

$$CM_{3p} = \langle r_p^3 \rangle - 3\langle r_p \rangle \sigma_p^2 - \langle r_p \rangle^3 \quad (6)$$

Gibbons et al estimated their calculations of R_p (tabulated in Ref 24) to have less than one percent error, the standard deviation to have a few percent error, and the third central moment to range from one to thirty percent error. They concluded that the choice of interaction potential most severely affects the third moment calculation.

2. Calculation of Implant Profiles. If an implanted profile can be adequately described by the first two moments, the implanted distribution can be written as

$$N(x) = \frac{\phi}{\sigma_p \sqrt{2\pi}} \exp\left[-\frac{(x-R_p)^2}{2\sigma_p^2}\right] \quad (7)$$

which is a Gaussian function of x , the depth from the surface. The constant ϕ is the total implanted dose, such that the integral of the normalized Gaussian over all x will yield all implanted atoms. R_p and

σ_p are obtained from the tabulated range statistics, such as Reference 24.

Gibbons and Mylorie (Ref 26) have shown that, if the asymmetry is not too extreme, the third central moment alone can be used to form a joined half-Gaussian profile. Here, there is a different standard deviation for each side of the profile centered at a modal range, R_M , and the profile can now be written as

$$N(x) = \begin{cases} \frac{\phi}{(\sigma_1 + \sigma_2)\sqrt{2\pi}} \exp \left[-\frac{(x - R_M)^2}{2\sigma_1^2} \right], & x \geq R_M \\ \frac{\phi}{(\sigma_1 + \sigma_2)\sqrt{2\pi}} \exp \left[-\frac{(x - R_M)^2}{2\sigma_2^2} \right], & x \leq R_M \end{cases} \quad (8)$$

A table is presented in Reference 24 which allows values of σ_1/σ_p and σ_2/σ_p to be interpolated from the tabulated values of a third moment ration CM_{sp}/σ_p^3 . Thus, using the tabulated value of σ_p one can find σ_1, σ_2 the standard deviations for the half-Gaussians forming the asymmetric distributions. Finally, the modal range is given by

$$R_M = R_p - 0.8 (\sigma_2 - \sigma_1) \quad (9)$$

For 120 keV carbon atoms implanted in GaAs, the tabulated values are

$$R_p = 2507 \text{ \AA} ; \sigma_p = 1099 \text{ \AA} ; CM_{sp}/\sigma_p^3 = -0.61$$

where the minus sign in the third moment ratio indicates that the roles of σ_1 and σ_2 are reversed in Eq (9). The half-Gaussian parameters for 120 keV carbon are found to be

$$R_M = 1757 \text{ \AA} ; \sigma_1 = 1099 \text{ \AA} ; \sigma_2 = 1523 \text{ \AA}$$

The third moment was found to be 947 \AA . It, therefore, satisfies the condition given in Reference 24 that the third moment should be less than the standard deviation for this procedure to be applicable to asymmetrical distributions.

Figure II-1 shows for comparison the single Gaussian and the joined half-Gaussian profiles for 120 keV carbon implanted into GaAs. It would appear that the theory predicts a strong influence of higher order moments on carbon profiles.

120 keV neon implants were also used in this experiment. Neon range statistics are not available in Reference 24, but a computer program available at the Avionics Laboratory at Wright-Patterson Air Force Base which implements similar calculations produced the following values for 120 keV neon implants

$$R_p = 1493 \text{ \AA} ; \sigma_p = 631 \text{ \AA}$$

The third moment ratio was not calculated.

Thus, from theoretical calculations we have found the expected distribution of implanted carbon and neon atoms, including the expected effects of higher order moments. The following discussion addresses the lattice damage effects which occur during the implantation process.

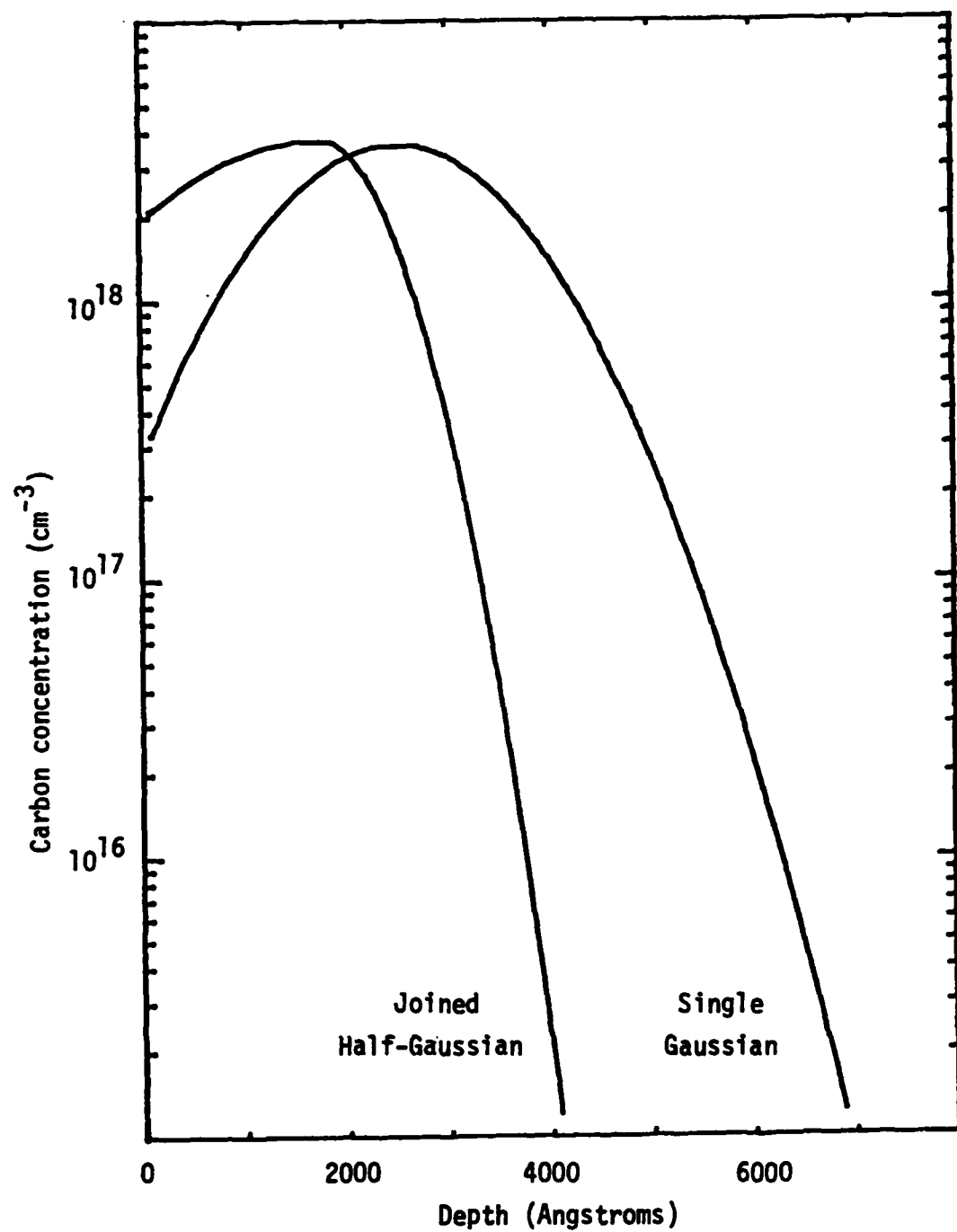


Figure II-1. Comparison of joined half-Gaussian and single Gaussian implant distribution for a $1 \times 10^{14} \text{ cm}^{-2}$, 120 keV carbon implant into GaAs. See text for description of calculation of the profiles.

3. Defect Production by Ion Implantation. The process of ion implantation into a crystalline solid involves numerous collisions of the incident ion with both the electrons and the nuclei of the solid. If the energy transferred to the target atom is sufficient to overcome the binding forces, the atom may be displaced from the crystal lattice and a defect produced. The possible point defects are generally categorized as a vacancy, interstitial or substitutional defect. Collections of point defects can form a variety of dislocations, which are macroscopic evidence of the imperfect crystal structure. When the damage caused by implantation is so extensive that no discernible lattice structure exists, the solid is described as amorphous.

Several theoretical approaches have been developed for ion implantation damage analysis. A review is given in Reference 27. Some of the earliest work was based on simple estimation of threshold energies required to form defects. These were determined from the sublimation energy or from the directional bond strengths. These led to the Kinchin-Pease model which gives order of magnitude estimates of numbers of displaced atoms. Before the spatial extent of the damage in the implanted region could be calculated, the LSS theory had to be developed. Their work can be extended to calculate the energy deposited in the solid by the ion beam as a function of depth. With some estimate of the threshold energy for displacement of lattice atoms, one can then estimate the degree of damage as a function of depth into the solid.

Figures II-2 and II-3 are generalized results of these types of calculations of ion implantation damage. They show the relationship of the mean of the damage profile $\langle X \rangle_D$ to the mean of the implanted profile $\langle X \rangle_R$ (Ref 27). In this notation, $\langle X \rangle_R$ is identical to the

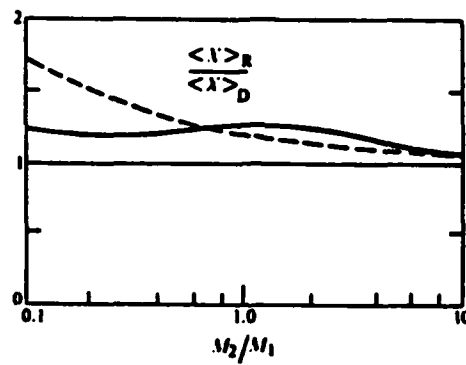


Figure II-2. Ratio of average range and damage distribution as a function of mass ratio. M_1 is mass of the implanted ion and M_2 is mass of the substrate ion. Dashed line for scattering potential with m of $1/3$ and solid line for m of $1/2$ (see text).

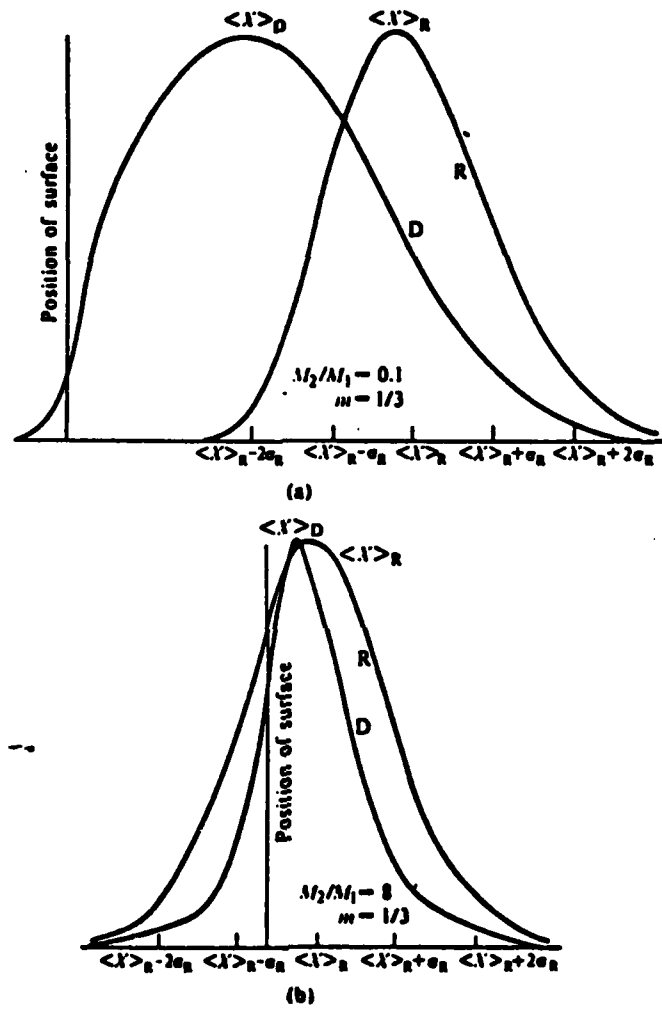


Figure II-3. Calculated range and disorder depth profiles for two implant and substrate mass ratios. Depth axis shown in terms of mean implanted range and standard deviation of the range distribution. (Reference 27).

projected range R_p discussed above in range statistics. M_1 and M_2 are the masses of the ion and the target atom, respectively. The choice of scattering potential

$$V(r) = \frac{1}{r^m}$$

is shown as $m = 1/2$ or $1/3$, ($1/3$ is a good approximation for low ion energies and $1/2$ is a better choice for energies up to the electronic excitation threshold).

From Figures II-2 and II-3, several observations can be made. First, the region of maximum damage is always less than the region of maximum implanted ion concentration. Second, for the particular case of carbon implanted in GaAs, we have $M_2/M_1 = 6$, similar to Figure II-3(b). Thus, the damage profile is expected to be more narrow than the implanted profile. For 120 keV carbon implants in GaAs, the implant profile has a standard deviation of 1099 \AA , thus the damage profile should have a standard deviation $< 1099 \text{ \AA}$. Finally, From Figure II-2, the carbon implant in GaAs would have

$$\frac{\langle X \rangle R}{\langle X \rangle D} = 1.1$$

Therefore, we can calculate the mean of the damage profile to be between 2200 \AA and 2300 \AA since we know the mean of the implant profile to be 2507 \AA .

4. Previous Carbon Implants in GaAs. Table II-1 is a summary of past carbon implants reported in the literature. In this section, we briefly discuss the implantation and anneal parameters used in the

TABLE III-1. CARBON IMPLANTED GALLIUM ARSENIDE, PARAMETER SUMMARY

| Implantation | Anneal | | | | | | Measurements | | | | |
|---------------------|----------------------|--|-----------------|-------------|----------------------------------|-----------|--------------------------------|------------|---------|---------------------|--------------------------|
| | Energy (KeV) | Dose (cm ⁻²) | Dual Implant | Time | Atm | Temp (°C) | Cap | Electrical | Optical | Other | Reference |
| Target Type | | | | | | | | | | | |
| SI(Cr) | 120 | 10 ¹³ -10 ¹⁴ | -- | 15 m | Ar | 600-900 | Si ₃ N ₄ | Profile | -- | -- | 21 (Shin) |
| SI(Cr) | 60 | 10 ¹⁴ | 120keV Ga | 15 m | Ar | 700,900 | Si ₃ N ₄ | Profile | -- | -- | 31 (Shin, et al) |
| SI(Cr) | Comb of 10,30,50 | 4x10 ¹³ 4x10 ¹⁴ | -- | 15 m | Vac | 500-700 | SiO ₂ | Surface | -- | -- | 29 (Sansbury, Gibbons) |
| SI(Cr) | 100-400 | 10 ¹³ -10 ¹⁶ | -- | 0 to 72 hrs | Vac | 600-800 | SiO ₂ | Surface | -- | Proton RBS | 28 (Harris) |
| LEC | Comb of 200,300, 400 | Designed for 10 ¹⁵ to 10 ¹⁷ cm ⁻³ | -- | 30 m | H ₂ | 850 | SiO ₂ | Surface | PL | -- | 30 (Stringfellow, et al) |
| SI(Cr) & VPE | 40,200 | 10 ¹³ -10 ¹⁶ | 200keV As or Ga | 30 m | H ₂ /AsH ₃ | 700-800 | None | Surface | -- | SIMS | 15 (Krautle) |
| SI(Cr) and un-doped | 6000 | 6x10 ¹⁵ -4.7x10 ¹⁶ | -- | 1 hr | Vac | 300-650 | -- | -- | -- | Infrared Absorption | 32 (Kreitman, et al) |
| SI(Cr) | 6000 | 5.1x10 ¹⁶ | -- | 1 hr | H ₂ | 300-900 | Si ₃ N ₄ | -- | -- | Infrared Absorption | 33 (Theis, et al) |

past experiments, reserving discussion of the luminescence, electrical and SIMS data until those sections are presented.

There are no identical sets of implantation and anneal conditions in these experiments. The total range of implant energies covers 10 to 400 KeV for implant doses of 1×10^{13} to 1×10^{16} cm $^{-2}$, except for two sets implanted at 6 MeV. The higher energy implants were prepared for absorption measurements for carbon local vibrational mode studies. Some implants were single energy (Refs 15, 21, 28), while others used multiple energies and doses to achieve a nearly uniform carbon concentration in the implanted layer (Refs 29, 30). A variety of anneal atmospheres and encapsulants were used, with only two pair of similar conditions (Refs 21, 31, and 28, 29). Only References 15, 30 and 31 specifically mention the use of control samples to help ensure that the results were due to carbon implantation. A very limited amount of dual implantation of carbon with either Ga or As has been reported (Refs 15, 31).

There was apparently a decline in interest in carbon implanted GaAs after initial studies reported low electrical activation (Refs 28, 29). Later, the use of higher temperature anneals, use of better encapsulants and dual implantation showed some improvements in the electrical activation (Refs 21, 31). Recent electrical measurements for carbon are reported in a study of all Group IVA dopants (Ref 15). The only published report on luminescence from carbon implants is Reference 30, while absorption experiments on carbon implants are reported in References 32 and 33.

B. Electrical Properties of GaAs

As described in the introductory section, it is the electrical properties of GaAs semiconductor material which make it useful for electronic device applications. In the following section, we present

the theory for calculating the electrical carrier concentration and the electrical transport properties of GaAs, with particular attention to room temperature measurements. We also present the van der Pauw equations and layer removal equations for calculating electrical properties from etched, four point contact samples of arbitrary shape. These latter two sections are particularly germane to understanding how the electrical measurements were performed in this experiment.

1. Electrical Carrier Concentration. The electrical carrier concentration in semiconductors is discussed in several texts (Refs 34, 35, 36, 37). The two general categories of electrical carriers refer to the source of the carriers. These are the intrinsic carriers due to the inherent energy band structure of the semiconductor crystal, and the extrinsic carriers due to the various doping impurities that may be present.

The intrinsic carrier concentration, n_i , is related to the electron concentration, n , and the hole concentration, p , as (Ref 34)

$$n_i^2 = np$$

The intrinsic concentration is also found to be

$$n_i = 2 \left(\frac{2\pi\sqrt{m_p^* m_n^*} kT}{h^2} \right) e^{-E_g/kT}$$

where m_p^* , m_n^* are the hole and electron density-of-states effective masses, respectively, E_g is the band gap energy between the conduction and valence bands, and T is the absolute temperature. Also, k and h

are Boltzmann's and Planck's constants, respectively. There is some variation in the quoted values of room temperature intrinsic carrier concentration, n_i , for GaAs. This reflects the variations in the experimental values of effective masses, particularly for holes. With m_0 being the electron rest mass, recent values of the density-of-states effective masses are $m_n^* = 0.066 m_0$ (Ref 38) and $m_p^* = 0.52 m_0$ (Ref 39). The calculated 300° K intrinsic carrier concentration for GaAs (with $E_g = 1.40$ eV) is found to be

$$n_i = 6 \times 10^6 \text{ cm}^{-3}$$

The procedures for finding the carrier concentrations when extrinsic carriers are contributed by donors and acceptors can become quite complicated (Ref 37). Several of the complicating factors can be multiple donor and acceptor energy levels, excited states of these levels and spin degeneracy of the levels. Some simplification results if the Fermi level, E_f , for the semiconductor is within the energy gap and several kT units away from the donor and acceptor levels. This condition assures that all donors and acceptors are ionized and hence contribute 100% to the electron and hole populations, respectively. The resulting approximate expressions for n-type and p-type semiconductors are

$$n = (N_d - N_a) + \frac{n_i^2}{(N_d - N_a)}$$

$$p = n_i^2 / (N_d - N_a)$$

} n-type

$$n = n_i^2 / (N_a - N_d)$$

$$p = (N_a - N_d) + \frac{n_i^2}{(N_d - N_a)}$$

p-type

where N_d and N_a are the donor and acceptor concentrations, respectively.

As a check on the validity of these expressions for room temperature carrier concentration measurements, the Fermi level must first be calculated. The Fermi level can be estimated from the expression (Ref 35)

$$E_g = \frac{E_q}{2} + kT \ln \left(\frac{m_p^*}{m_n^*} \right)^{3/4} + kT \sinh^{-1} \left(\frac{N_d - N_a}{2n_i} \right)$$

which holds if

$$N_d \ll \left(\frac{2\pi m_n^* kT}{h^2} \right)^{3/2} \exp \left(- \frac{E_c - E_d}{kT} \right)$$

$$N_a \ll \left(\frac{2\pi m_p^* kT}{h^2} \right)^{3/2} \exp \left(- \frac{E_a - E_v}{kT} \right)$$

where $(E_c - E_d)$ and $(E_a - E_v)$ are the donor and acceptor ionization energies, respectively. Using values given above for effective masses and intrinsic carrier concentration at room temperature, with typical ionization energies of 5 meV for donors and 25 meV for acceptors, the criteria become

$$N_d \ll 2 \times 10^{17} \text{ cm}^{-3} ; \quad N_a \ll 3 \times 10^{18} \text{ cm}^{-3}$$

For p-type samples of GaAs with carrier concentrations ranging from $1 \times 10^{14} \text{ cm}^{-3}$ to $1 \times 10^{18} \text{ cm}^{-3}$, we estimate the E_f will range from 450 meV to 200 meV above the valence band. Hence, at room temperature, E_f is at least several kT (25 meV) away from the shallow acceptor levels (20 to 40 meV) in GaAs. Furthermore, the effect of increased donor-acceptor compensation at a fixed temperature is to move the Fermi level even farther into the energy gap (Refs 37, 40). Thus, compensation effects will make the expressions given above for n and p even more accurate.

Since $n_i = 1 \times 10^7 \text{ cm}^{-3}$, we conclude that, for p-type concentrations ranging from $1 \times 10^{15} \text{ cm}^{-3}$ to $1 \times 10^{18} \text{ cm}^{-3}$, we can use the expression

$$p = N_a - N_d$$

for room temperature electrical measurements with a percent error less than 1×10^{-4} .

2. Electromagnetic Transport Properties. The most general development of semiconductor transport properties begins with the Boltzmann transport equation defined in quantum mechanical phase space (Refs 34, 41). Solutions to this equation are then examined when electric and magnetic fields are applied and are used to deduce the resulting electrical transport properties. The specific energy, momentum and spatial relationships that result for electrons in semiconductor

crystals produce the unique electrical properties of semiconductors. Reviews of recent semiconductor transport theory are available (Refs 38 and 39) for electrons and holes, respectively. In this section, we present the relevant theory to allow interpretation of room temperature mobility and resistivity measurements of ion-implanted Gas.

Application of an electric field E to a semiconductor causes an electric current density J , which are related as

$$J = \sigma E$$

where the conductivity σ and resistivity ρ are reciprocals,

$$\rho = 1/\sigma$$

In general, J and E are vectors related by the conductivity tensor σ . However, for crystals with cubic symmetry (like GaAs), the tensor reduces to a scalar and the current density is isotropic.

The expression for conductivity

$$\sigma = n e \mu_e + p e \mu_h$$

reflects the fact that both electrons and holes contribute to the conductivity. Here n and p are the electron and hole densities, μ_e and μ_h are the electron and hole mobilities and e the electron charge. Often, carriers of one type predominate and the conductivity expression reduces to a single term. Some conditions to check for this case are described below. Conductivity can be measured by many techniques

(Ref 79) with one particular method due to Van der Pauw described in Section II.B.3.

The net carrier concentration is usually determined by Hall measurements. Van der Pauw has derived a formula which defines the Hall coefficient in terms of the measured Hall voltage and magnetic field for flat samples, to be discussed in Section II.B.3. The theoretical Hall coefficient for a semiconductor which has both electrons and holes present has the form (Ref 41)

$$R_H = -\frac{1}{e} \frac{r b^2 n - r' p}{(bn + p)^2}$$

where $b = \mu_e/\mu_h$, $r = \langle T_e \rangle^2 / \langle T_e^2 \rangle$ and $r' = \langle T_h \rangle^2 / \langle T_h^2 \rangle$ with T_e and T_h the mean time between collisions of electrons and holes, respectively. These r factors (or Hall factors) are also the ratios of the measured Hall mobilities to the true drift (conductivity) mobilities in non-degenerate semiconductors. Recent estimates of this ratio for electrons in room temperature GaAs, shown in Figure II-4, are 15 to 20% greater than unity. Calculations of an equivalent ratio for holes has not been done, but it is reasonable to assume that a value of unity is also appropriate (Ref 39).

If the GaAs sample is strongly n- or p-type, the Hall coefficient becomes simply

$$R = -1/n_e , \quad \text{n-type}$$

$$R = 1/p_e , \quad \text{p-type}$$

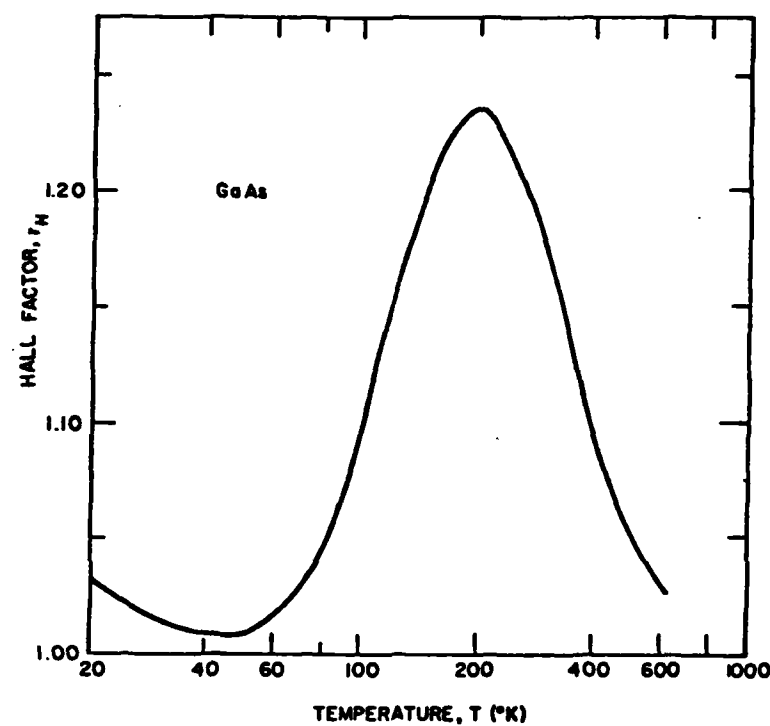


Figure II-4. Theoretical temperature dependence of Hall factor for n-type GaAs (Reference 38).

An expression can be developed to check for mixed conduction. As shown in Reference 40, an equation can be developed which relates the Hall mobility, $\mu_H = R\sigma$, to the electron and hole mobilities as

$$\frac{\left[\frac{1}{2}(\mu_e - \mu_h) + \mu_H\right]^2}{(\mu_e + \mu_h)^2/4} + \frac{1/\sigma^2}{1/(4e^2 \mu_e \mu_h n_i^2)} = 1$$

where n_i is the intrinsic carrier concentration. Solving this for the Hall mobility, we find

$$\mu_H = \pm \sqrt{\left(1 - \frac{4e^2 \mu_e \mu_h n_i^2}{\sigma^2}\right) \left(\frac{\mu_e + \mu_h}{2}\right)^2 - \frac{(\mu_e - \mu_h)^2}{4}}$$

This shows that μ_H will be equal to either μ_e (for n-type) or μ_h (for p-type) unless mixed conduction effects cause the approximate equality

$$\sigma^2 \approx 4e^2 \mu_e \mu_h n_i^2$$

For room temperature GaAs where $n_i \approx 10^7 \text{ cm}^{-3}$ and using typical GaAs values of $\mu_e = 5500 \text{ cm}^2/\text{volt-sec}$, $\mu_h = 250 \text{ cm}^2/\text{volt-sec}$, we find we need

$$\rho = \frac{1}{\sigma} = 3 \times 10^8 \Omega \text{-cm}$$

Thus the resistivities should be of this magnitude before mixed conduction effects are present. Resistivities $\ll 3 \times 10^8 \Omega\text{-cm}$ are not indicative

of mixed conduction in GaAs.

For room temperature GaAs, the two main scattering mechanisms are lattice vibrations and ionized impurity scattering. The total mobility due to each process is found by

$$\frac{1}{\mu_{\text{total}}} = \frac{1}{\mu_L} + \frac{1}{\mu_I} \quad (10)$$

where μ_L and μ_I are the lattice limited and ionized impurity limited mobilities, respectively.

Figure II-5 shows a theoretical plot of room temperature electron mobilities versus free electron concentration (Ref 38) which has been very successful in interpreting experimental data. Figure II-6 (Ref 39) shows various room temperature hole mobility experimental data with a curve fit by using Eq (10) with $\mu_L = 400 \text{ cm}^2/\text{volt-sec}$ and μ_I from the Brooks-Herring formula

$$\mu_I = (3.28 \times 10^{15}) \frac{T^{3/2}}{N_I \left(\frac{m_h}{m_0} \right)^{1/2}} \left[\ln(1+b) - \frac{1}{(1+b)} \right]^{-1}$$

$$b = (1.29 \times 10^{14}) \frac{m_h}{m_0} \frac{T^2 K}{n'}$$

where K is the static dielectric constant, N_I is the ionized impurity concentration and n' is the free electron concentration. For room temperature p-type GaAs, $N_I = (N_a + N_d)$ and $n' = (N_a - N_d)$. As Wiley explains in Reference 39, the curve has no real theoretical significance

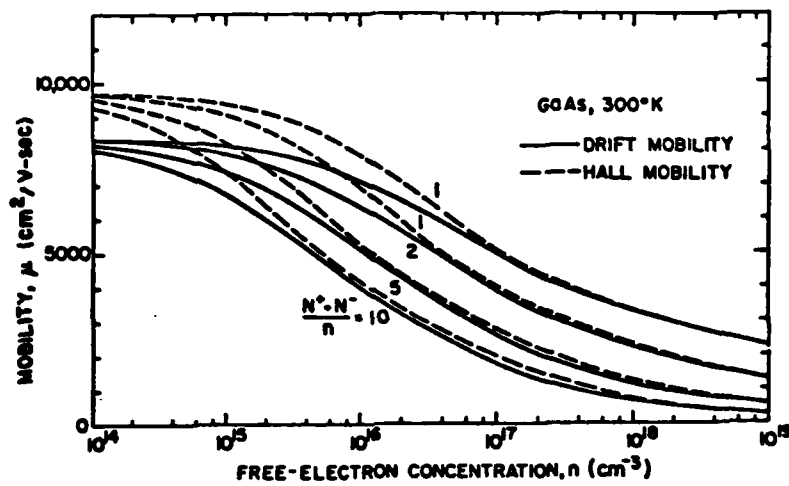


Figure II-5. 300^0 K Hall and drift mobilities versus electron concentration in GaAs (Reference 38).

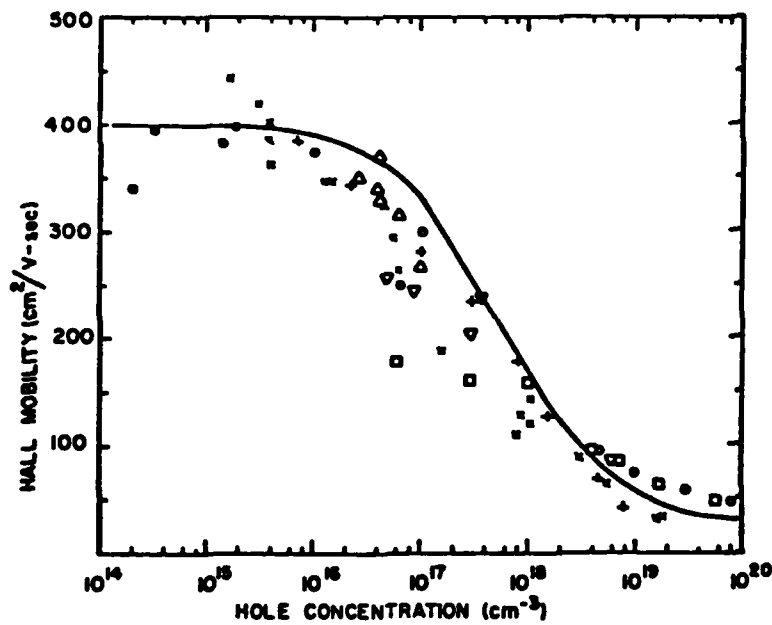


Figure II-6. 300^0 K Hall mobility versus hole concentration in GaAs (Reference 39).

since the development is based on an analogy to electrons which is not strictly true. However, it provides a phenomenological model which allows comparisons and extrapolations of hole mobility data.

Therefore, with room temperature measurements of mobility and electrical carrier concentration under conditions where (1) the carrier concentration is equal to $(N_a - N_d)$, (2) the ionized impurity mobility is described by the Brooks-Herring formula and (3) the lattice mobility is a known constant, there is sufficient information to calculate the ionized impurity concentration $(N_a + N_d)$. It is then also easy to solve for N_a and N_d . Such a procedure was used for ion-implanted silicon electrical profiles where other methods were used to correlate impurity concentration to measured mobility values (Ref 42).

3. Van der Pauw Equations. Historically, Hall measurements were made on bar shaped samples with up to eight accurately placed electrical contacts. Resistivity measurements, while not as complex, also required some accuracy in sample preparation. Thus, these techniques required samples of rather precise geometry which, especially for semiconductor crystals, were difficult to construct. Van der Pauw (Refs 43, 44) showed that equations could be developed for flat wafer samples, or "lamella," of arbitrary shape with four electrical contacts on the periphery. His results are presented below.

For the sheet resistivity, ρ_s , the expression for a sample of thickness t is

$$\rho_s = \frac{\rho}{t} = \frac{\pi}{\ln 2} \left(\frac{R_{MN,OP} + R_{NO,PM}}{2} \right) f \left(\frac{R_{MN,OP}}{R_{NO,PM}} \right)$$

where M, N, O, P refer to the four contact points located, in order, around the periphery of the sample. Thus, for example, $R_{MN,OP}$ refers to a resistance measurement made with a current flowing in at M and out at N, while the voltage is read across points O and P. The resistance ratio, indicated as the argument of the function f , determines the value of f from a solution of the transcendental equation

$$\cosh \left\{ \frac{(R_{MN,OP}/R_{NO,PM}) - 1}{(R_{MN,OP}/R_{NO,PM}) + 1} \left(\frac{\ln 2}{f} \right) \right\} = \frac{1}{2} \exp \left(\frac{\ln 2}{f} \right)$$

which is usually plotted or tabulated as a function of the resistance ratio. The geometrical placement of the contacts is, therefore, not explicitly used, but is reflected in the value of f , which is in general less than one, but is equal to one for a symmetric sample with symmetric contact placement.

For Hall measurements with the magnetic field, B , applied normal to the wafer, the sheet Hall coefficient is

$$R_{HS} = \frac{R}{t} = \frac{\Delta R_{MO,NP}}{B}$$

with $\Delta R_{MO,NP}$ being the change in resistance which occurs when the magnetic field is applied. In this case, the current flows between contacts M and O while the Hall voltage is measured across N and P.

Van der Pauw made some estimates of errors introduced by the finite size contacts on circular samples, as opposed to the dimensionless point contacts assumed in the theoretical derivation. Further analysis was reported in Reference 45 for the case of square and triangular contacts

in the corners of square samples. In both studies, the correction factor is greater than unity (i.e., the Hall measurement and resistivity measurements are too low), and the effect of finite contacts is greater on the Hall measurements than on the resistivity measurements. Assuming a square sample with triangular contacts that are 1/8 the length of the sample edge (a close approximation to the samples in this experiment), Reference 45 finds a correction factor of 1.002 for the resistivity and a factor of 1.1 for the Hall voltage. Thus, the expected error for the Hall mobility, $\mu_H = \frac{R_H}{\rho}$, would be on the order of 10%.

4. Layer Removal Equations. The surface electrical measurements described above can be combined with layer removal techniques to obtain the electrical carrier concentration and carrier mobility as a function of depth. Petriz has shown (Ref 46) that, if the carrier concentration and mobility are functions of depth (as they are for ion-implanted samples), the resulting expressions for the sheet Hall coefficient, R_{H_s} , and the sheet resistivity, ρ_s , are

$$R_{H_s} = \frac{\int n(x) \langle \mu(x) \rangle^2 dx}{e [\int n(x) \langle \mu(x) \rangle dx]^2}$$

$$\sigma_s = \frac{1}{\rho_s} = e \int n(x) \langle \mu(x) \rangle dx$$

where $n(x)$ is the carrier concentration, $\langle \mu(x) \rangle$ is the drift mobility averaged in momentum space, and e is the electron charge.

The typical single surface electrical measurement characterization of ion-implanted semiconductors attempts to measure the sheet carrier

concentration, N_s , and the average conductivity mobility, μ_c , which are

$$N_s = \int n(x)dx$$

$$\mu_c = \frac{\int n(x)\langle\mu(x)\rangle dx}{\int n(x)dx}$$

while the measured surface values for the measurement actually measure effective values shown as

$$(N_s)_{\text{eff}} = \frac{1}{eR_{H_s}} = \frac{[\int n(x)\langle\mu(x)\rangle dx]^2}{\int n(x)\langle\mu(x)\rangle^2 dx}$$

$$(\mu_c)_{\text{eff}} = R_{H_s} \sigma_s = \frac{\int n(x)\langle\mu(x)\rangle^2 dx}{\int n(x)\langle\mu(x)\rangle dx}$$

This shows part of the motivation for profiling ion-implanted semiconductors to obtain $n(x)$ and $\mu(x)$ since the weighting of the results by the mobility can obscure the results of a single surface electrical measurement.

As shown in Reference 42, the equations for sheet Hall coefficient and sheet resistivity can be solved for the Hall mobility and carrier concentration as

$$\mu_H(x) = \frac{d(R_{H_s} \sigma_s^2)}{dx} \quad / \quad \frac{d\sigma_s}{dx}$$

$$n(x) = \frac{\mu_H(x)}{e\mu_c(x)} \left(\frac{d\sigma_s}{dx} \right)^2 \quad / \quad \frac{d(R_H \sigma_s)^2}{dx}$$

As described above in Section II.B.2., for room temperature GaAs, the ratio of Hall to conductivity mobility is very close to unity. After expressing the derivatives as small incremental differences, the layer removal equations for the Hall mobility and electrical carrier concentration are

$$\mu_i = \frac{\frac{(R_H \sigma_s)_i}{(\rho_s)^2} - \frac{(R_H \sigma_s)_{i+1}}{(\rho_s)^2}}{\frac{(\frac{1}{\rho_s})_i - (\frac{1}{\rho_s})_{i+1}}{d_i}}$$

$$n_i = \frac{\frac{1}{\rho_s}_i - \frac{1}{\rho_s}_{i+1}}{e\mu_i d_i}$$

where the subscript i refers to the i th layer and d is the layer thickness.

Since these equations combine the measurement of two adjacent layers, one bad measurement can influence two calculated values of mobility and carrier concentration. Also, the equations involve subtractions of the reciprocals and squares of reciprocals of sheet resistivity. This makes the results very sensitive to measurement errors. Several data smoothing techniques have been reported. The one used in this experiment consisted of calculating and plotting several combinations of the data where one

or two adjacent layer data sets were skipped. This has the merit of using actual data values. In addition, the logarithm of actual sheet Hall coefficients and sheet resistivities were plotted as a function of depth. These plots generally were very smooth curves with anomalous data points clearly displaced. This procedure identified values that should be ignored in calculating the depth profiles.

5. Previous Electrical Measurements for Carbon Implants in GaAs.

As was shown in Table II-1, the majority of electrical measurements performed on carbon implanted GaAs were surface electrical measurements. Only two (Refs 21, 31) performed chemical etching to determine the electrical activity as a function of depth. Also, only two of the studies use surface electrical measurements as the primary experimental procedure (Refs 15, 28). Some reports only quote very limited electrical measurement results for carbon implants (Refs 28, 29, 30).

Taken together, the surface electrical measurements show a distinct trend of decreased electrical activation as the carbon implant dose is increased. The highest electrical activation is achieved for the lower doses, which for carbon implant doses of $1 \times 10^{13} \text{ cm}^{-2}$ has ranged from 2% to 50% (Refs 15, 21, 30). An apparent saturation occurs as the dose increases to 1×10^{15} to $1 \times 10^{16} \text{ cm}^{-2}$, where the electrical activation is much less than 1%. Thus, there is some mechanism which prevents carbon from increasing the p-type electrical activity in proportion to the increase in implant dose. Suggestions for the lower electrical activation have included self-compensation of carbon donors and acceptors, electrically inactive carbon complexes or interstitial carbon, or electrically compensating defect centers produced by implantation. Reports on dual implantation of Ga or As along with carbon show some steering of the

electrical activity of carbon in an expected fashion (Refs 15, 31). That is, for example, co-implantation of carbon with Ga should increase As vacancies and enhance carbon acceptor behavior. However, the effects are much less dramatic for carbon than equivalent dual implants with other Group IVA dopants where electrical type conversion has even been demonstrated (Refs 13, 15).

There is no clear trend of the sheet Hall mobility determined by surface electrical measurements. In some cases, the mobility decreases as the dose is increased (Refs 15, 28), while in other cases the sheet mobility increases with increasing carbon dose (Refs 21, 29). There are no explanations suggested for this behavior.

Only References 21 and 31 performed electrical profiles of carbon implants. With an assumed lattice mobility of $450 \text{ cm}^2/\text{volt}\cdot\text{sec}$, the electrical measurements of mobility and p-type carrier concentration were used to find the donor and acceptor concentration (as described in Section II.B.4.). Reference 21 analyzes a $1 \times 10^{13} \text{ cm}^{-2}$ carbon implant, which had a doping efficiency of 50%, and concluded from the close correlation of the LSS profile and the calculated acceptor concentration profile that, at this dose, all the carbon went substitutional on As sites. Reference 31 analyzes a higher dose, $1 \times 10^{14} \text{ cm}^{-2}$, carbon implant which had a doping efficiency of 4%. In this case, the interpretation made of the electrical profile measurements was that less than 20% of the carbon went on As sites and that the remainder of the carbon could not be accounted for. Reference 31 also used dual implantation of carbon with Ga, which is reported to increase the acceptor concentration to 60% of the available carbon and to increase the doping efficiency to 12%.

In summary, the results of past carbon implants into GaAs have indicated that the maximum achievable doping efficiency is 50% at low doses and that higher doses produce even lower efficiencies. Dual implantation of carbon with Ga or As does not produce as strong a change in the electrical activity as do dual implants with other Group IVA dopants. Various mechanisms have been proposed to explain the observed behavior.

C. Luminescence Properties of GaAs

Induced luminescence is one of the experimental techniques used to collect data on semiconductor materials. Some of the merits of luminescence experiments include the relative ease of data collection and sensitivity of the technique, especially for direct bandgap materials such as GaAs. Bebb and Williams (Ref 47) have written a thorough review of the theory of photoluminescence of semiconductors. References 48 and 49 offer surveys of reported results and analyses for GaAs. In this section, we present a brief review of the applicable theory of luminescence of GaAs.

1. Excitation Theory. The generation of induced luminescence in semiconductors can be separated into three general steps. First, the incident radiation is absorbed in the material creating electron-hole pairs. The generation of these electron-hole pairs is usually some function of distance from the surface which depends on the type of radiation. Second, the excess, or non-equilibrium, electron and hole charge carriers diffuse some distance (characterized by the minority carrier diffusion length) before recombining. There are various recombination possibilities, not all of which lead to photon emission (e.g., Auger transitions), but in direct bandgap semiconductors such as GaAs

at low temperatures the photon emission processes are most likely to occur (Ref 50). The radiative recombination rate as a function of depth from the surface can be strongly influenced by non-radiative recombination sites on the surface of the GaAs. The third step in the generation of induced luminescence is the propagation of radiation from the recombination site, possibly to be absorbed again, but some fraction escaping from the surface, potentially to be detected in a luminescence experiment (Ref 48).

In the following paragraphs, we elaborate on these three steps, starting with the absorption of the incident radiation. Today, lasers are probably the most common excitation sources, partly because of their relative ease of operation and because of the range of control they allow over experimental parameters such as illumination intensity. The photon flux of the incident radiation decreases exponentially as $\exp(-2\alpha X)$ where the absorption coefficient α is a function of the wavelength λ of the incident light

$$\alpha = 2\pi k/\lambda$$

where k , the extinction coefficient, is the imaginary part of the index of refraction. Thus, the radiation intensity is decreased to $1/e$ of its value at the surface at a depth

$$X = 1/2\alpha$$

Table II-2 lists values of k from Reference 51 (with the exception of the 3500 Å data) for GaAs at 21° K, which is approximately the temperature of the samples used in these luminescence experiments.

TABLE II-2
ABSORPTION DEPTHS IN GALLIUM ARSENIDE AT 21° KELVIN

| Approximate Source (\AA) | Wavelength (\AA) | k | $1/2 \alpha$ (\AA) |
|--|--------------------------------|-------|----------------------------------|
| 3500, Kr Laser | 3400 | | 160 ⁽¹⁾ |
| 4880, Ar Laser | 4900 | 0.370 | 1054 |
| 5145, Ar Laser | 5150 | 0.310 | 1322 |
| 6328, HeNe Laser | 6300 | 0.194 | 2584 |

(1) Estimated at 21° K from 300° K data where absorption is calculated to be 144 \AA

The recombination radiation will have a wavelength at or below the bandgap energy and has a penetration depth which can be 10 to 1000 times longer than the penetration depth of the excitation radiation (Ref 47); thus, reabsorption is much less likely than the initial absorption process.

After the electrons and holes are formed, they diffuse some distance before recombining. It is the minority carrier lifetime which limits the process for semiconductors which are strongly n- or p-type because it is the minority carrier population which is most significantly affected by the generation of excess carriers in a process such as photoluminescence. Thus, in p-type material, it is the generation of excess electrons which governs the rate at which holes, the majority carrier, will recombine (Refs 34, 35). Hence, the electron diffusion length L_n , given by

$$(L_n)^2 = (\mu_e kT/e) t_e$$

(where μ_e is the electron mobility, e is the electron charge, k is Boltzmann's constant, T is the absolute temperature, and t_e is the electron lifetime) is the characteristic linear dimension of p-type material which would give rise to recombination radiation following absorption.

Values of L_n for GaAs at low temperature (10° K) are not readily available. Most experiments on carrier diffusion lengths are performed at room temperature (Ref 52). These results show that, as the hole concentration increases from 10^{15} to 10^{19} cm^{-3} , the electron diffusion length decreases from 100μ to 10μ or less. Cone (Ref 53) has performed a theoretical calculation of cathodoluminescence from Mg implanted GaAs which fit 10° K luminescence by including an electron diffusion length of 0.21μ . He also estimated the theoretical value of L_n at 10° K to be 0.28μ by using theoretical values of electron lifetime along with experimental values of electron mobility.

Almost all of the 120 keV carbon atoms are expected to lie within 0.7μ from the surface. Using values above for laser penetration depth and electron diffusion length, most of the carbon implanted layer should be a source of recombination radiation when illuminated with a helium-neon laser. For the shallowest illumination, the UV lines of a Kr laser only penetrate 0.02μ with maximum expected electron diffusion reaching to 0.3μ .

2. Luminescence of GaAs. The spectral lines seen in a luminescence experiment are directly related to the energy difference of the electron energy states involved in the radiative recombination process. Some of these energy states are due to the intrinsic characteristics of the GaAs crystal structure, such as free excitons. Other energy states can also be created by extrinsic additions to the GaAs lattice, such as impurity atoms or crystal defects, and radiative recombinations through these energy levels can be used to monitor the extrinsic states. Also, phonon coupling with optical transitions can introduce peaks in the observed spectra which are shifted down in energy at energies characteristic of the type of phonon and the number of phonons participating in the radiative transition. Since phonons arise from lattice vibrations, their presence can give indications of the amount of lattice disorder present in the crystal. A diagram showing, in general, the levels involved for luminescence from GaAs is Figure II-7.

Figure II-7 represents the energy level structure of electron states in GaAs which are involved in the luminescence transitions seen in this experiment. The arrows in the diagram indicate luminescence transitions, which are arranged in order (from left to right) as they appear in the luminescence spectra taken in this experiment. The bandgap exists between the conduction band, E_C , and the valence band, E_V . Within several meV of the conduction band are exciton levels, E_X ; donor levels, E_D ; and excitons bound to defect complexes, E_{XC} . While these are indicated as single levels, some structure is observed in the spectrum of transitions from these levels to the valence band. Several decades of meV above the valence band are the shallow acceptor levels, E_{AS} , and acceptor complexes, E_{AC} . Transitions from the valence band

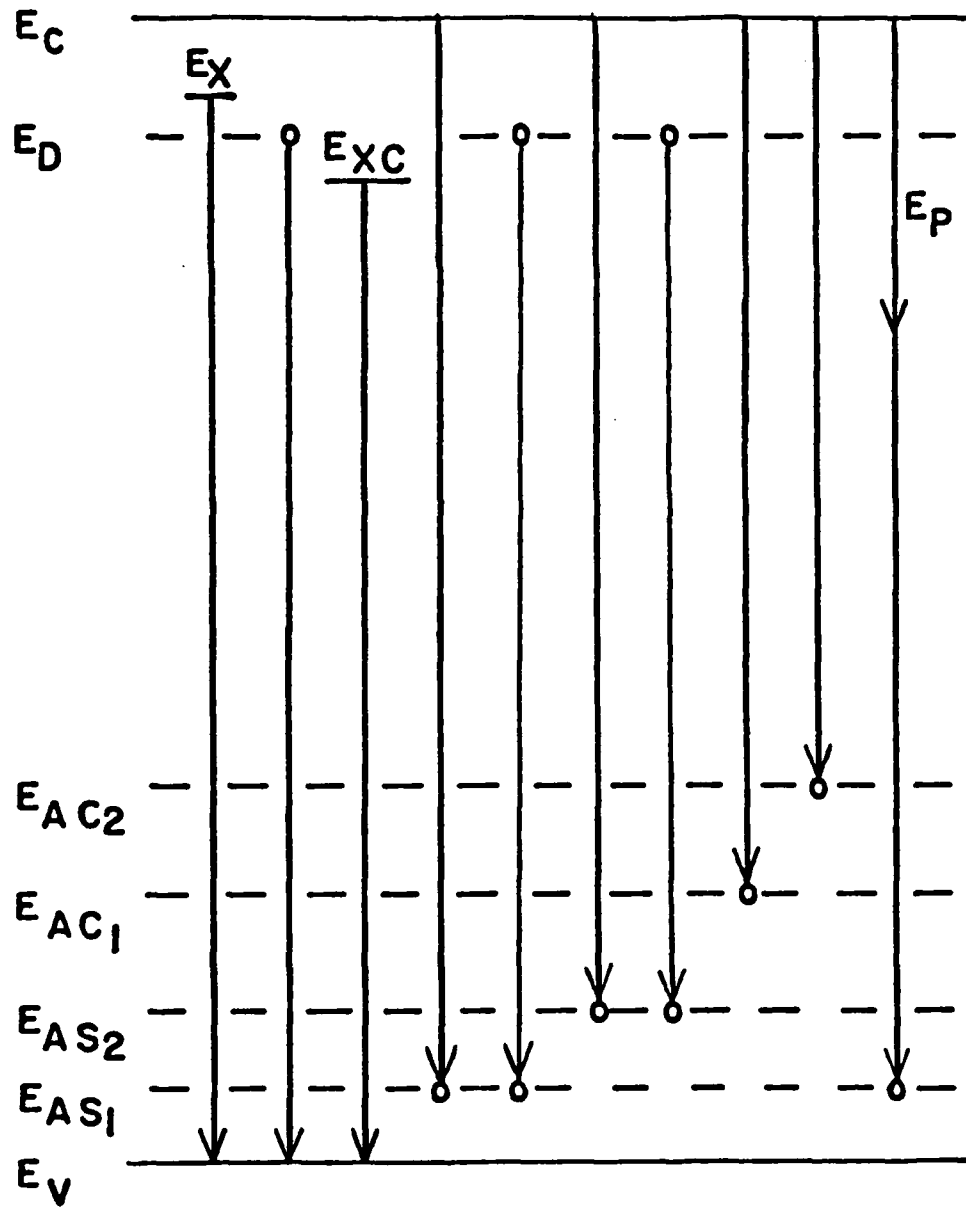


Figure II-7. Luminescence transitions in GaAs. Diagram represents the energy level structure (not to scale) in GaAs which gives rise to the luminescence transitions seen in this experiment. See text for a description of the energy levels and the observed transitions.

to shallow acceptors tend to overlap in energy the donor to shallow acceptor transitions. Only conduction band to acceptor transitions are observed. The last transition indicated in Figure II-7 symbolizes the phonon coupled transitions involving a phonon of energy E_p . The shallow acceptor levels are replicated in the luminescence spectra shifted in energy depending on the number and type of phonons involved in the transition. Thus, while only one phonon assisted transition is indicated in Figure II-7, multiple luminescence lines arise from a transition involving a single shallow acceptor. Finally, Figure II-7 is not an exhaustive presentation of all possible luminescence lines from GaAs but, instead, attempts to highlight those transitions seen in this experiment.

There are several ways to present the spectral lines seen in GaAs. This discussion will arbitrarily group the spectra into three categories corresponding to the order in which the lines appear as the energy decreases below the bandgap energy. The bandgap energy is 1.5202 eV from GaAs below 20° K (Refs 54, 55).

2a. Exciton Band. Within an interval of about 3 meV and down to approximately 5 meV from the bandgap energy are the exciton related lines and the donor free to bound lines. These are the highest energy transitions since the direct conduction band to valence band transition is not observed. The energies and line assignments given by Williams and Bebb (Ref 49) are as follows:

| <u>Energy (eV)</u> | <u>Description</u> |
|--------------------|-----------------------------------|
| 1.5156 | Free exciton |
| 1.5145 | Exciton bound to neutral donor |
| 1.5137 | Donor free to bound |
| 1.5135 | Exciton bound to ionized donor |
| 1.5125 | Exciton bound to neutral acceptor |

More detailed discussion of the exciton lines and their assignments is given in Reference 56. Some experimental results from high resolution spectrometers using controlled doping vapor phase epitaxial GaAs and molecular beam epitaxial GaAs are given in References 57 and 58, where they assign particular donors and acceptors to lines in the exciton band. However, the PL system used in this experiment was utilized with a maximum resolution of approximately 0.2 meV, and, hence, the identification of particular donors and acceptors from exciton related spectral lines is not possible. Also, the 1.5137 and 1.5135 eV lines were not resolvable. Within the 0.2 meV resolution, the general identifications of the exciton lines are: (1) the 1.5156 eV line is characteristic of the intrinsic GaAs structure, (2) the 1.5145, 1.5137 and 1.5133 eV lines are donor related, and (3) the 1.5125 eV line is acceptor related. The kT linewidths of the exciton lines are approximately 0.5 meV at 6° K and 2.2 meV at 25° K, with a skew towards higher energy by the factor

$$\exp[-(hv - E_x)/kT]$$

(Ref 47). Thus, low temperatures are required to resolve exciton structure.

There have been more recent experimental results for high purity GaAs which have identified lines at slightly lower energies which are related to the presence of impurities or defects. A line at 1.51165 eV was identified as being a donor-acceptor complex in high purity VPE GaAs (Ref 59). Experiments with Be doped molecular beam epitaxial GaAs identified a family of lines between 1.511 eV and 1.504 eV as excitons bound to point defects (Ref 60). Particular lines would increase with increased doping levels of Be.

2b. Shallow Acceptor Band. With all donor states approximately 5.6 meV down from the conduction band, the donor free to bound transitions appear as a single line within the band described above as the exciton band. However, the acceptor free to bound transitions in GaAs are generally separated by several meV for each separate acceptor species and appear in a separate band from approximately 26 to 40 meV below the bandgap energy. Here, the carbon free to bound transition appears at 1.4935 eV as one of the shallowest acceptors in GaAs, with beryllium the only other candidate at this energy.

One complication in clearly identifying acceptor species in this band is the simultaneous appearance of donor-acceptor lines (grouped as a single unresolved line in GaAs, as opposed to the family of lines seen in GaP) appearing at approximately 3 meV down from the acceptor line. For several acceptors (carbon, zinc and silicon), 3 meV is also the approximate separation of the acceptor free to bound lines, leading to an overlapping effect. This problem (and one solution) was addressed by Rossi, Wolfe and Dimmock (Ref 61, and discussed in Ref 47) where a magnetic field variation was used to help unravel free-to-bound and donor-acceptor line assignments. They concluded that a set of three lines frequently seen in epitaxial GaAs were really four lines, with the following assignments:

| | <u>Acceptor #1</u> | <u>Acceptor #2</u> |
|----------------|--------------------|--------------------|
| free-to-bound | 1.4933 eV | 1.4890 eV |
| donor-acceptor | 1.4899 eV | 1.4861 eV |

Subsequent work by Ashen, et al. (Ref 17) shows that acceptors 1 and 2 were carbon and zinc, respectively, and that silicon acceptors appear at 1.4850 eV. Therefore, GaAs with these three impurities (C, Zn, Si)

would have overlapping free-to-bound and donor-acceptor lines separated by less than 1 meV. Further confirmation of these line assignments, along with plots clearly showing the overlapping conduction band to acceptor transitions with the donor-acceptor transitions, is given in Reference 18.

Two luminescence techniques which can also be used to help separate line assignments in this region are variations of sample temperature and luminescent intensity. Increasing sample temperature from 5° K to 25° K will ionize donors and, hence, extinguish donor-acceptor lines. Also, during the temperature increase, donor-acceptor lines shift to higher energy. Increasing luminescent intensity by a few orders of magnitude will also shift donor-acceptor lines to higher energy.

Lines appearing in the shallow acceptor band are observed to appear with longitudinal optical phonon (LO) replicas which lie 36.0 meV down in energy. Hence, the shallow acceptor lines appear in the same relative order, but differences in phonon coupling strength may cause differences in intensity. One reason is that phonon coupling can be weaker for the less tightly bound (shallower) acceptors. More than one phonon can be involved in the radiative transition, causing spectral lines down in energy at multiples of the single LO phonon energy. For GaAs, the two LO phonon replicas may begin to overlap the next band, called the deep acceptor band.

Photon-phonon interactions have been used in Raman spectroscopy to analyze the crystal structure of ion-implanted GaAs (Ref 62). The strength of the phonon spectra can be monitored as the implant is etched away and spatial regions identified as amorphous, partly crystalline or crystalline. While similar experiments have not been done with photoluminescence, the concept may also be applicable.

2c. Deep Acceptor Band. Williams and Bebb (Ref 47)

described the lines appearing from approximately 1.4 eV to 1.2 eV as vacancies bands because they had been identified with vacancies or vacancy complexes. We choose to call this the deep acceptor band (relative to the previous shallow acceptor band) since the primary peaks seen in the experimental spectra are due to Mn acceptors and possibly Cu acceptors.

The line assignments in this energy region are not as clearly defined as those in the shallow acceptor band. The 1.41 eV band (or broad peak) had been associated with As vacancies or complexes involving As vacancies (Ref 47). However, a variety of doping experiments for GaAs intentionally doped with Mn by ion-implantation (Ref 63), by molecular beam epitaxy (Ref 64) and in boule grown GaAs (Ref 65) clearly show that a sharp line at 1.408 eV is due to Mn. A second line commonly seen in this energy region is the 1.35 eV peak, which has been variously assigned to complexes with both As vacancies or Ga vacancies. Copper is sometimes identified as part of the 1.36 eV complex center (Refs 47, 66, 67). Both the 1.41 eV line and the 1.36 eV line demonstrate phonon replicas, including the 9 meV transverse acoustic (TA) phonon in addition to the 36 meV longitudinal optical (LO) phonon. A third deeper and much broader (200 meV full width at half-maximum) band is sometimes observed near 1.2 eV in n-type GaAs. One complex was reported at 1.179 eV for a Ga vacancy complex coupled to Si on Ga sites. By analogy with other dopant complexes near this energy, a similar complex for carbon would lie at an energy less than 1.18 eV. In conclusion, for the deep acceptor bands in GaAs over the energy range observed in this experiment, there are three deep acceptor bands at 1.41, 1.36 and 1.2 eV which are likely to be observed.

3. Doping Concentration Effects on Luminescence. Impurity doping concentrations have been observed to have large effects on luminescence from GaAs. As the impurity concentration increases, the spectral lines characteristic of relatively pur samples, such as resolved exciton lines and resolved shallow acceptor lines, exhibit changes in character. As shown in Figure II-8 (reproduced from Ref 68), as the impurity concentration of a n-type sample changes from $2 \times 10^{16} \text{ cm}^{-3}$ to $1 \times 10^{17} \text{ cm}^{-3}$, the exciton and shallow acceptor bands begin to change from their resolved line structure to relatively broad bands. Further increases in impurity concentration, up to $1 \times 10^{18} \text{ cm}^{-3}$ in Figure II-8, practically quench the exciton band and simultaneously merge the acceptor band into one broad band, which shifts towards higher energy. This shift is characteristic of donor-acceptor lines. Similar concentration dependent behavior of high purity GaAs has been reported in References 64 and 69.

Spectral peak shifts with increased doping levels have been found to be related to the electrical type of the GaAs samples. The effect of increased doping level on cathodoluminescence spectra was first reported by Cusano (Ref 70). The peaks characteristic of the shallow acceptor band were found to shift for impurity concentrations $> 5 \times 10^{17} \text{ cm}^{-3}$, and the shift was in opposite directions for n-type and p-type material. For n-type material, increased doping shifts the peak to higher energies. This shift for n-type material was attributed to a shift in the Fermi level into the conduction band (Burstein-Moss effect). For p-type GaAs, increased doping shifts the spectral peak to lower energies and was attributed to the onset of dominant donor-acceptor pair recombinations. An extension of the doping effect experiment was done by Tuck using

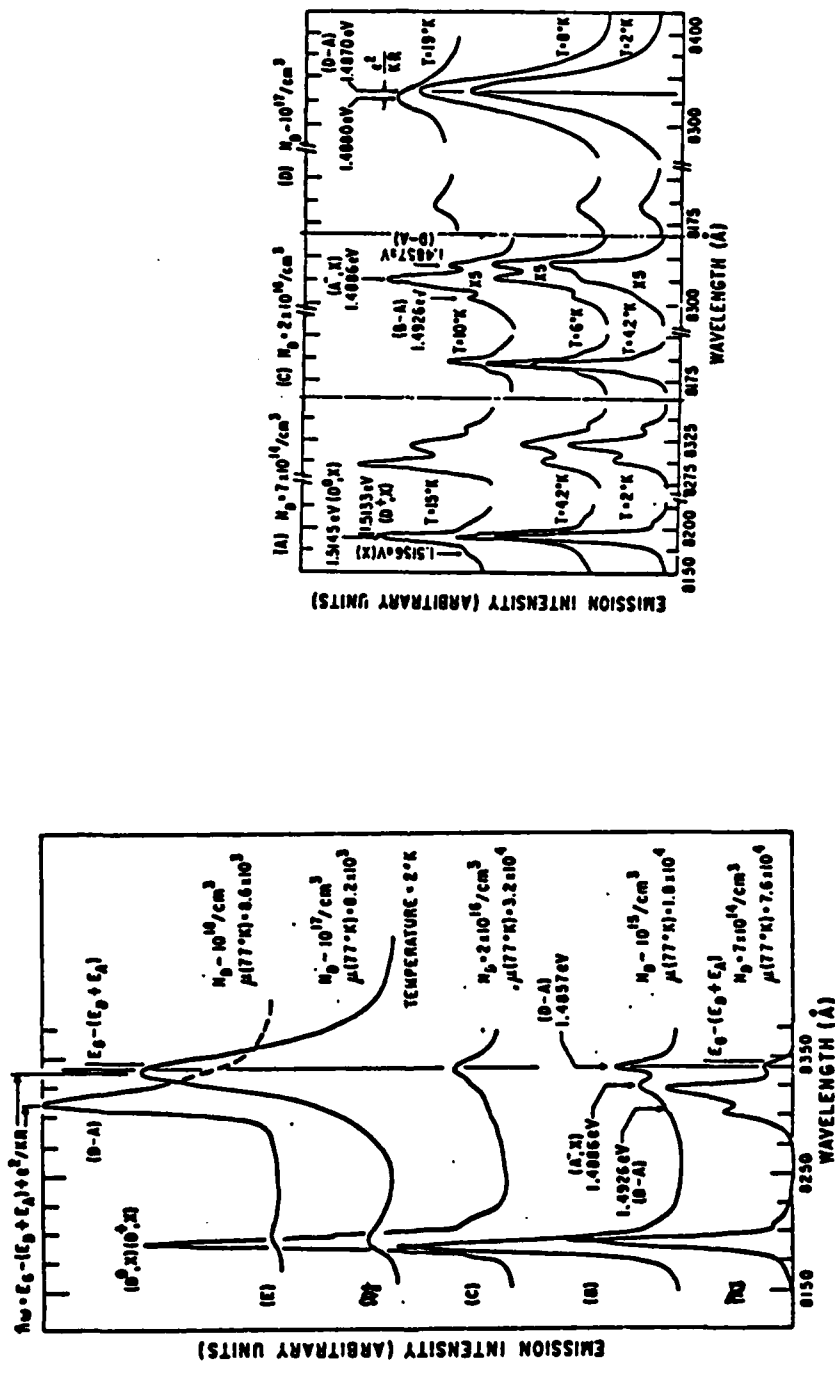


Figure II-8. GaAs luminescence spectra changes with doping level (Reference 68).

photoluminescence from p-type GaAs (Ref 71). His work verifies the p-type peak shifts to lower energies as acceptor concentration increases, but he also demonstrated that donor-acceptor compensation is a key factor. Specifically, the peak shift with concentration can be reversed as the concentration level of acceptors approaches the concentration level of the donors (i.e., approaches exact compensation). The explanation of this shift to lower energies for a spectral peak in p-type material was that the Fermi level moves up through the finite width of the acceptor impurity band as exact compensation is approached. A later photoluminescence experiment verified this compensation dependence on the doping effect (Ref 72). However, their explanation involved tunnel assisted radiative recombinations between electrons and holes localized in spatially separated regions by charge fluctuations due to heavy doping.

A theoretical description of heavy doping in semiconductors is reviewed in Reference 73. In lightly doped samples, the wave functions do not overlap and the energy levels associated with the impurity are discrete and may lie within the band gap. At intermediate doping levels, the wave functions begin to overlap, and the discrete energy levels become impurity bands, still separate from the conduction or valence bands. Finally, at heavy doping levels, the impurity levels merge with the band edges and effectively reduce the valence band to conduction band edge.

For 120 keV carbon implanted GaAs with doses of $1 \times 10^{13} \text{ cm}^{-2}$ to $1 \times 10^{15} \text{ cm}^{-2}$, the peak carbon concentration increases from approximately $3 \times 10^{17} \text{ cm}^{-3}$ to $3 \times 10^{19} \text{ cm}^{-3}$. Therefore, large doping levels and attendant changes in spectral peaks would be expected. An example of

the type of spectral changes one could expect from implanted epitaxial GaAs is shown in Reference 74 for a $1 \times 10^{15} \text{ cm}^{-2}$ dose silicon implant. They combined low energy (2 keV) cathodoluminescence with chemical etches to detect the luminescence from relatively thin layers throughout the implanted region and also performed electrical profiling measurements throughout the implanted region. Their results show that the exciton and shallow acceptor bands are not present until the n-type electrical carrier concentration is reduced below approximately $1 \times 10^{17} \text{ cm}^{-3}$.

4. Previous Luminescence Results for Carbon Implanted GaAs.

There has been very little published on luminescence from carbon implanted GaAs (Ref 30). Two unpublished theses (Refs 75, 76) utilized luminescence to characterize carbon implanted GaAs. The qualitative features were seen to depend strongly on the type of GaAs used. The materials used were bulk grown semi-insulating Cr doped material, GaAs:Cr (Ref 75); GaAs grown by vapor phase epitaxy, VPE GaAs (Ref 76); and GaAs grown with the liquid encapsulated Czochralski technique, LEC GaAs (Ref 30).

The bandedge luminescence of the carbon implanted GaAs:Cr samples consists of one relatively broad peak which was observed to shift to higher energy as the implant dose is increased. The other higher purity VPE and LEC samples show more resolved luminescence lines (excitons and shallow acceptors, as discussed above) whose positions in energy remain essentially constant as implant dose is increased. Luminescence from unimplanted GaAs samples show that the GaAs:Cr material is already exhibiting luminescence characteristic of moderate to heavy doped material. Thus, the addition of impurities through implantation of GaAs:Cr makes it difficult to isolate shallow acceptors in luminescence from these implanted substrates. However, carbon implantation into high purity

GaAs indicates that a clearly resolved carbon acceptor line at 1.4935 eV will be present.

The results of Reference 30 indicate that, for the range of carbon concentrations examined ($1 \times 10^{15} \text{ cm}^{-3}$ to $1 \times 10^{17} \text{ cm}^{-3}$), the 1.4935 eV carbon acceptor line increases in intensity proportional to the carbon concentration. This was proposed as a potential semi-quantitative technique to track trace amounts of carbon in high purity GaAs.

With these results in hand, it was clear that high purity GaAs material was required to directly track the behavior of the optically active carbon acceptors introduced by ion implantation. These would be clearly resolved as a peak at 1.4935 eV in the high purity material, in contrast to a broad shallow acceptor band in chromium doped GaAs.

D. Secondary Ion Mass Spectrometry (SIMS)

SIMS is one of many mass spectrographic techniques used to determine the chemical composition of materials. Equipment available today can detect trace impurities in solids at levels of parts per million to parts per billion (Refs 77, 78). The SIMS technique has been developed, mostly since 1962, as a method for analyzing thin films and surface layers. It combines the spatial resolutions formerly realized with electron microprobes while maintaining sensitivities characteristic of spark source techniques. In this section, we present a brief review of SIMS and discuss the calibration technique used to convert the SIMS data from counts per channel into concentration versus depth.

1. SIMS Techniques. There are several ways to produce ions from a solid for mass spectrographic analysis. SIMS utilizes a relatively low energy ion beam at fairly high current densities both to sputter off

layers from the surface and to ionize the secondary ions removed by this procedure. Typical beam energies can be 5-20 keV with ion current densities of 5 to 50 mA/cm². Ionization efficiencies of about 1% can be achieved, i.e., about 1% of the atoms of interest which are removed become ionized. The choice of primary ion was discovered to have a strong effect on the ionization efficiency and on the uniformity of the secondary ion yield. For atoms with a low ionization energy (e.g., chromium), a beam of positive O₂ ions is typically used, while for atoms with a high ionization energy (e.g., carbon), a beam of positive cesium ions is used.

The mass spectrometer includes both electric and magnetic fields to separate the secondary ions according to their mass and then guide them on to a detector. For determining depth distribution of an impurity, the beam can simply be directed into an electron multiplier and the data recorded as a function of time. However, one capability of current SIMS systems is to form a two dimensional image of a surface whose intensity is proportional to the number of secondary ions of interest. For this experiment, only the former technique was used, which is known as the depth profiling mode.

In the depth profiling mode, the ion beam is rastered through at least a beam width and the data recorded only at times corresponding to the center of the raster. In this way, the loss of depth resolution by cratering is minimized. The host matrix is also monitored (As⁷⁵ for GaAs) along with the ion of interest. Thus, by assuming the density of the host matrix to be constant, systematic fluctuations in the data can be monitored and corrected. There are usually some anomalous counts seen for the first 100 to 200 \AA before sputtering equilibrium is established.

The SIMS data to be presented in Section IV were collected by Charles Evans and Associates of San Mateo, California. The instrument used was a CAMECA IMS-3F Ion Microanalyzer operated in the depth profiling mode. The data provided were uncalibrated counts detected for a specified mass per channel with each channel corresponding to a fixed time interval of measurement. The sputtered crater depths were subsequently measured at the Avionics Laboratory with a Sloan Technology Dektak Profilometer. Knowledge of the carbon implant dose allows calculation of the carbon concentration as a function of depth. Lack of a calibration standard for the other species tested (Si, Cr, Mn) only permits determination of relative concentration versus depth.

2. SIMS Data Calibration. In this section, we discuss the technique used to calculate the carbon mass profiles. The basic assumption is that the ion counts per channel recorded are proportional to the integral of the concentration over the depth sputtered. Thus, we assume the proportionality

$$\text{SIMS counts/channel} \propto \int_{x_{i-1}}^{x_i} n(x)dx$$

where $n(x)$ is the concentration as a function of depth and x_i and x_{i-1} correspond to the beginning and the end of the sputtered layer, respectively. When data collection has stopped at some depth, x_d , the relation between the sum of the counts and the integrated concentration is

$$K \cdot \sum_{\substack{\text{all} \\ \text{channels}}} (\text{counts/channel}) = \int_0^{x_d} n(x) dx$$

where K is the proportionality constant to be determined. For sufficiently deep sputtering of an implanted layer, such that practically all the implanted ion is removed, the right hand side of the equation is simply the implanted dose, a known implant parameter. Thus, K can be found once the recorded counts are corrected for noise. The two largest noise contributions were the anomalously high count rates that occur in the first few channels and the background count rate. An estimate of how many surface channels to omit was gained from a SIMS profile on a high purity VPE GaAs sample which showed that up to three channels could produce anomalously high count rates. The background counts for carbon were observed to be continuously decreasing during the data collection periods. A logarithmic linear least squares fit was used for the background counts beyond the implanted region and then used to calculate the background counts in each channel, including the carbon implanted region. Knowing these corrections to the total recorded counts, the proportionality constant K is found from

$$K = (\text{implanted dose}) / (\text{total corrected counts} - \text{surface counts})$$

where the total corrected counts are found by first subtracting the least square fit background from each channel before doing the summation.

Finally, for a small enough sampling rate such that the concentration $n(x)$ does not change too rapidly, we have

$$\int_{x_{i-1}}^{x_i} n(x)dx \approx n(x_i)\Delta x$$

and

$$n(x_i) = \frac{K}{\Delta x} \cdot \left(\frac{\text{counts}}{\text{channels}} \right)_i$$

The Δx is found by dividing the measured crater depth by the total number of recorded channels.

3. Previous SIMS Results for Carbon Implanted GaAs. There has been very little SIMS data reported for carbon implanted GaAs. Krautle (Ref 15) reports uncalibrated SIMS data for 40 keV carbon implants, as well as dual implants of 40 keV carbon with 200 keV Ga or As, at doses of 10^{15} cm^{-2} which were subsequently annealed at 800° C . These were capless anneals. Krautle reports that carbon shows a slight tendency for outdiffusion, apparently by comparison of the SIMS profile peak to the LSS projected range. This outdiffusion was reduced by co-implantation with As. Finally, no comments were made on how well the SIMS data were fit by any theoretical predictions, such as the LSS Gaussian profiles.

III. Description of Experiment

In the following section, the sample preparation procedures and the experimental measuring systems will be described. As will be seen, there are some sample preparation procedures which are unique for VPE GaAs. The description of the electrical and luminescence systems also includes an overview of the operating procedures.

A. Sample Preparation

The substrate material used for the vapor phase epitaxial (VPE) GaAs was semi-insulating chromium doped GaAs (GaAs:Cr). As supplied by the vendor, the GaAs:Cr boule was cut into wafers and polished on one side, whose surface is approximately 2° off the perpendicular to the <100> surface of the GaAs crystal. The <100> orientation is particularly helpful when preparing the final size samples because the cleavage planes allow for making square or rectangular samples with little difficulty. The slight 2° misorientation with the <100> surface has been found to inhibit the formation of hillocks which often occur during VPE growth on <100> surfaces.

The VPE GaAs was grown by the Electronic Research Branch of the Avionics Laboratory at the Air Force Wright Aeronautical Laboratories, Wright-Patterson Air Force Base, Ohio. The VPE growth furnace used was dedicated to growing high purity undoped GaAs. Approximately 5 to 40 μ of VPE GaAs were deposited on several substrates approximately 2 cm square. The layer depth was determined by cleaving a sample, staining the junction, and inspecting the layer under a calibrated microscope. All wafers were screened with surface electrical measurements (using the system described

in Section III.B.), and an estimate of the carrier concentration made from the thickness measurement described above. A capacitance-voltage (CV) measurement of the electrical carrier concentration profile was also performed on several wafers. An acceptable VPE sample would have a carrier concentration of 10^{14} to 10^{15} carriers/cm³ for several microns in depth. One sample from the VPE wafer subsequently used for the carbon implants was measured by D. Look using surface electrical measurements at room temperature and 77° K. For n-type GaAs, methods exist for calculating the donor and acceptor concentration if the layer thickness is known. In this case, the layer was approximately 40 μ thick with a total carrier concentration estimated at 4×10^{13} cm⁻³. The Hall measurement data indicated a donor concentration of 4×10^{14} cm⁻³ and an acceptor concentration of 3.6×10^{14} cm⁻³.

The VPE wafers were subsequently cut into 4.5 x 4.5 mm squares for SIMS and electrical measurement samples and into sizes of 4.5 x 2.5 mm (or less) for luminescence samples. A scribing tool was used to etch identifying numbers on the back of each sample (using the numbering system shown in Table IV-2). This helped to ensure traceability through procedures where several samples were combined in a single processing step, such as the annealing procedure. The following paragraphs describe the sample preparation steps of cleaning, implantation, encapsulation and annealing. A set of control samples was also prepared in a similar fashion, except for the implantation, and are called the capped and annealed (C/A) control samples.

The GaAs samples were always given a cleaning treatment in preparation for ion implantation or for Si₃N₄ encapsulation. The sample cleaning station used had a small vacuum chuck suspended in a metal beaker which

held the small GaAs samples during the following procedure:

- 1) The surface was washed with a solution of 10% aquasol detergent in deionized water, applied with a small sponge.
- 2) The surface was flushed with a stream of deionized water and then blown dry with dry nitrogen gas.
- 3) The following solvents were applied, in order, from squeeze bottles, in 5 to 10 second applications: trichloroethylene, acetone, methanol.
- 4) The surface was blown dry with nitrogen gas.

A final step was performed just prior to the actual implantation process. For non-epitaxial samples, this is typically a strong etch of $H_2SO_4:H_2O_2:H_2O$ in the proportions 3:1:1 for about one minute. This etch will remove several microns from the GaAs surface and is appropriate for the cut and polished wafers which can have residual damage near the surface due to mechanical polishing. However, the epitaxial samples do not have this damage layer and are frequently only a few microns thick themselves. Thus, the pre-implantation treatment consisted of a one minute soak in HF acid.

The implantation was performed by the Electronic Research Branch of the Avionics Laboratory. All implants reported in this experiment were performed at 120 keV. Figure III-1 shows a schematic of the ion implantation machine. A radio-frequency source was used to produce carbon and neon ions from carbon dioxide and neon gas, respectively. The beam current was 0.38 microampere for the majority of the carbon implants, with one set having a 0.32 microampere beam current. The neon implants were done with a 0.57 microampere beam current. Samples were mounted with their surface 7° off from the beam current direction to minimize

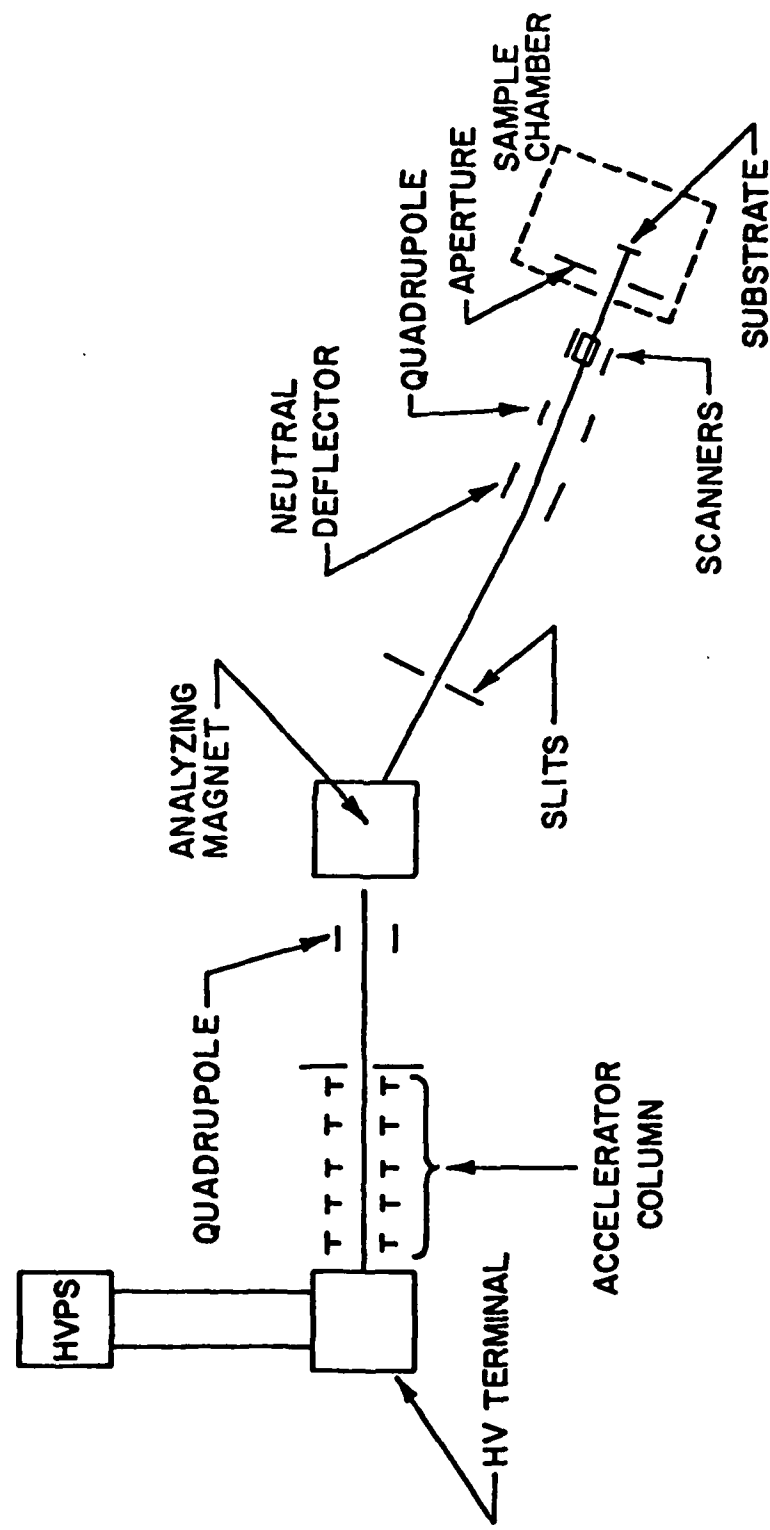


Figure III-1. Schematic diagram of ion-implantation machine

channeling effects. The samples were implanted at ambient temperature, reported as room temperature (RT).

Following implantation, the samples were encapsulated with approximately 1000 \AA of chemical vapor deposited Si_3N_4 (also called CVD or pyrolytic). Just prior to encapsulation, the samples were cleaned in the same manner described above for pre-implantation cleaning, followed by a one minute HCl acid soak to remove surface oxides. The encapsulation was performed by personnel of the Electronic Research Branch. In this procedure, ammonia gas (HN_3) and silane (SiH_4) diluted with nitrogen are combined in a gas mixture which is directed to flow down over samples heated on a carbon strip heater. A temperature of approximately 650° C (achieved in about six seconds) was maintained for about 45 seconds to deposit a layer of Si_3N_4 that is 1000 \AA thick. Prior to encapsulation of the actual experimental samples, the encapsulant quality is checked on GaAs test samples which are measured on an ellipsometer coupled to a mini-computer, which calculates the thickness and index of refraction of the encapsulant. Anomalous values of the index of refraction indicate potential leaks in the system which may introduce oxygen and cause "soft" encapsulants which fail upon annealing.

The annealing step was performed in a closed system furnace with flowing H_2 gas. Annealing temperatures ranged from 850° to 950° C. Samples were placed with the encapsulated surface face down on a piece of undoped GaAs in a quartz boat. This procedure was found to maintain encapsulant integrity at the higher temperature anneals, where the Si_3N_4 had been seen to fracture catastrophically in face up anneals. After the furnace had achieved the desired temperature, the sample boat was pushed into the center of the furnace with a rod attached to the boat.

The rod exits to the outside through an O-ring seal at one end of the furnace. After a temporary reduction in the temperature (one to two minutes), the automatic temperature controller recovers and controls the temperature to within 1° C. All anneals were done for 15 minutes, timed from when the sample boat was inserted into the furnace. At the end of 15 minutes, the furnace is immediately turned off. The samples are then withdrawn (but still kept in the gas flow) and allowed to cool to room temperature before removal.

The 1000 Å of Si_3N_4 encapsulant was removed by soaking the sample in HF acid. Initially, the etch was done for three to four minutes while the sample's surface color change was monitored. Recovery to a metallic appearance indicated that all the encapsulant had been removed. However, as described in more detail in Appendix C, this procedure was not adequate to remove all of the Si_3N_4 along the edges of the samples. This became a problem when subsequent electrical measurements were combined with layer removal by chemical etching. The final procedure adopted was to soak the sample in HF for 25 minutes, followed by examination under a microscope to verify that all encapsulant was removed from the edges. Normally, the encapsulant was left on until just prior to electrical or luminescence experiments.

Samples to be used for electrical measurements needed ohmic contacts applied to the GaAs surface. In general, the metal-semiconductor junction forms a non-ohmic contact which is characterized by a non-linear current-voltage characteristic curve. Also, the voltage drop across the junction can be a significant part of the total voltage measured across the sample. For the square van der Pauw samples used in this experiment, high purity indium solder was applied by hand with a low power soldering

iron to each of the four corners. The samples were then placed in an open furnace in a flow of argon gas and heated at 300° C for three minutes. This procedure produces a small layer of GaInAs alloy between the In and GaAs and effectively removes the potential barrier of the metal-semiconductor contact. The result is very low contact resistance and a linear current-voltage curve for forward and reverse current flow. The ohmic behavior was verified on a voltage versus current curve tracer display.

Table III-1 summarizes the experimental samples used in this experiment.

B. Electrical Measurements - System and Procedures

In this section, a description of the electrical measurement equipment and the operational procedures is provided. The equipment described had been installed at the Electronic Research Branch at the Avionics Laboratory.

The electrical measurements were based on the van der Pauw configuration described previously in Section II.B.3. Figure III-2 shows the six arrangements of current flow and voltmeter connections used for a square van der Pauw sample. Arrangements (a) through (d) are for resistivity measurements, while (e) and (f) are for Hall measurements with the magnetic field applied perpendicular to the sample surface. In general, for resistivity measurements, as discussed previously, two different contact configurations are required to account for sample asymmetry. However, in practice, all four configurations are used and combined with reversed current flows to produce eight measurements. The "f factor" in the van der Pauw resistivity equation, which is determined by the resistance ratio of two resistivity configurations, was always unity for the square

TABLE III-1
SUMMARY OF EXPERIMENTAL SAMPLES

| Implant Dose (cm ⁻²) | 15 Minute Anneal Temperature (°C) | | | |
|-------------------------------------|---------------------------------------|--------------------|-----|------------------|
| | NONE | 850 | 900 | 950 |
| 1 x 10 ¹⁵ carbon | X ^(a) | X ^(b) | X | X ^(c) |
| 3 x 10 ¹⁴ carbon | -- | X | X | X |
| 1 x 10 ¹⁴ carbon | -- | X ^(b) | -- | -- |
| 1 x 10 ¹³ carbon | X ^(a) | X ^(b,c) | -- | -- |
| 1 x 10 ¹⁵ neon | -- | X | -- | -- |
| 1 x 10 ¹⁴ neon | -- | X | -- | -- |
| 1 x 10 ¹³ neon | -- | X ^(c) | -- | -- |
| None | C/A control As grown VPE | -- | X | X ^(d) |
| | | X ^(b) | -- | -- |

In general, the samples indicated with an X were used for electrical profiles and surface luminescence, except as noted below:

- (a) SIMS only
- (b) SIMS also
- (c) PL etch profile also
- (d) No electrical profile

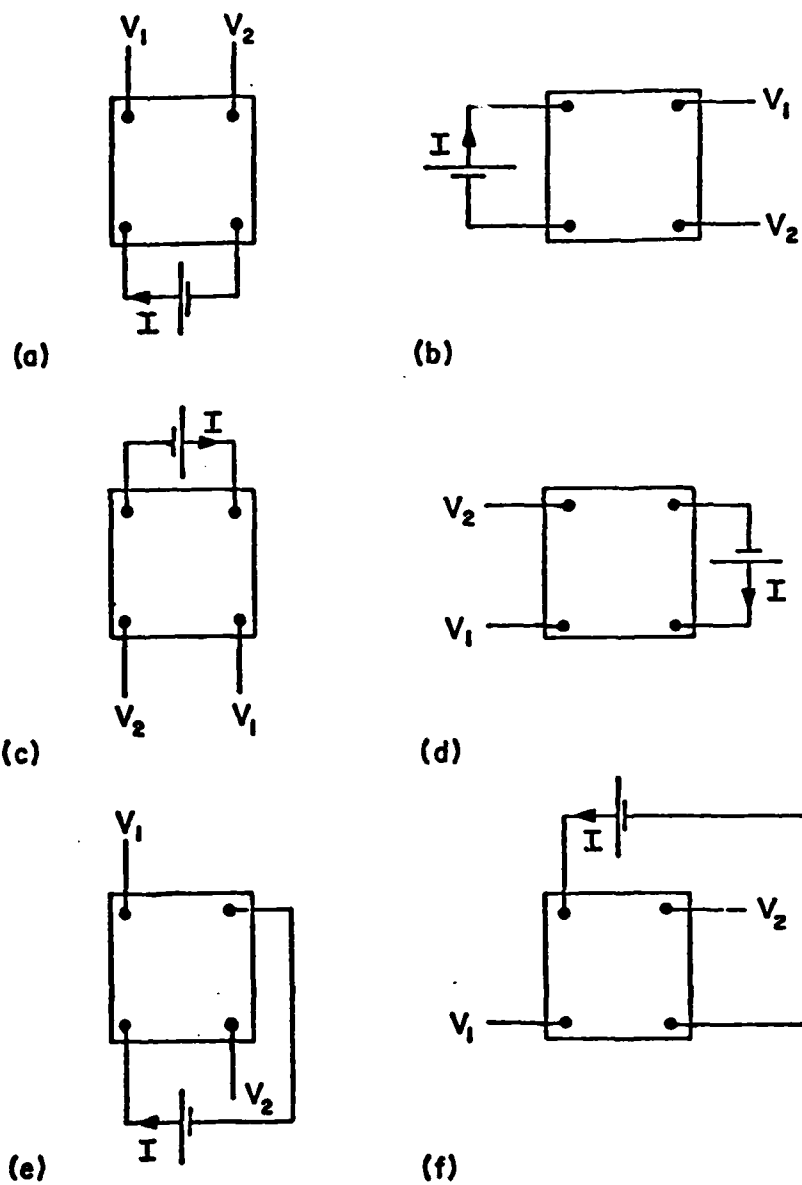


Figure III-2. Current flow and voltage contacts for square van der Pauw sample.

VPE GaAs samples used in this experiment. Thus, the measured sheet resistivity was effectively the average of eight separate readings across the sample. The two Hall measurement configurations ((e) and (f)) are also combined with current and magnetic field reversals to produce eight measurements of the sheet Hall coefficient. In addition to averaging out random noise, it can be shown (Ref 79) that this procedure allows cancellation of magnetic effects such as the Nernst and Righi-Leduc voltages and thermoelectric voltages. Only the Ettinghausen voltage remains, which is ordinarily quite small. The sign of the voltage difference between the voltage readings with and without the magnetic field applied indicates the electrical type of the carrier.

The electrical measurement system used was a semi-automated, guarded DC Hall measurement system. The electronic design of this system uses electrometers as unity gain amplifiers between the sample and the measuring equipment (Ref 80). Figure III-3 shows how a single rotary switch connects a differential digital voltmeter (DDVM), a constant current source and ammeter (AM) plus ammeter relay (AR) to the four sample contacts. The rotary switch positions were designated A through F, indicating the six configurations shown in Figure III-2. The coils C1 through C4 activate reed relays in pairs when switched in with battery relay (BR) to bypass the electrometers when current flows through leads to the sample. This guarded system has very low leakage current and little stray capacitance, which results in a small system time constant even for samples with high resistance. Typically, data could be taken on the GaAs samples in this experiment after waiting less than ten seconds following application of current or magnetic fields.

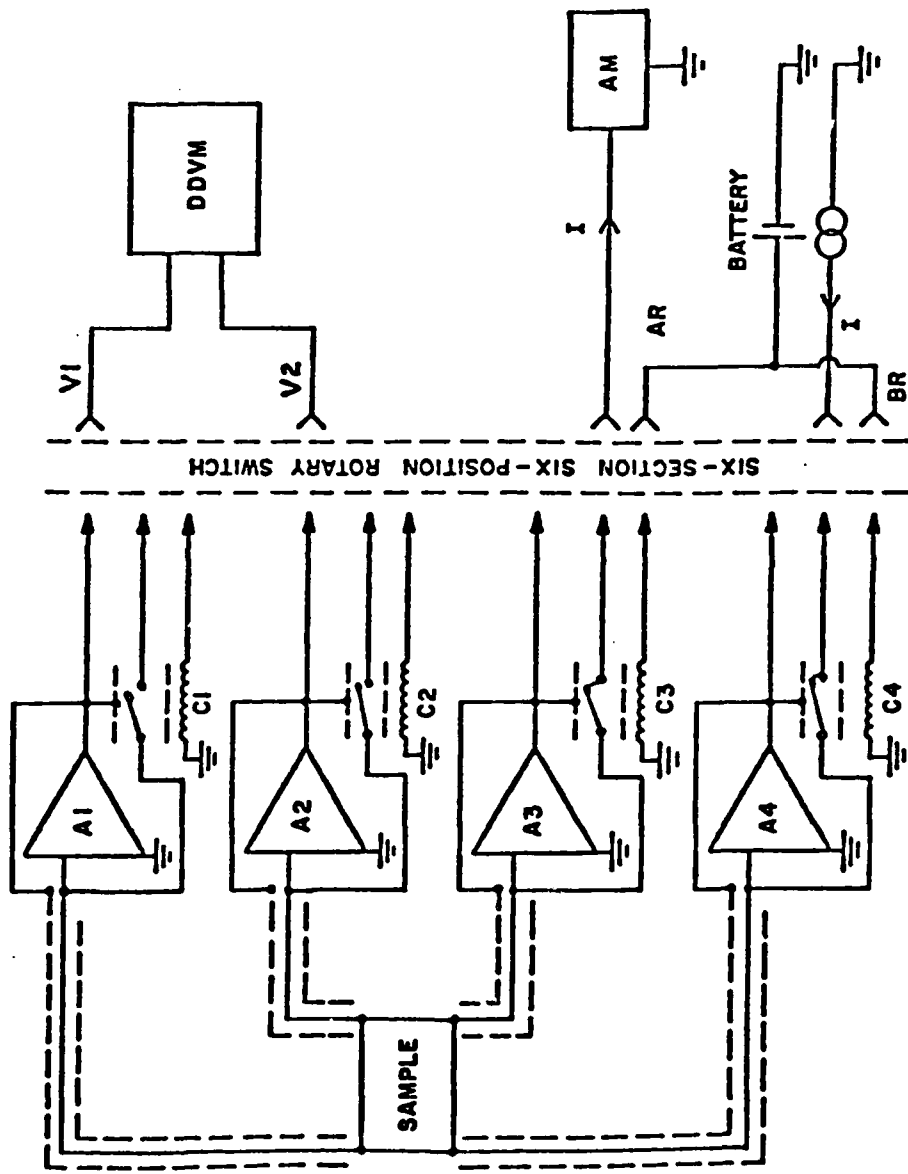


Figure III-3. Rotary switch connections from van der Pauw sample to measuring electronics.

Figure III-4 shows the automated resistivity and Hall measurement system diagram, shown configured for a resistivity measurement. Manual operations which were performed include operation of the rotary switch, application and reversal of the magnetic field, and initiation of data recording. The automated functions were controlled by a Digital Equipment Corporation PDP 11-03 computer. Programs loaded from disk could record and store single surface electrical measurements or store and combine a series of surface electrical measurements for the electrical profiling measurements. These programs would prompt the operator at the typewriter terminal for subsequent data collection steps (e.g., rotary switch settings); set the constant current source per operator input and automatically reverse current flow as needed; sample and record digital readings of current and voltage; plus, calculate and output final results to a typewriter or disk files. The automated functions made it possible to perform up to 35 etches in a single day, and the display of intermediate electrical profile results (using an estimated etch rate) was a very helpful guide to subsequent etches on a sample.

The sample holder for the electrical measurements was a flat fiberglass paddle attached to a wooden rod. Shielded cables from the electrical measurement system were routed along the rod and terminated at junction pins to which small teflon coated copper wires were soldered. The GaAs sample was attached to the fiberglass with a small amount of rubber cement, and the copper wires soldered with pure indium, using a low temperature soldering iron, to the previously prepared ohmic contacts. If the sample were to be etched, the indium contacts were protected with black wax, thinned with trichloroethylene and applied under a microscope with a small eye dropper. The copper wires were also tacked to the

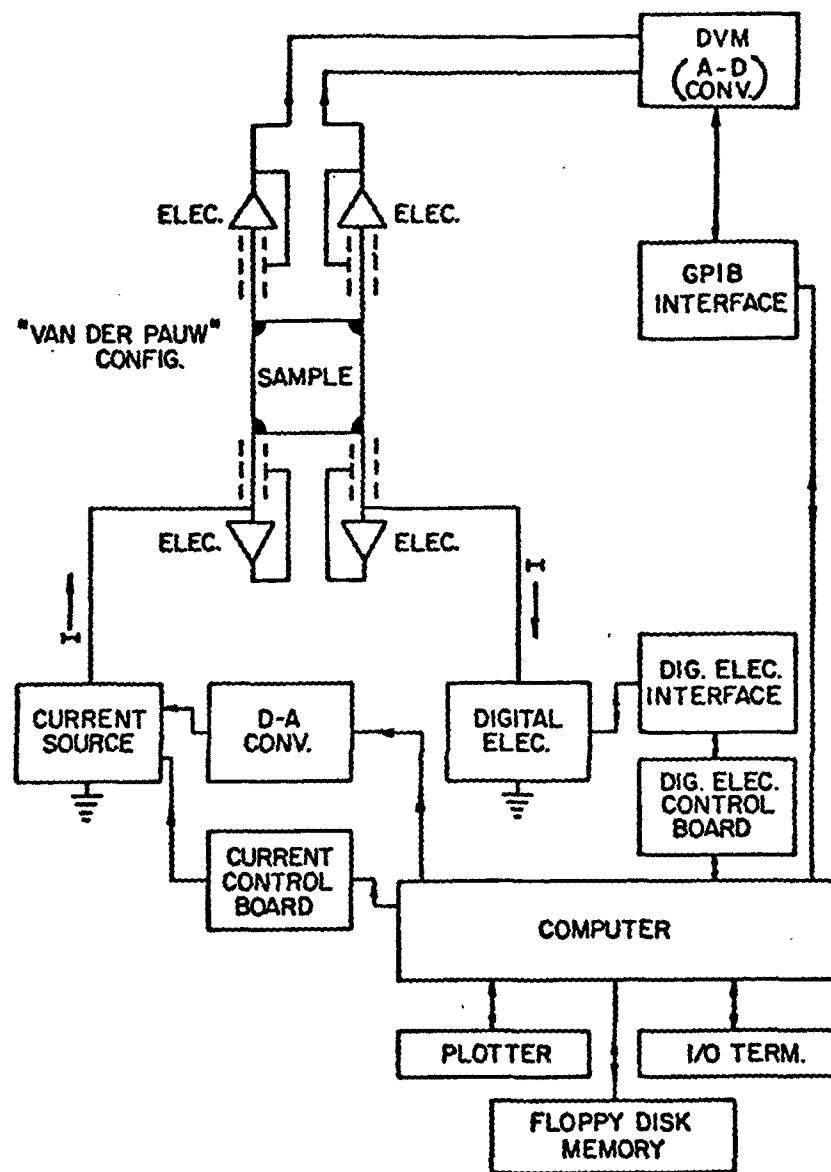


Figure III-4. Electrical measurement system diagram.

fiberglass sample holder with the black wax to provide strain relief. The sample holder was then clamped between the pole pieces of an 8100 Gauss water cooled DC magnet, oriented so the magnetic field was normal to the surface. Finally, the magnet was covered with a black cloth to prevent room light from producing photo-conductive effects during the measurements.

The repeated etchings for the differential Hall measurements were made while the sample remained attached to the fiberglass sample holder. The etching solution was $H_2SO_4:H_2O_2:H_2O$, usually prepared in a ratio of 1:1:50 in a total of 300 ml of solution. Fresh etchant was prepared for each electrical profile and maintained in an ice bath throughout the data collection. A magnetic stirrer was used to assure a uniform solution and to maintain a flow over the sample surface. Etch rates were typically $200 \text{ \AA}/\text{minute}$ and the etches timed with a stopwatch to within one-half second. To stop the etch, the sample was quickly removed from the etching solution and immersed in and flushed with deionized water. The samples were then blown dry and allowed to air dry for about two minutes before the next measurements were started.

As the final step in the electrical profiles, the black wax is removed with trichloroethylene and the sample unsoldered. The etching depth was determined from both etch rate controls, which had been partially covered with black wax, as well as from the profiled samples themselves which had small unetched mesas near the indium contacts. A Sloan Dektak Profilometer was used to measure the step height on the sample's surface. Usually an average of eight or more readings was used from different locations across the steps, with an observed spread of about 5%. Then, assuming a constant etch rate, the total depth is divided by the total etch time to obtain the etch rate.

C. Luminescence Measurements - Systems and Procedures

Most luminescence data were obtained from photoluminescence experiments using three different laser sources. Some cathodoluminescence data were also collected. Common to all systems were the spectrometer/detector and the digital data recording systems. A general system diagram is shown in Figure III-5.

The optical detection system consisted of a Spex 1702, 3/4 meter Czerny-Turner spectrometer used with a liquid nitrogen cooled S-1 cathode photomultiplier tube (PMT). A 1200 lines/mm grating, blazed for a maximum response at 5000 Å, was used. Both the grating efficiency and the S-1 response were monotonically decreasing over the observed spectral region. Measurements with a blackbody source as a standard showed a decrease of about 30% from 1.51 eV to 1.35 eV, the observed region. A system correction function was calculated, but not used because the relatively sharp line spectra were not changed in energy and because of noise in the correction function. The spectrometer dispersion was 11 Å/mm at the exit slit, which for the typical slit settings used, 200 μ and 1mm, corresponds approximately to 0.4 meV and 2 meV resolutions, respectively.

The detection electronics operated in a photon counting mode. The output of the PMT was processed by a Princeton Applied Research Model 1121 amplifier/discriminator. The operating manual describes how to set the noise threshold and the high voltage to the PMT for the optimum signal to noise ratio. The FAST NIM output of the amplifier/discriminator consisted of 1 volt pulses, which were additionally amplified to about 5 volts and sent to a multichannel analyzer (MCA). Either a Hewlett-Packard Model 5400 or a Canberra 8100/e were used. The HP MCA stored data on punched paper tape, and the Canberra MCA was coupled to a Techtran

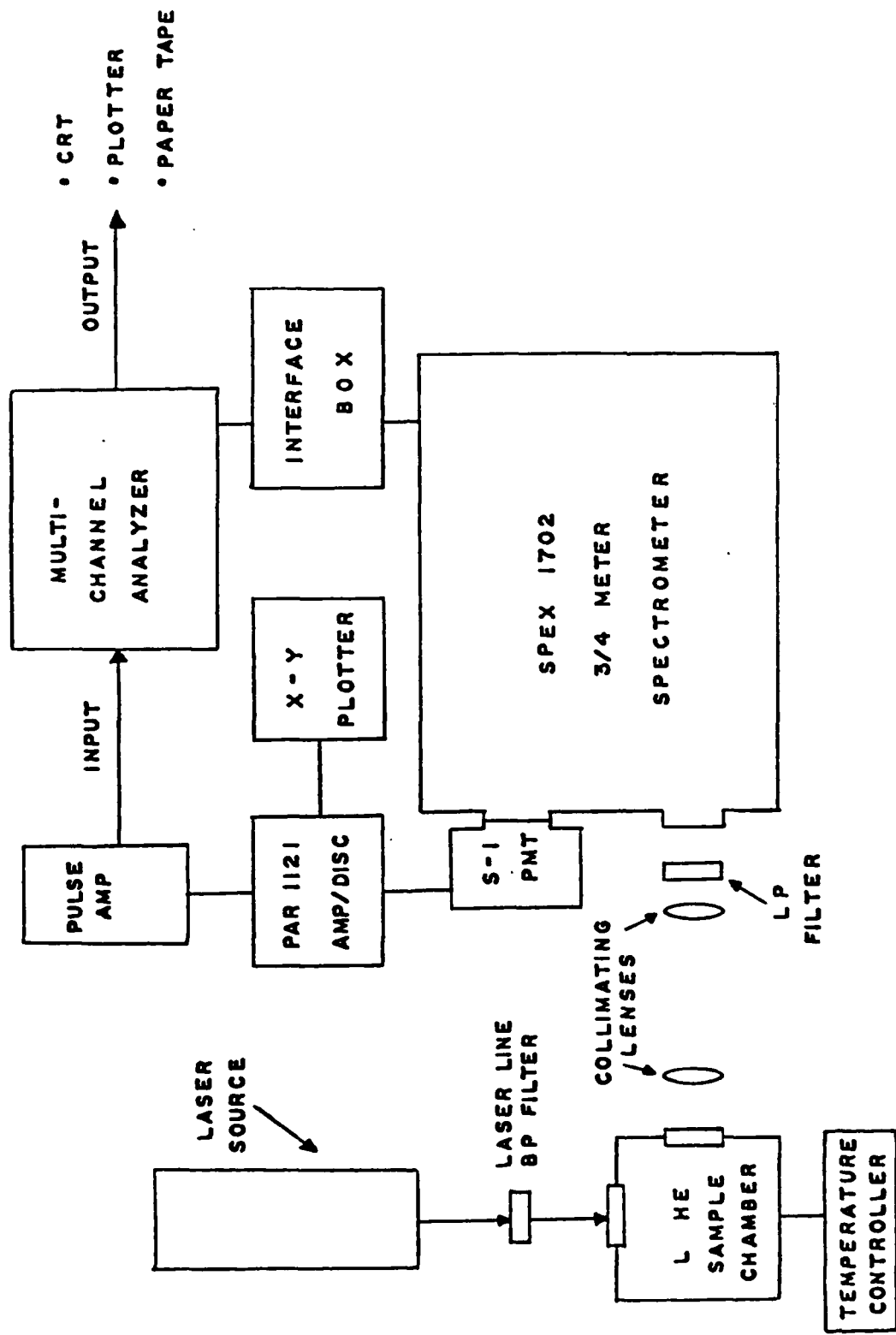


Figure III-5. Luminescence measurements system diagram.

cassette tape unit. While the formats were slightly different, each MCA recorded photon counts in each of 1024 channels, and most all data were ultimately converted to punched card or 9 track magnetic tape plus hard-copy printout. The dynamic range of the MCA was six orders of magnitude with a restart of counting if the channel saturated. Thus, it was feasible to manually examine the data and add appropriate digits in some cases of saturation.

An interface box controlled the spectrometer's digital drive motor and the MCA channel advance by switch selectable motor speeds and divider factors for the MCA. Also variable was the gear ratio of the spectrometer drive. Combination of these three settings produced a given number of $\text{\AA}/\text{channel}$ for a specified sampling time. The procedure was generally to match the spectrometer resolution to the MCA resolution at a scan speed to provide sufficient signal strength. In this experiment, most runs had the MCA recording at $1.7361 \text{ \AA}/\text{channel}$ ($0.3 \text{ meV}/\text{channel}$).

Three different laser sources were used for various types of luminescence experiments. For intensity variation experiments where a range of laser power was needed, a Spectra-Physics Model 164 argon laser was used which was capable of an output of 1 Watt on the 5145 or 4880 \AA lines with a 1.5 mm beam diameter. By using neutral density filters with a 200 mW output on the 5145 \AA line, data was collected for power densities of 5.7 mW/cm^2 to 11 W/cm^2 on the sample. For deeper penetration into the GaAs (to illuminate the majority of the carbon implanted region), a Spectra-Physics Model 124A helium-neon (HeNe) laser was used. It provided a constant output of 11 mW at 6328 \AA with a 1.1 mm beam diameter. The estimated power density at the sample was 0.6 W/cm^2 . The third laser source used was a Coherent Radiation Model CR-500K SG krypton laser

with ultra violet option which put out three lines at 3375, 3507 and 3564 Å in a 1.5 mm diameter beam. The output power was maintained at 10 mW, measured at the dewar windows, for an estimated power density at the sample of 1 W/cm². The shallow penetration of the UV lines was combined with chemical etches of the samples to do the PL etch experiments, and in those experiments power levels were monitored at the beginning and end of each run.

The luminescence system optics included filters and reflective mirrors to direct the laser beam onto the sample through the dewar windows. Narrowband filters (approximately 10 Å wide) were used with the 4880 and 6328 Å laser lines and a 3500 Å colored glass bandpass filter (approximately 1000 Å wide) was used with the UV laser. These filters removed other argon and krypton gas lines which could appear as first or second order lines in the detected spectra. The collecting optics consisted of two lenses and a long pass filter. The first lens is selected for best collection efficiency at the dewar window (e.g., 76.5 mm focal length), and it collimates the radiation. The second lens focuses the radiation on the entrance slit of the spectrometer and is chosen to best match the f-number of the spectrometer. Long pass filters were placed near the entrance slit to block the reflected laser light and to reduce stray room light.

The best procedure found for aligning the system was to use a high intensity light source with a fiber optics cable to illuminate the sample installed in the dewar. The receiving optics can then be moved to position and to focus the image of the sample on the entrance slit such that the sample is centered on the entrance slit. With the spectrometer set on an expected luminescence line, the detector output can be visibly monitored by connecting the PHA output on the PAR amplifier/discriminator through

an amplifier with an adjustable time constant (such as a Keithley 127 current amplifier) and then into an X-Y recorder. Then, the laser beam can be positioned on the sample while monitoring the pen deflection on the X-Y recorder for maximum deflection, thus ensuring that the sample center is being illuminated. This procedure helps ensure repeatable luminescence conditions on a sample by verifying that the same point of the sample is imaged on the entrance slit. This was particularly necessary in the PL etch experiment. In those experiments, a single sample was inserted for each run following etching, and the procedure usually became an alignment verification, without any adjustments needed.

At the start of a data collection run, the spectrometer slits were closed to 50μ or less and the 8006.16 \AA line from an argon calibration lamp recorded in one channel within the first several channels of the MCA. The spectrometer slits were then opened to 100 to 200μ to record the exciton and shallow acceptor bands. Ultimately, the procedure was adopted where the slits would be opened to 1 mm just before the deep acceptor bands appear, near 8500 \AA , thus increasing the system response by trading off resolution. However, peaks in this region are more broad, and the precision of the recording MCA could still locate peak positions to values better than the spectrometer resolution.

Several liquid helium cryogenic systems were used in the course of the experiment. The one most frequently used was a Janus dewar which could provide cooling for about five hours on one fill of liquid helium. The sample holder for this system was connected to an active temperature control system by Lakeshore Cryogenics which could maintain sample temperatures within 0.1° K (for sample temperatures of about 5° K and higher). Other cryogenic systems used did not have active temperature control. These

were an Andonian dewar and a Helitran liquid helium transfer line which was installed with the cathodoluminescence system. Since the Andonian dewar and the Helitran both cool by thermal conduction from a liquid helium reservoir, these systems were limited by the conduction paths and thermal loads to minimum temperatures of about 10 to 20° K. The Janus dewar cools by direct contact of the sample with the liquid helium or helium gas and could, therefore, cool to near 4.2° K.

The sample holder is a copper block to which a piece of copper foil can be attached by four screws. The foil has one or more holes in it which are slightly smaller than the samples so that, when the samples are held between the copper block and the foil, the center section of the sample's surface is exposed. For economy of use of liquid helium up to four samples could be accommodated, but ultimately only one sample was inserted at a time to help guarantee repeatability of illumination and collected emission from the sample.

The chemical etching performed in the PL etch experiments was very similar to the electrical profile etching. The samples were attached with rubber cement to a teflon rod which was manually held, or clamped in place for long etches, in the constantly stirred etch solution. Some samples had to be etched over several days, so new etch solution was prepared each day that data were taken and new etch rate control samples used to account for differences in solution strength.

IV. Results and Discussion

This section has been organized in such a manner that the results due to carbon in GaAs can be easily separated from results due to the native GaAs material itself or from results introduced by processing steps. The control samples are presented and analyzed first. These include high purity VPE GaAs, encapsulated and annealed VPE GaAs, and neon implanted VPE GaAs. Then, the results for the carbon implanted VPE GaAs samples are presented and analyzed in a manner parallel to the control samples. This approach allows results due to carbon in GaAs to be clearly distinguished.

A. Characterization of Control Samples

Control samples were prepared in an attempt to separate effects due to the implanted carbon atoms from effects due to the original VPE material, the implantation kinetics or the post-implantation processing steps. The preparation and analysis of control samples in this experiment proved to be quite necessary since strong effects were produced independent of the presence of implanted carbon.

There were three categories of control samples. First, the "as delivered" high purity VPE GaAs was characterized to establish a basis for comparison. Analysis of this control sample should isolate effects due to the native GaAs material, such as native impurities or crystal defects. Second, unimplanted VPE GaAs samples were encapsulated with pyrolytic Si_3N_4 and then annealed under the same conditions as the implanted samples. These control samples would exhibit effects due to the capping and annealing (C/A) steps and are called the C/A controls. A third category of control samples was a set of neon implanted VPE GaAs which were capped

and annealed in the same manner as the carbon implanted samples. These control samples should exhibit, in addition to capping and annealing effects, the lattice damage effects due to implantation kinetics, where the use of electrically inert neon helps to ensure that the implanted ion itself does not contribute to observed changes. With data from this combined set of control samples for comparison, it is easier to isolate results due to carbon in GaAs.

1. High Purity VPE GaAs. High purity VPE GaAs was chosen as the carbon implant substrate for several reasons. The expected structure of the carbon implants was a p-type carbon doped layer on top of the n-type VPE GaAs. Thus, it was expected that the electrical measurements on the carbon layer would be isolated by the p-n junction. Also, for luminescence experiments, epitaxial GaAs exhibits relatively sharp line luminescence with the potential to resolve specific impurity lines, especially the carbon acceptor to conduction band transition line. For the electrical, luminescence and SIMS experiments, the use of high purity VPE GaAs was expected to effectively remove the GaAs substrate impurities as the source for any changes observed in the course of the experiment. This was not strictly true, as will be seen.

1a. Electrical Measurements: VPE GaAs. The electrical measurements performed on the VPE GaAs samples included the surface electrical measurements along with electrical profiling on selected samples. In addition, some CV measurements of electrical carrier concentration were provided by the Electronic Research Branch.

All available VPE GaAs were screened with the surface electrical measurements. The surface electrical measurements were used to ensure

that the VPE GaAs selected for implantation had equivalently high mobility values and low carrier concentration. The results for the wafers used in this experiment are listed in Table IV-1. Table IV-2 summarizes the sample numbering system and the general allocation of the wafer in the experiment.

TABLE IV-1
SURFACE ELECTRICAL MEASUREMENTS
VPE GaAs Screening

| Wafer # | μ_H (cm ² /volt-sec) | N_s (carriers/cm ²) | Thickness (microns) | Elec Type |
|---------------------------------------|--|--|------------------------|--------------|
| HP-C-13-2-23 | 6912 | 5.93×10^{10} | 6 (Est) | n |
| HP-C-13-3-4 | 7074 | 2.16×10^{11} | 9 | n |
| | 6206 | 1.24×10^{11} | | n |
| | 6231 | 1.25×10^{11} | | n |
| HD-C-14-2-4 | 7978 | 1.10×10^{11} | 20 (Est) | n |
| | 7320 | 1.40×10^{11} | | n |
| | 8527 | 1.23×10^{11} | | n |
| | 8544 | 1.29×10^{11} | | n |
| HP-C-16-1-32 (measured by D. Look) | 7019 | 1.83×10^{11} ($n=4.58 \times 10^{13}$ cm ⁻³) | 40 | n |

TABLE IV-2
SAMPLE NUMBERING SYSTEM

| <u>Wafer #</u> | <u>ith Sample</u> | <u>General Use</u> |
|----------------|------------------------------|---|
| HP-C-13-2-23 | 23-i | Elec meas C/A controls |
| HP-C-13-3-4 | 13-i | Carbon implants (850 C) C/A controls |
| HP-C-14-2-4 | 4-i | Neon implants C/A controls |
| HP-C-16-1-32 | 2-i | Carbon implants |

A typical CV measurement for two different contact placements on the wafer is shown in Figure IV-1 for wafer HP-C-13-3-4. The staining technique described above for determining epitaxial thickness showed nine microns of epilayer. The roll-off from the uniform carrier concentration of $5 \times 10^{14} \text{ cm}^{-3}$ as determined from the CV measurement occurs at approximately 3μ . Since the maximum extent of the 120 keV carbon implant profile is less than 1μ , a uniform layer of high purity VPE GaAs was present for implantation.

Three attempts were made to electrically profile the VPE samples to confirm the CV carrier concentration measurements and to gain familiarity with the electrical profiling procedures. Problems with the etching solution were the apparent cause of scatter in the measured data. Figure IV-2 shows the sheet resistivity and sheet Hall coefficient plotted as a function of depth. These plots show how the scatter in the

RD-A138 094

ELECTRICAL LUMINESCENCE AND SIMS (SECONDARY ION MASS
SPECTROSCOPY) CHARAC. (U) AIR FORCE INST OF TECH

2/4

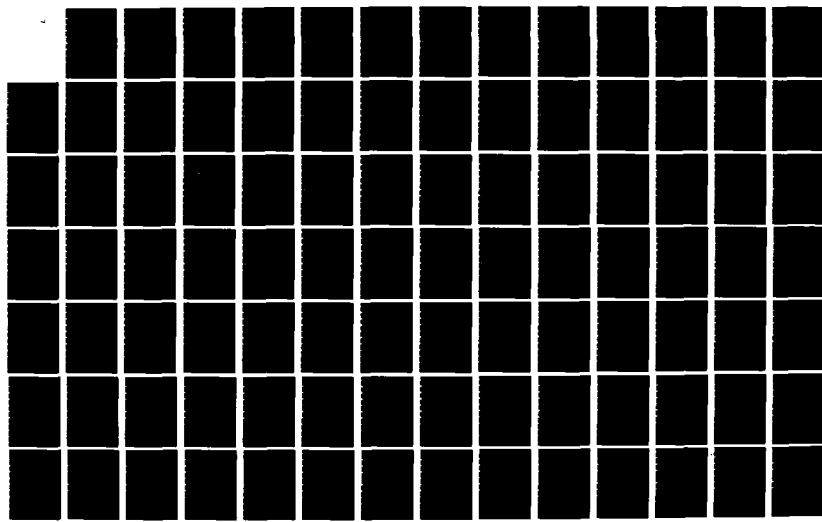
WRIGHT-PATTERSON AFB OH SCHOOL OF ENGI.

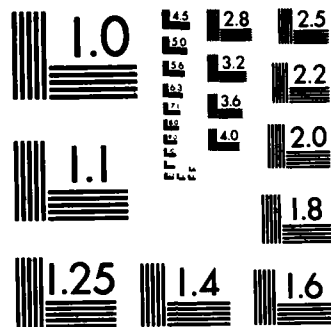
UNCLASSIFIED

R M SYDENSTRICKER DEC 83 AFIT/DS/PH/83-4

F/G 20/12

NL





MICROCOPY RESOLUTION TEST CHART
NATIONAL BUREAU OF STANDARDS-1963-A

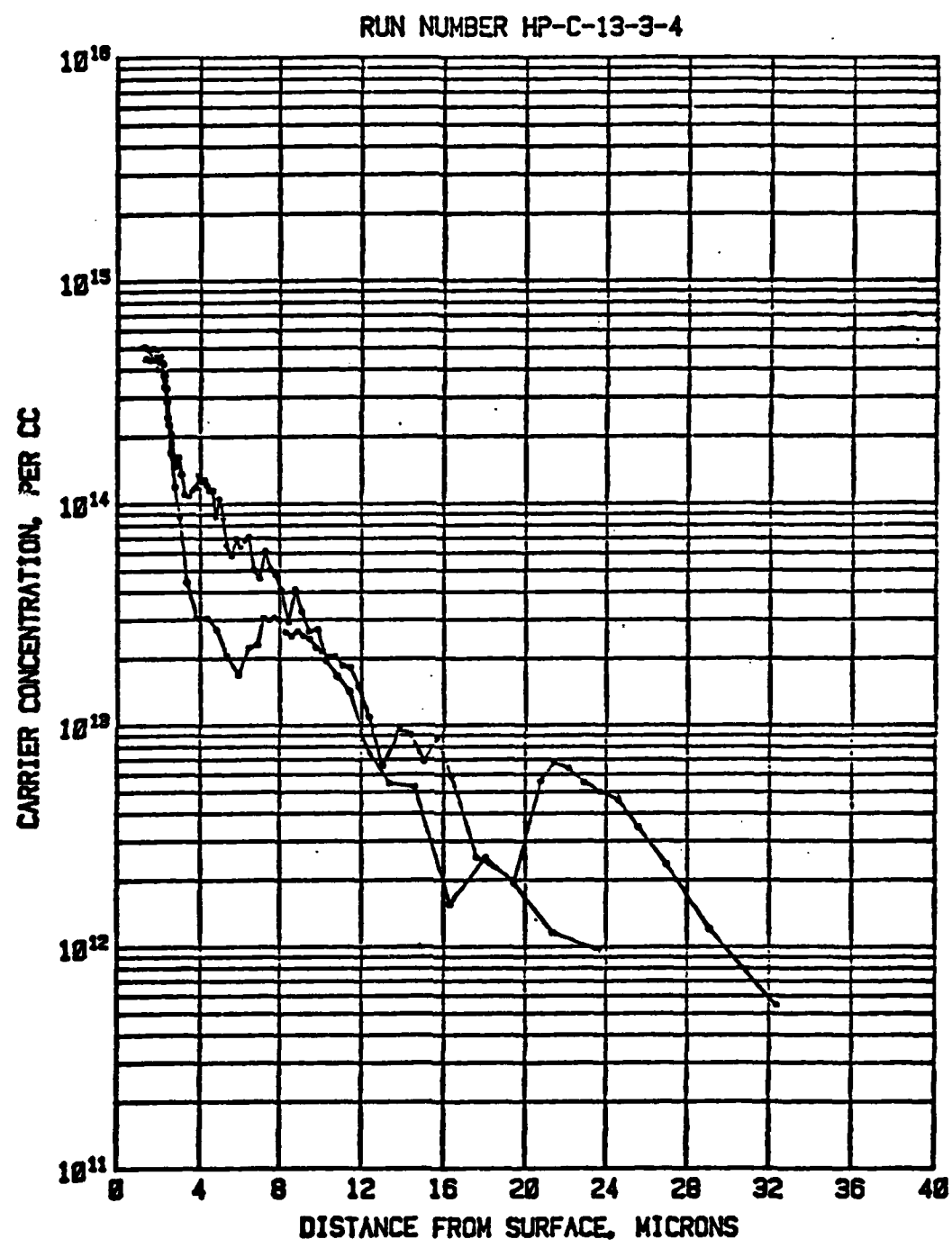


Figure IV-1. Typical CV measurement of electrical carrier concentration profile in high purity VPE GaAs.

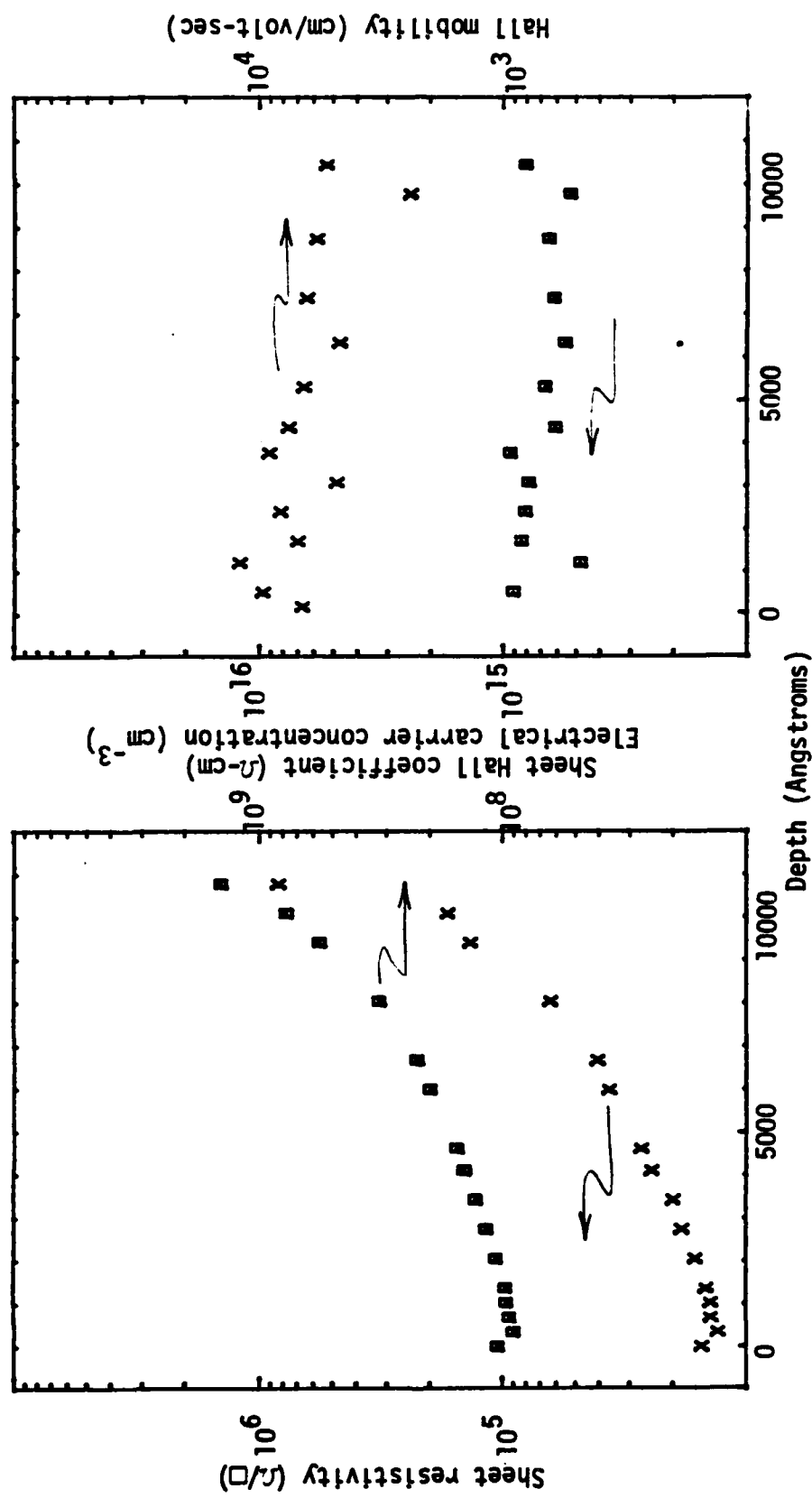


Figure IV-2. Electrical profiling data for VPE GaAs, sample 23-3. Plot on left displays sheet resistivity and sheet Hall coefficient vs. depth. X=sheet resistivity; \square =sheet Hall coefficient. Plot on right shows the calculated Hall mobility and n-type electrical carrier concentration vs. depth. X=Hall mobility; \square =carrier concentration

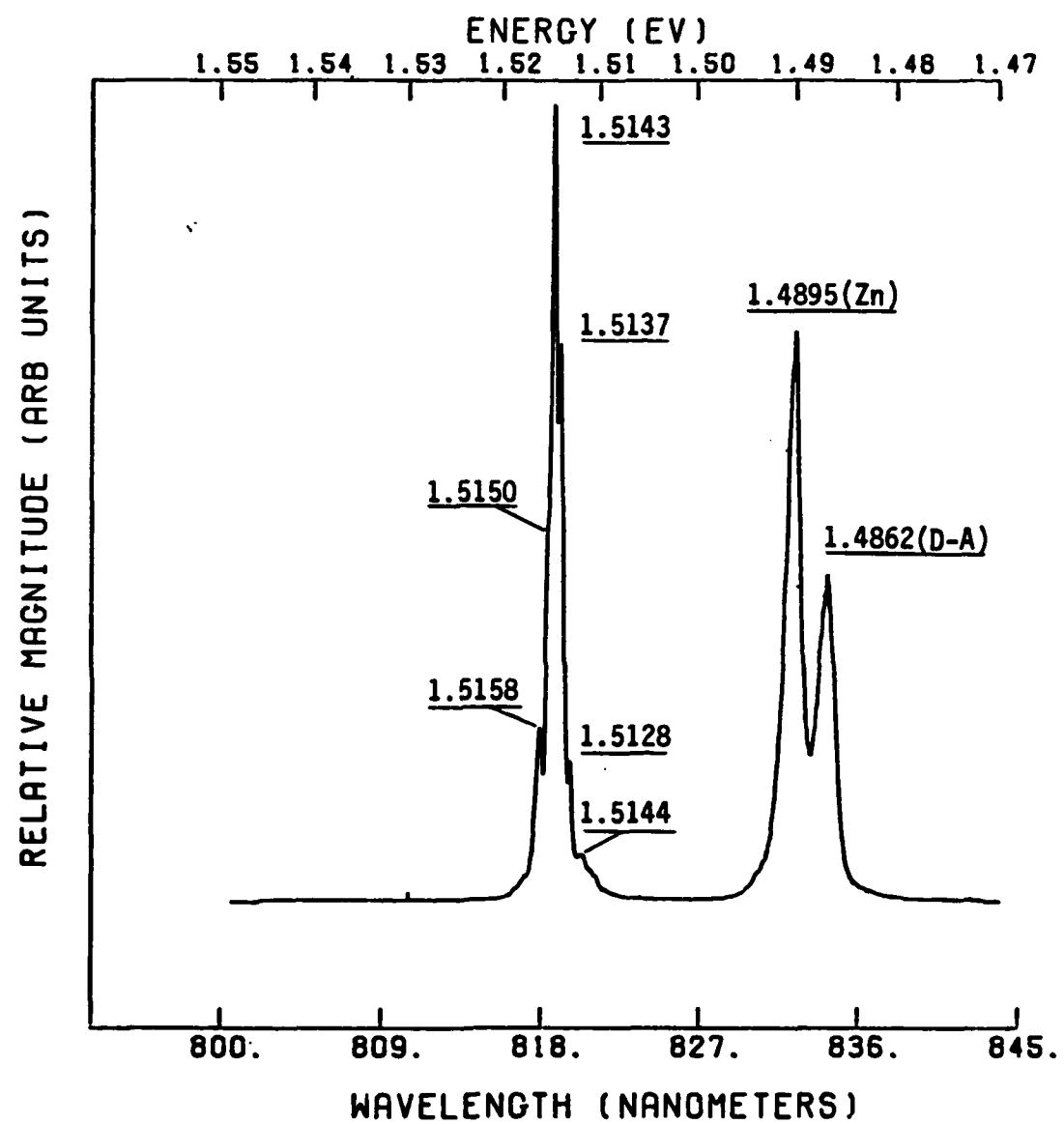


Figure IV-3. PL spectra at 10^0 K of high purity VPE GaAs. Illumination with 5145 \AA line of argon laser with 0.1 W/cm^2 .

| <u>LINE (eV)</u> | | <u>ASSIGNMENT</u> |
|------------------|---|---|
| 1.5158 | (X) | Free exciton |
| 1.5150 | | Excited states of (D ⁰ ,X) |
| 1.5143 | (D ⁰ ,X) | Exciton bound to neutral donor |
| 1.5137 | (D ⁺ ,X) or (D ⁰ ,h) | Exciton bound to ionized donor Valence band to neutral donor |
| 1.5126 | (A ⁰ ,X) | Exciton bound to neutral acceptor |
| 1.5114 | | Two electron transition of 1.5143 eV (?) |

The acceptor species is most likely Zn, as described below, while the identity of the donors is unknown. Given the predominance of the 1.5143 eV line, the line at 1.5114 eV could be a two electron transition of that line.

The shallow acceptor band has two resolved lines at 1.4895 eV and 1.4862 eV. Both intensity and temperature variations were used to isolate donor-acceptor line behavior from conduction band-acceptor behavior.

Increasing the temperature from 10° K to 26° K resulted in the extinction of the 1.4862 eV peak, characteristic of donor-acceptor lines. Increasing the PL excitation by a factor of 100 shifted this peak to higher energy by about 1 meV, also characteristic of donor-acceptor lines. The acceptor species is most likely Zn, a common residual impurity in VPE GaAs, which has a conduction band-acceptor line reported at 1.4888 eV (Ref 17). The overall conclusion is that zinc is the only shallow acceptor impurity that appears in the luminescence at the excitation levels used in this experiment. There was no detectable carbon acceptor line at 1.4935 eV or silicon acceptor at 1.4850 eV.

There was some evidence at high excitation levels (11 W/cm²) at 10° K that another impurity was present at concentrations much less than the zinc. A small shoulder appeared at 1.4796 eV. Its identity was not

pursued since it did not appear in the lower intensity PL, but it is conceivably due to germanium (Ref 17).

Figure IV-4 shows the PL spectra of two different VPE samples. Here the illumination was the 6328 Å line of a HeNe laser at 0.6 W/cm². The system resolution is 0.3 meV down to approximately 1.45 eV. Past this point, the spectrometer slits were opened wider to increase the signal level, and the resolution is 2 meV. The sample temperatures are different for the two spectra in Figure IV-4, but the deep acceptor levels are relatively unaffected by this difference.

One of the most striking features is the difference in the 1.41 eV and 1.36 eV bands. Spectra from sample 13-20 (VPE used for the carbon implants annealed at 850° C and some C/A controls) has no detectable 1.41 eV band. Spectra from sample 4-10 (VPE used for neon implants) has a 1.41 eV band which is stronger than the 1.36 eV band, but in this case the 1.41 eV band is a relatively broad peak which appears at 1.4007 eV and is thus about 7 meV away from the Mn related line at 1.408 eV (to be seen in the capped and annealed control samples and the implanted samples). Also, when normalized to the free exciton line at 1.5158 eV, these deep acceptor bands are about four times weaker in sample 4-10 than sample 13-20. From the absence of the sharp Mn line at 1.408 eV in the VPE GaAs, we conclude that there was little, if any, Mn contamination during growth.

1c. SIMS Measurements: VPE GaAs. One unimplanted VPE GaAs sample was analyzed for carbon using SIMS. The carbon counts versus depth are shown in Figure IV-5. The data are not converted to carbon concentration since there was no standard for calibration (as there was for the carbon implanted samples) to use the procedure in Section II.D.2.

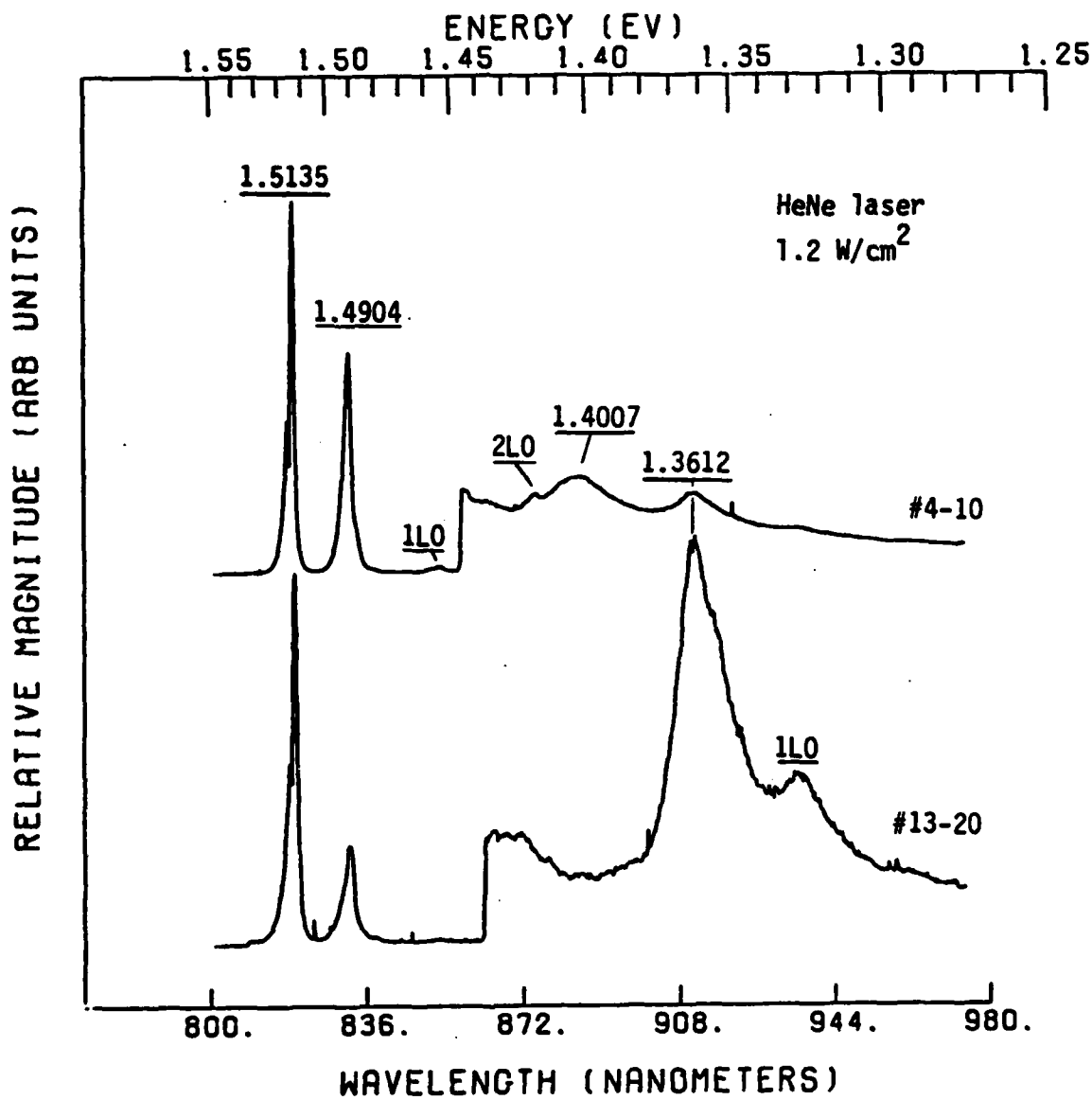


Figure IV-4. PL spectra of two high purity VPE GaAs samples. Sample 4-10 was at 14° K; sample 13-30 was at 21° K. Illumination was 6328 Å HeNe laser at 1.2 W/cm². Peak positions indicated in eV and plots normalized to the 1.5135 eV line.

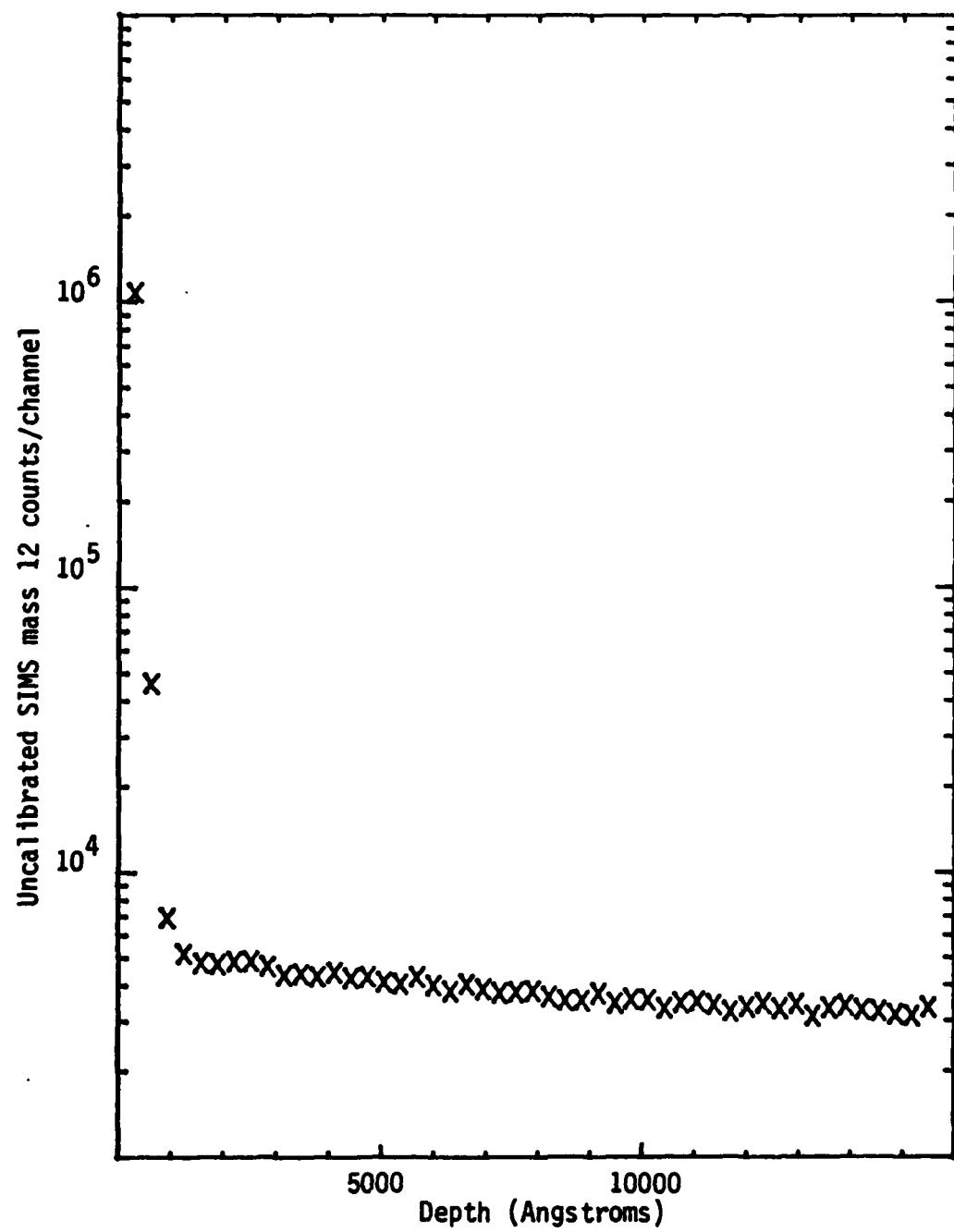


Figure IV-5. SIMS data for carbon in VPE GaAs, sample 13-23.

The first two channels of data, which correspond to 630 \AA in depth, show relatively high counts. Thereafter, the carbon counts slowly subside over the sputtered depth of about 1.6μ . The first two channels in the near surface region are attributed to anomalous results which occur before sputtering equilibrium is established (Ref 81).

It is not likely that the carbon counts arising from the deeper sputtering depths on the VPE GaAs are due to carbon in the GaAs. First, the luminescence data presented above did not detect any carbon acceptors. Second, comparison to the SIMS carbon counts for the carbon implanted samples shows that the count rates beyond the implanted region are almost identical. Third, the PL etch data for a C/A control (to be presented) show that, while carbon is detectable at depths greater than 3000 \AA , the levels are much lower than other acceptors. Therefore, the SIMS data for carbon in VPE GaAs is most likely due to some background source of carbon, such as residual hydrocarbons in the SIMS vacuum system.

However, while not detecting any carbon in the VPE GaAs, this sample was useful in showing that at least the first two, and perhaps three, channels of SIMS data should be neglected in any calibration procedure for the carbon implants. It also demonstrated that the background carbon counts were a monotonically decreasing function that could potentially be described with a logarithmic linear least squares fit. This information from the SIMS data on the VPE GaAs sample influenced the procedures adopted as a part of the background subtraction technique for the carbon implanted samples.

2. Capped and Annealed VPE GaAs. Ideally, only the implanted atom causes any change in the implanted GaAs and does so in a controlled, predictable manner. Thus, the C/A controls for an ideal substrate would

exhibit no change after being encapsulated with the pyrolytic Si_3N_4 and then annealed. The VPE samples in this experiment exhibited strong effects due to the capping and annealing steps, thus separate control samples were essential in interpreting the experimental results.

2a. Electrical Measurements: C/A VPE GaAs. Table IV-3 summarizes the surface electrical measurements made on several C/A VPE GaAs samples used as controls. In all cases, the Hall measurements indicated electrical type conversion to p-type conductivity. Most measurements were for samples annealed at 850°C for 15 minutes since these were the annealing parameters used most often.

The mobilities vary from approximately 170 to 220 $\text{cm}^2/\text{volt}\cdot\text{sec}$, and the sheet carrier concentrations from 7×10^{12} to $2 \times 10^{13} \text{ cm}^{-2}$. As will be seen, these results from surface electrical measurements were in the same range as results from carbon implanted samples. Thus, from a surface electrical measurement alone, the effects of carbon implantation were difficult to deduce..

Electrical profiling of the C/A controls was performed on three samples annealed at 850°C for 15 minutes in flowing hydrogen. Problems with the unetched ridge (Appendix C) prevented good data from being collected beyond 1000 \AA on two samples, but the third was successful. Figure IV-6 shows the resulting electrical carrier concentration and Hall mobility versus depth for sample 23-4.

Over the range of good data, all three samples profiled showed near surface mobilities of almost $200 \text{ cm}^2/\text{volt}\cdot\text{sec}$ and p-type electrical carrier concentrations near $1 \times 10^{18} \text{ cm}^{-3}$. Figure IV-6 shows that these values are nearly constant for a region approximately 2000 \AA thick, followed by a rapid transition near 2500 \AA . At this transition point,

TABLE IV-3
SURFACE ELECTRICAL MEASUREMENTS
Capped and Annealed VPE GaAs

| Sample # | Anneal T (°C) | μ_H (cm ² /volt-sec) | N_S (carriers/cm ²) | Electrical Type | Control Wafer For |
|--------------|------------------|--|--------------------------------------|-----------------------|-----------------------------------|
| 13-3* | 850 | 180 | 8.16×10^{12} | p | |
| 13-6* | 850 | 186 | 6.93×10^{12} | p | |
| 13-5 | 850 | 173 | 1.11×10^{13} | p | |
| 23-4* | 850 | | | p | |
| 4-9 | 850 | 173 | 1.33×10^{13} | Ne^+ Implant | |
| HP-C-13-2-23 | 850 | 200 | 2.00×10^{13} | p | |
| 22-2 | 850 | 217 | 9.10×10^{12} | p | |
| 2-11 | 900 | 220 | 2.33×10^{12} | p | Higher Temp Carbon Implants |
| 2-16 | 950 | 258 | 1.66×10^{12} | p | |

* Also electrically profiled with chemical etch

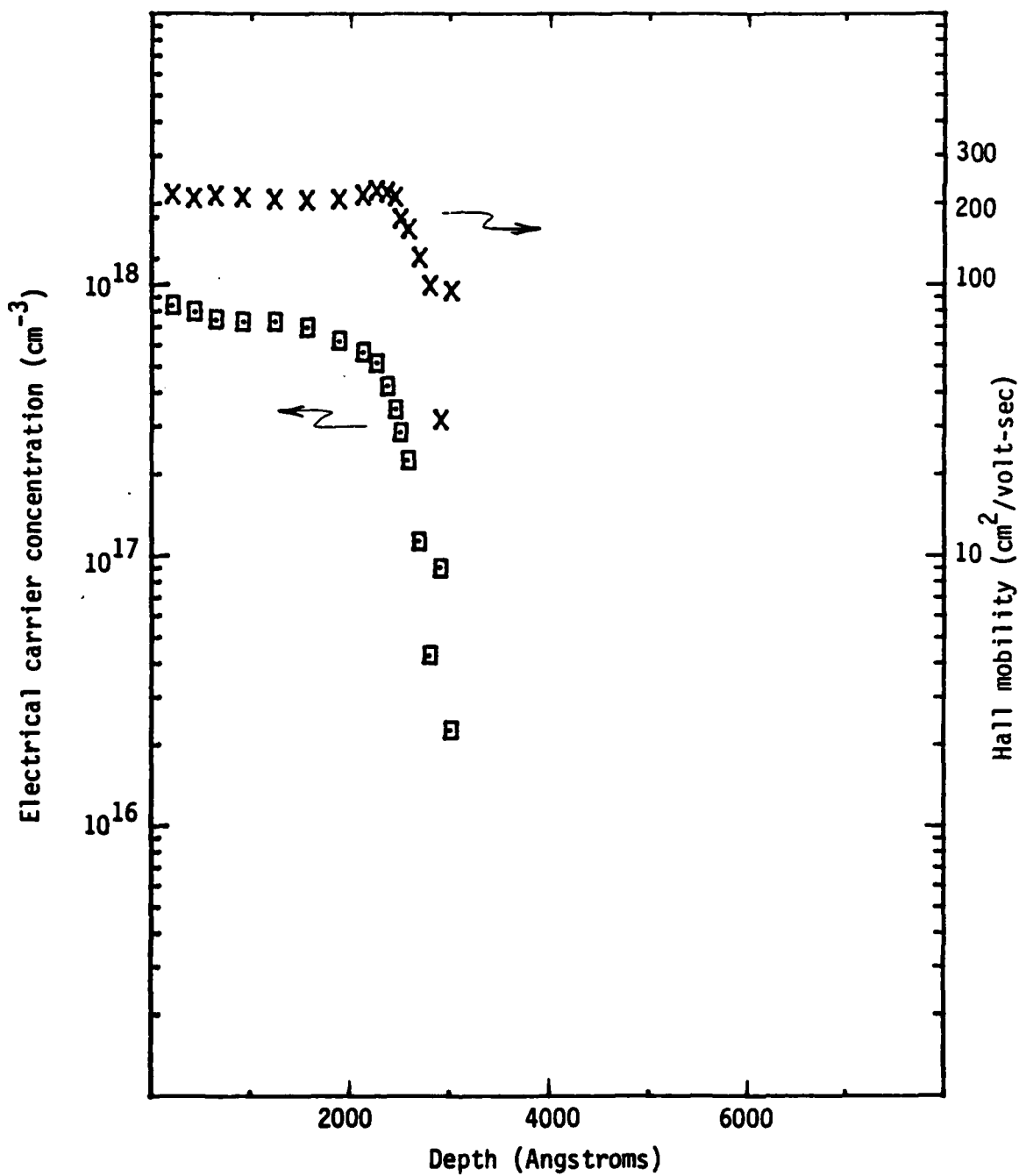


Figure IV-6. Electrical profile for capped and annealed control sample #23-4, VPE GaAs. Annealed at 850°C for 15 min. in H_2 . (X=Hall mobility data; \square =p-type electrical carrier concentration).

the carrier concentration drops off quickly and the sample becomes highly resistive.

An attempt was made to etch beyond the conversion layer with a previously measured C/A control sample (#22-2). Knowing that sample 23-4 had shown a 2500 \AA layer, 5000 \AA were etched off sample 22-2 and new indium contacts placed on the sides of the sample surface. The Hall measurement still showed p-type activity. Then, the last data points of sample 23-4 (at about 3000 \AA) were combined with the new 5000 \AA data point of sample 22-2. The resulting calculation showed the Hall mobility to be $170 \text{ cm}^2/\text{volt-sec}$ with a carrier concentration of $7 \times 10^{15} \text{ cm}^{-3}$ at the average depth of 4000 \AA . Thus, the converted layer was at least 5000 \AA deep, but the carrier concentration had continued to drop off quickly.

In summary, for the electrical measurements on the capped and annealed VPE GaAs, it is clear that a strong p-type thermal conversion layer occurs within several thousand \AA of the surface. While the p-type activity drops off rapidly for the deepest successful etch, it is also clear that the thermal conversion phenomenon will complicate detection of electrical activity of 120 keV carbon implants which are located in approximately the same region.

2b. Luminescence Measurements: Capped and Annealed VPE GaAs.

The luminescence results for the capped and annealed (C/A) VPE GaAs will show clearly that silicon acceptors have been introduced, most likely from the Si_3N_4 encapsulant during the annealing process. Also, manganese acceptors are introduced. PL etch profiling shows that these two acceptors persist to at least 3μ in depth. While carbon acceptors appear in the PL etch of a 950 $^{\circ}\text{C}$ C/A control sample, carbon acceptors are undetectable throughout the implant region, or in any other surface luminescence of C/A control samples.

A VPE sample (#13-22) which had been capped and annealed at 850° C was run in a PL experiment under conditions identical, except for sample temperature, to those for an unannealed VPE sample (HP-C-14-2-4). The results are shown in Figure IV-7. The exciton lines appear at the same energies in both the unannealed and annealed samples, with a few differences. The 1.5127 eV line is stronger in the annealed sample, indicative of more acceptors in the type-converted annealed sample. Also, a weak line appears at 1.5103 eV when the C/A sample was cooled to 5° K. The acceptor related lines appear at 1.4897, 1.4857, and 1.4824 eV. To reduce the donor-acceptor line components for the PL spectra, the sample temperature was increased from 8.5° K to 16° K. The center line at 1.4857 eV increases to become the dominant line in this band. At this elevated temperature, the 1.4824 eV line is almost extinguished, as expected for donor-acceptor lines. Recalling that the 1.4897 eV line, characteristic of the unannealed VPE GaAs, is due to residual Zn acceptor and that the 1.4857 eV line aligns well with the reported position for Si acceptors (Ref 17), we see that the predominant shallow acceptor is now Si. Diffusion into the sample from the Si_3N_4 encapsulant is the most likely source.

PL data covering the 1.41 eV and 1.36 eV bands for C/A sample 13-22 is shown in Figure IV-8, under the same conditions as Figure IV-7, except that the system resolution is approximately 2 meV. Another sample (not shown) also annealed at 850° C had identical spectra for these deeper bands, characterized by lines at 1.408 eV and 1.359 eV and their phonon replicas. SIMS data to be presented for the carbon implanted samples (Section IV.B.3.b) show a near surface accumulation of Mn. Thus, it appears that the annealing step has introduced Mn from an unknown source.

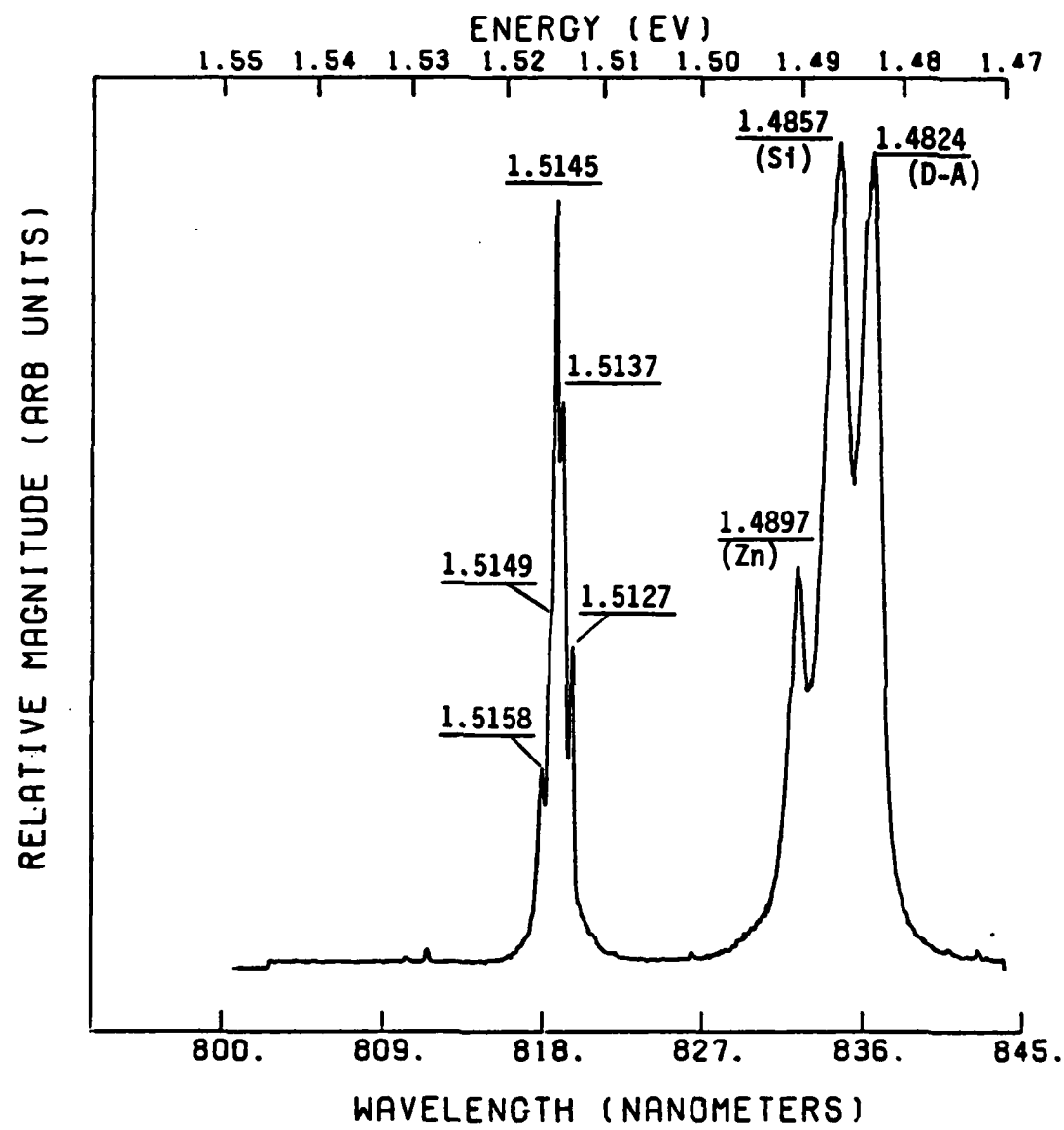


Figure IV-7. PL of VPE GaAs after 850° C anneal with Si_3N_4 encapsulant. Illumination with 5145 Å line of argon laser at 0.1 W/cm^2 and sample at 8.5° K.

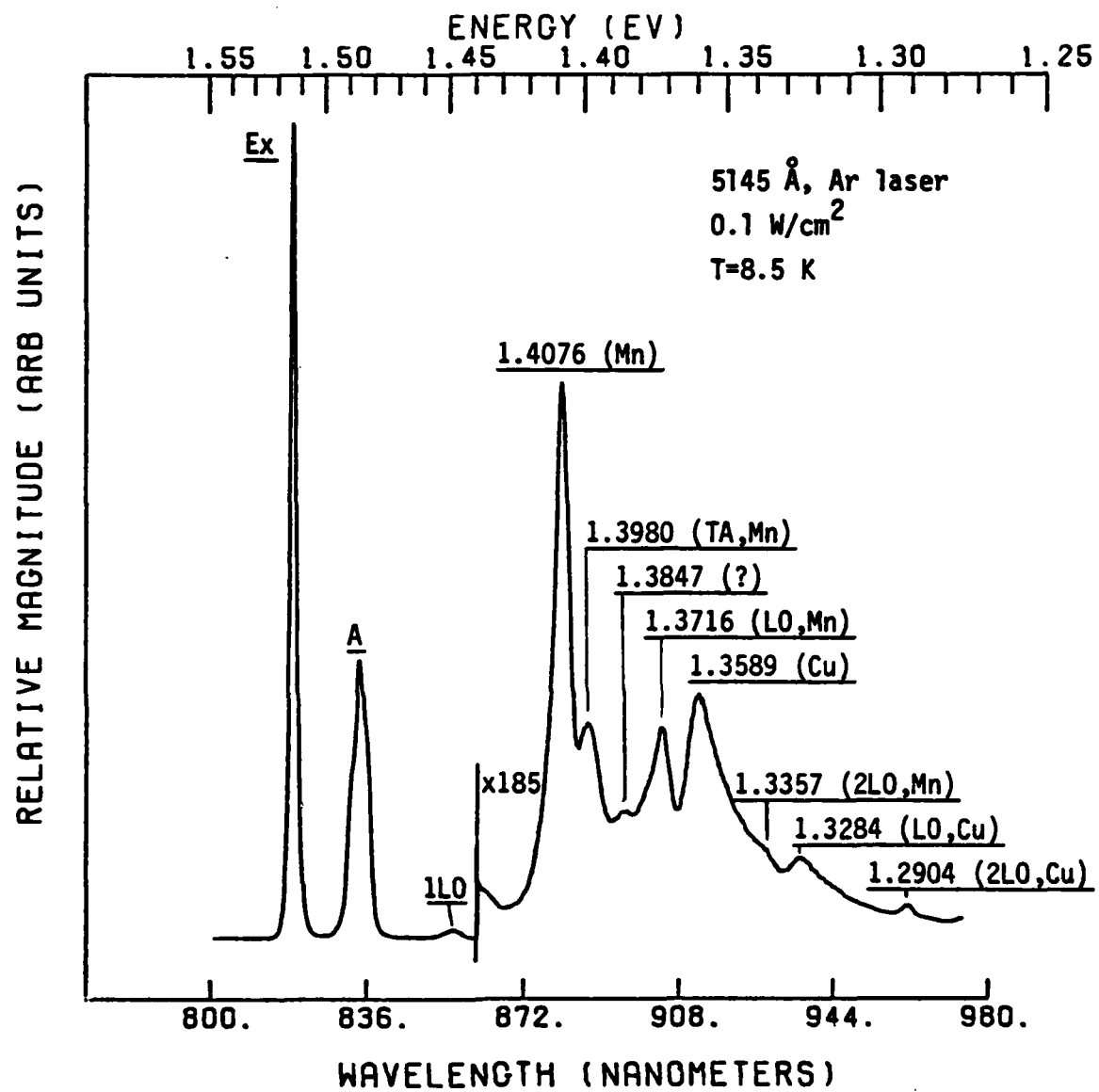


Figure IV-8. PL spectra of VPE GaAs sample annealed at 850 °C. With system resolution at 2 meV, all excitons have merged into band labeled Ex and shallow acceptors have merged into band labeled A.

The phonon replicas of the 1.408 eV and 1.359 eV lines are easily accounted for, as indicated in Figure IV-8. The line at 1.384 eV does not fit any combination of GaAs vibration modes (Refs 82, 83) and does not appear in other Mn PL spectra (Refs 63, 64, 65). This line also appears in the carbon implanted and neon implanted samples, and is therefore common to all annealed samples. PL profiling data to be presented show that, in a 10^{13} cm^{-2} dose carbon implant, this 1.384 eV line remains after several microns are etched off, and it remains after there is no further evidence of the 1.408 eV line or its phonon replicas. Thus, the 1.384 eV line is related to some energy level created by the capping and annealing process.

The effects of higher temperature anneals on the luminescence from the C/A control samples are illustrated in Figure IV-9. Several observations can be made on the behavior of Si and Zn acceptors. The exciton band is about a factor of 10 less intense than the shallow acceptor band for the 850° C and 950° C annealed samples. The Si acceptor line at 1.4854 eV does not increase monotonically, compared to the free exciton line, but at 950° C it still indicates the strongest presence of Si in the three C/A control samples. Also, even though it is an unresolved shoulder in the spectra, the Zn acceptor line at 1.4894 eV for the 950° C C/A control has grown larger than the exciton band.

The higher temperature anneals also have clear effects on the exciton lines. At 950° C, lower energy exciton lines appear at 1.5112, 1.5102, and 1.5083 eV. The 1.5112 eV line was seen in some of the VPE GaAs samples. The 1.5102 eV line appeared in other PL spectra for some 850° C C/A control samples, but has grown strongest in the 950° C anneal sample. The line at 1.5083 eV had not been observed for the lower temperature anneals. Since these lines appear at energies consistent

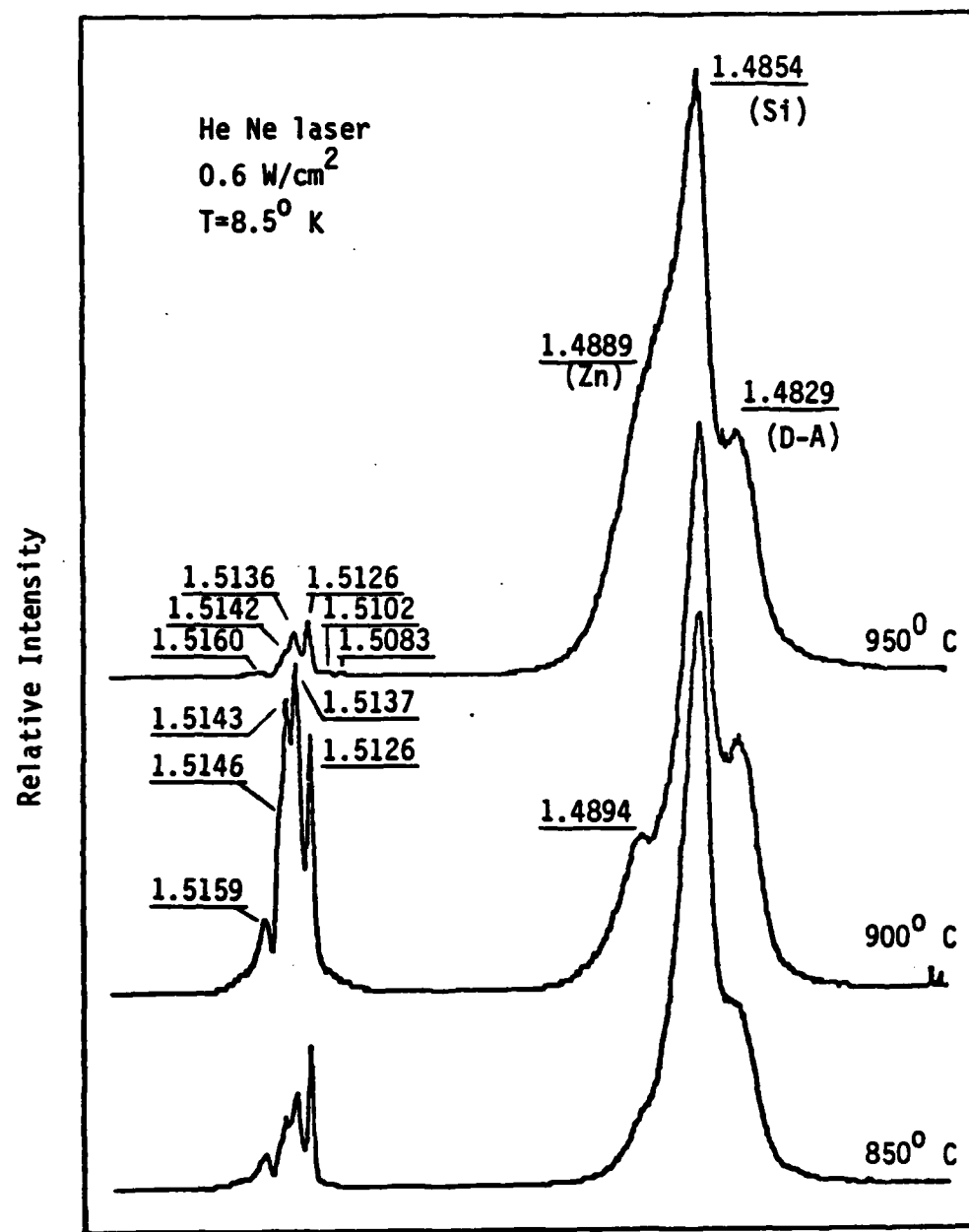


Figure IV-9. Photoluminescence spectra from unimplanted VPE GaAs control samples which were encapsulated with Si_3N_4 and annealed at three temperatures for the same conditions as the carbon implants, 15 min. in H_2 . Peak energies shown in eV.

with the band of defect induced bound excitons described in Reference 60, they may be indicating the production of defects by the annealing procedure.

In order to see how the luminescence changed as a function of depth, a PL etch experiment was performed with a 950° C C/A control. It was etched simultaneously with a 10^{15} cm^{-2} dose carbon implant (whose PL data is presented in Section IV.B). PL etch spectra are shown in Figures IV-10 and IV-11. Plots of spectral peak heights versus depth are shown in Figures IV-12 and IV-13, where Plot A is the exciton band, Plot B is the shallow acceptor band, and Plot C is the deep acceptor band. The peak height reported is the number of photon counts in the MCA channel where the peak occurs. The PL etch data for depths less than 2700 Å were collected at 2 meV resolution and 5° K sample temperature. Deeper PL etches were run at 8.5° K sample temperature with 0.3 meV resolution over the exciton and shallow acceptor band.

Due to the system resolution for the near surface etches, the exciton band is not well resolved and consists of a main peak at 1.5132 eV. Some exciton structure is observed, however, with the 1.5103 eV line detectable at the surface and at 709 Å, and at 2257 Å the 1.5129 eV line appears as a shoulder on a 1.5138 eV peak. In this near surface region, the exciton band shows a slight increase in strength away from the surface. For the deeper etches, run with better resolution, the 1.5138 eV and 1.5129 eV lines are resolved, and the free exciton line at 1.5161 eV is detectable. The 1.5103 eV and 1.5084 eV lines persist, and the relative intensities of all exciton lines are quite uniform, though the absolute intensities vary by a factor of 2, from 1 to 3μ in depth. However, the 1.5024 eV line is undetected until almost 3μ in depth where it appears at a strength comparable to the 1.5103 eV and 1.5084 eV lines.

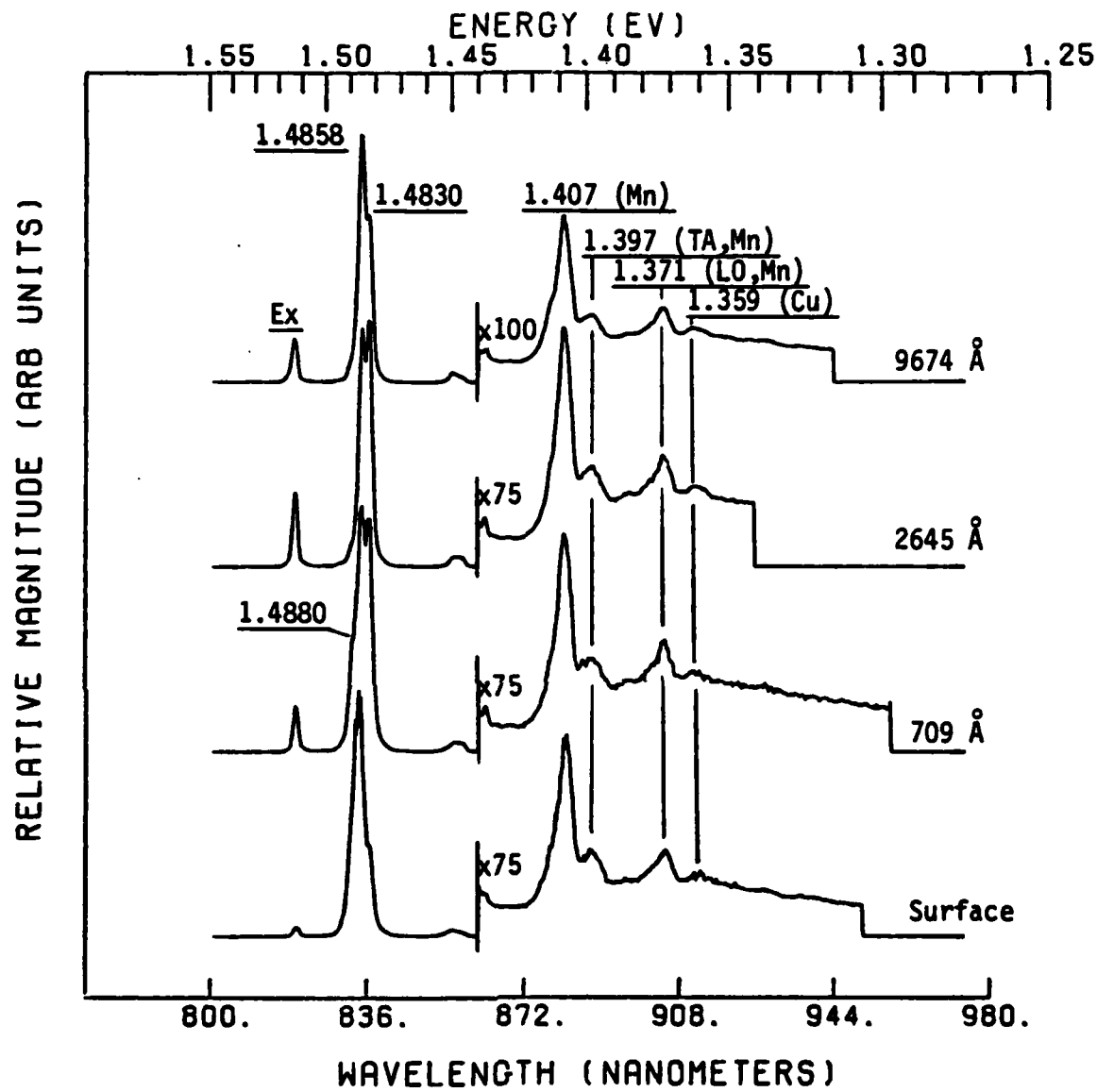


Figure IV-10. PL etch spectra for 950°C capped and annealed control sample etched from original surface to approximately one micron in depth. All spectra from samples at 5°K , except for deepest etch which was at 8.5°K . Ex denotes exciton band. Peak positions in eV.

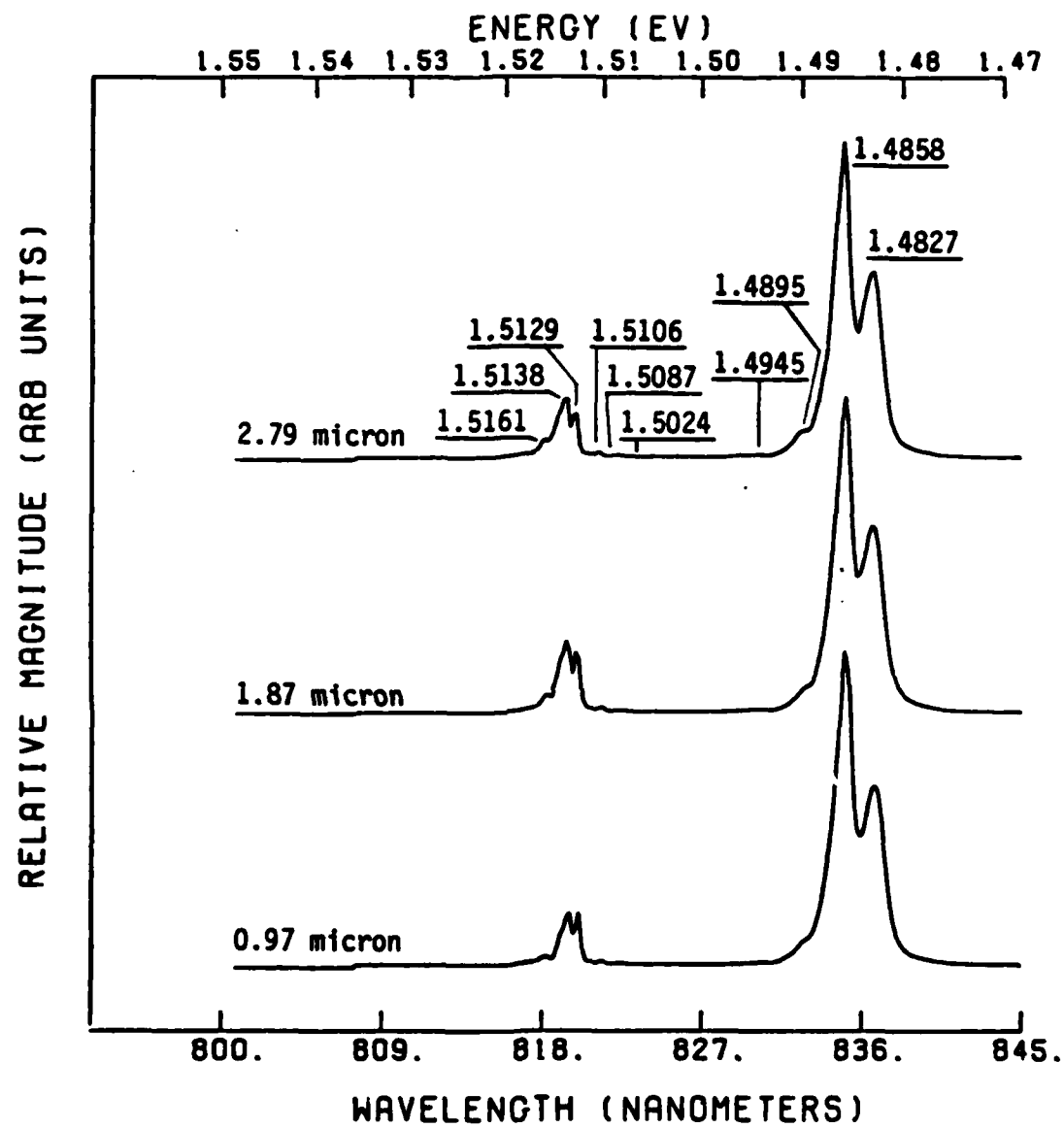


Figure IV-11. PL etch spectra for 950° C capped and annealed control sample showing exciton and shallow acceptor bands for deep etches.

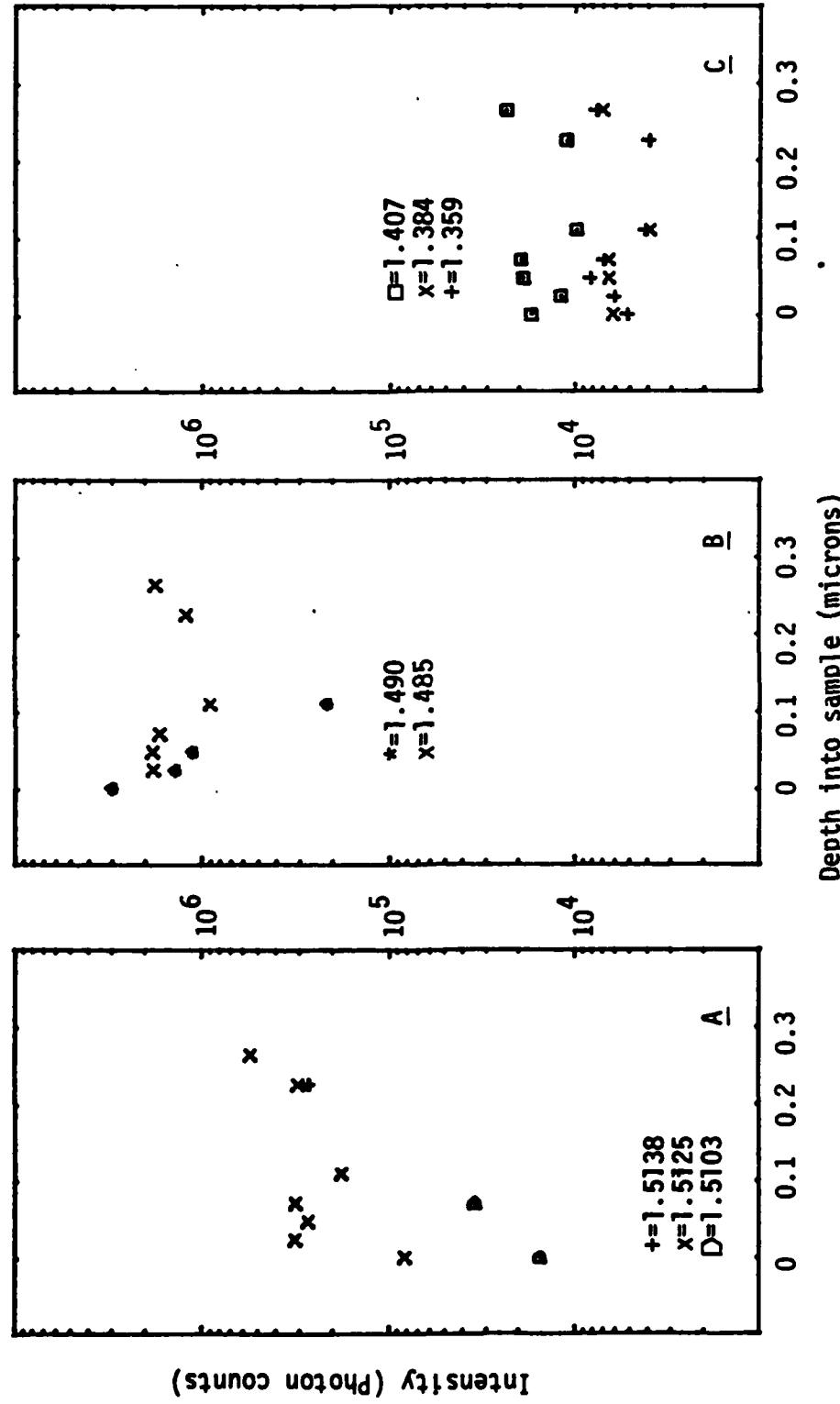


Figure IV-12. PL etch data for near surface region of 950° capped and annealed control sample of VPE GaAs. Plot A is exciton band; $+=1.5138$ eV, $X=1.5125$ eV, $D=1.5103$ eV. Plot B is shallow acceptor band; $*=1.490$ eV, $X=1.485$ eV. Plot C is vacancies band; $\square=1.407$ eV, $X=1.384$ eV, $+=1.359$ eV. Sample temperature was 5° K; illumination with UV lines of krypton laser.

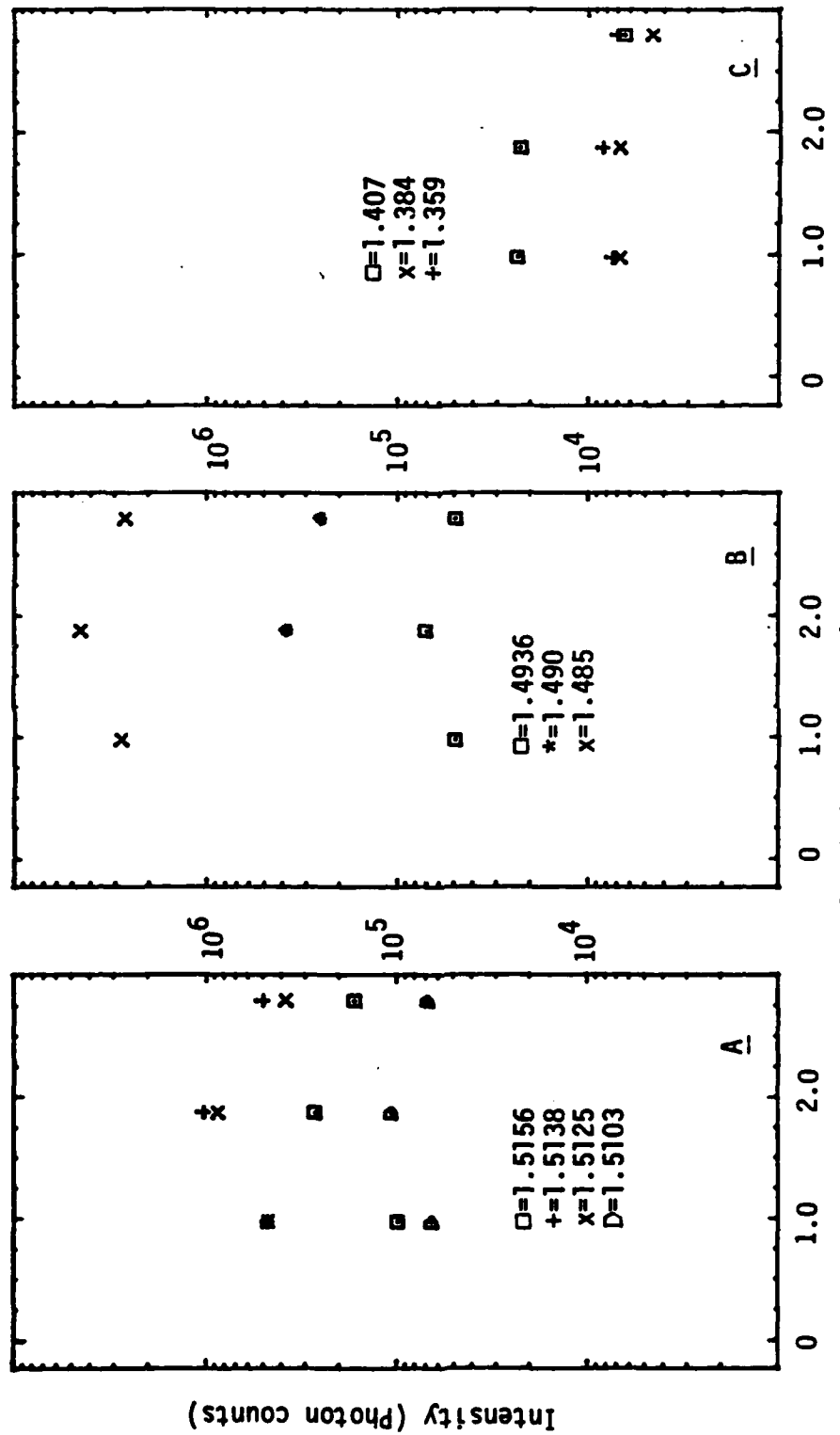


Figure IV-13. PL etch data for 950° C capped and annealed control sample of VPE GaAs. Factor of 20 applied to plots A and B to approximately correct for differences in system resolution and sample temperature from Figure IV-12. Plot A is exciton band; $\square = 1.5161$ eV, $+$ $= 1.5138$ eV, $x = 1.5125$ eV, $D = 1.5103$ eV. Plot B is shallow acceptor band; $\square = 1.4936$ eV, $*$ $= 1.490$ eV, $x = 1.485$ eV. Plot C is vacancies band; $\square = 1.407$ eV, $x = 1.384$ eV, $+$ $= 1.359$ eV. Sample temperature was 8.5° K.

Some fairly clear trends are seen in the shallow acceptor line intensities. The Zn acceptor line at 1.490 eV decreases by a factor of 10 from the surface to about 1100 Å and is subsequently undetectable until approximately 2μ have been etched off. This indicates that Zn has accumulated in the near surface region. The Si acceptor line at 1.485 eV is the dominant shallow acceptor and maintains a nearly constant intensity from the surface up to 3μ in depth. Recalling the lack of Si in the original VPE GaAs, it seems most likely that the Si has indiffused from the Si_3N_4 encapsulant and has diffused uniformly over 3μ in the 15 minute anneal at 950° C. Outdiffusion of residual Si from the GaAs:Cr substrate for the VPE GaAs cannot be ruled out, but this source of Si is unlikely to be as strong as the Si_3N_4 encapsulant. For depths of 1μ or more, the carbon acceptor line appears as a weak shoulder near 1.494 eV which is 50 to 60 times less intense than the Si acceptor line. In this case, outdiffusion from the GaAs:Cr substrate is the more probable source. These data show that carbon shallow acceptor luminescence from 120 keV carbon implants into the VPE GaAs can be completely attributed to the implanted carbon for depths less than 1μ , and that even beyond 1μ the carbon contribution from the substrate is very weak.

A plot of the $1\text{ L}0/0\text{ L}0$ phonon ratios versus depth for the Si acceptor line is shown in Figure IV-14. There is a slight increase (a factor of 1.5 to 2) in the phonon coupling strength from the surface to about 2300 Å, with a more gradual increase beyond this point to about 3μ . The implication is that the GaAs crystal structure has been most strongly perturbed in the near surface region by the encapsulation and annealing procedure.

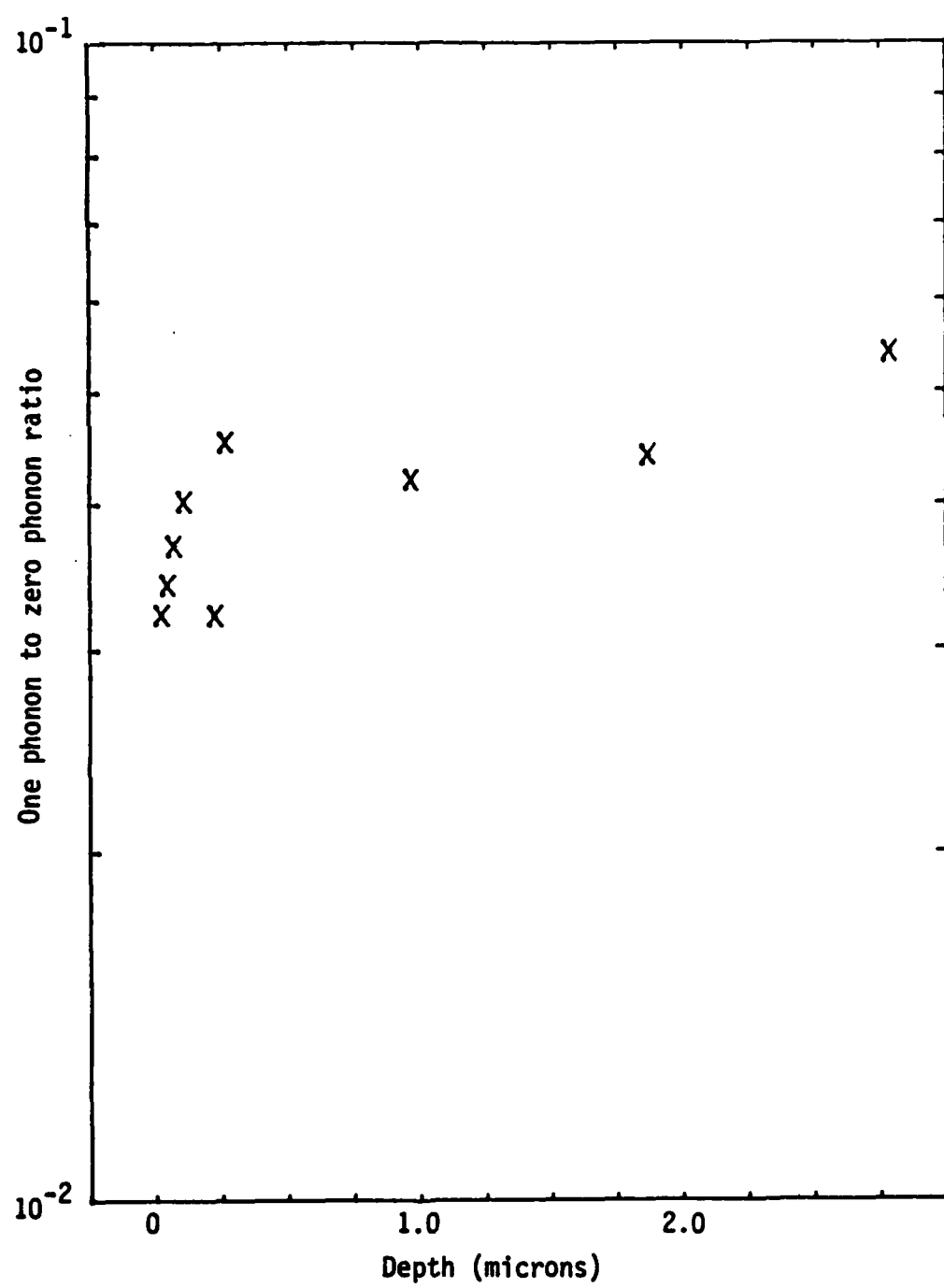


Figure IV-14. One phonon to zero phonon spectral peak ratio vs. etch depth for the 1.4855 eV (silicon) line from a 950^0 C capped and annealed control sample.

Referring to Plot C in Figures IV-12 and IV-13, the deep acceptor lines show some scatter (factor of 2), but in general they are fairly uniform from the surface to 3μ in depth. The 1.407 eV Mn line remains the strongest line in this band until 2.8μ in depth where it decreases to become comparable to the other deep acceptor lines.

In summary, for all the luminescence results from the C/A control samples for VPE GaAs: (1) there is no detectable carbon in the region where the 120 keV carbon implant is expected; (2) there is a significant amount of Si indiffusion; (3) there is a near surface accumulation of Zn; (4) L0 phonon ratios for Si indicate degraded GaAs crystal structure near the surface; (5) Mn acceptors appear to be uniformly distributed in depth for the 950° C C/A sample; (6) an unknown line at 1.384 eV is introduced by the capping and annealing process; and (7) increasing the anneal temperature from 850° C to 950° C enhances both the Si acceptor line and the appearance of exciton lines at 1.5112, 1.5103, and 1.5024 eV.

3. Neon Implanted VPE GaAs. Neon implanted VPE GaAs samples were prepared as control samples to isolate effects due to implantation kinetics. Vacancies and defects created by inert neon atoms would be, under ideal circumstances, annealed out during the post-implantation annealing step. That is, the original lattice would be recovered except for the introduction of electrically inert neon atoms and, ideally, electrical and optical parameters would also be recovered. The extent to which these parameters do not recover can be used as a measure of lattice damage caused by the implant which remains after annealing and which is distinct from the introduction of implanted dopants.

Neon was implanted at 120 keV for three doses ($1 \times 10^{13} \text{ cm}^{-2}$, $1 \times 10^{14} \text{ cm}^{-2}$, $1 \times 10^{15} \text{ cm}^{-2}$) to correspond to the carbon implants.

The LSS profile for 120 keV neon is more shallow and narrow than the 120 keV carbon (see Figure IV-15) due to the mass differences and differences in the nuclear and electronic stopping powers of GaAs for neon and carbon. Thus, the effects of the neon implant are more shallow than the carbon implants.

3a. Electrical Measurements: Neon Implanted VPE GaAs.

Surface electrical measurements on the neon implants are shown in Table IV-4.

TABLE IV-4
SURFACE ELECTRICAL MEASUREMENTS FOR 120 keV NEON IMPLANTS
IN VPE GaAs, ANNEALED AT 850° C FOR 15 MINUTES IN H₂

| Dose (cm ⁻²) | Sample # | Mobility (cm ² /volt-sec) | Sheet Carrier Concentration (cm ⁻²) | Type |
|-----------------------------|----------|---|--|------|
| 1 x 10 ¹³ | 4-2 | 195 | 4.8 x 10 ¹² | p |
| 1 x 10 ¹⁴ | 4-4 | 136 | 2.4 x 10 ¹² | p |
| 1 x 10 ¹⁵ | 4-5 | 108 | 4.5 x 10 ¹² | p |

There is a consistent trend to lower mobility values as the implanted dose of neon is increased. However, there is no trend evident in the measured sheet carrier concentration. Compared to the 850° C C/A control samples surface electrical measurements (Table IV-3), the sheet carrier concentrations for the neon implants are still in the same range as the C/A controls. Thus, from surface electrical measurements alone, the effects of neon implantation are most clearly seen as a reduction in the p-type carrier mobility, with no clear effect on sheet carrier concentration.

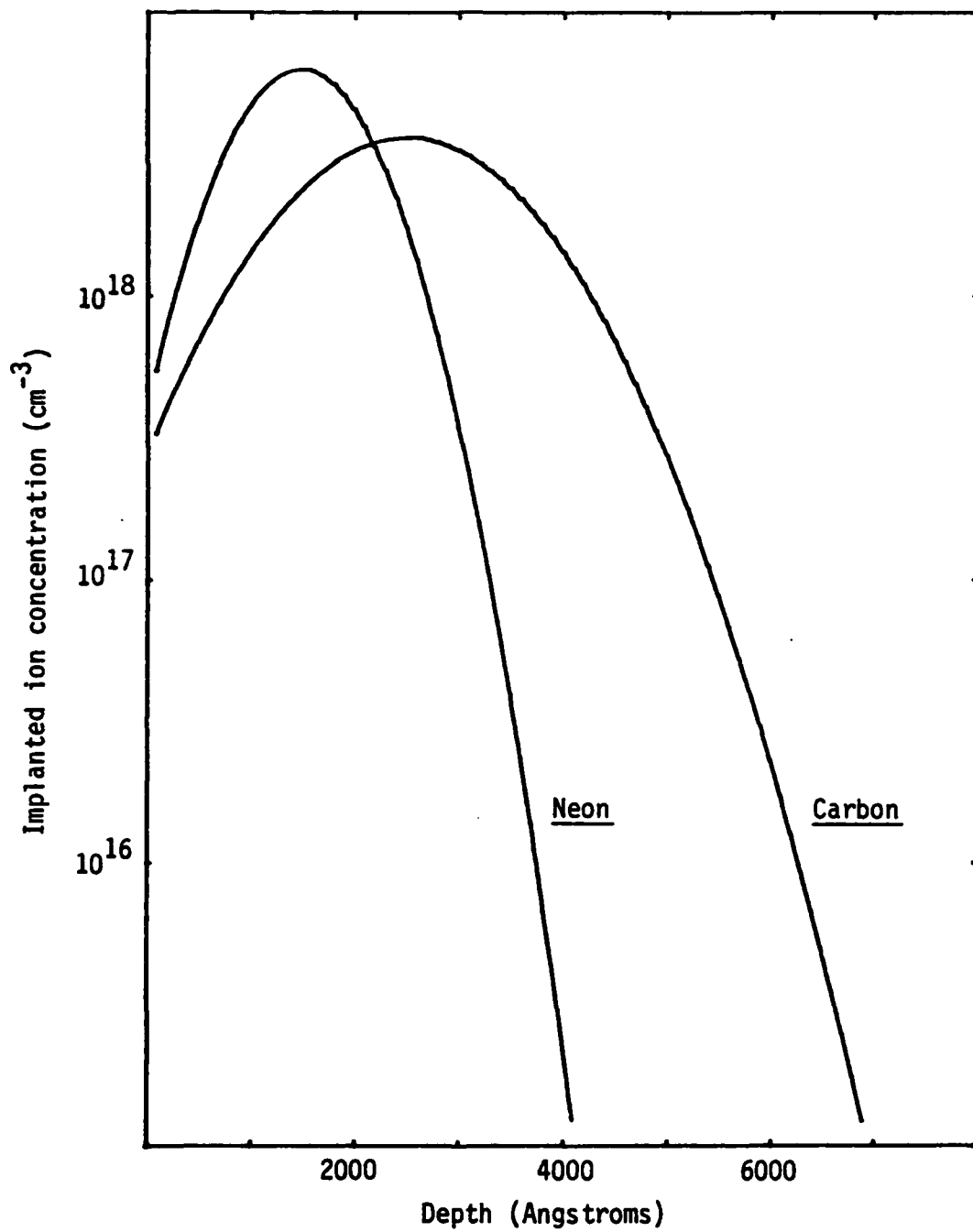


Figure IV-15. Theoretical LSS implant profiles for 120 keV carbon and neon with a dose of $1 \times 10^{14} \text{ cm}^{-2}$.

Electrical profiles were attempted on all neon implanted samples. The $1 \times 10^{14} \text{ cm}^{-2}$ and $1 \times 10^{15} \text{ cm}^{-2}$ neon implants both exhibited sheet resistivities and sheet Hall coefficients which quickly saturated to constant values as the samples were profiled, while the $1 \times 10^{13} \text{ cm}^{-2}$ dose sample did not (Figure IV-16). This saturation is discussed in Appendix A and it affects the results of the calculation for the carrier concentration and Hall mobility (as discussed in Section II.A.4) because the result of the subtraction of the reciprocals or squares of reciprocals of two numbers differing only slightly is strongly affected by small errors. A typical result is a negative value of calculated carrier concentration or mobility. Thus, when the calculation results in negative values, examination of the measured sheet resistivity and sheet Hall coefficient versus depth can reveal whether the negative values are due to either scatter in the data or to a plateau in the data. The plateau region in the data was observed for the neon implants and, as will be seen, for the high dose carbon implants.

The measured p-type carrier concentration and Hall mobility for the $1 \times 10^{13} \text{ cm}^{-2}$ neon implant are plotted in Figure IV-17 along with the LSS implant profile. Recalling the 850° C C/A control profile (Figure IV-6) the effect of the $1 \times 10^{13} \text{ cm}^{-2}$ neon implant has been to cause the near surface carrier concentration to decrease more rapidly with depth. There is a close correlation of the low carrier concentration region past the rolloff with the maximum of the LSS implant profile for neon. The minimum value for mobility occurs more near the surface at approximately 600 \AA . Therefore, if mobility correlates with residual lattice damage, the region of maximum damage occurs closer to the surface than the LSS peak for maximum implant concentration. The mobility recovers past the implanted

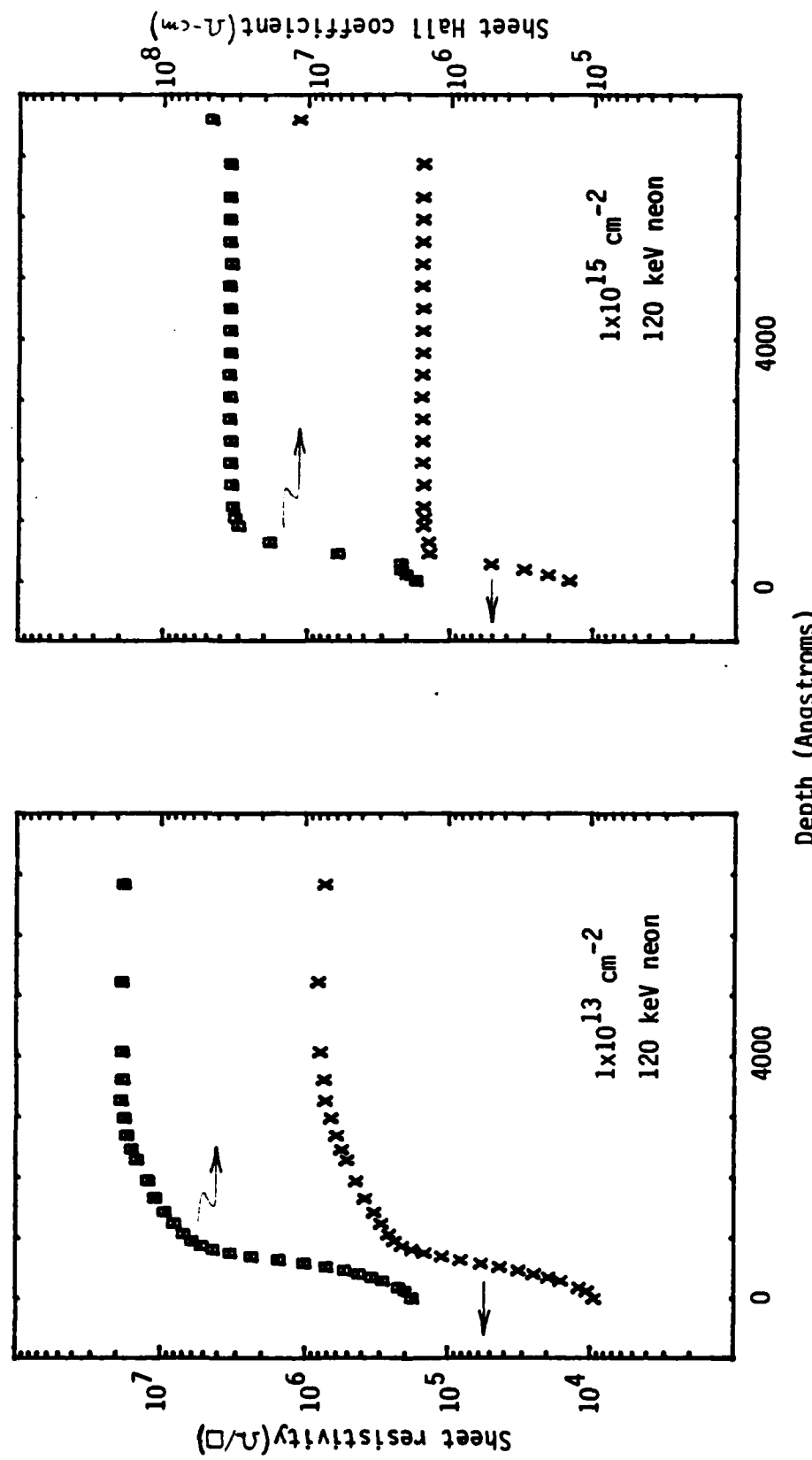


Figure IV-16. Sheet resistivity and sheet Hall coefficient vs. depth for 120 keV neon implanted VPE GaAs for doses of $1 \times 10^{13} \text{ cm}^{-2}$ and $1 \times 10^{15} \text{ cm}^{-2}$. Samples annealed at 850°C for 15 min. in H_2 . (X=sheet resistivity; \square =sheet Hall coefficient).

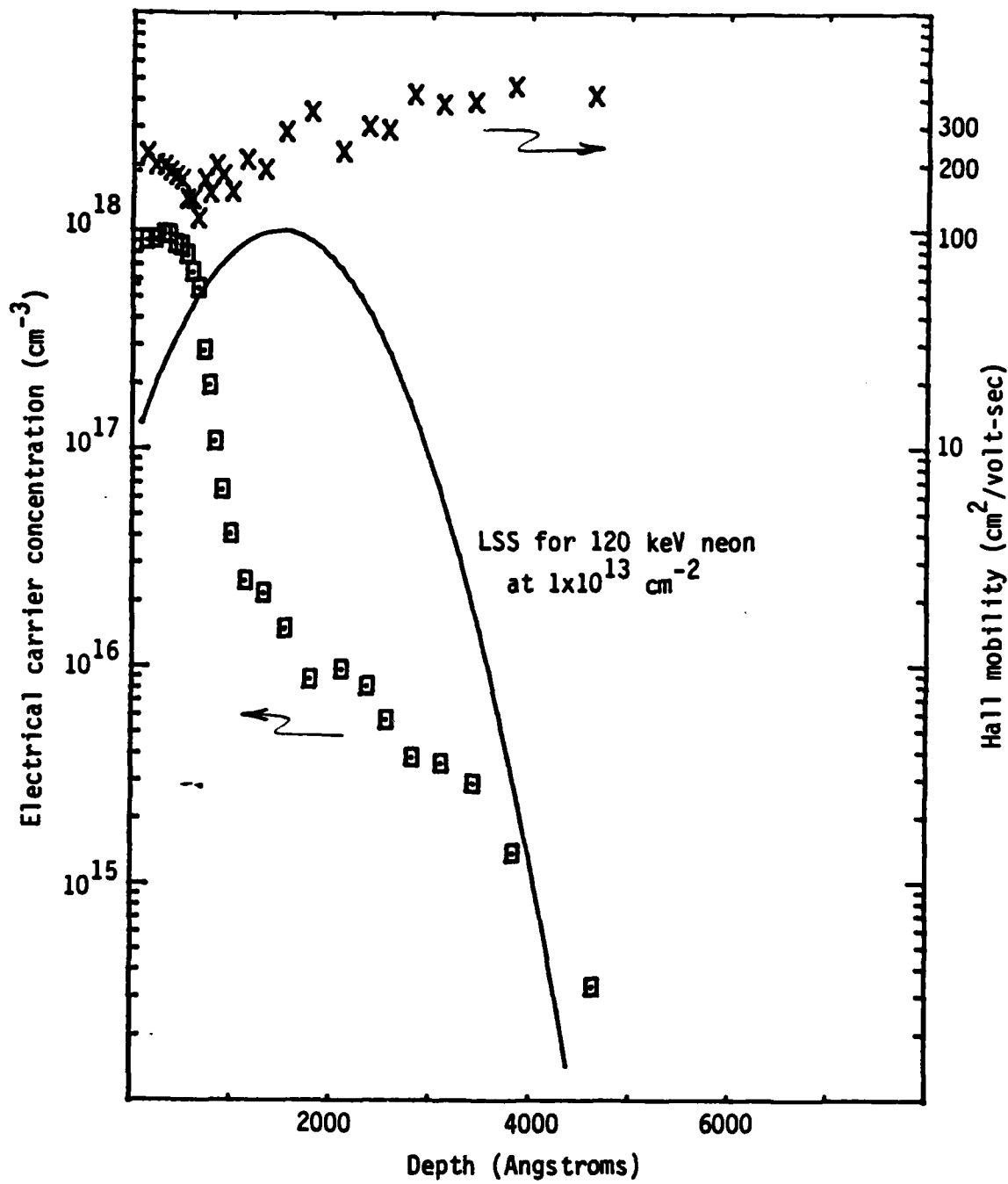


Figure IV-17. Electrical profile results for $1 \times 10^{13} \text{ cm}^{-2}$ dose of 120 keV neon implanted in VPE GaAs, annealed at 850° C for 15 min. in H_2 . Also shown is the LSS theoretical prediction for the neon concentration. (X=Hall mobility; □=electrical carrier concentration, p-type).

region to values near $450 \text{ cm}^2/\text{volt}\cdot\text{sec}$. This exceptionally high p-type mobility value allows the calculation of the very low carrier concentrations which are trending to less than $1 \times 10^{14} \text{ cm}^{-3}$ past the implanted region.

In summary, for the electrical measurements on neon implanted VPE GaAs, the primary effect of the neon implant has been to alter the p-type electrical carrier concentration profile, which now decreases more rapidly with depth (for the successfully etched $1 \times 10^{13} \text{ cm}^{-2}$ dose sample). Surface electrical measurements as a function of implant dose show no clear trend in electrical carrier concentration, but do indicate that neon implants produce approximately the same degree of p-type activity as the thermally converted capped and annealed VPE GaAs control samples.

3b. Luminescence Measurements: Neon Implants. The PL spectra of the neon implanted control samples, along with the spectra of the C/A control and unprocessed VPE GaAs are shown in Figure IV-18. The illumination source was the HeNe laser with the sample temperature near 10° K . As with previously shown spectra, the spectrometer resolution was changed from 0.2 meV to 2.0 meV beyond 1.45 eV . The spectra were normalized to the largest peak in the data. Qualitatively, the neon implanted PL spectra are quite similar to the C/A control samples. Generally, there is not much difference in the 1.408 eV line for any sample which has been annealed. The 1.359 eV line is increased in relative strength for the annealed samples when compared to the original VPE material; however, there is no clear trend observed with increasing implant dose of neon.

The exciton and shallow acceptor bands are labeled E_x and A in Figure IV-18, respectively. The exciton band shows the enhancement of the 1.5125 eV line for all annealed samples. For the $1 \times 10^{13} \text{ cm}^{-2}$ dose

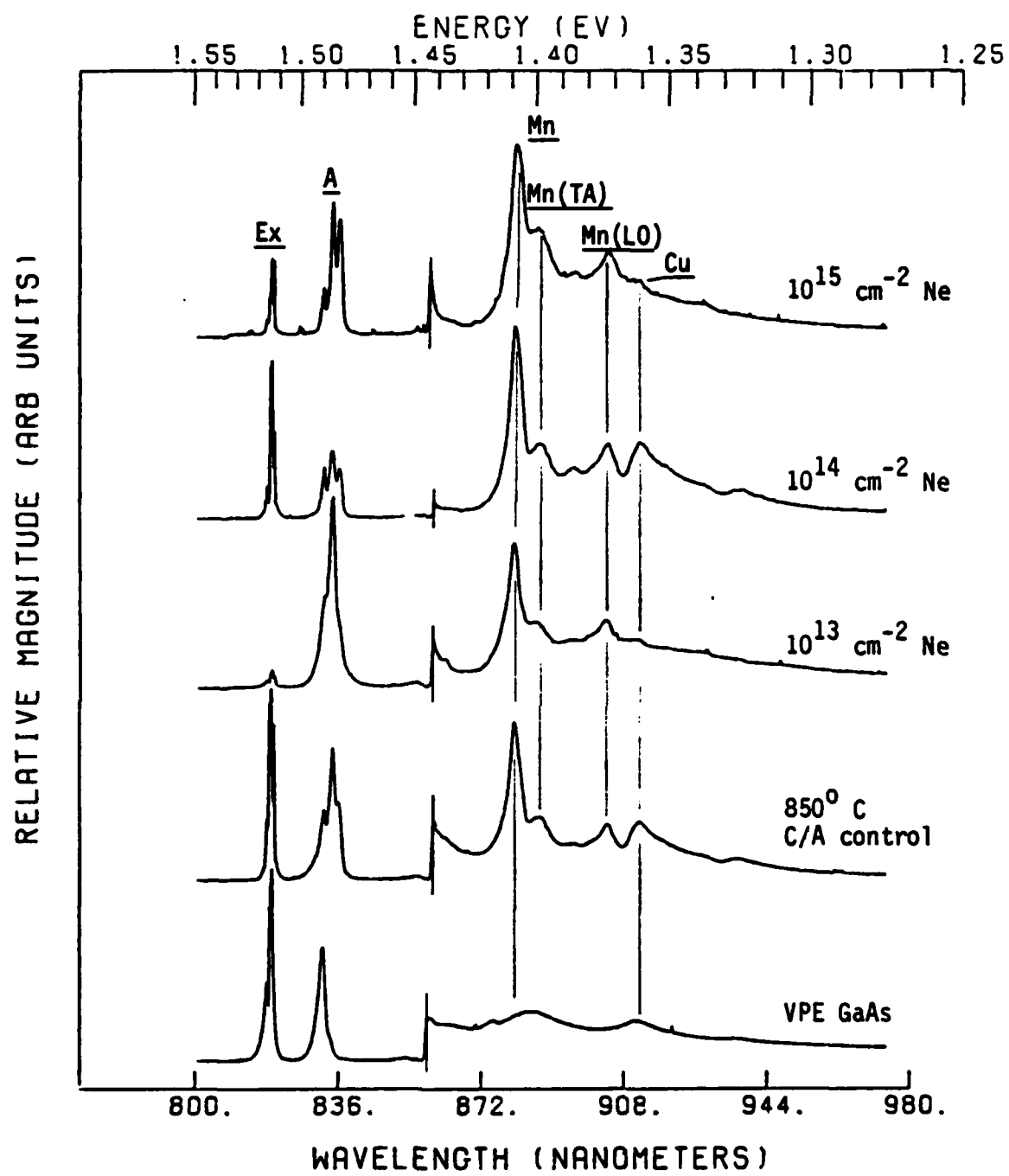


Figure IV-18. Comparison of PL spectra from three neon implanted VPE GaAs samples along with the spectra from the capped and annealed control and the unannealed VPE GaAs. Illumination was from HeNe laser at 0.1 W/cm^2 .

neon implant, the exciton band appears reduced in overall intensity. The shallow acceptor band shows the silicon acceptor at 1.4858 eV in all annealed samples, with the strongest presence indicated in the $1 \times 10^{13} \text{ cm}^{-2}$ dose neon implant. None of the samples show any new spectral lines or any evidence of high doping levels (i.e., line broadening or peak shifts).

The $1 \times 10^{13} \text{ cm}^{-2}$ dose neon implant was used in a PL etch experiment (etched simultaneously with a $1 \times 10^{13} \text{ cm}^{-2}$ dose carbon implant whose PL etch data are presented in Section IV.B.2). Data were taken from the original surface to 2.6μ in depth using the UV laser with the sample held at 8.5° K . The PL spectra are shown in Figures IV-19 and IV-20, with peak heights versus depth shown in Figure IV-21. The PL spectra plots are normalized to the 1.4858 eV (silicon) line. The peak height data are, again, the MCA channel counts in the peak channel.

By comparison to the PL etch data from the 950° C C/A control sample (Figures IV-10 through IV-13), we can identify some effects which are due to implantation of neon. Plot A in Figure IV-21 shows the dominant exciton peak to be 1.5128 eV, as it was for the C/A control, until 2.6μ are etched off. The 1.5128 eV intensity is nearly uniform except for the surface and at 0.2μ . This behavior is also true for the 1.5138 eV line. However, the 1.5161 eV line shows a gradual increase up to 0.85μ . Of the lower energy exciton structure previously seen, only the 1.5113 eV line appears at 836° A .

Plot B in Figure IV-21 shows the accumulation of silicon (1.4858 eV) and zinc (1.4898 eV) near the implant region, with silicon being dominant. The near surface zinc accumulation is not as strong as that observed for the 950° C C/A sample. The silicon accumulation and gradual decrease in the $1 \times 10^{13} \text{ cm}^{-2}$ neon implant contrasts with the almost uniform silicon

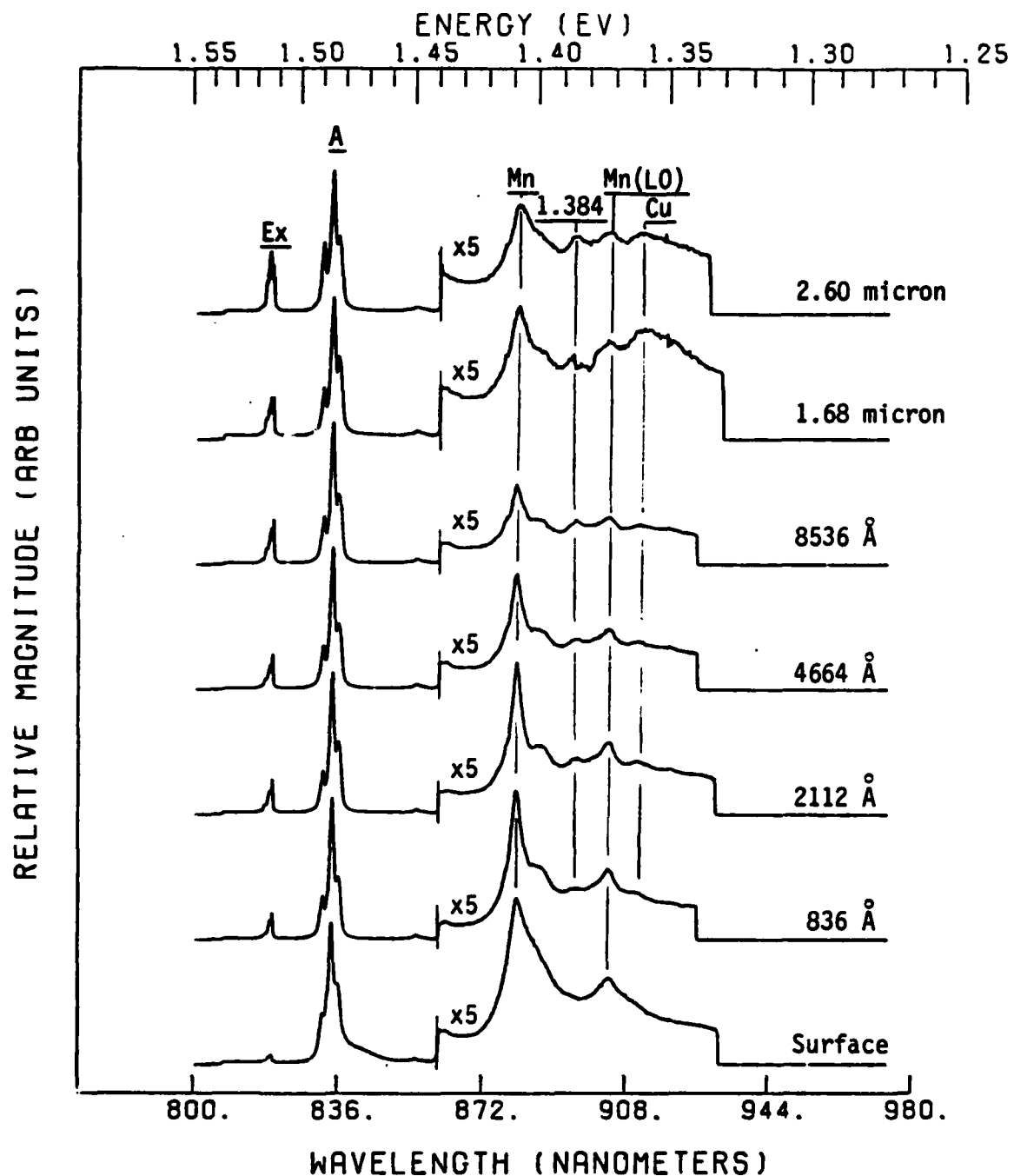


Figure IV-19. PL etch spectra from a 10^{13} cm^{-2} dose neon implanted VPE GaAs sample, annealed at 850° C . Illumination with UV lines of krypton laser, sample at 8.5° K .

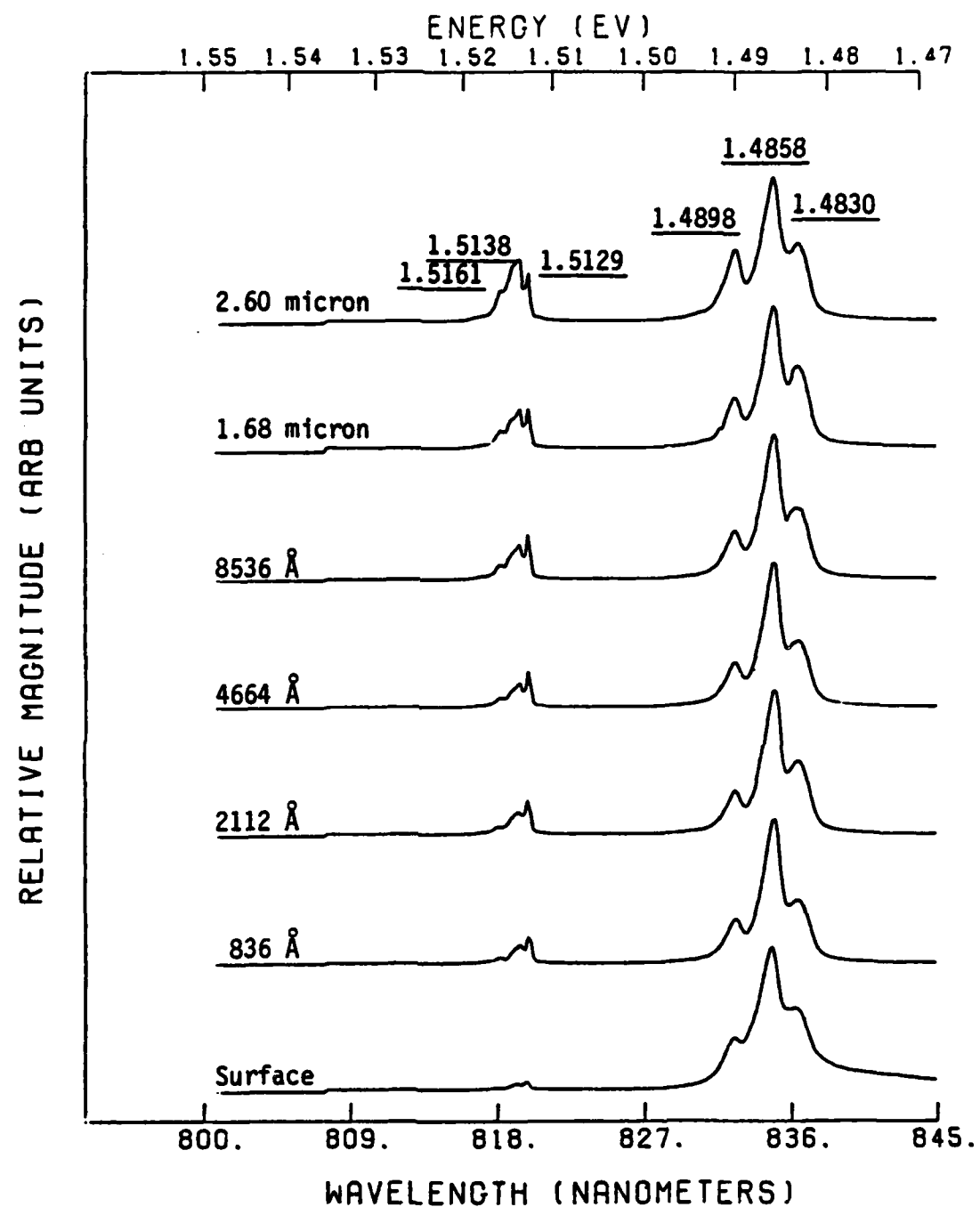


Figure IV-20. PL etch spectra from a 10^{13} cm^{-2} dose neon implant in VPE GaAs. Same data as Figure IV-19 expanded to show exciton and shallow acceptor bands in more detail.

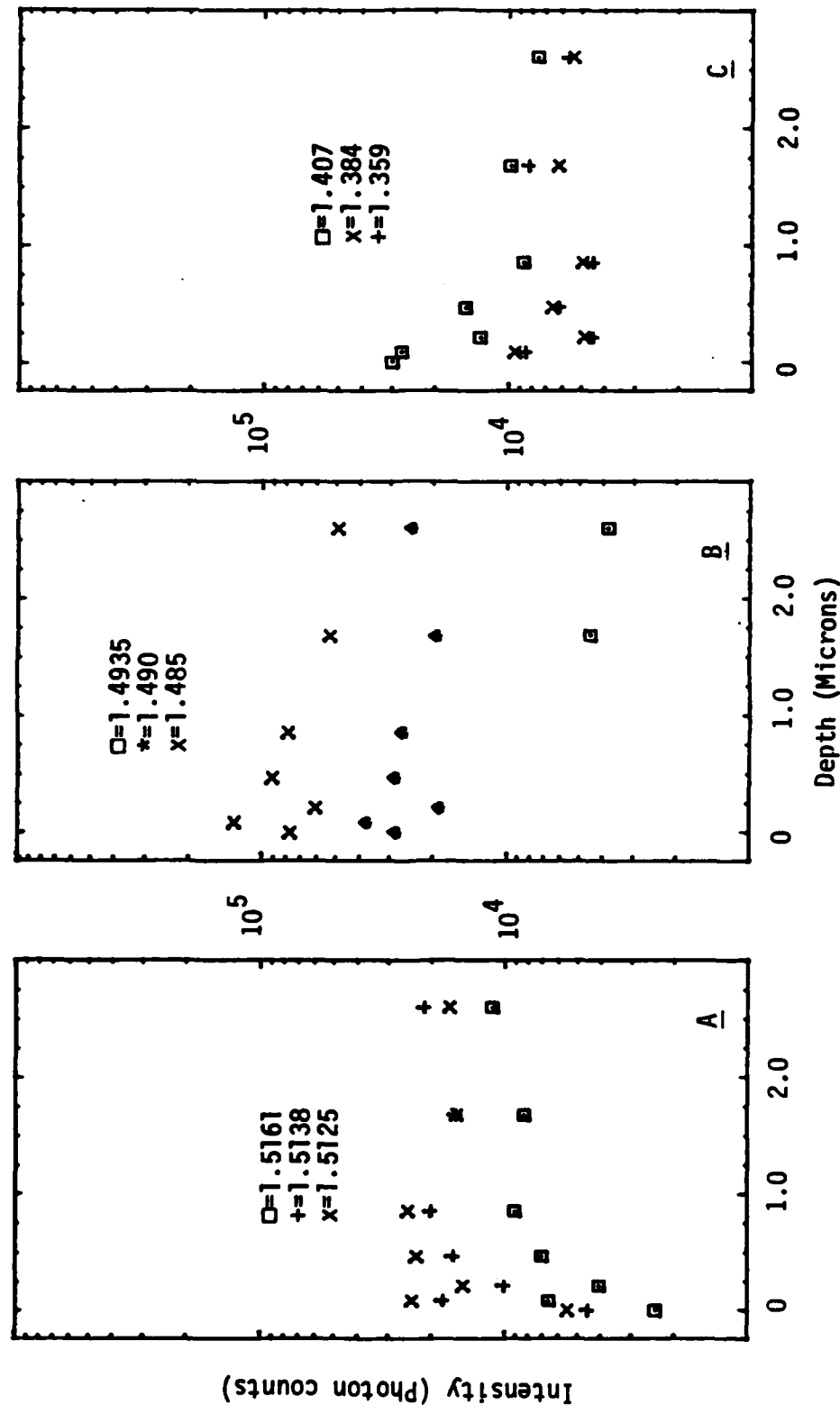


Figure IV-21. PL etch data for 10^{13} cm^{-2} dose neon implant into VPE GaAs, annealed at 850°C . Plot A is exciton band; $\square = 1.5161$ eV, $+\ast = 1.5138$ eV, $x = 1.5125$ eV. Plot B is shallow acceptor band; $\square = 1.4935$ eV, $\ast = 1.490$ eV, $x = 1.485$ eV. Plot C is vacancies band; $\square = 1.407$ eV, $x = 1.384$ eV, $+\ast = 1.359$ eV. Sample temperature was 8.5°K , illumination with UV lines of krypton laser.

distribution seen in the 950° C C/A control sample. For the exciton and shallow acceptor bands, the effect of implanting neon has been most evident in the free exciton line, and the silicon and zinc acceptor lines. From the quantitative data in Figure IV-21, it becomes obvious that the apparent growth of the exciton band in the spectra of Figures IV-19 or IV-20 is really a case of the shallow acceptor band decreasing in intensity to become comparable to the exciton band, which remains relatively constant after the first etch.

The deep acceptor lines (Plot C of Figure IV-21) also show an accumulation near the surface which decreases out to approximately 1μ . The effect is strongest for the Mn line, and less for the 1.384 and 1.359 eV lines. In this sample, the 1.384 and 1.359 eV lines track very closely as the sample is etched.

The $1 LO/0 LO$ phonon ratio for the silicon acceptor line was calculated as a function of depth for the neon implant PL profile data. It was approximately uniform over the entire depth.

In summary, it appears reasonable to associate the observed intensity effects on the PL etch data for the $1 \times 10^{13} \text{ cm}^{-2}$ neon implant with implantation effects for depths less than 1μ . These effects are not strongly correlated with the LSS implant profile (where $R_p = 0.15\mu$), but appear as a gradual change in spectral peak heights from the surface to about 1μ in depth. A gathering of shallow and deep acceptors into the neon implanted region has occurred. The free exciton line intensity indicates a reduced periodicity of the lattice, but other luminescence indicators of damage, such as the lack of excitons bound to point defects and constant LO phonon ratios, show the $1 \times 10^{13} \text{ cm}^{-2}$ neon implant to be relatively undamaged. No new spectral lines are introduced, and there is

no evidence of high doping levels.

B. Characterization of Carbon Implanted VPE GaAs

The carbon implanted samples were characterized using electrical measurements, both surface and etch profiling, photo- and cathodo-luminescence, photoluminescence etch profiling, and SIMS. Because of the strong p-type thermal conversion which occurred with the VPE GaAs, isolation of the effects due to implanted carbon requires analysis of the results of the control samples (previous section IV.A). Despite the thermal conversion, several results are clearly due to the presence of carbon.

1. Electrical Measurements: Carbon Implanted VPE GaAs. The initial electrical measurements were done for three doses of carbon, subsequently annealed at 850° C. The results are shown in Table IV-5. Also included is the $3 \times 10^{14} \text{ cm}^{-2}$ sample which was prepared later for etch profiling tests.

TABLE IV-5
SURFACE ELECTRICAL MEASUREMENTS FOR 120 keV CARBON IMPLANTED
VPE GaAs, ANNEALED AT 850° C FOR 15 MINUTES IN H_2

| Dose (cm^{-2}) | Sample | Mobility ($\text{cm}^2/\text{volt}\cdot\text{sec}$) | Sheet Carrier Concentration (cm^{-2}) | Activation Efficiency (%) |
|------------------------------|--------|--|---|---------------------------------|
| 1×10^{13} | 13-12 | 274 | 7.7×10^{12} | 77 |
| 1×10^{14} | 13-9 | 247 | 9.7×10^{12} | 9.7 |
| 3×10^{14} | 4-1 | 198 | 9.9×10^{12} | 3.3 |
| 1×10^{15} | 13-2 | 207 | 6.6×10^{12} | 0.7 |

The surface electrical measurements of the carbon implanted VPE GaAs appear, at first, to be comparable to past results for carbon implants into semi-insulating, chromium doped GaAs (Refs 28, 29, 31). Some improvement is even indicated for the $1 \times 10^{13} \text{ cm}^{-2}$ implant, which shows an apparent 77% electrical activation with a relatively high mobility of $274 \text{ cm}^2/\text{volt-sec}$. The trend to lower activation efficiencies with higher implant dose also appears to be consistent. Thus, with this evidence alone, it appeared that carbon implants into VPE GaAs had achieved higher mobilities and electrical activation than previously seen for carbon implants into GaAs:Cr.

However, comparison with the surface electrical measurements on the capped and annealed controls (Table IV-3) shows that the variation of sheet carrier concentrations for the 850° C control samples bounds the observed values for the carbon implanted samples. This clearly shows that the p-type electrical thermal conversion of the VPE GaAs is responsible for most of the observed sheet carrier concentration for the carbon implants into VPE GaAs. Partly for this reason, chemical etch electrical profiles were required to collect data through the implanted region to determine what effects were contributed by the carbon atoms.

Figures IV-22 and IV-23 show the calculated electrical carrier concentration and Hall' mobility versus depth of four implant doses of carbon into VPE GaAs. It is worth noting at this point the strong similarity of the results of the high dose carbon implant in Figure IV-23 to the reported results for an n-type silicon implant into epitaxial GaAs (Ref 84). The similarities are the dip in the electrical carrier concentration, the location of the dip nearer to the surface than the peak implanted concentration and the maximum carrier concentration

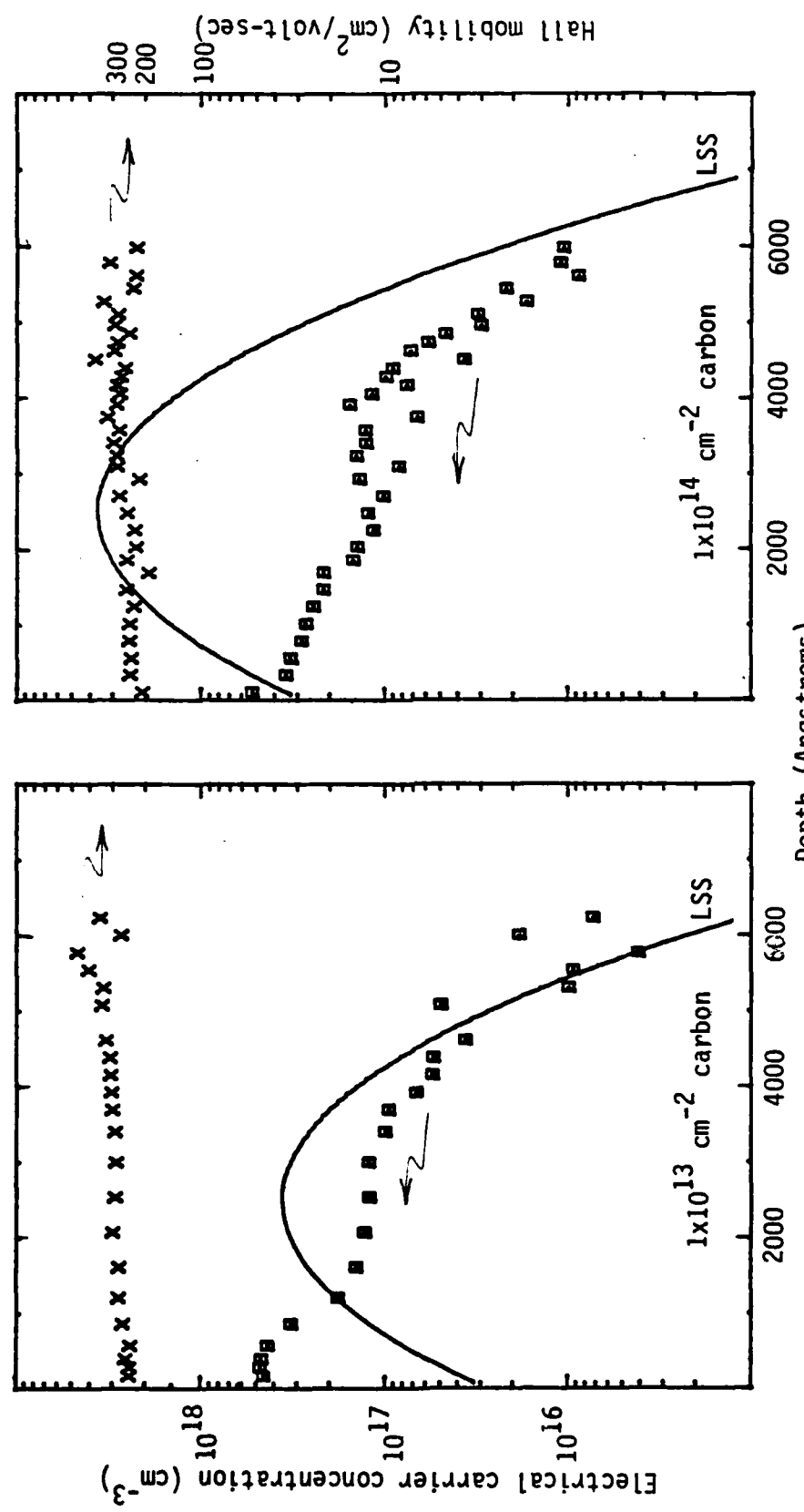


Figure IV-22. Electrical profiles for $1 \times 10^{13} \text{ cm}^{-2}$ and $1 \times 10^{14} \text{ cm}^{-2}$ carbon implant dose in VPE GaAs, annealed at 850^0 C for 15 min. in H_2 . Also shown is the LSS prediction for the carbon concentration for a 120 keV implant at those doses. (X=Hall mobility; \square =p-type electrical carrier concentration).

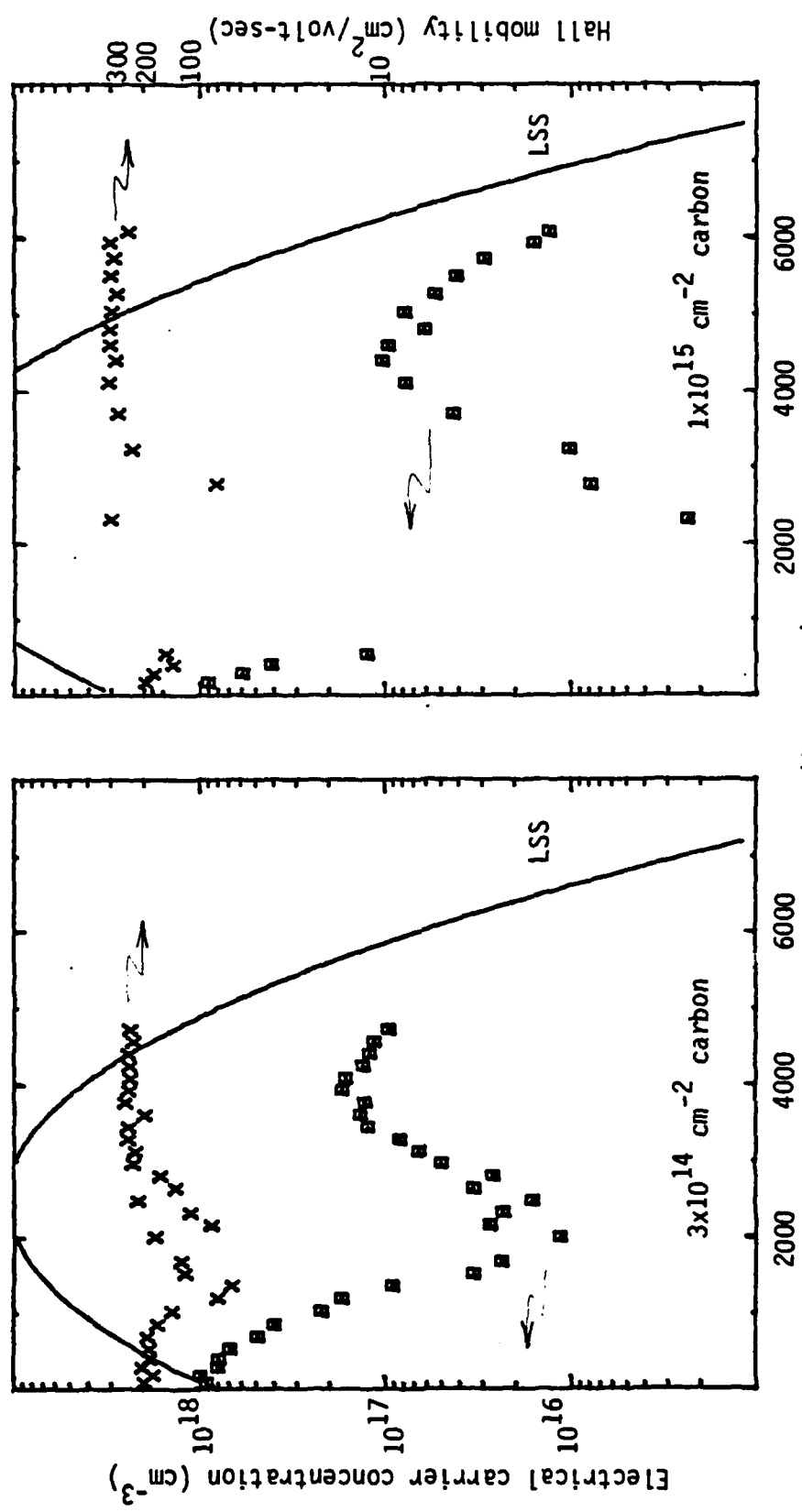


Figure IV-23. Electrical profiles for $3 \times 10^{14} \text{ cm}^{-2}$ and $1 \times 10^{15} \text{ cm}^{-2}$ carbon implant dose in VPE GaAs, annealed at 850°C for 15 min. in H_2 . Also shown is the LSS prediction for the carbon concentration for a 120 keV implant at those doses. (X=Hall mobility; \square =p-type electrical carrier concentration).

(approximately $3 \times 10^{17} \text{ cm}^{-3}$). Results of profiles on the control samples have to be recalled to understand the results for the carbon implants. With comparison to the control samples, three spatial regions can be identified.

Within approximately 1000 \AA of the surface is the first region. This is characterized by the highest carrier concentration of the profile, near $1 \times 10^{18} \text{ cm}^{-3}$ and Hall mobility near $200 \text{ cm}^2/\text{volt}\cdot\text{sec}$. By comparison to the capped and annealed control sample, Figure IV-6, the near surface results have most likely been caused by the thermal conversion which occurred during the anneal step. As the profile for the carbon implanted samples extends past 1000 \AA , the carrier concentration decreases. Comparison to the profile for the 1×10^{13} neon implanted sample, Figure IV-17, shows a similar decrease of carrier concentration. Thus, it seems likely that the thermal conversion layer for the carbon implants has been modified by the implant damage in the same manner as occurred for the neon implant.

An assessment of how much this thermal conversion layer affects the results of a single surface electrical measurement is shown in Table IV-6. For this table, the electrical carrier concentration has been integrated to a depth X_D , which was selected from the profiles as the measurable extent of the thermal conversion layer. The relation of the thermal conversion layer's electrical activity is expressed in the last column as a percent of the total sheet carrier concentration. This comparison shows that the thermal conversion layer is a major contribution to the single surface measurement of electrical activity. For the higher doses, more than 70% of the measured surface electrical activity can be attributed to the thermal conversion layer.

TABLE IV-6

COMPARISON OF SINGLE MEASUREMENT SHEET CARRIER CONCENTRATION, N_s ,
 RESULTS AND INTEGRATED CARRIER CONCENTRATION THROUGH THE THERMAL CONVERSION LAYER

| Implant Dose (cm^{-2}) | Depth, X_D (\AA) | N_s (10^{12} cm^{-2}) | $\int_0^{X_D} n(x) dx$ (10^{12} cm^{-2}) | $\frac{\int_0^{X_D} n(x) dx}{N_s} \times 100$ (%) |
|--------------------------------------|----------------------------------|--|---|--|
| 1×10^{13} | 1039 | 8.62 | 2.35 | 27 |
| 1×10^{14} | 1128 | 3.96 | 8.99 | 44 |
| 3×10^{14} | 2002 | 7.30 | 9.94 | 73 |
| 1×10^{15} | 463 | 4.27 | 5.90 | 72 |

The second general spatial region which appears in the profiles of the carbon implants extends from approximately 1000 \AA to 3000 \AA (see Figures IV-22 and IV-23). Here, increasing the implant dose of carbon has a fairly dramatic effect on both the mobility and the electrical carrier concentration. The trend with increased dose is for decreasing values of mobility and electrical carrier concentration. The effects are minimal for the $1 \times 10^{13} \text{ cm}^{-2}$ and $1 \times 10^{14} \text{ cm}^{-2}$ implant doses, which correspond to peak concentrations of $3.5 \times 10^{17} \text{ cm}^{-3}$ and $3.5 \times 10^{18} \text{ cm}^{-3}$, respectively. The $3 \times 10^{14} \text{ cm}^{-2}$ sample shows a clear effect, while the $1 \times 10^{15} \text{ cm}^{-2}$ had a region of negative values of carrier concentration and mobility from approximately 500 \AA to 2000 \AA . Clearly, some mechanism related to the higher dose carbon implants had caused this.

Some further insight into this spatial region can be gained by examining plots of the actual electrical profiling data, sheet resistivity, ρ_s , and sheet Hall coefficient, R_{Hs} . These are shown in Figure IV-24 for the three highest dose carbon implants. As the implant dose increases, there is a plateau in the data which occurs in the 1000 to 3000 \AA region. This plateau broadens and becomes more flat as the implant dose increases. In the center of the plateau for the $1 \times 10^{15} \text{ cm}^{-2}$ carbon implant dose, the sheet resistivity is changing less than 0.3%. Appendix A analyzes this plateau region in more detail and interprets this plateau as a region characterized by a relative maximum in the bulk resistivity. However, the key point is that the negative values for the mobility and the carrier concentration are not due to scatter in the data.

To help isolate unannealed implant damage as a cause of the high resistivity layer, several higher temperature anneals were done. The basic assumption here is that more damage is annealed out at higher

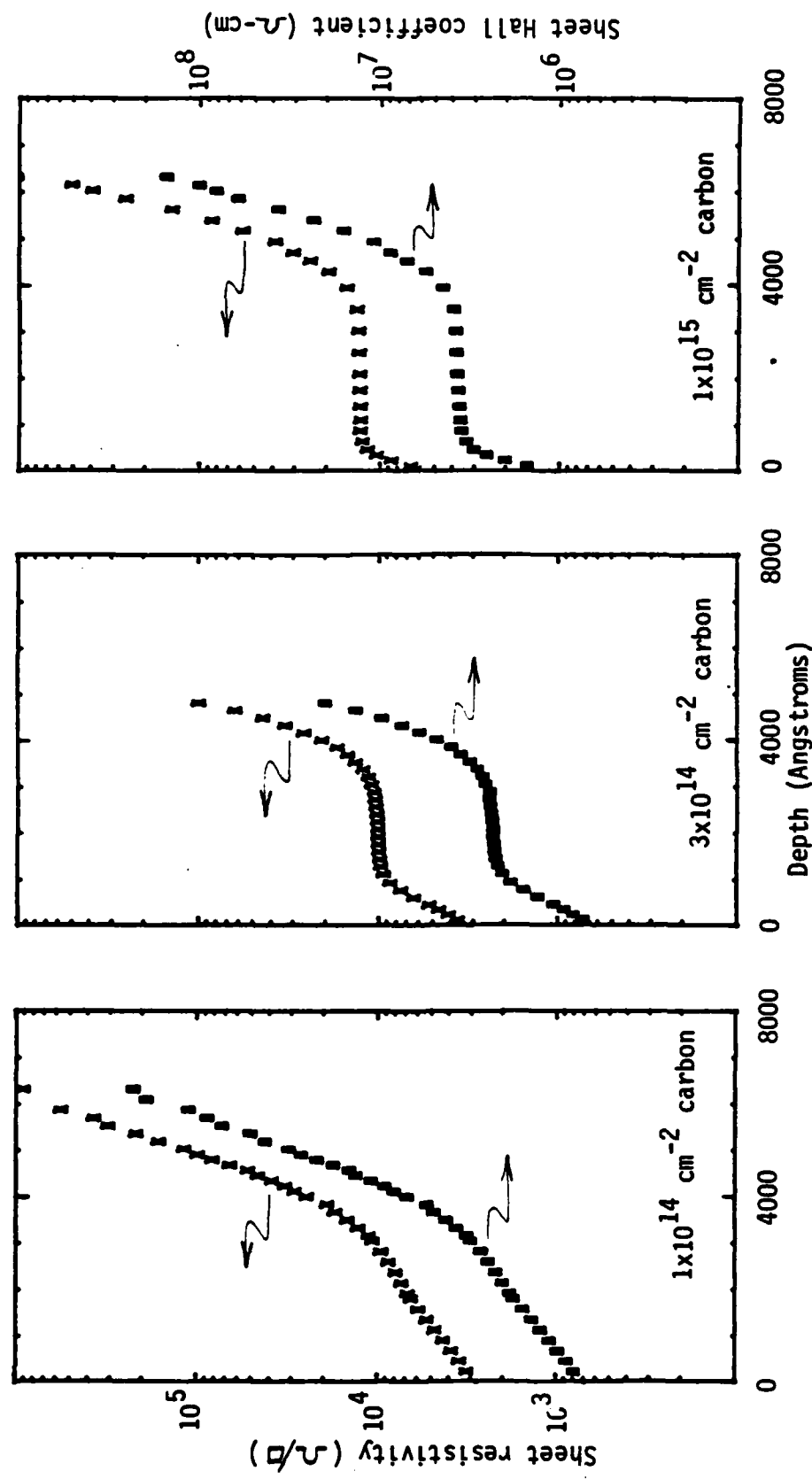


Figure IV-24. Electrical profile data v. depth for three implant doses of carbon in VPE GaAs, annealed at 850°C for 15 min. in H_2 . (X=sheet resistivity data; \square =sheet Hall coefficient data).

temperatures. The maximum practical upper limit was 950° C. Table IV-7 summarizes the results of the surface measurements for the higher temperature anneals.

TABLE IV-7
SURFACE ELECTRICAL MEASUREMENTS FOR HIGH TEMPERATURE ANNEALS

| Dose (cm ⁻²) | Sample | Temp (°C) | Mobility (cm ² /volt-sec) | Sheet Carrier Concentration (cm ⁻²) |
|-----------------------------|--------|--------------|---|--|
| 3×10^{14} | 4-1 | 850 | 198 | 9.9×10^{12} |
| | 2-18 | 900 | 202 | 1.2×10^{12} |
| | 2-17 | 950 | 229 | 1.1×10^{12} |
| 1×10^{15} | 13-2 | 850 | 207 | 6.6×10^{12} |
| | 2-3 | 900 | 179 | 7.3×10^{12} |
| | 2-2 | 950 | 214 | 9.3×10^{12} |

The results of electrical profiles for the higher temperature annealed samples are shown in Figures IV-25 and IV-26. For the 3×10^{14} cm⁻² carbon implant (Figure IV-25), the increased anneal temperature has a clear effect on the 1000 Å to 3000 Å region. Over the temperature range examined, the carrier concentration has increased in this region. The mobility values have also increased in this region and show less scatter as the temperature increases. This indicates that for the 3×10^{14} cm⁻² carbon implant, an increase in the anneal temperature from 850° C to 950° C has improved the lattice.

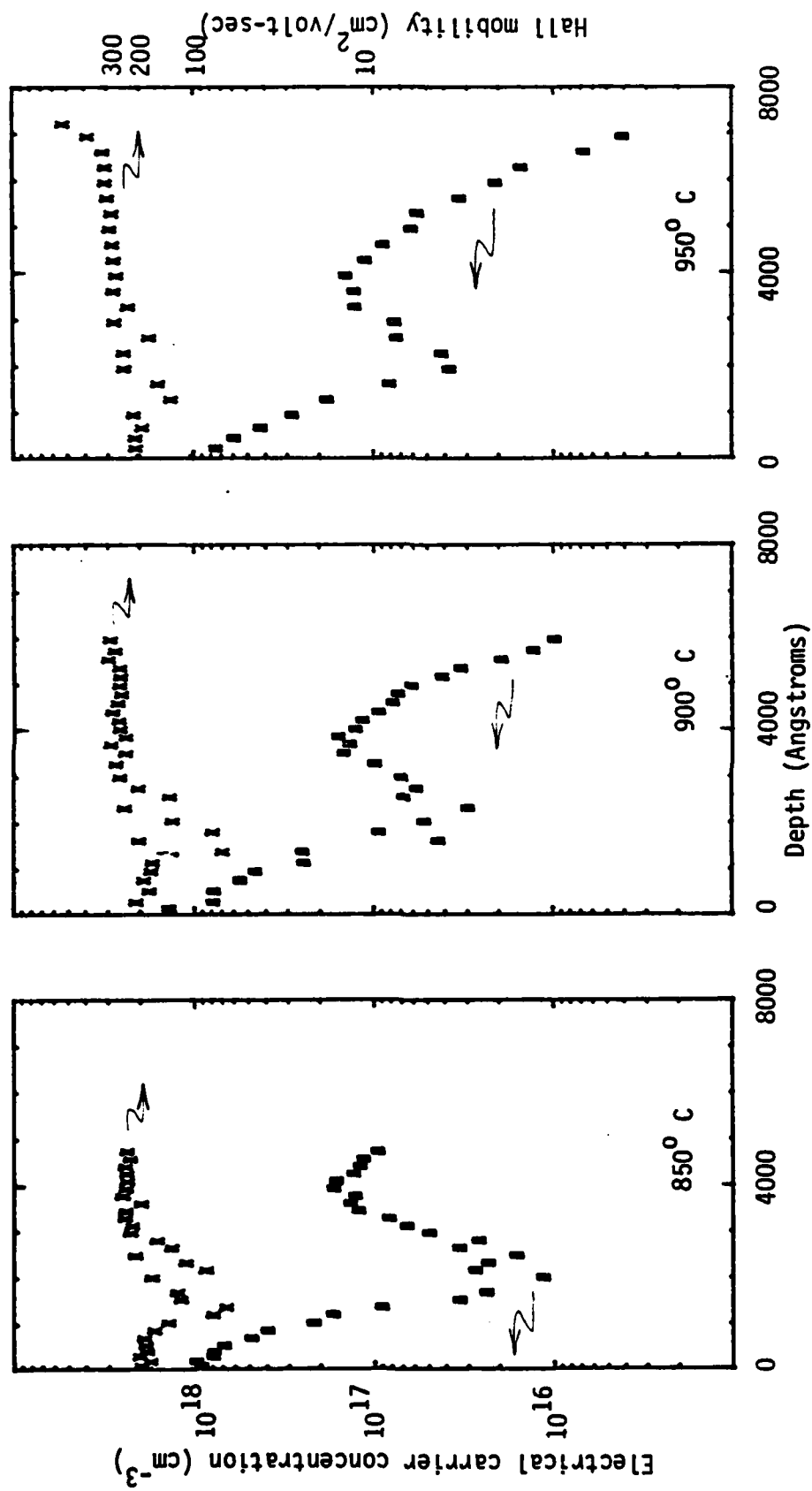


Figure IV-25. Electrical profiles of $3 \times 10^{14} \text{ cm}^{-2}$ dose carbon implant in VPE GaAs, annealed at three temperature for 15 min. in H₂. (x=Hall mobility data; □=p-type electrical carrier concentration).

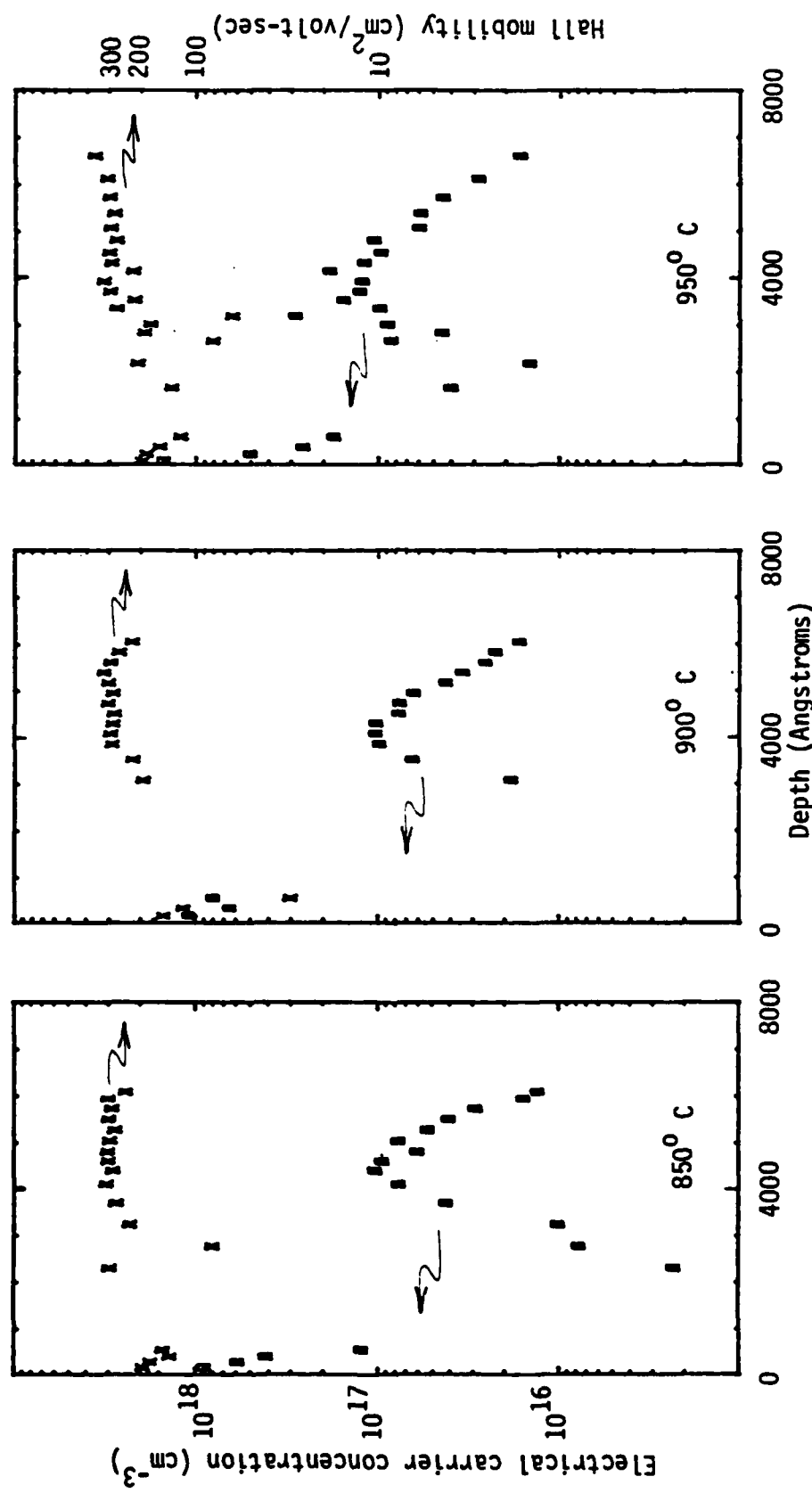


Figure IV-26. Electrical profiles of $1 \times 10^{15} \text{ cm}^{-2}$ dose carbon implant in VPE GaAs, annealed at three temperatures for 15 min. in H₂. (X=Hall mobility data; □=p-type electrical carrier concentration).

Further evidence for the relationship of the minimum in the electrical profile and the unannealed damage comes from the calculation done in Section II.A.3. There the maximum of the damage profile was estimated to be approximately 2300 Å. The multiple temperature anneals for the $3 \times 10^{14} \text{ cm}^{-2}$ sample shows the most distinct minimums in the electrical profile, which lie roughly between 2000 and 2500 Å. This correlation of maximum predicted damage and minimums in the electrical profile suggest that damage is a related phenomenon.

Figure IV-26 shows the effect of increasing the anneal temperature on the $1 \times 10^{15} \text{ cm}^{-2}$ carbon implant profile. The high resistivity region again shows some changes in the carrier concentration and mobility. The carrier concentration profile moves towards the surface into the high resistivity region. The mobility values do not show much change until the temperature reaches 950° C. For this high temperature anneal, some scattered mobility values appear in the 1000 Å to 3000 Å region. Thus, for the $1 \times 10^{15} \text{ cm}^{-2}$ carbon implant, the 15 minute anneals up to 950° C have either not removed as much damage as for the $3 \times 10^{14} \text{ cm}^{-2}$ implant, or there is some other mechanism causing the dip in this region. And for both doses ($3 \times 10^{14} \text{ cm}^{-2}$ and $1 \times 10^{15} \text{ cm}^{-2}$) annealed at 950° C, this effect still persists more strongly than for the lower dose $1 \times 10^{14} \text{ cm}^{-2}$ implant annealed at 850° C (Figure IV-22).

It is interesting that higher temperatures do not noticeably affect the near surface profile of the thermal conversion layer's electrical carrier concentration or mobility values. This indicates that damage is likely to be more extensive closer to the surface. Thus, the higher temperature anneals improve only the deeper portion of this 1000 Å to 3000 Å region. Also, it appears that higher temperature anneals do not

increase the magnitude of the near surface value of electrical carrier concentration, which remains at approximately $1 \times 10^{18} \text{ cm}^{-3}$.

We now address the final spatial region of the electrical profiles of the carbon implants. This region beyond the previous layer is clearly showing effects due to the implanted carbon. This can be seen by comparison to the profiles for the control samples. For the capped and annealed control sample, the profile did not extend beyond 3000 Å (Figure IV-6). For the neon implanted control sample, the profile is even more shallow (Figure IV-17). Only the carbon implanted VPE GaAs samples show the $1 \times 10^{16} \text{ cm}^{-3}$ to $1 \times 10^{17} \text{ cm}^{-3}$ levels of carrier concentration beyond 3000 Å. Also, the slope of the electrical profile in this region is very similar to the LSS implant profile for the 120 keV carbon implants (Figures IV-22 and IV-23). The conclusion drawn is that the electrical activity observed beyond approximately 3000 Å is due to the implanted carbon atoms.

Two $1 \times 10^{15} \text{ cm}^{-2}$ dose carbon implants into GaAs:Cr annealed at 850° C were also profiled. No control samples were available, so the thermal conversion effects cannot be clearly identified. Also, the data is much more scattered than the results shown in Figures IV-23 and IV-26 (due partly to poor etchant for one sample). However, there are some similarities to the implants into VPE GaAs. One is the near surface electrical concentration of about $1 \times 10^{18} \text{ cm}^{-2}$. Another is either a minimum or strong variation of the calculated values of mobility and carrier concentration in the region near 2000 to 2500 Å. Finally, there is a relative maximum near 4000 Å. Thus, there are qualitative similarities for a $1 \times 10^{15} \text{ cm}^{-2}$ dose carbon implant into either GaAs:Cr or VPE GaAs.

Several observations can be made for the electrical profile results for the VPE GaAs in the region where carbon atoms are clearly responsible for the electrical activity. Regardless of the implant dose or anneal temperature, the maximum electrical activity obtained is a carrier concentration of about $1 \times 10^{17} \text{ cm}^{-3}$. For the high dose implants, this maximum value occurs as the electrical carrier concentration profile decreases toward the surface. However, the carrier concentration plateau in the lower dose samples is also approximately $1 \times 10^{17} \text{ cm}^{-3}$. If one can assume that the uniform mobility values for the $1 \times 10^{13} \text{ cm}^{-2}$ and $1 \times 10^{14} \text{ cm}^{-2}$ samples in the high resistivity region implies that there is minimal unannealed damage, then the electrical profiles in these samples have shown the effects of carbon from 1000 \AA and beyond. These observations suggest that the maximum p-type electrical carrier concentration ($N_a - N_d$) is $1 \times 10^{17} \text{ cm}^{-3}$, regardless of the level of carbon concentration or anneal temperature. However, the concentration dependence is complicated by the following observations.

When the profile results for the 850° C anneal samples are examined beyond 3000 \AA , there is some increase in carrier concentration for the $1 \times 10^{14} \text{ cm}^{-2}$ sample over the $1 \times 10^{13} \text{ cm}^{-2}$ sample. However, the three highest doses of 1×10^{14} , 3×10^{14} , and $1 \times 10^{15} \text{ cm}^{-2}$ have profiles which remain essentially constant; that is, the profiles of ($N_a - N_d$) essentially overlap for these higher doses. These observations also hold for the higher temperature annealed samples. As mentioned before, the slopes of the profiles are similar to the LSS predicted distribution for the 120 keV carbon implants.

These results alone present conflicting evidence on the effect of the carbon concentration on electrical activation. From the profile on an

individual sample, the profile follows the shape of the LSS distribution. Thus, the carrier concentration appears to be a function of the carbon concentration up to the observed limit of $1 \times 10^{17} \text{ cm}^{-3}$. However, as the implant dose is varied from $1 \times 10^{13} \text{ cm}^{-2}$ to $1 \times 10^{15} \text{ cm}^{-2}$, with an expected variation of the carbon concentration at a given depth by a factor of 100, the profiles are unchanged. Hence, the carrier concentration appears to be invariant with carbon concentration when samples of different implant doses are examined. A partial solution to this behavior was found from the SIMS data (to be presented in Section IV.B.3) which will show that the actual implant distributions for individual implant doses of $1 \times 10^{13} \text{ cm}^{-2}$ to $1 \times 10^{15} \text{ cm}^{-2}$ of 120 keV carbon are not simple Gaussians and that they actually tend to overlap for depths of 4500 \AA° or greater.

Some further insight into this apparent conflict of the effect of carbon concentration can also be gained from the following analysis. In general, when the Hall mobility is plotted as a function of the carrier concentration for the electrical profiling data, the data is scattered with no apparent correlation. However, for some samples a correlation exists when the data are restricted to those beyond approximately 3000 \AA° , the region where the electrical activity is due to carbon (as discussed above).

Figure IV-27 shows the data for the $3 \times 10^{14} \text{ cm}^{-2}$ dose carbon implant annealed at 950° C . The Hall mobility and carrier concentration are fit fairly well using the expression presented in Section II.B.2, using a constant lattice mobility of 315 cm/volt-sec and $N_I = 2.5(N_a - N_d)$, where $(N_a - N_d)$ is the measured carrier concentration at room temperature. All of the profiling data were examined in the manner (1) to identify the

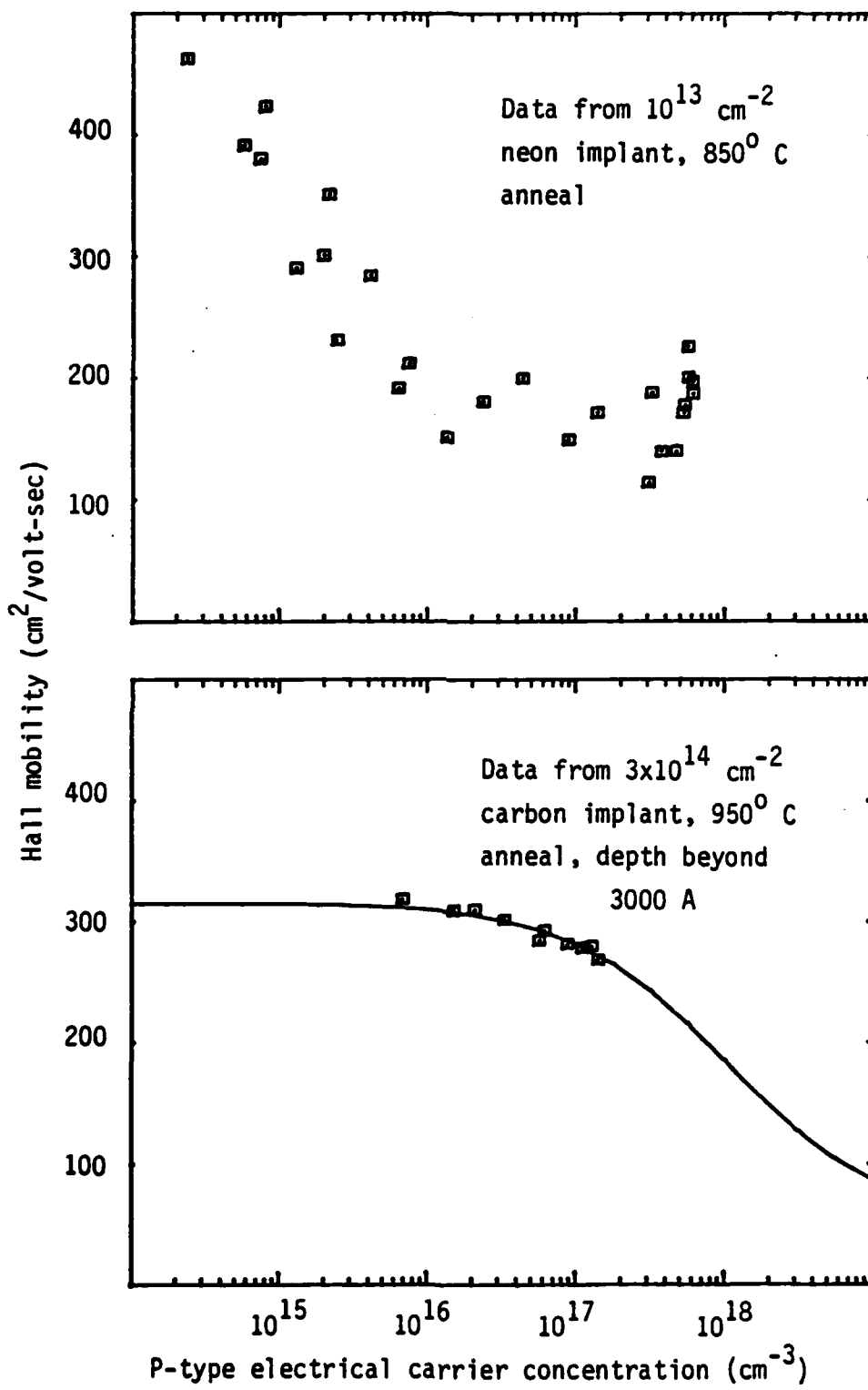


Figure IV-27. Measured Hall mobility vs. electrical carrier concentration for neon and carbon implanted VPE GaAs. (See text).

spatial region where it appears valid to use a constant lattice mobility value in combination with the theoretical ionized impurity mobility, and (2) to find the best value of constant lattice mobility to use in the next step of the analysis. As an example of data where this procedure would not be valid, Figure IV-27 shows a similar plot for the neon implanted control sample. Here, the theoretical expression does not fit the data, with the likely explanation that other scattering mechanisms are now important, such as neutral impurities.

As explained in Section II.B.2, there is now enough information (using the data validated above) to calculate the ionized impurity concentration, $(N_a + N_d)$, from the measured electrical carrier concentration, $(N_a - N_d)$, and mobility data. Figure IV-28 displays the results as a function of depth for two samples. One is the $1 \times 10^{13} \text{ cm}^{-2}$ dose carbon implant annealed at 850° C , and the other is the $3 \times 10^{14} \text{ cm}^{-2}$ dose carbon implant annealed at 950° C . The higher temperature anneal was required before useful electrical data was available at comparable depths (3000 \AA) for a high dose sample. For the $1 \times 10^{13} \text{ cm}^{-2}$ dose sample, the profile of the ionized impurities matches the LSS profile fairly well, for the range of validated data (approximately 3000 to 4500 \AA). Thus, it appears that for this sample almost all the carbon has gone on lattice sites for concentrations up to $3 \times 10^{17} \text{ cm}^{-2}$ as electrically active donors and acceptors. However, as the carbon concentration increases, self-compensation of the carbon prevents the electrical carrier concentration from exceeding $1 \times 10^{17} \text{ cm}^{-3}$. As the carbon concentration decreases, the carbon tends to go preferentially to As sites as acceptors.

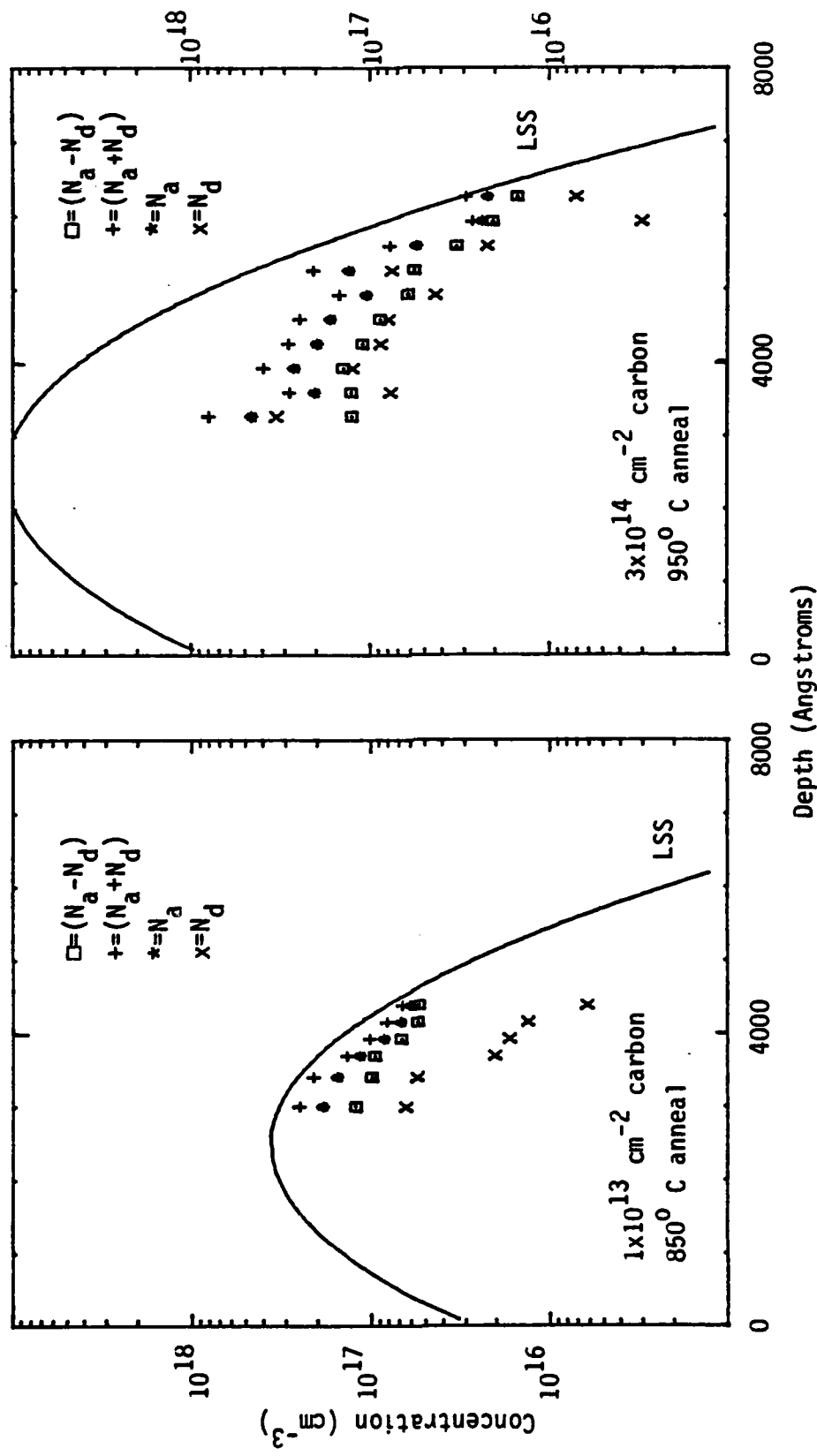


Figure IV-28. Results of ionized impurity calculations from measured electrical carrier concentration and Hall mobility (see text). Plot symbols: $\square = N_a - N_d$ (measured data); $+ = N_a + N_d$ (Brooks-Herring formula); $\ast = N_a$; $x = N_d$. Also shown is LSS profile for 120 keV carbon implant concentration at specified doses.

Also shown in Figure IV-28 are the results for the $3 \times 10^{14} \text{ cm}^{-2}$ dose implant, where, at equal depths, the LSS profiles predict that the carbon concentration is a factor of 30 higher than the $1 \times 10^{13} \text{ cm}^{-2}$ implant. For this higher dose sample, the ionized impurity concentration does not follow the total carbon concentration profile for concentrations $> 3 \times 10^{17} \text{ cm}^{-3}$. Hence, it appears that carbon at concentrations $> 3 \times 10^{17} \text{ cm}^{-3}$ begins to go to electrically inactive locations. The possibilities for these locations include interstitial sites or precipitated clusters of carbon. As with the lower dose implant, those carbon atoms which are electrically active tend to self-compensate and maintain a maximum electrical carrier concentration of $1 \times 10^{17} \text{ cm}^{-3}$. However, the main reason that there is almost a factor of 30 less electrical activation at the peak carbon concentration of $3 \times 10^{19} \text{ cm}^{-3}$ is that the carbon has not gone to electrically active (i.e., substitutional) lattice locations. This effect is definitely not due to carbon self-compensation.

To summarize the electrical measurements for carbon implanted VPE GaAs: (1) Electrical profiling data was found to be essential to separate the strong thermal conversion contribution from the carbon contribution to the electrical activity of the implanted layer. (2) A dip is observed in the electrical carrier concentration profiles which is very similar to a past study of Si implanted GaAs (Ref 84). However, that study's conclusion of dopant self-compensation has been ruled out for the carbon implants studied here. In these carbon implants, unannealed damage may be a partial contribution to the dip, but the magnitude of the carbon concentration causes a much stronger effect. (3) A new technique has been demonstrated to determine regions in an implanted layer where it is reasonable to assume a carrier mobility limited by lattice and ionized impurity scattering.

(4) Application of this technique and subsequent determination of the profiles of total ionized impurities, donors and acceptors gives results for carbon for concentrations approaching $3 \times 10^{19} \text{ cm}^{-3}$. The clear indication is that carbon substitutional behavior saturates at $3 \times 10^{17} \text{ cm}^{-3}$, with strong acceptor behavior below this concentration and electrically inactive behavior above this concentration.

2. Luminescence Measurements: Carbon Implanted VPE GaAs. In this section, we present the luminescence results for the carbon implanted VPE GaAs samples. The results will show that surface illumination of these implants can yield information on the implanted layer, but, analogously to the electrical measurements, the implants can cause strong variations of luminescence properties with depth. Thus, the PL etch profiles were very helpful, especially with high dose implants, in understanding the effects of carbon implants on GaAs.

Figure IV-29 shows the PL spectra of the exciton and shallow acceptor bands for four implant doses of carbon annealed at 850° C using a HeNe laser for illumination. These spectra have been normalized to the strongest shallow acceptor line. The dominant line in the exciton band is either the 1.5145 eV or the 1.5138 eV line. While the 1.5125 eV line is strong enough to resolve, it is not the dominant exciton line. The damage related excitons at 1.5115 eV and 1.5106 eV were observed for the $1 \times 10^{13} \text{ cm}^{-2}$ and $1 \times 10^{15} \text{ cm}^{-2}$ doses of carbon, with a line at 1.5087 eV appearing additionally for the $1 \times 10^{15} \text{ cm}^{-2}$ dose implant. The appearance of the carbon acceptor line at 1.4937 eV is clearly seen which (by comparison to the control samples) is obviously due to the presence of the implanted carbon. While the carbon acceptor at 1.4937 eV is a dominant peak, it

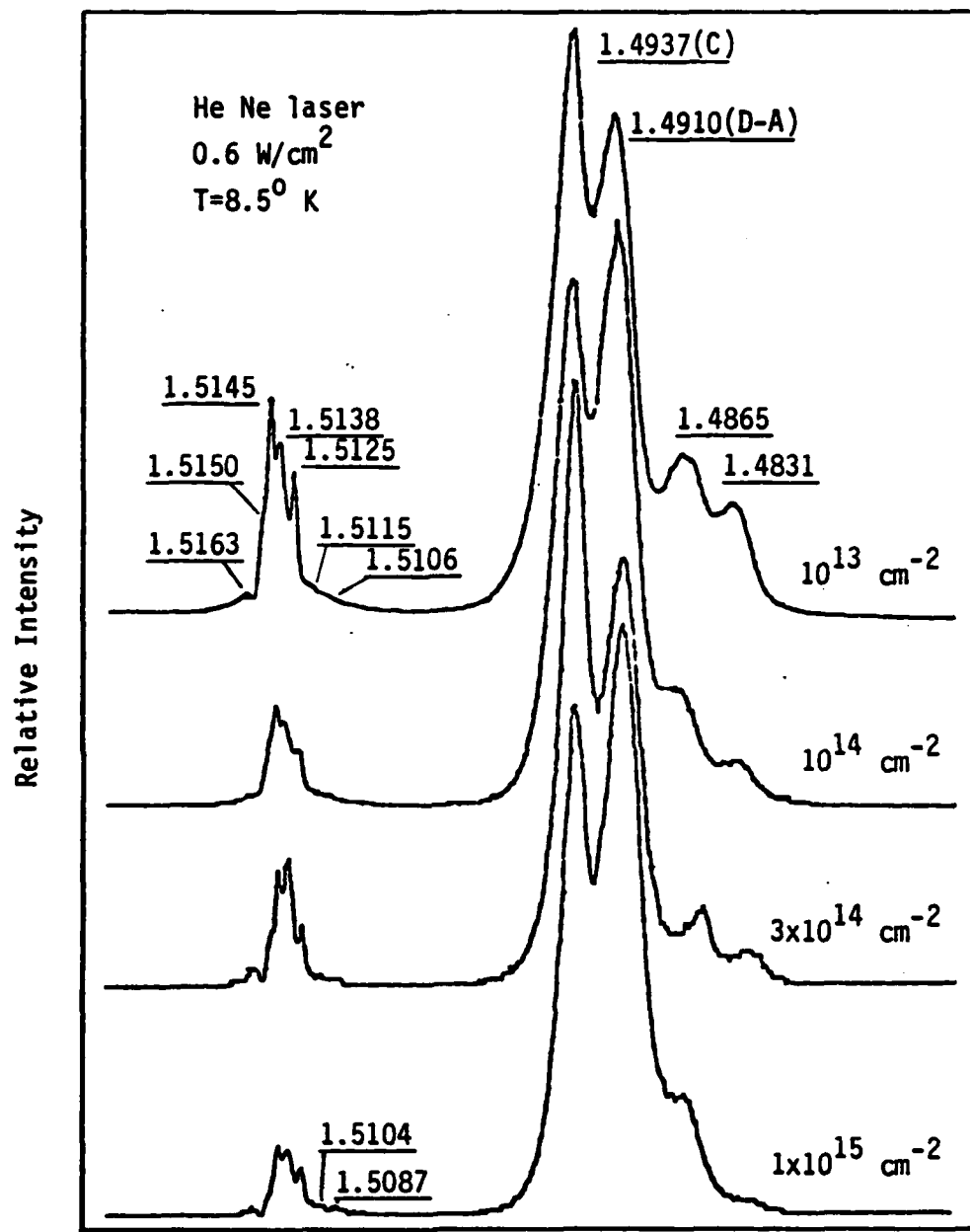


Figure IV-29. Photoluminescence spectra from VPE GaAs samples implanted with 120 keV carbon at four doses and annealed at 850^0 C for 15 min. in H_2 . The $3 \times 10^{14} \text{ cm}^{-2}$ sample was from different VPE wafer. Peak energies shown in eV.

switches with the 1.4910 eV line as the strongest line in the shallow acceptor band as the implanted carbon dose increases. The silicon acceptor and donor-silicon acceptor lines appear at 1.4865 eV and 1.4831 eV, respectively.

To verify the shallow acceptor line assignments, the sample temperature was varied from 5 to 26° K for the $1 \times 10^{13} \text{ cm}^{-2}$ dose carbon implanted sample. The illumination was the 5145 Å line from an argon laser at moderately high power (11.3 w/cm^2). At 26° K, where the donor-acceptor lines are extinguished, the shallow acceptor band shows the presence of carbon, zinc and silicon, in that order of intensity. It is perhaps surprising to see so strong a presence of zinc, but, from the analysis of the control samples, the near surface accumulation of zinc is a likely possibility.

Figure IV-30 serves the dual purpose of showing the deep acceptor spectra observed for carbon implanted VPE GaAs along with a typical spectra observed for carbon implanted GaAs:Cr semi-insulating substrate material. In the VPE material (Plots B and C of Figure IV-30), there are qualitative similarities for the deep acceptor levels to the control samples, with the Mn acceptor line generally being the dominant line in this band. The LO phonon replicas are strong enough and the Mn acceptor line weak enough in the $1 \times 10^{15} \text{ cm}^{-2}$ carbon implant that the two LO replicas of the shallow acceptor band dominate the Mn acceptor peak (seen at 1.4068 eV in the $1 \times 10^{14} \text{ cm}^{-2}$ dose carbon implant) and produce a maximum peak height at 1.4112 eV.

The $1 \times 10^{14} \text{ cm}^{-2}$ dose carbon implant into GaAs:Cr produces a PL spectra much different than the implanted VPE GaAs (Plot A in Figure IV-40). The exciton band is not observed and individual shallow acceptor

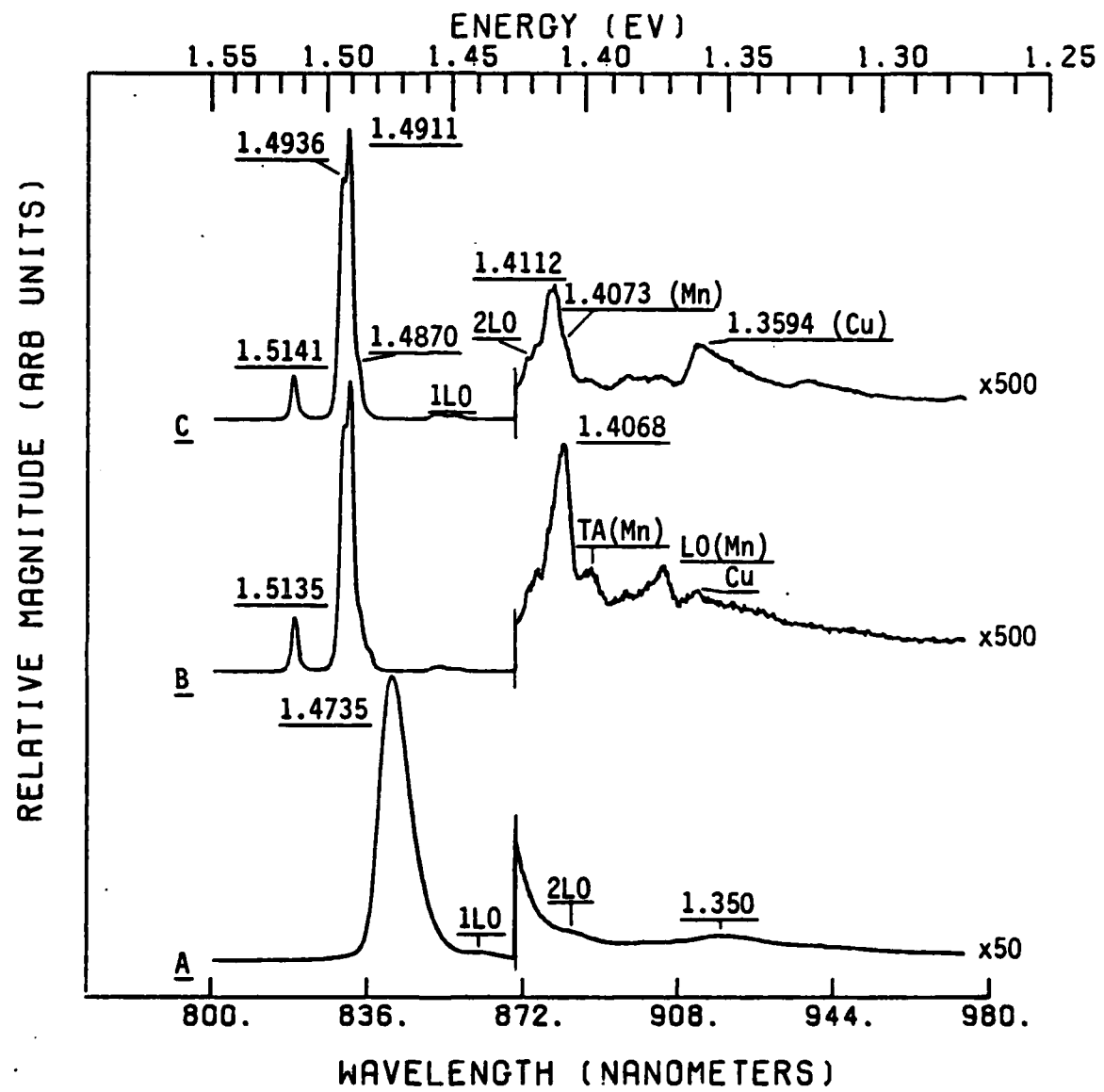


Figure IV-30. Comparison of PL spectra for carbon implants into GaAs:Cr (plot A) and VPE GaAs (plots B, C). Plots A and B for 10^{14} cm^{-2} dose implants and plot C for 10^{15} cm^{-2} dose implant, all annealed at 850° C . Samples at 8.5° K , illumination with HeNe laser with 0.6 W/cm^2 .

lines are not present. The shallow acceptor band is a relatively broad peak centered at 1.4735 eV along with phonon replicas of this line. The broad nature of these LO phonon bands may be obscuring any evidence of the Mn acceptor band. Finally, the copper vacancy complex appears as a broad band centered at 1.350 eV. This type of spectra is typical of high doping levels and relatively impure GaAs.

The results of higher temperature anneals on the surface luminescence of the two highest dose implants are shown in Figures IV-31 and IV-32. These spectra have been normalized to the largest acceptor line. The exciton band shows stronger effects of higher temperature anneals, in general, than does the shallow acceptor band. The higher temperature anneals increase the 1.5102 eV and 1.5083 eV exciton lines, relative to the other exciton lines. For the 950° C anneal with the $1 \times 10^{15} \text{ cm}^{-2}$ dose carbon implant, the 1.5102 eV line has become the dominant exciton line. The effect is similar, but not as strong, for the $3 \times 10^{14} \text{ cm}^{-2}$ dose carbon implant annealed at 950° C. Finally, the high temperature anneal has reduced the overall exciton band strength (relative to the shallow acceptor band) at the 950° C anneal for the $1 \times 10^{15} \text{ cm}^{-2}$ dose carbon implant. Thus, judging from the exciton luminescence, the higher temperature anneals are introducing defect bound excitons and, therefore, these anneals are introducing defects as opposed to annealing out defects.

Figures IV-33 and IV-34 show quantitatively the effects of increased dose and increased temperature on spectral peak heights for surface luminescence for the exciton band and shallow acceptor band discussed above. From the data in Figure IV-33, it is apparent that increasing the implant dose reduces the intensity of both the exciton and shallow acceptor band, but that the effect is stronger on the exciton band. The

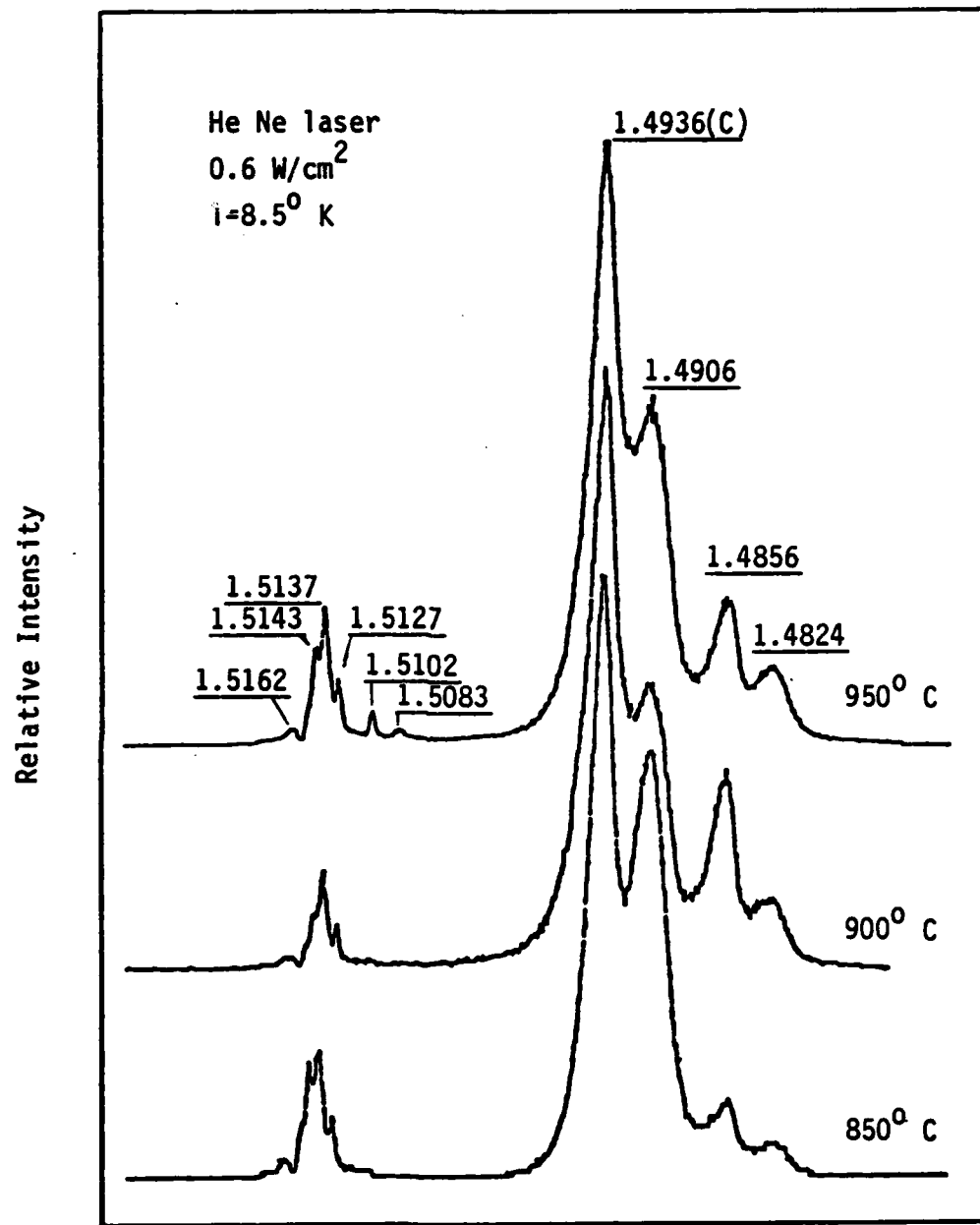


Figure IV-31. Photoluminescence spectra from VPE GaAs samples implanted with 120 keV carbon at $3 \times 10^{14} \text{ cm}^{-2}$ dose and annealed at three temperatures for 15 min. in H_2 . Peak energies shown in eV.

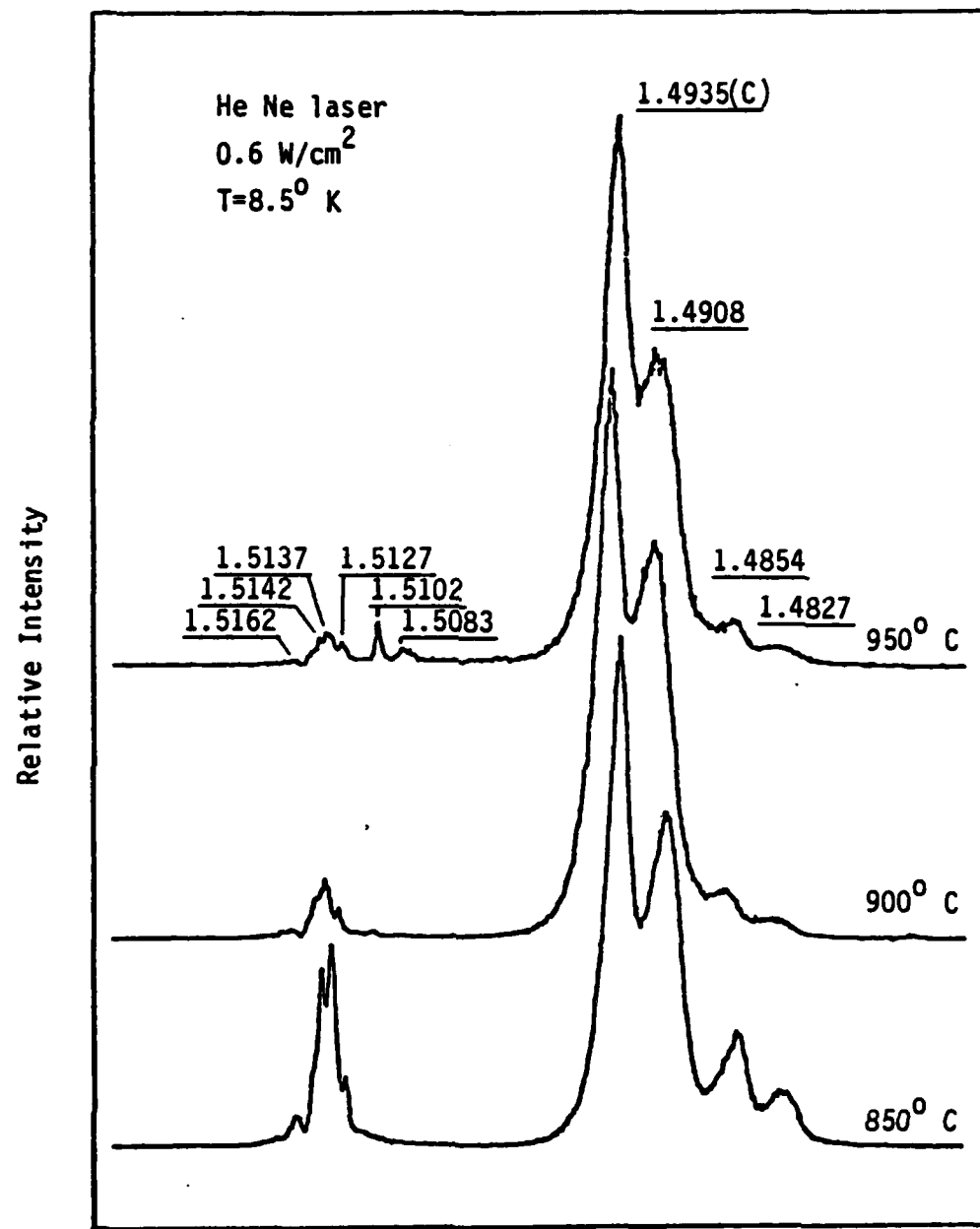


Figure IV-32. Photoluminescence spectra from VPE GaAs samples implanted with 120 keV carbon at $1 \times 10^{15} \text{ cm}^{-2}$ dose and annealed at three temperatures for 15 min. in H_2 . Peak energies shown in eV.

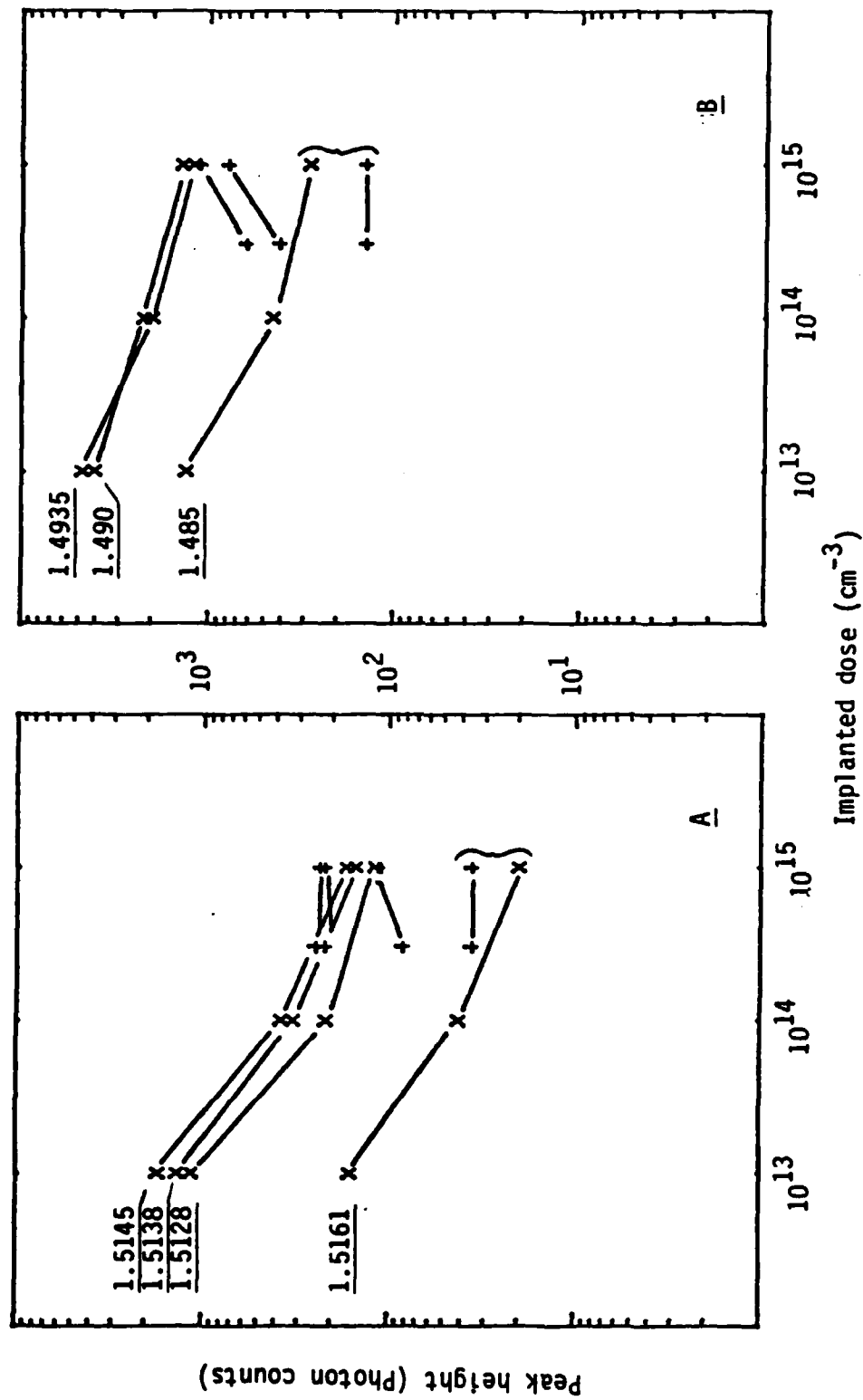


Figure IV-33. PL peak heights vs. implanted carbon dose. Plot A is exciton band, plot B is shallow acceptor band. Symbols X and + indicate different VPE substrates. Peak positions in eV. Illumination was HeNe laser with 0.6 W/cm^2 and samples at 8.5° K .

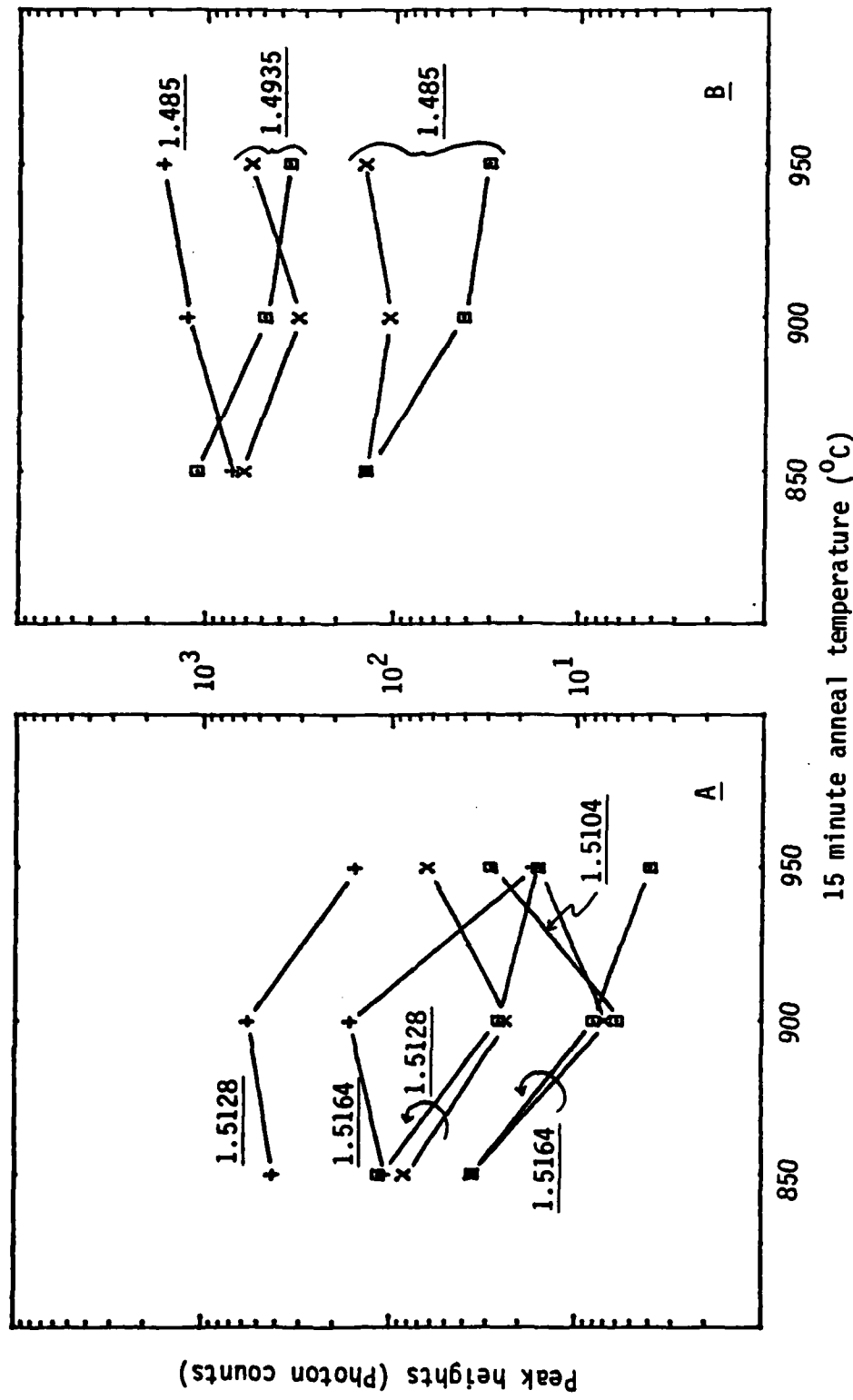


Figure IV-34. PL peak heights vs. anneal temperature. Plot A shows several representative exciton lines, plot B shows shallow acceptor lines (1.4935 eV, carbon; 1.485 eV, silicon). Illumination was HeNe laser with 0.6 W/cm² and sample at 8.5° K. $\times=3 \times 10^{14}$ cm⁻² carbon; $\square=1 \times 10^{15}$ cm⁻² carbon; + = capped and annealed control.

results for the shallow acceptor band are somewhat mixed, showing an unexpected dependence on the VPE material. For one wafer of VPE, there is a consistent decrease of intensity for the acceptor band as the implant dose increases (for all acceptors). For the other VPE wafer, there is indication that there are more carbon acceptors as the dose increases (with a neutral effect on the silicon acceptors).

Figure IV-34 shows the effect of anneal temperature on the exciton and shallow acceptor band peak heights, which are not as clearly directed as were the implant dose variations. The exciton band for the C/A controls and the two highest dose implants actually diverge at the 900° C anneal, but the exciton band for the implants is generally lower in intensity than the C/A controls' exciton band. For clarity, only the 1.5164, 1.5128 and 1.5104 eV peak heights were plotted in Figure IV-34, but these show the trends for the exciton band. The 950° C anneal is seen to reduce the exciton band luminescence in the control sample while having mixed results with the implanted samples. However, one of the strongest trends in the exciton band is the strong increase of the defect related exciton peaks as anneal temperature increases, demonstrated with the 1.5104 eV peak. In Plot B of Figure IV-34, we see that the silicon acceptor peak for the C/A control indicates more silicon indiffusion with increasing anneal temperature, but this effect is apparently reversed or neutralized with the $3 \times 10^{14} \text{ cm}^{-2}$ and the $1 \times 10^{15} \text{ cm}^{-2}$ dose implants, respectively. A very similar behavior is seen for the carbon acceptor line.

To summarize the surface luminescence results for carbon, it appears that increasing implant doses of carbon from $1 \times 10^{13} \text{ cm}^{-2}$ to $1 \times 10^{15} \text{ cm}^{-2}$ does not result in more optically active carbon shallow acceptors, and

that for the highest doses ($3 \times 10^{14} \text{ cm}^{-2}$ and $1 \times 10^{15} \text{ cm}^{-2}$) increases of anneal temperature from 850° C to 950° C do not substantially increase carbon acceptors.

The resulting PL etch profile spectra for the $1 \times 10^{13} \text{ cm}^{-2}$ dose carbon implant are shown in Figure IV-35, with an expanded version of the exciton and shallow acceptor bands in Figure IV-36, normalized to the largest peak in the exciton or shallow acceptor band. Quantitative plots of peak heights versus depth are shown in Figure IV-37. These data were all taken with the sample at 8.5° K and a system resolution of 0.2 meV over the exciton and shallow acceptor band, and 2.0 meV over the deep acceptor band.

Plot A of Figure IV-37 shows the results for the exciton band in the $1 \times 10^{13} \text{ cm}^{-2}$ dose carbon implanted VPE GaAs sample. The exciton band shows a general increase in intensity for all lines up to 2112 Å in depth. The free exciton (1.5161 eV) then continues a gradual increase in intensity out to 2.6μ . This behavior is similar to the neon implanted control, except the near surface extinction of the free exciton is stronger for the carbon implant. For the UV laser illumination conditions used, the 1.5103 eV defect related exciton line only appears at 836 and 2112 Å in depth. The donor and acceptor related exciton lines are strongest near the center of the implanted layer, especially the 1.5123 eV line, showing a correlation with the carbon implant.

The acceptor band PL etch data are shown in Plot B of Figure IV-37. The carbon acceptor line increases in strength with the first two etches, to a depth near R_p (2500 Å) for the carbon implant. This increase is directly proportional to the carbon concentration as predicted by a LSS implant profile (where the concentration increases from $2 \times 10^{16} \text{ cm}^{-3}$ to

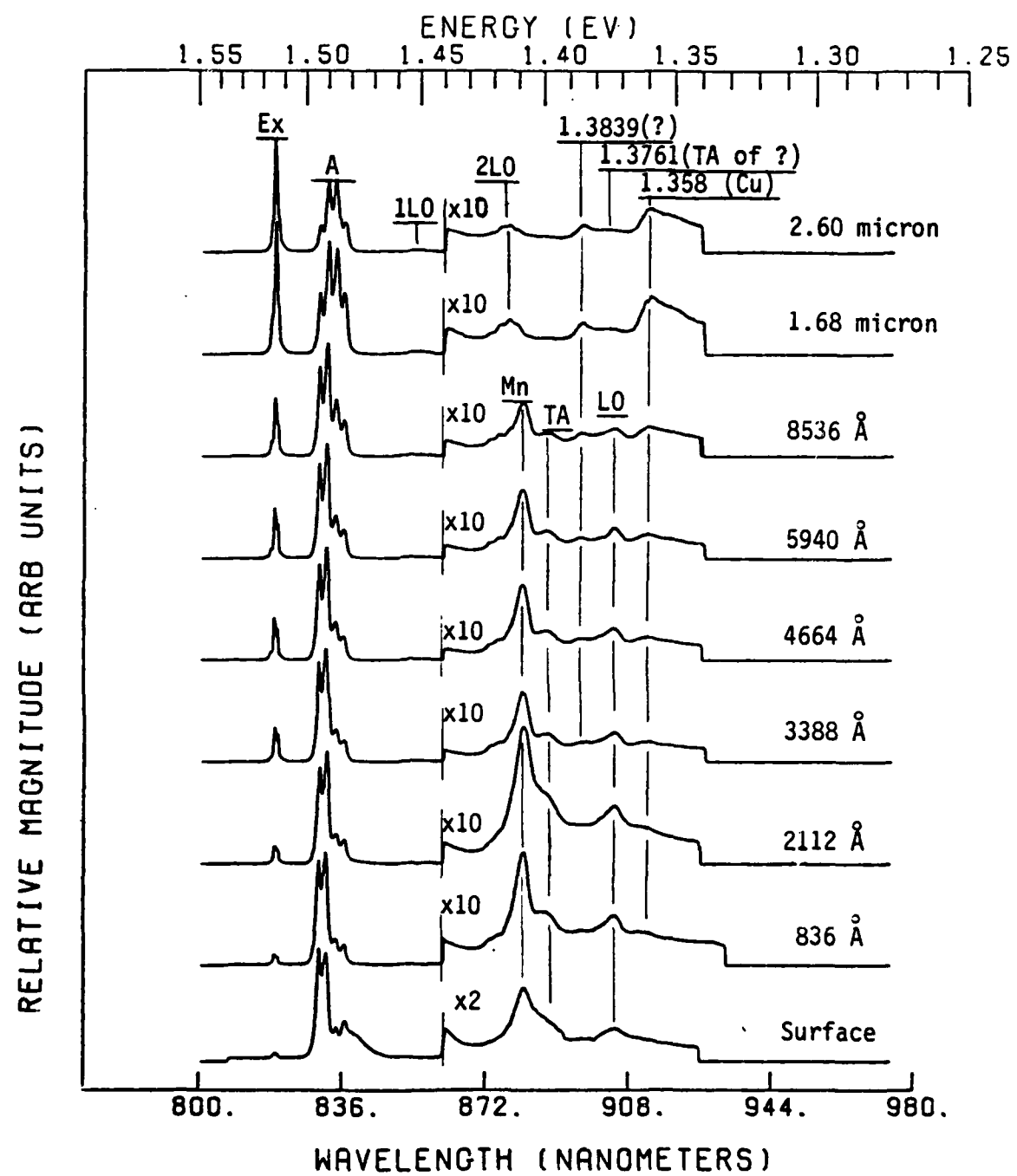


Figure IV-35. PL etch spectra for 10^{13} cm^{-2} dose carbon implant in VPE GaAs. Illumination with UV lines of Kr laser at 1.0 W/cm^2 , sample at 8.5° K .

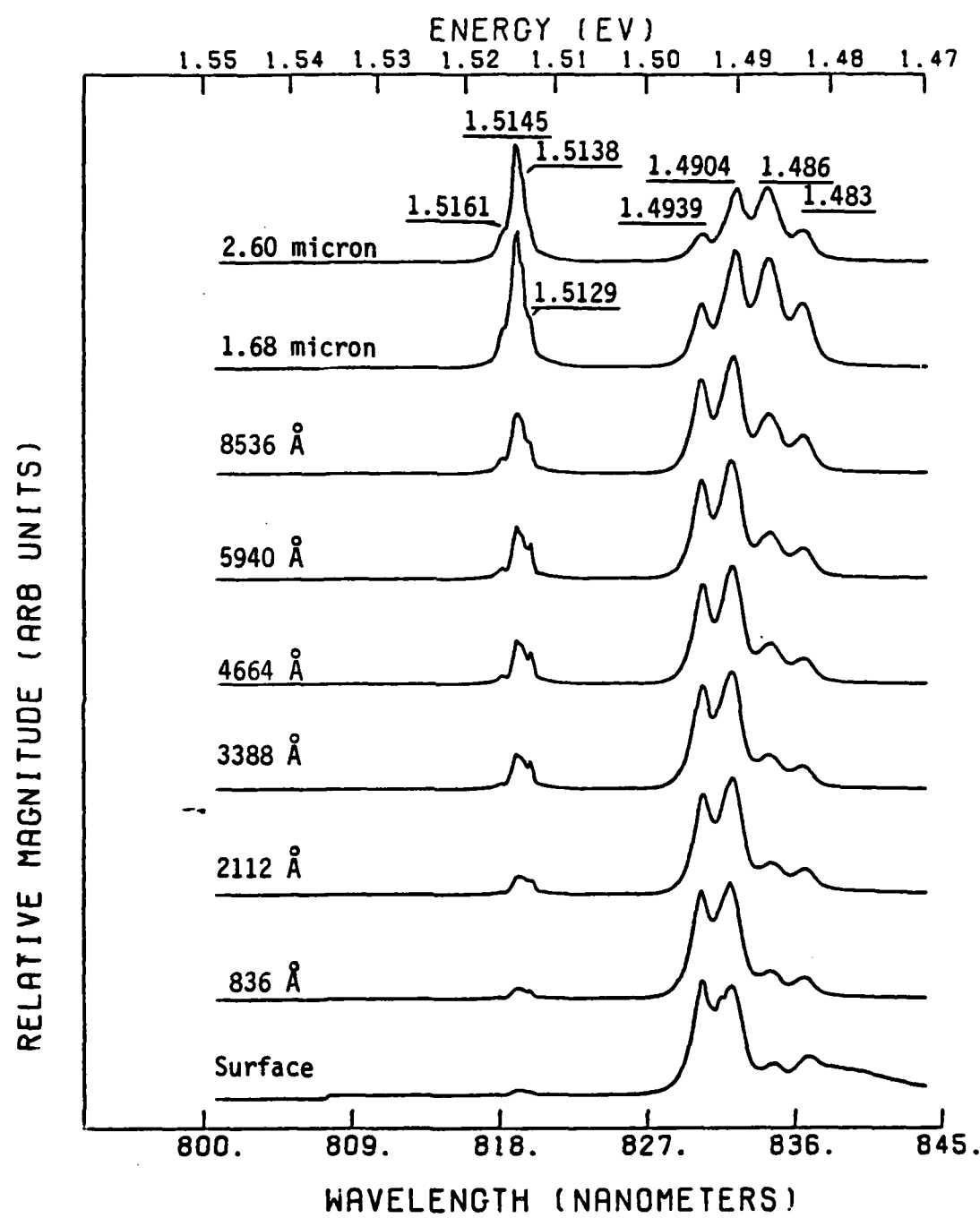


Figure IV-36. Expanded PL etch spectra for 10^{13} cm^{-2} dose carbon implant in VPE GaAs. Same data as Figure IV-35.

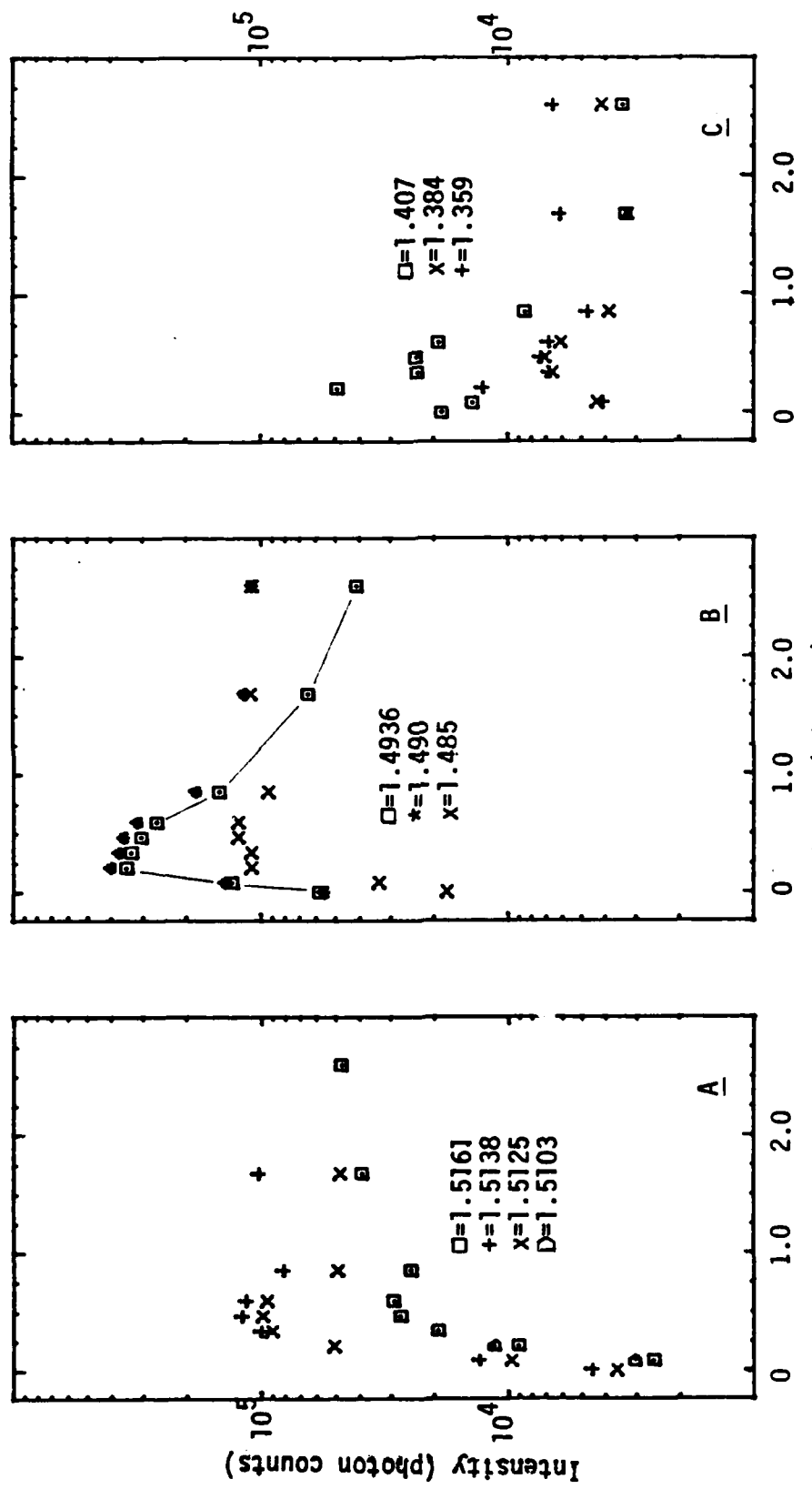


Figure IV-37. PL etch data for 10^{13} cm^{-2} dose carbon implant into VPE GaAs, annealed at 850° C . Plot A is exciton band; $\square=1.5161 \text{ eV}$, $\times=1.5138 \text{ eV}$, $\diamond=1.5125 \text{ eV}$, $D=1.5103 \text{ eV}$. Plot B is shallow acceptor band; $\square=1.4936 \text{ eV}$, $\times=1.490 \text{ eV}$, $\diamond=1.485 \text{ eV}$. Plot C is deep acceptor band; $\square=1.407 \text{ eV}$, $\times=1.384 \text{ eV}$, $\diamond=1.359 \text{ eV}$. Sample temperature was 8.5° K , illumination with UV lines of krypton laser.

$3 \times 10^{17} \text{ cm}^{-3}$). However, all exciton lines and all shallow acceptor lines increase in the same fashion for these etches. Therefore, the rise in intensity for the carbon acceptor line appears to be related to a general increase in luminescence efficiency of the exciton and shallow acceptor bands as the first 2000 \AA are etched off. This near surface reduction in luminescence efficiency was not observed in the PL etch spectra for either the 950° C C/A control sample or the $1 \times 10^{13} \text{ cm}^{-2}$ dose neon implanted sample. Thus, there appears to be a relation to the presence of carbon. Beyond 2000 \AA the 1.4936 eV carbon acceptor line decreases in intensity, followed by the 1.490 eV line (largely composed of donor-carbon acceptor components at this point), to approximately 8500 \AA , at which point it begins a more gradual decrease and the 1.490 eV (zinc) and 1.485 eV (silicon) peaks remain at comparable intensity. Comparison to the PL etch data for the $1 \times 10^{13} \text{ cm}^{-2}$ neon implant (Figure IV-13) shows that the carbon acceptor line in the neon implant is a factor of 10 less intense when it finally does appear beyond 1μ in depth than it appears in the $1 \times 10^{13} \text{ cm}^{-2}$ carbon implanted sample. Thus, the carbon has indiffused to at least 2.6μ from the implanted layer, and it remains the dominant shallow acceptor until 8500 \AA in depth, where zinc and silicon become the more dominant acceptors for this sample.

The 1.485 eV silicon line remains essentially constant after the first 2000 \AA are removed, not showing the slight near surface accumulation observed with the neon implant, but behaving more like the uniform distribution observed with the 950° C C/A control. But, again, silicon has rapidly diffused to at least 2.6μ during the 15 minute anneal.

Plot C in Figure IV-37 shows the deep acceptor band behavior as a function of depth for the $1 \times 10^{13} \text{ cm}^{-2}$ dose carbon implant. The Mn

acceptor line at 1.408 eV indicates an accumulation of Mn for depths less than 1μ . As the surface is etched off, the Mn line intensity is fluctuating up to 2000 \AA and then stabilizes and decreases. It actually disappears at depths greater than 1 μ where even the TA phonon replica of the Mn line is not observed below the 2 LO phonon replicas of the shallow acceptor band.

After being initially undetectable at the surface, the 1.384 eV line and the 1.359 eV lines again track each other fairly closely in intensity up to 1μ in depth. Their maximum intensity occurs at about 4700 \AA in depth. Beyond 1μ , the 1.359 eV line begins a slight increase in intensity to 2.6μ in depth.

Perhaps the most interesting behavior in this deep acceptor band for the $1 \times 10^{13} \text{ cm}^{-2}$ dose carbon implant is the 1.384 eV line. Here, for the first time, the Mn acceptor line and its associated phonon replicas have been reduced so much in intensity beyond 1μ (perhaps due to the near surface gettering effect for Mn) that the 1.3839 eV line clearly stands alone with its own TA phonon replica at 1.3761 eV. Thus, clearly, the 1.384 eV line is not a phonon replica of the Mn acceptor line. Enough of the line is present to see that it has a line shape very similar to the 1.359 eV line. Thus, the type of vacancy complex that causes the 1.359 eV line is a likely candidate for the 1.384 eV line, with the particular impurity species remaining to be identified.

A PL etch was also performed on a $1 \times 10^{15} \text{ cm}^{-2}$ dose carbon implant in VPE GaAs. The etch steps were smaller through the implanted region, thus more data was collected. Procedures were changed after approximately 2000 and 4000 \AA had been etched off, with several repeated runs to track the effects of the changes. In general, the near surface luminescence was taken with the sample temperature at 5° K and the system resolution

at 2 meV for the entire spectra, largely because the luminescence was comparatively weak. Past 2000 Å in depth, the sample temperature was increased to 8.5° K to enhance the 1.4936 eV carbon line, and past 4000 Å in depth the system resolution was increased to 0.2 meV for the exciton and shallow acceptor bands.

The spectra and peak height plots are shown in groups corresponding to the data groups described in the previous paragraph. However, the discussion will tend to address the luminescence bands as a group throughout the etch from the surface of the final etch at about 3 μ in depth. Figure IV-38 shows the PL etch spectra at 5° K, up to a depth of approximately 3000 Å, with Figure IV-39 showing an expanded view. Peak height plots corresponding to these spectra are shown in Figure IV-45. Figure IV-40 shows the exciton and shallow acceptor bands at 8.5° K for depths of 2000 to 4000 Å, approximately, while Figure IV-41 shows the deep acceptor spectra for nearly equivalent depths of 3000 to 5000 Å. Figure IV-42 shows the spectra of the remaining PL etches, for 5000 Å to 2.9 μ in depth, with Figure IV-43 showing the exciton and shallow acceptor bands in expanded form. Figure IV-45 shows peak height plots versus depth for the 8.5° K spectra for depths of 2000 Å or more. Correction factors have been applied to the exciton and shallow acceptor lines to account for the change in system resolution that occurred at 5000 Å in Figure IV-45 which allows trends to be observed more clearly from 2000 Å to 3 μ in depth for the $1 \times 10^{15} \text{ cm}^{-2}$ carbon implant. These correction factors are also fairly good for the differences in sample temperature, so trends observed in Figure IV-44 for the 5° K data from the surface to 3000 Å can be continued onto Figure IV-45 for the excitons and shallow acceptor bands at 8.5° K (Plots A and B in the figures). Since the deep acceptor band was recorded at the same system resolution for all etches and

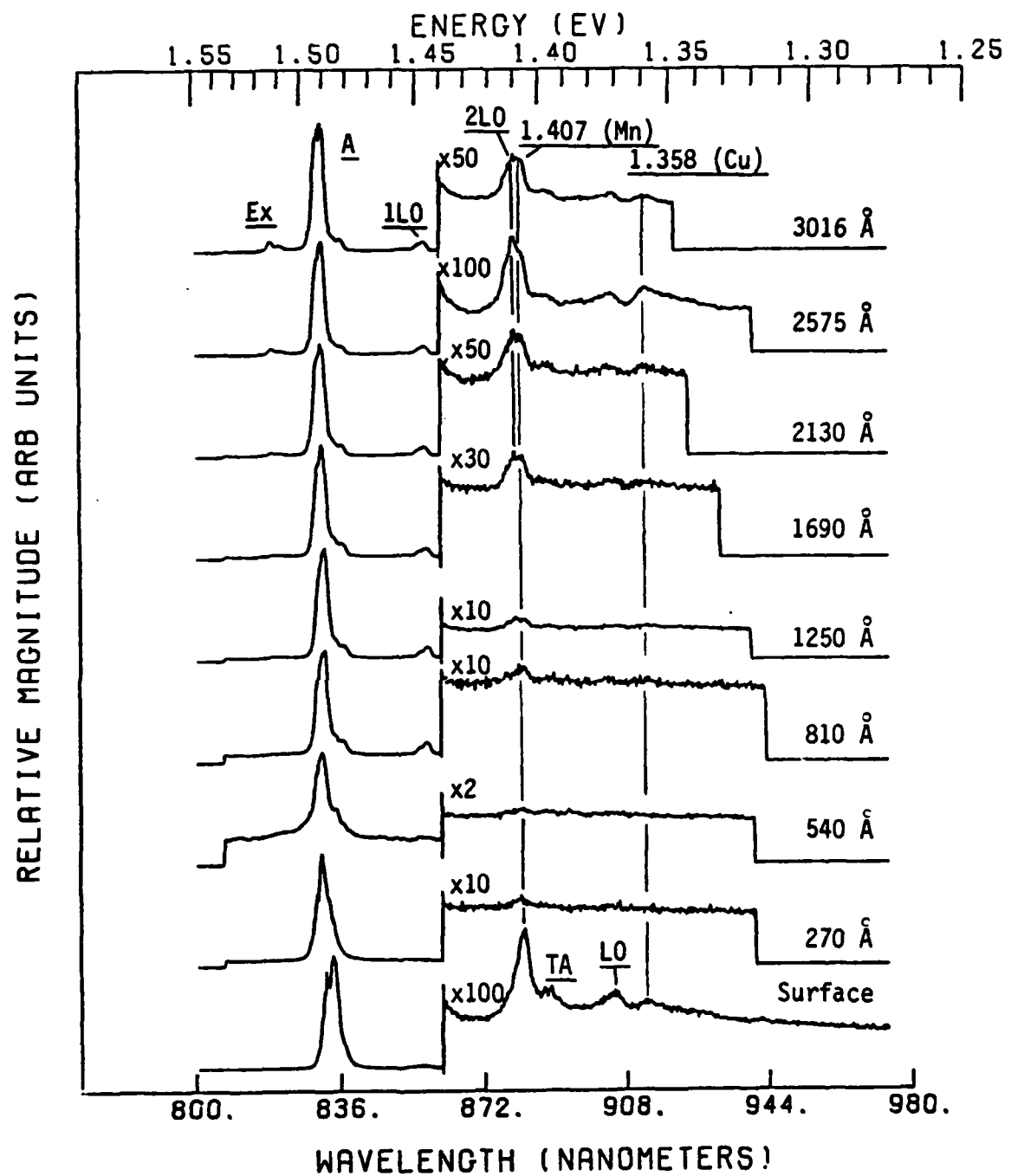


Figure IV-38. Near surface PL etch spectra for 10^{15} cm^{-2} dose carbon implant in VPE GaAs. Illumination with UV lines of Kr laser at 1.0 W/cm^2 , sample at 5° K .

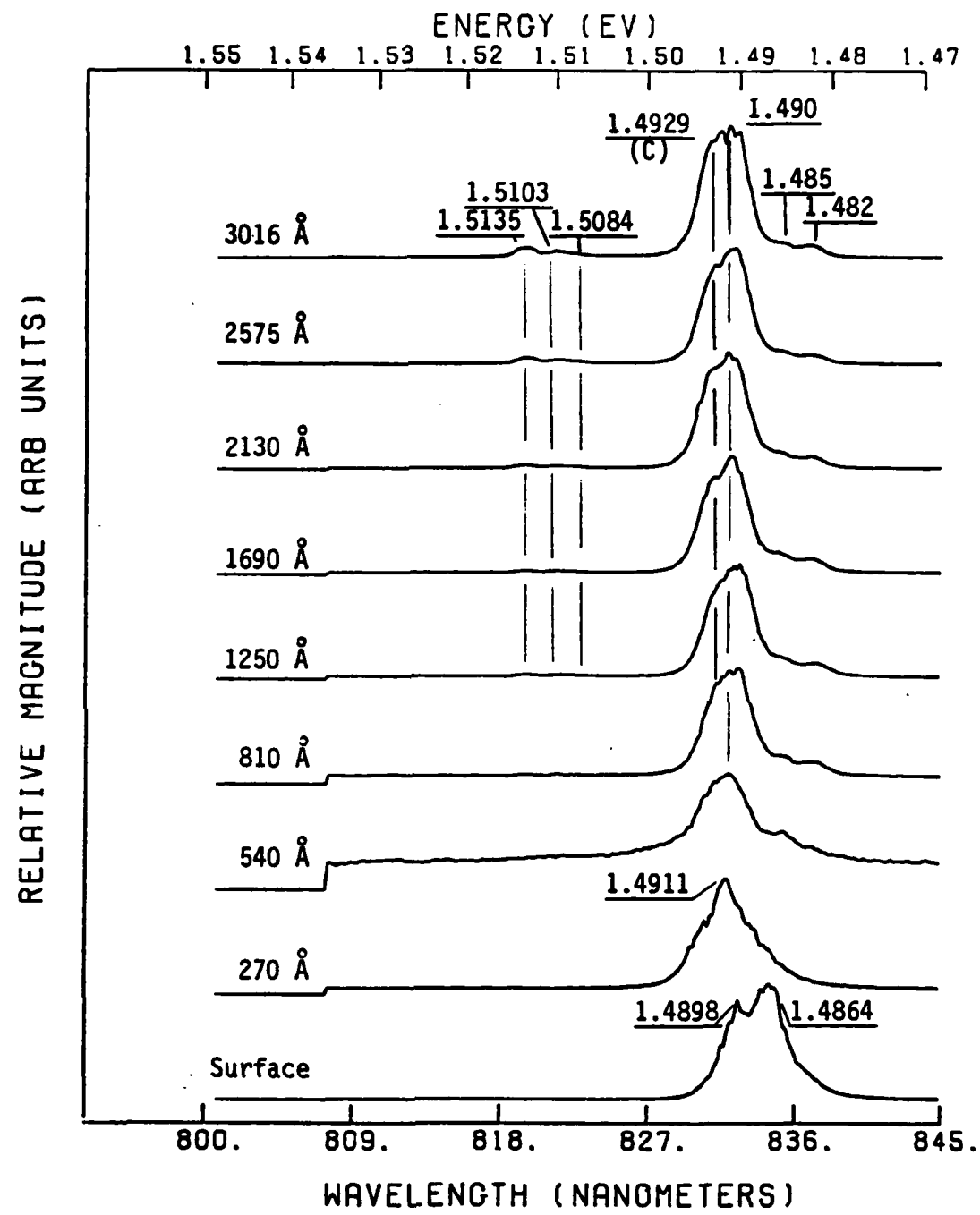


Figure IV-39. Expanded PL etch spectra of near surface region of 10^{15} cm^{-2} dose carbon implant in VPE GaAs. Same data as Figure IV-38.

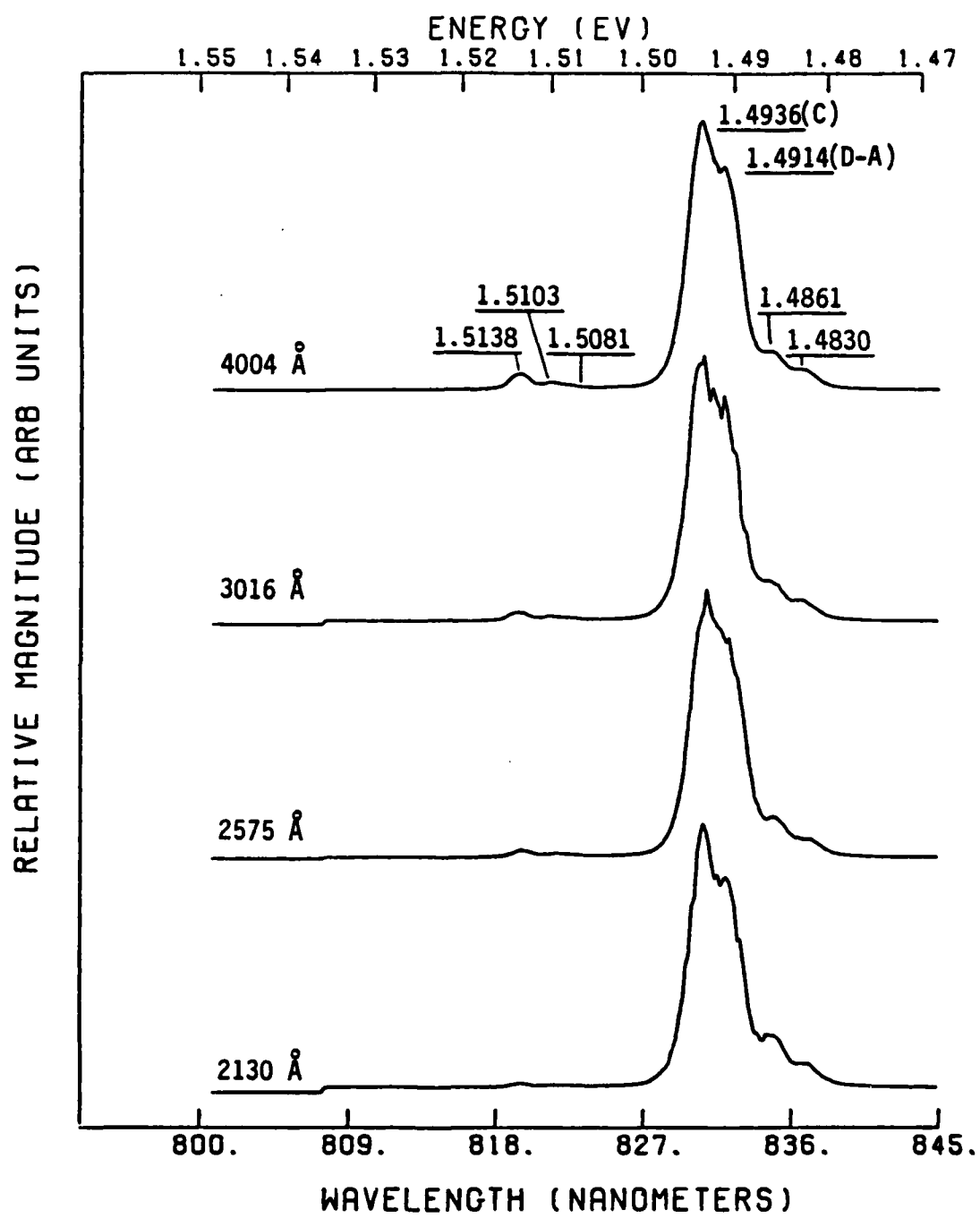


Figure IV-40. Shallow level PL etch spectra for 10^{15} cm^{-2} dose carbon implant in VPE GaAs, annealed at 950° C . Sample temperature was 8.5° K . Illumination with UV lines of Kr laser with 1.0 W/cm^2 .

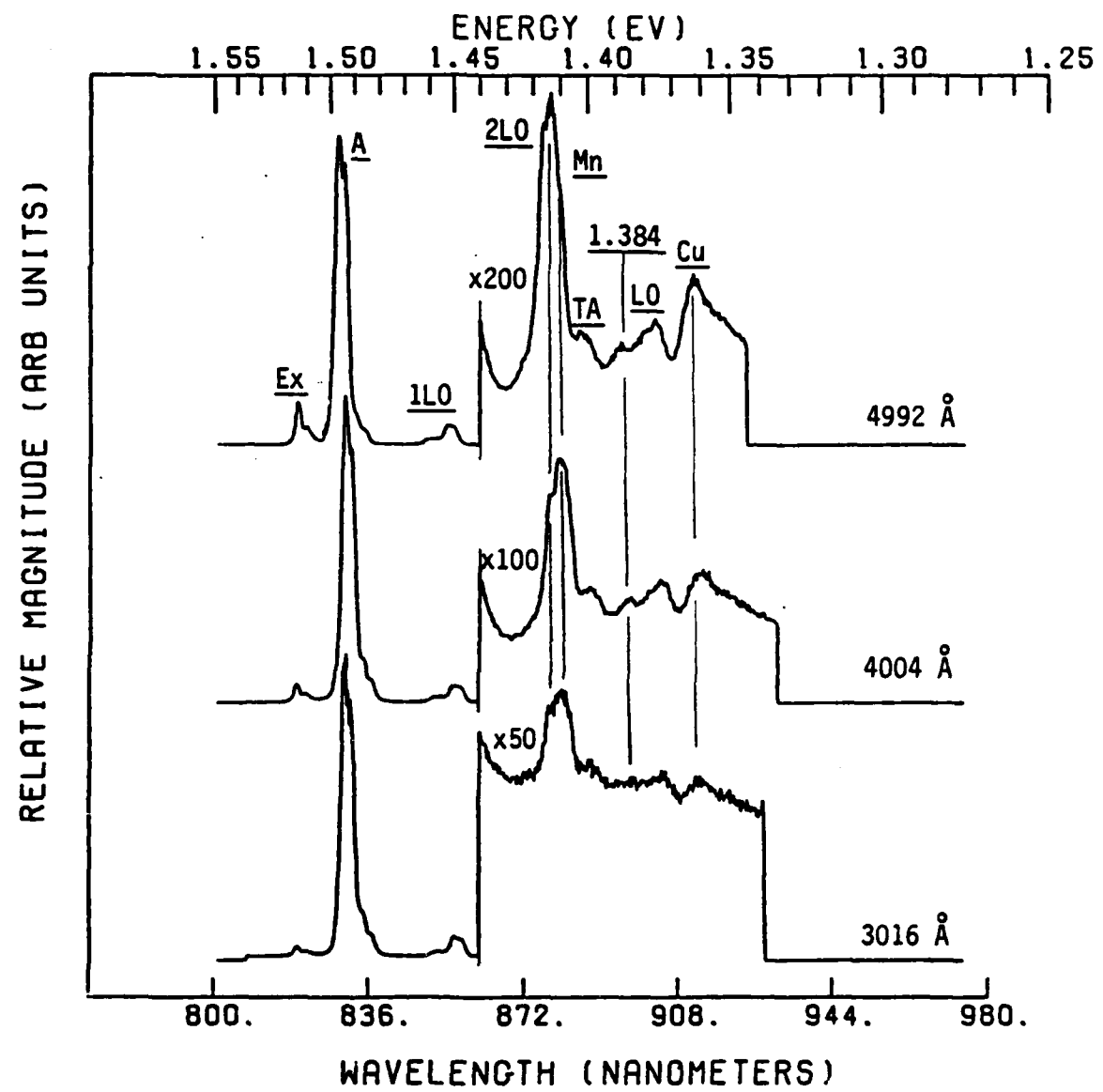


Figure IV-41. Deep level PL etch data for 10^{15} cm^{-2} dose carbon implant in VPE GaAs, annealed at 950° C . Sample temperature was 8.5° K . Illumination with UV lines of Kr laser with 1.0 W/cm^2 .

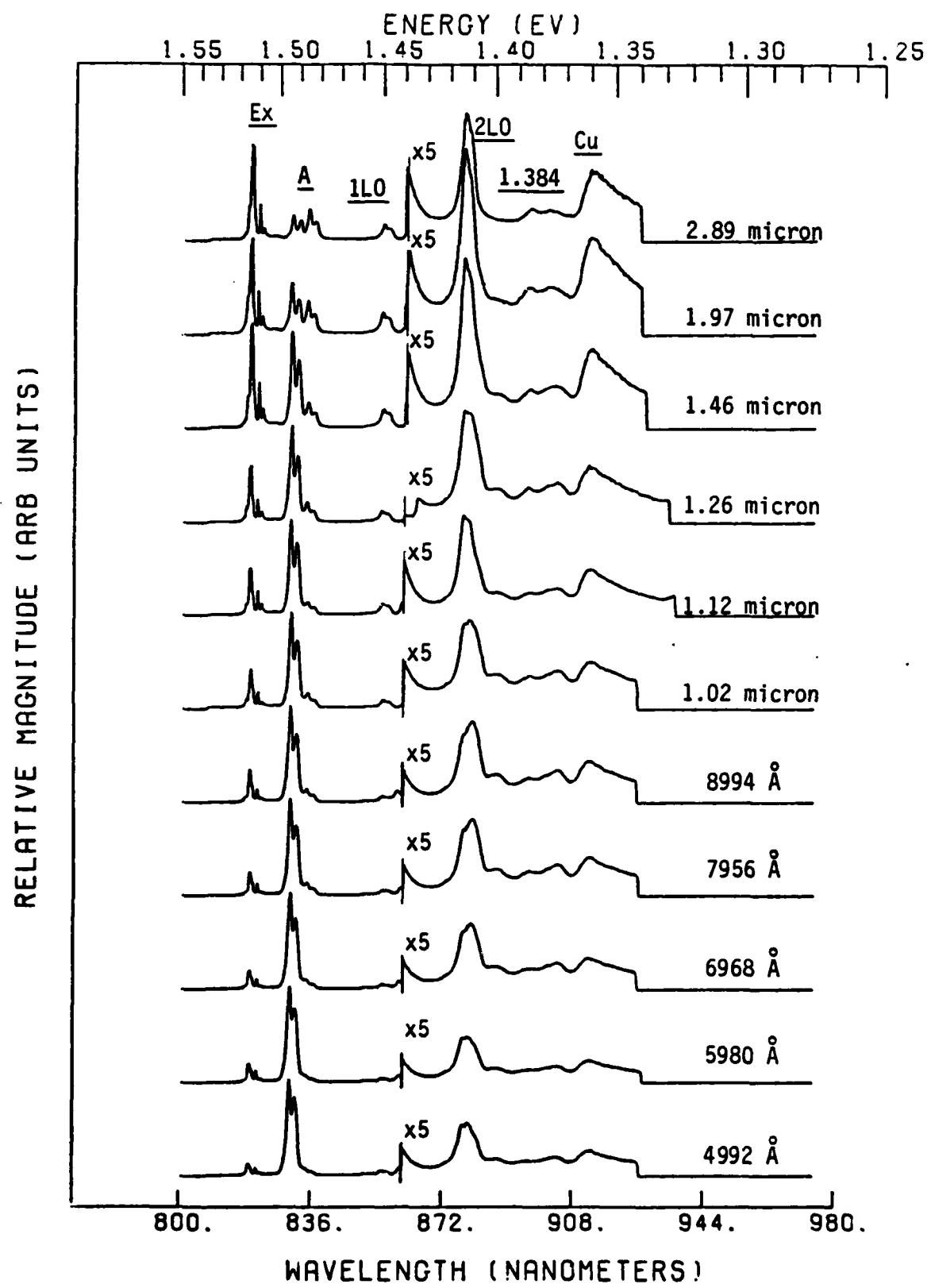


Figure IV-42. PL etch spectra for 10^{15} cm^{-2} dose carbon implant in VPE GaAs for depths of 5000 Angstroms and greater.

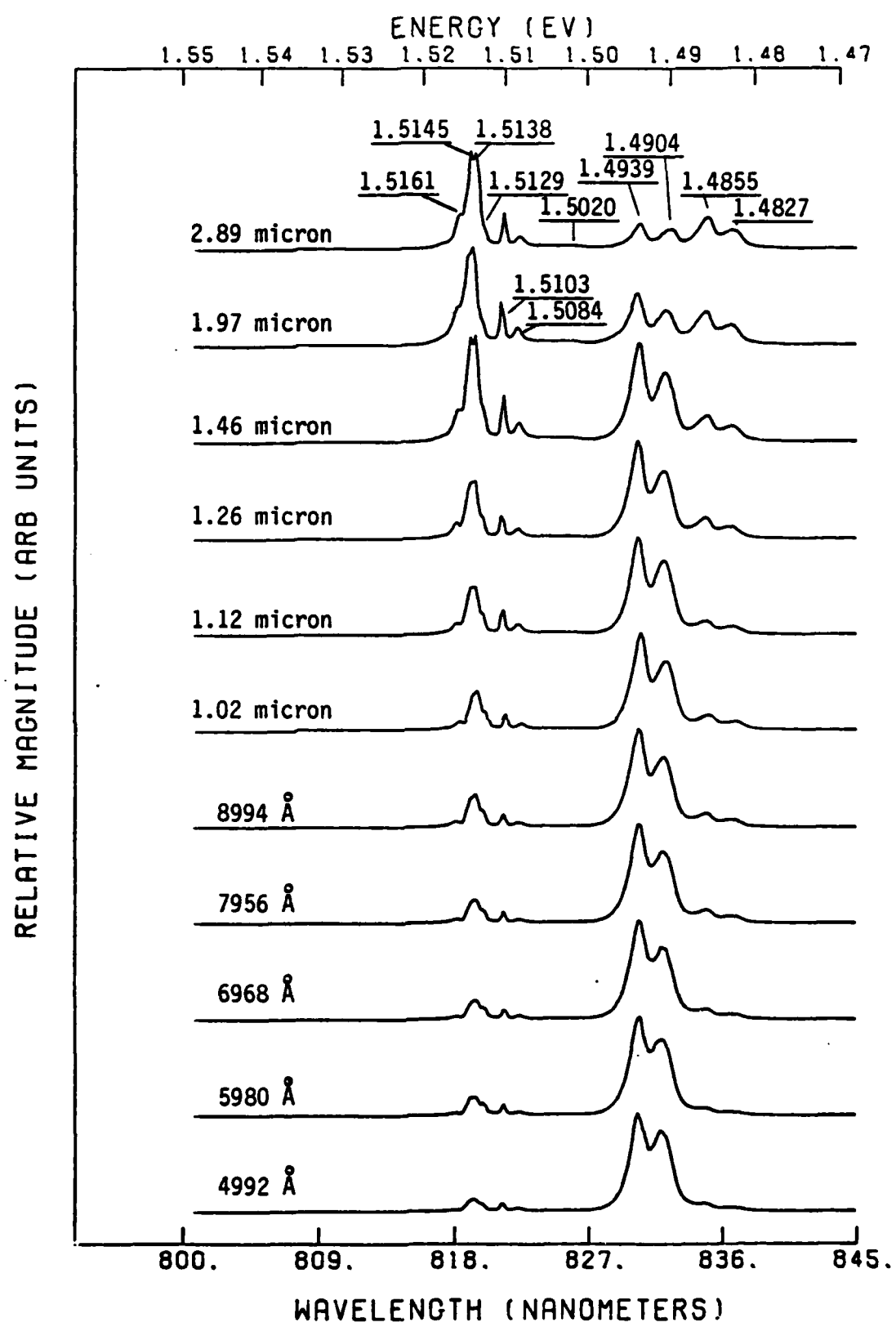


Figure IV-43. Expanded PL etch spect for 10^{15} cm^{-2} dose carbon implant in VPE GaAs for depth of 500 Angstroms and greater.

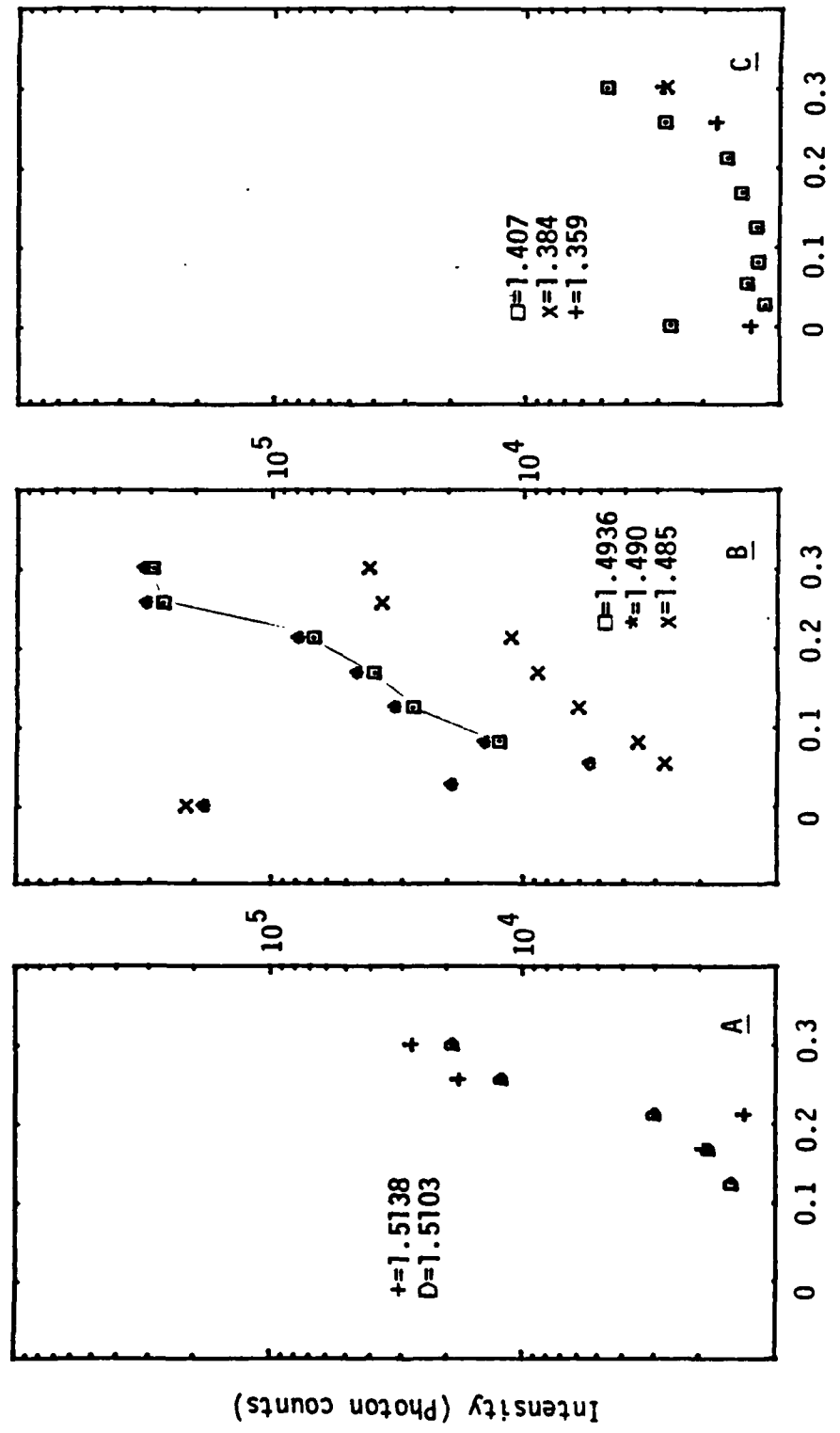


Figure IV-44. PL etch data for near surface region of 10^{15} cm^{-2} dose carbon implant in VPE GaAs, annealed at 950° C . Plot A is exciton band; $+1.5138 \text{ eV}$, $D=1.5103 \text{ eV}$. Plot B is shallow acceptor band; $\square=1.4936 \text{ eV}$, $\ast=1.490 \text{ eV}$, $x=1.485 \text{ eV}$. Plot C is deep acceptor band; $\square=1.407 \text{ eV}$, $x=1.384 \text{ eV}$, $+1.359 \text{ eV}$. Sample temperature was 5° K , illumination with UV lines of krypton laser.

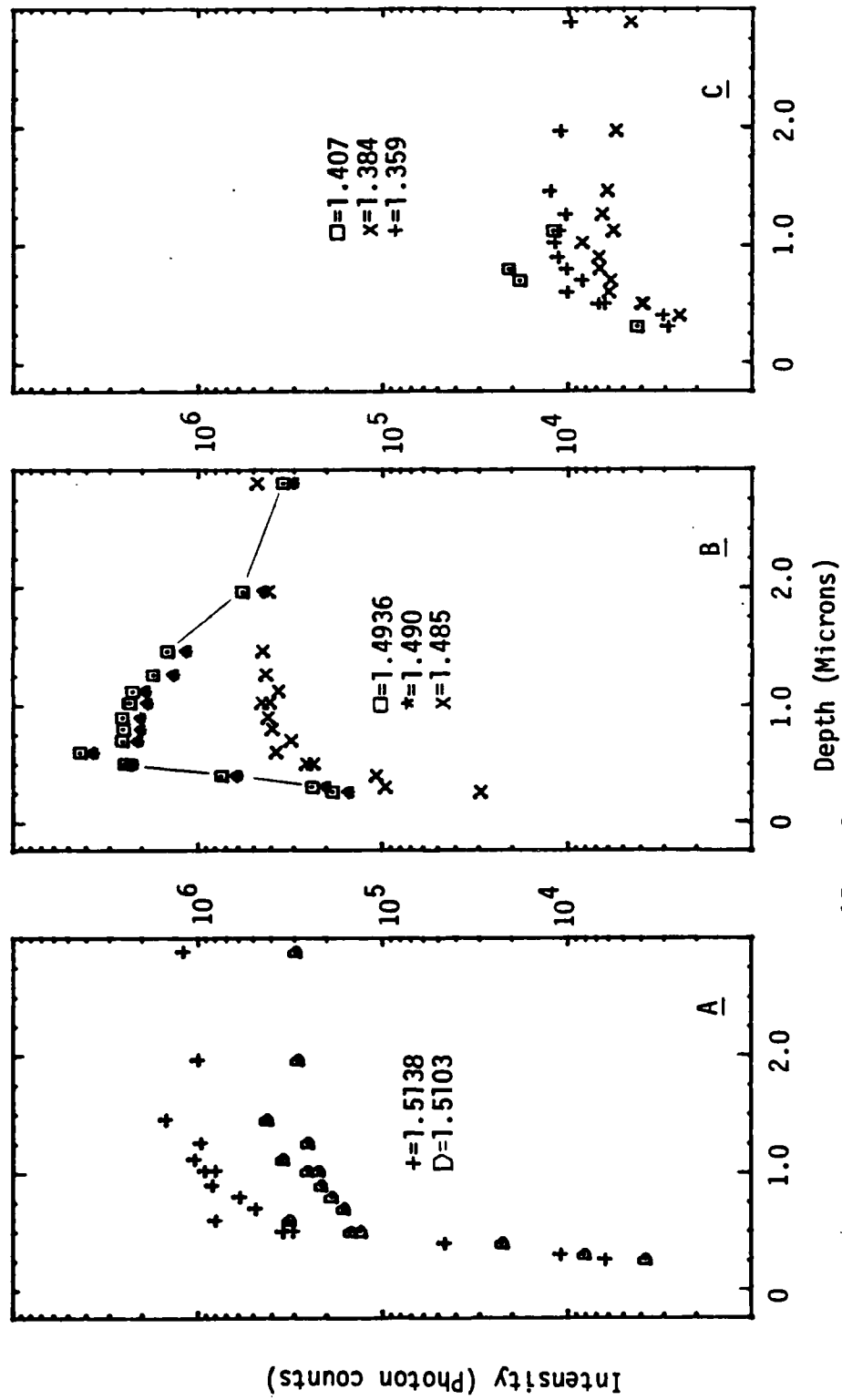


Figure IV-45. PL etch data for 10^{15} cm^{-2} dose carbon implant in VPE GaAs, annealed at 950° C . A correction factor applied to plots A and B to reflect system resolution change at 0.5 microns. Plot notation the same as Figure IV-44. Sample temperature was 8.5° K , illumination with UV lines of krypton laser.

since the differences between the 5° and 8.5° K data are almost undetectable, the data for Plot C can be followed directly from Figure IV-44 to Figure IV-45.

We first discuss the behavior of the exciton band in the PL etch data. Even with the 2 meV system resolution, excitons are undetectable until 1250 Å are etched off. Thereafter, there is a rapid increase in intensity (about a factor of 250) out to 5000 Å in depth. There is a much more gradual increase (factor of 3) in the next 5000 Å out to 1 μ in depth, and then a relatively uniform intensity out to 3 μ . The defect related excitons at 1.5103 eV and 1.5084 eV are present throughout the detectable exciton spectra, with an additional line appearing at 1.5020 eV for depths of 1 μ or greater with an intensity approximately 1/3 that of the 1.5084 eV line. As before with the PL etch data for the $1 \times 10^{13} \text{ cm}^{-2}$ dose carbon implant, the apparent growth of the exciton band in the PL spectra plots in Figures IV-42 and IV-43 is, again, really a case of the shallow acceptor band reducing in intensity to become comparable to the exciton band. By comparison to the PL etch data for the previous control samples and the $1 \times 10^{13} \text{ cm}^{-2}$ dose carbon implant, we see that there are more point defects throughout the $1 \times 10^{15} \text{ cm}^{-2}$ dose carbon implanted sample. The exciton band shows the effect of the $1 \times 10^{15} \text{ cm}^{-2}$ dose carbon implant to have the greatest effect on luminescence efficiency from the surface to near 5000 Å in depth, with a more gradual effect beyond this point.

The shallow acceptor band also shows strong effects due to the high dose carbon implant. The carbon acceptor line is not present at the surface, but begins to be detectable near 800 Å. In the 5° K spectra, it tends to be obscured by the 1.490 eV line, appearing as a shoulder at 1.4929 eV. However, the 8.5° K spectra in Figure IV-40 shows the

clear presence of the 1.4936 eV carbon acceptor line at 2130 Å. The presence of carbon is indirectly indicated at 270 Å and beyond by the shift of the 1.490 eV line from a resolved 1.4898 eV (zinc acceptor) line at the surface to a 1.4911 eV (donor-carbon acceptor) band after the first etch of 270 Å. The intensity behavior of the carbon line parallels that of the exciton band out to 5000 Å, increasing in intensity by a factor of about 250. Thereafter, the carbon line exhibits a behavior reminiscent of the PL etch data for the $1 \times 10^{13} \text{ cm}^{-2}$ dose carbon implant, showing a gradual decay in intensity, but persisting well beyond the implanted region out to 3μ.

It is particularly noteworthy of the PL etch spectra of the shallow acceptor band that there is no evidence of the relatively large peak shifts (i.e., several decades of meV) or line broadening indicative of high doping levels.

The other shallow acceptor lines (zinc, silicon) are detectable at the surface, but drop rapidly in intensity as the first 540 Å are removed. The silicon acceptor line then increases in intensity from 540 to 5000 Å in depth, and subsequently remains fairly uniform in intensity out to 3μ in depth.

The $1 \times 10^{15} \text{ cm}^{-2}$ dose carbon implant produces a strong effect on the luminescence from the deep acceptor band, which is practically extinguished at 540 Å in depth. Both the 1.407 eV and 1.360 eV lines are detectable at the surface, but the 1.360 eV line is subsequently undetectable until more than 2000 Å are etched off, and the 1.407 eV line is barely above the noise level until approximately 1700 Å are etched off. The 1.407 eV line increases gradually for the remaining etches out to 1μ and then decreases. It becomes difficult to track this line directly because of

the strong 2 LO phonon replica of the shallow acceptor band, but the TA phonon replica of the 1.407 eV line is detectable out to 1.5μ . The 1.359 eV line increases in intensity past 2000 \AA° to 5000 \AA° and then remains uniform in intensity. The 1.384 eV line is not detectable until 4000 \AA° and thereafter follows the intensity behavior of the 1.359 eV line out to 3μ . Again, as with the $1 \times 10^{13} \text{ cm}^{-2}$ dose carbon implant, the extinction of the 1.407 eV line and its phonon replicas past 1.5μ in depth shows clearly that the 1.384 eV line is unrelated to Mn.

Figures IV-46 and IV-47 show the PL etch spectra obtained for the deepest etches for the carbon implants and the control samples. The persistence of the 1.384 eV band in the carbon implanted samples is clear, but it also appears in the control samples where carbon acceptors have been seen to be present at much lower concentrations. The surface luminescence of unprocessed VPE GaAs (Figure IV-4) shows that the 1.384 eV line is missing. Therefore, the relation of this band to carbon impurities is not as strong as the relation to an impurity introduced in the control samples, with Mn having been excluded. This makes silicon a likely candidate. In the exciton band (Figure IV-47), the defect related excitons are most pronounced in the highest dose carbon implant. While the high temperature anneal control sample also introduced these defect excitons, the presence of carbon has significantly enhanced the intensity of the 1.5103, 1.5084, and 1.5020 eV lines.

The results of the one LO phonon to zero LO phonon ratio calculation for the shallow acceptor lines for the $1 \times 10^{13} \text{ cm}^{-2}$ and $1 \times 10^{15} \text{ cm}^{-2}$ dose carbon implants are shown in Figure IV-48. These results indicate that the lattice coupling for carbon acceptors decreases to a minimum near the implanted region and then gradually increases out to 3μ in depth.

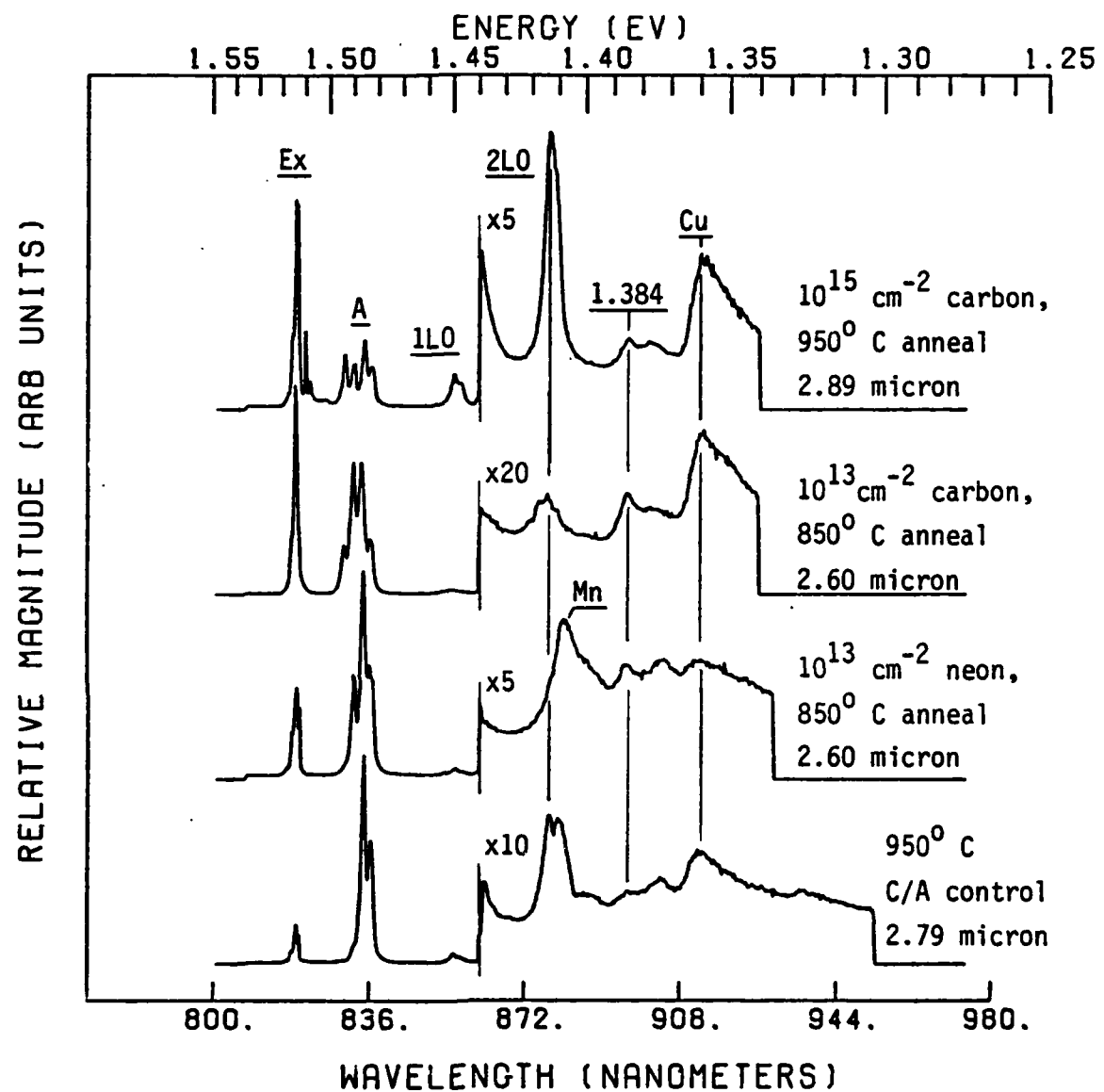


Figure IV-46. Comparative PL etch spectra for deep etches of carbon implanted VPE GaAs and control samples.

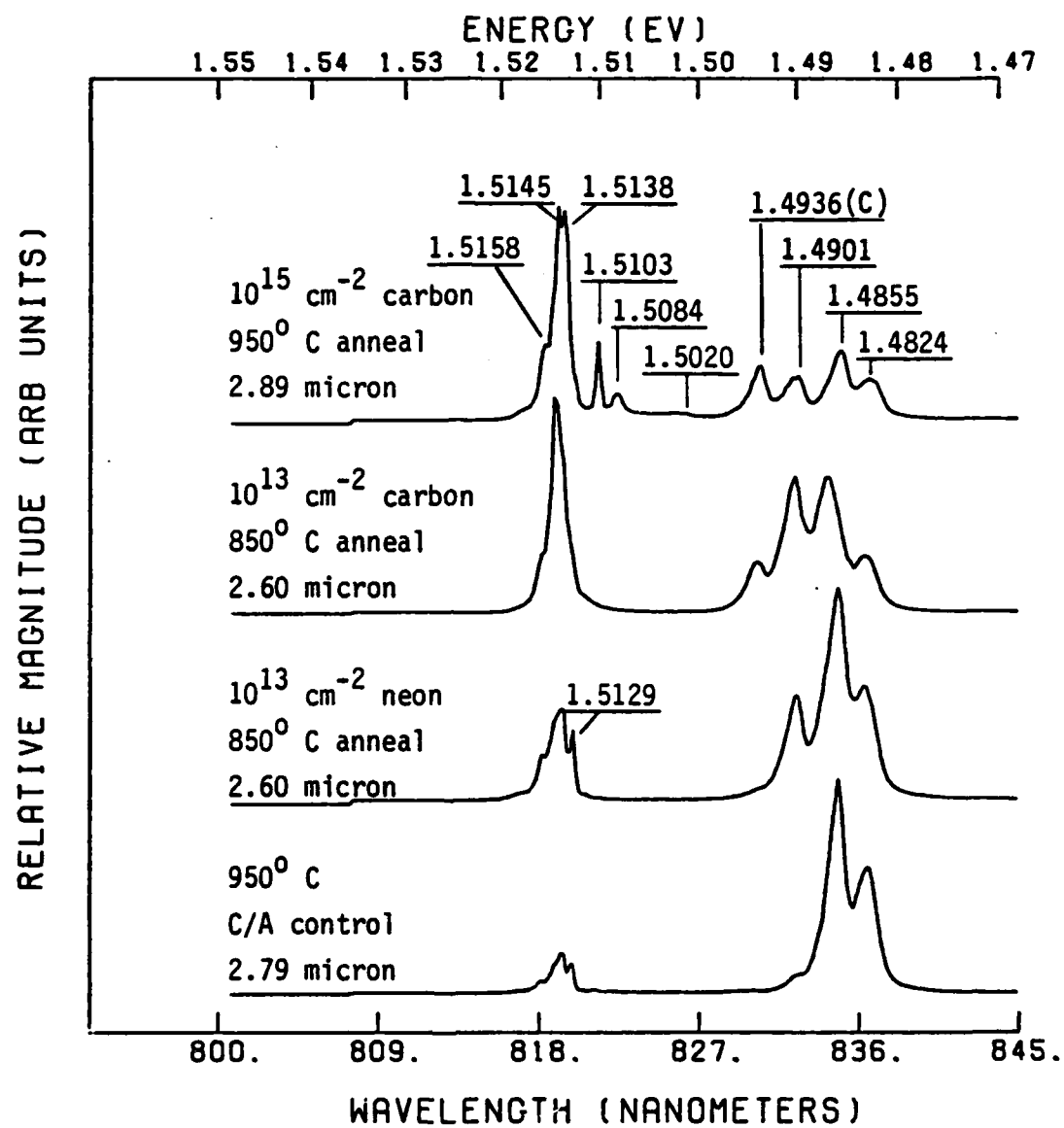


Figure IV-47. Comparative PL etch spectra for deep etches of carbon implanted VPE GaAs and control samples (expanded section of Figure IV-46).

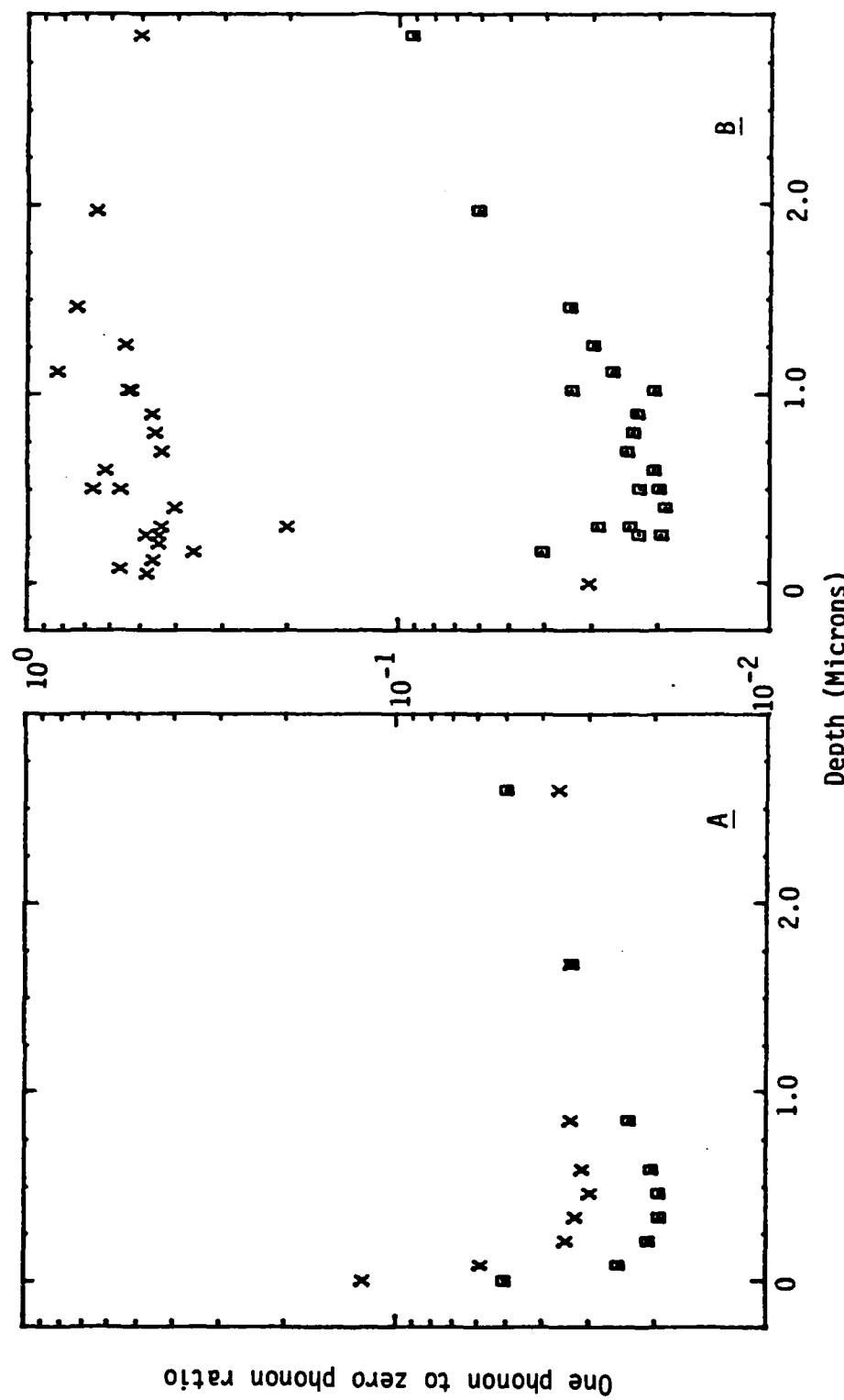


Figure IV-48. One phonon to zero phonon line intensity ratios for 10^{13} cm^{-2} dose carbon implant (plot A) and 10^{15} cm^{-2} dose carbon implant (plot B) in VPE GaAs. \square =1.4936 eV zero phonon line; x =1.485 eV zero phonon line.

The coupling strength does not follow the implant profile. The behavior of the silicon acceptor coupling is quite different for the two samples. For the low dose carbon implant, the silicon lattice coupling quickly decreases after 2000 Å, but remains at a more constant level thereafter than do the carbon acceptors. For the high dose carbon implant, the silicon lattice coupling is approximately a factor of 10 larger than carbon, or the silicon in the low dose implant. Some manifestations of this were (1) an unusual phonon replica of the shallow acceptor band where the usual "mirror image" of the shallow acceptor band did not occur, and (2) an unusually large 2 LO replica near the deep acceptor band (Figure IV-46).

To summarize the results of the PL etch data for carbon, the data indicate: (1) that carbon implantation clearly introduces carbon acceptors, (2) that the implanted carbon indiffuses well beyond the LSS implant profile, (3) that the effect of high carbon concentration on the carbon acceptor spectra is a decrease in luminescence efficiency with no shift in peak position or lineshape. A strong implication of the third observation is that carbon is not uniformly distributed and is not going substitutional, otherwise there would be shifted donor-acceptor pair lines or impurity banding effects in the luminescence.

3. SIMS Measurements: Carbon Implanted VPE GaAs. Several carbon implanted VPE GaAs samples were analyzed with SIMS. The primary ion of interest was carbon, but several other ions which may be related to the thermal conversion phenomenon were also examined. These were Si, Cr, and Mn. Only the carbon data, by comparison to the total implanted dose, could be converted to an atomic concentration profile. The other ion data are simply reported as relative number of counts versus depth.

Table IV-8 summarizes which samples were analyzed by SIMS.

TABLE IV-8
SUMMARY OF CARBON IMPLANTED SAMPLES ANALYZED WITH SIMS

| Carbon Dose (cm ⁻²) | Anneal (°C) | Ion Analyzed |
|------------------------------------|----------------|---------------|
| 1×10^{13} | None | C |
| | 850 | C |
| 1×10^{14} | 850 | C |
| 1×10^{15} | None | C, Si |
| | 850 | C, Si, Cr, Mn |

3a. SIMS for Carbon. Three implant doses of carbon were prepared for SIMS analysis, as shown in Table IV-8. Three samples were annealed at 850° C, similar to the previous samples for electrical and luminescence measurements, while two other samples were implanted but not annealed. A 1×10^{15} cm⁻² dose carbon implant was encapsulated, but not annealed, while a 1×10^{13} cm⁻² was not treated with any procedure following implantation with carbon.

Some of the objectives of doing the SIMS for carbon were to establish the actual implanted profile versus the LSS prediction and to determine the effects of the annealing steps on the implanted profiles. Interpretation of the PL and electrical measurement profiles could then more directly relate to carbon concentration effects.

The SIMS carbon profiles were converted to atomic concentration by the previously described normalization procedure (Section II.D.2).

Figure IV-49 (Plot A) shows the SIMS profiles for the unannealed carbon implants and Figure IV-49 (Plot B) shows similar data for the annealed samples. Also drawn for comparison are the single Gaussian LSS predicted profiles. It should be noted that the near surface data points are also shown, but they were not included in the normalization procedure and are not considered near surface carbon due to implantation.

Several observations can be made. First, the limit for SIMS sensitivity for carbon was approximately $1 \times 10^{16} \text{ cm}^{-2}$, with the vacuum background the limiting factor, as previously discussed. Second, by comparison of the unannealed and annealed samples, the profile is not significantly affected by a 15 minutes anneal at 850° C . The anneal has affected the peak of the $1 \times 10^{13} \text{ cm}^{-2}$ dose implant and the near surface region of the $1 \times 10^{15} \text{ cm}^{-2}$ dose implant in a way that may suggest some outdiffusion, but the profiles beyond the peak concentration appear relatively unaffected. Finally, it is clear from the LSS profiles that the lower dose implants are deeper by approximately 500 \AA and that a single Gaussian profile does not adequately describe the asymmetric behavior of the high and low dose implants.

The asymmetric behavior switches for the high and low dose implants. For the highest dose implant, there is a relatively rapid decrease in the profile, while the lower dose implants have a tail beyond the LSS profile. The $1 \times 10^{14} \text{ cm}^{-2}$ dose implant is fit fairly well with the single Gaussian profile if the Gaussian profile is translated 400 \AA deeper. One effect of this variable asymmetric behavior and variable depth of peak concentration is that the $1 \times 10^{14} \text{ cm}^{-2}$ and $1 \times 10^{15} \text{ cm}^{-2}$ dose implant profiles

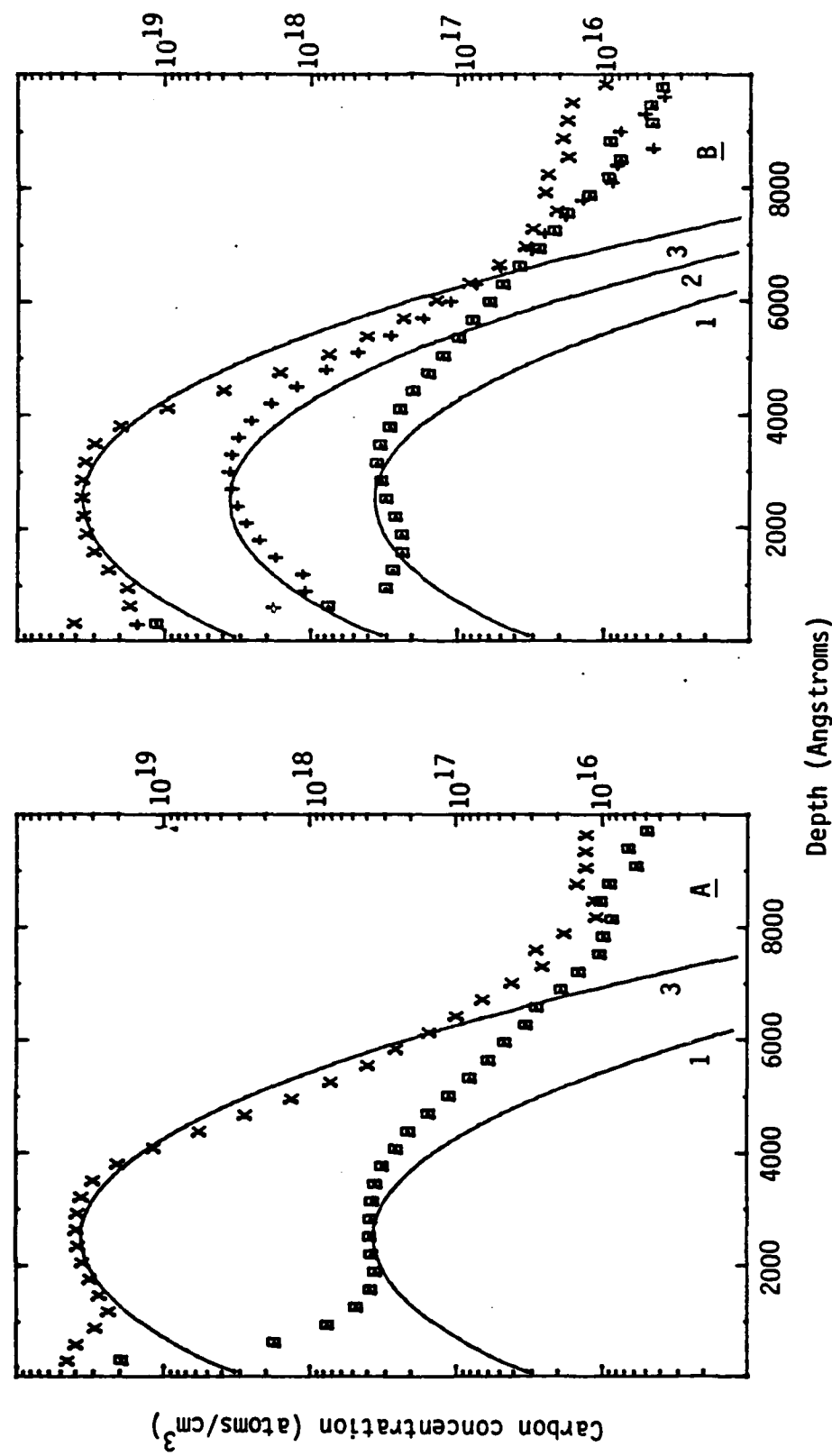


Figure IV-49. Comparison of SIMS data for carbon for unannealed (plot A) versus 850°C , 15 minute anneals (plot B). Solid lines indicate LSS predicted profiles for 120 keV carbon implants; $1=10^{13}\text{ cm}^{-2}$, $2=10^{14}\text{ cm}^{-2}$, $3=10^{15}\text{ cm}^{-2}$ doses, respectively. Plot symbols indicate calibrated SIMS data; $\square=10^{13}\text{ cm}^{-2}$, $\div=10^{14}\text{ cm}^{-2}$, $\times=10^{15}\text{ cm}^{-2}$ dose carbon implanted samples, respectively.

overlap beyond approximately 4500 \AA , and all three doses tend to overlap beyond 5500 \AA for the annealed samples. This behavior helps explain the very similar electrical measurement results at these depths for the carbon implants, as discussed in Section IV.B.1.

Recalling the discussion in Section II.A.1 and Figure II-1, we see that the qualitative features of asymmetric behavior of the $1 \times 10^{15} \text{ cm}^{-2}$ dose implant is predicted using higher order moments in the joined half-Gaussian approach for implanted profiles. However, strict application of this approach produces a distribution which is too shallow for all doses and which is definitely not in agreement with the asymmetric behavior of the lower dose implants.

Figure IV-50 shows a comparison of SIMS data for carbon with the PL etch data for the 1.4935 eV (carbon acceptor) line intensity for the $1 \times 10^{13} \text{ cm}^{-2}$ and $1 \times 10^{15} \text{ cm}^{-2}$ dose implants. While the PL data for the $1 \times 10^{15} \text{ cm}^{-2}$ dose implant is from a sample annealed at 950° C , the lack of carbon diffusion observed for the relatively high temperature 850° C anneal samples suggests the carbon distribution would be the same for the 950° C anneal.

To determine the relationship of the intensity of the carbon acceptor line (1.4935 eV) to the carbon concentration in GaAs, the PL etch data and the SIMS data for carbon were analyzed. Table IV-9 shows the input data at depths through the implanted layer, where the differences in PL and SIMS depths were less than 100 \AA . The entries in Table IV-9 disregard the anomalous surface counts in the SIMS data and the PL data which did not show a clearly resolved carbon acceptor line. These criteria set the limit on the shallow depths. The maximum depth shown in Table IV-9 is the point where the SIMS signal for carbon falls into the background noise.

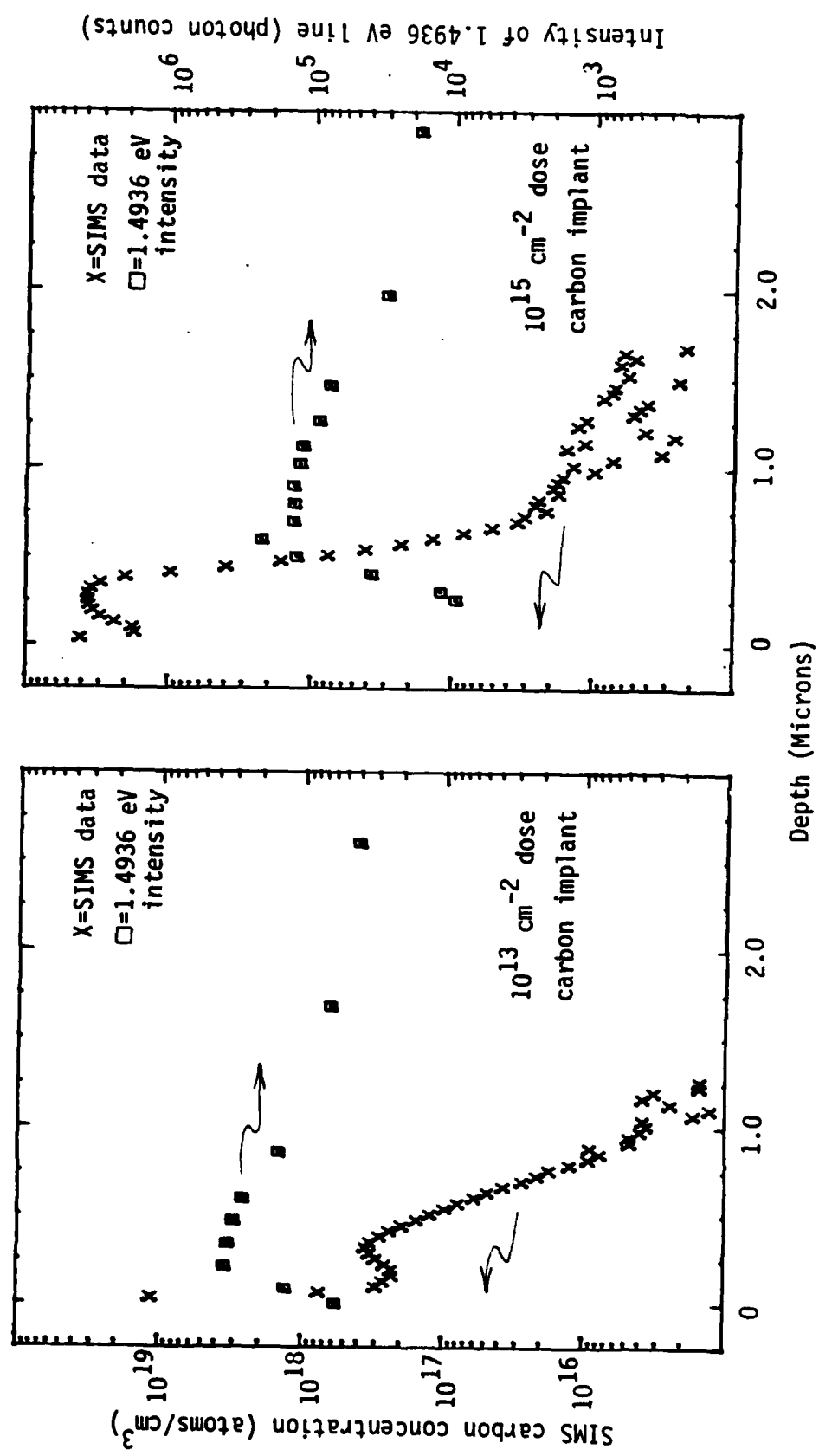


Figure IV-50. Comparison of SIMS data for carbon concentration and the data for the 1.4936 eV carbon acceptor line intensity for two carbon implant doses. PL etch data taken with illumination from UV lines of krypton laser.

TABLE IV-9
RELATIONSHIP OF CARBON CONCENTRATION AND 1.4935 eV LINE STRENGTH

A. $1 \times 10^{13} \text{ cm}^{-2}$ Dose Carbon Implant:

| Approx Depth (\AA) | [C] (cm^{-3}) | Intensity (counts) |
|----------------------------------|-----------------------------|-----------------------|
| 2200 | 2.60×10^{17} | 3.48×10^5 |
| 3400 | 3.34×10^{17} | 3.34×10^5 |
| 4700 | 1.56×10^{17} | 3.05×10^5 |
| 6000 | 6.04×10^{16} | 2.65×10^5 |
| 8500 | 7.73×10^{15} | 1.48×10^5 |

B. $1 \times 10^{15} \text{ cm}^{-2}$ Dose Carbon Implant:

| Approx Depth (\AA) | [C] (cm^{-3}) | Intensity (counts) |
|----------------------------------|-----------------------------|-----------------------|
| 2100 | 3.58×10^{19} | 2.99×10^3 |
| 2600 | 3.64×10^{19} | 9.74×10^3 |
| 3000 | 3.50×10^{19} | 1.26×10^4 |
| 4000 | 9.63×10^{18} | 3.92×10^4 |
| 5000 | 7.60×10^{17} | 1.27×10^5 |
| 6000 | 1.38×10^{17} | 2.24×10^5 |
| 7000 | 3.40×10^{16} | 1.33×10^5 |
| 8000 | 2.50×10^{16} | 1.31×10^5 |
| 9000 | 1.77×10^{16} | 1.33×10^5 |
| 10200 | 1.40×10^{16} | 1.22×10^5 |
| 11200 | 1.56×10^{16} | 1.17×10^4 |
| 12600 | 1.15×10^{16} | 9.00×10^4 |
| 14600 | 7.15×10^{15} | 7.60×10^4 |

Figure IV-51 shows the resulting plot of the intensity of the carbon acceptor PL line as a function of the carbon concentration. Figure IV-51 clearly shows a saturation occurring for the optically active carbon as the carbon concentration increases above $1 \times 10^{17} \text{ cm}^{-3}$ to $3 \times 10^{17} \text{ cm}^{-3}$. This compares very well with the electrical measurements (Figure IV-28) which showed an equivalent range of saturation for the electrically active carbon acceptors. A linear least squares fit for the data in Figure IV-51 (i.e., Table IV-9) produced a slope of 0.35 ± 0.04 for the data up to the saturation point. That is, the PL line intensity is proportional to the cube root of the carbon concentration before saturation. Beyond that point, the intensity decreases with a slope of -0.56 ± 0.06 . As was discussed in Section IV.B.2, this quenching of the carbon line was a general effect for all the luminescence lines in the $1 \times 10^{15} \text{ cm}^{-2}$ dose carbon implanted sample (Figures IV-44, IV-45).

The increase in the PL line intensity is similar to that reported in Reference 30. While the illuminating laser was different (6471 \AA versus 3500 \AA), the most comparable intensity (5 W/cm^2 vs 1 W/cm^2) data shows a slope of approximately 0.3.

It can be noted at this point that Figure IV-51 demonstrates the feasibility of quantitatively correlating PL etch data obtained with a relatively shallow penetration laser with a relatively rapid variation of implant concentration. The fact that the SIMS, electrical and luminescence etch data agree so well indicates that the assumption of minority carrier diffusion lengths of 1μ or greater is not justified.

In summary, the SIMS results for carbon on the carbon implanted VPE GaAs samples were essential in understanding both the electrical and PL etch data. Use of the simple Gaussian LSS profile predictions were simply

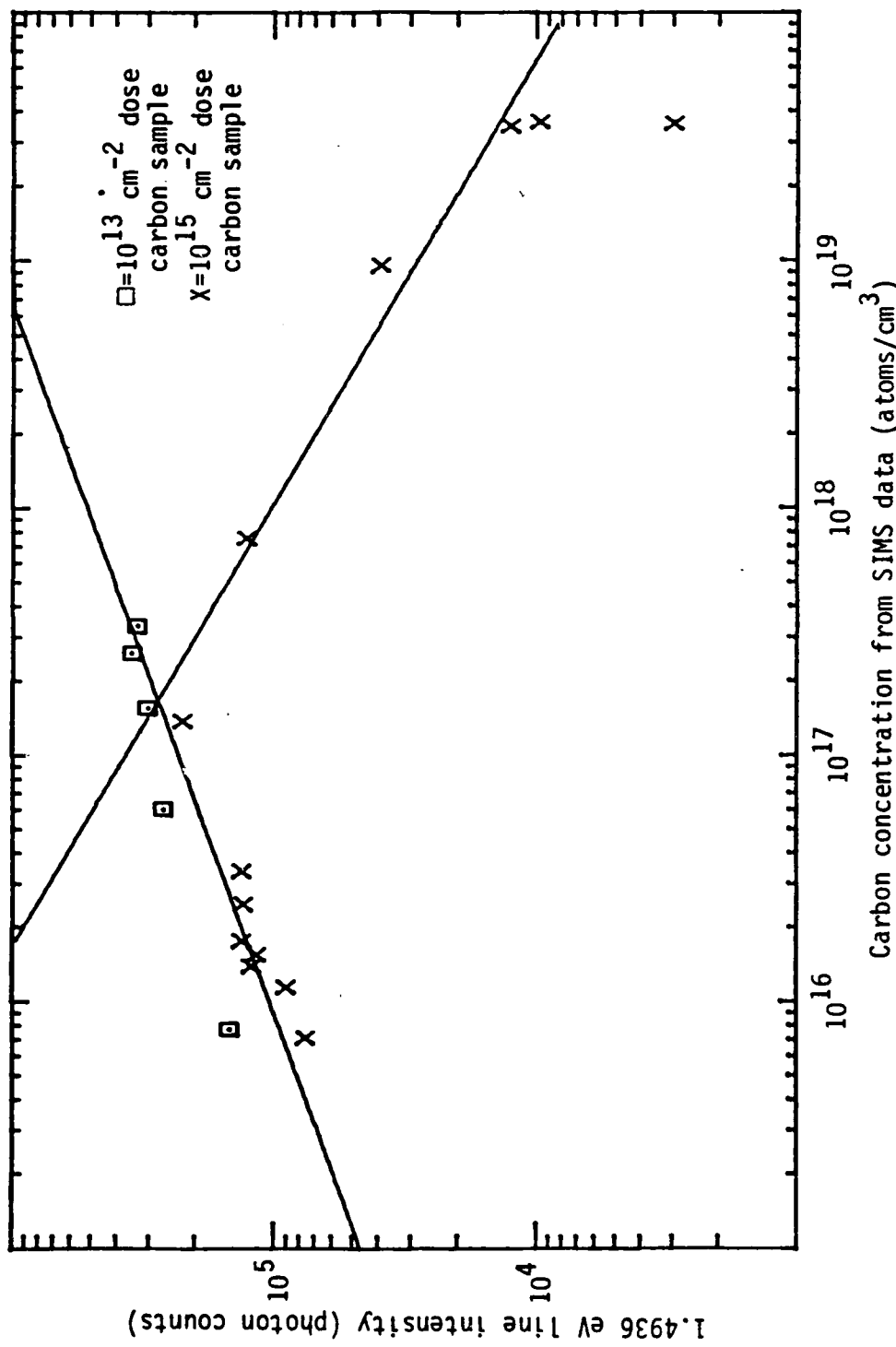


Figure IV-51. 1.4936 eV line intensity versus carbon concentration. Straight lines are logarithmic least square fits of data points above and below the saturation concentration of approximately $3 \times 10^{17} \text{ cm}^{-3}$ (see text).

AD-1138 094

ELECTRICAL LUMINESCENCE AND SIMS (SECONDARY ION MASS
SPECTROSCOPY) CHARAC. (U) AIR FORCE INST OF TECH

314

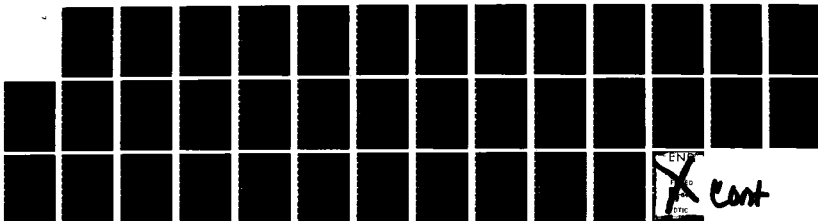
WRIGHT-PATTERSON AFB OH SCHOOL OF ENGI..

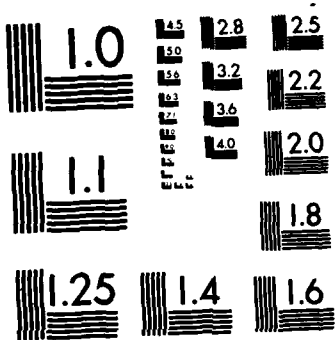
UNCLASSIFIED

R M SYDENSTRICKER DEC 83 AFIT/DS/PH/83-4

F/G 20/12

NL





MICROCOPY RESOLUTION TEST CHART
NATIONAL BUREAU OF STANDARDS-1963-A

not adequate to correctly interpret the data. Knowledge of the actual carbon distribution with depth, which tended to overlap at certain depths, allowed resolution of ambiguous electrical carrier concentration profiles and allowed more precise correlation of PL etch data for the 1.4935 eV carbon acceptor line to carbon concentration.

3b. SIMS for Si, Cr and Mn. The $1 \times 10^{15} \text{ cm}^{-2}$ dose carbon implanted VPE GaAs samples were also analyzed for silicon, chromium and manganese (see Table IV-8). These impurities were considered likely candidates for the thermal conversion phenomena. Silicon indiffusion from the encapsulant is likely, while chromium outdiffusion from the GaAs:Cr substrate was possible. Manganese has been postulated to indiffuse from such sources as the heated stainless steel tubing used in the hydrogen flow anneal furnace or to outdiffuse and accumulate near the surface from the substrate GaAs. The SIMS data for these ions were uncalibrated and, therefore, only present a relative abundance versus depth.

The SIMS data for silicon was, unfortunately, obscured by the carbon implant in the sample. The SIMS mass spectrometer was set to mass number 28 to obtain that isotope of silicon. However, CO also appears at mass 28 (carbon 12 and oxygen 16), and there is a strong correlation with the carbon data and the mass 28 data for the two samples examined. Specifically, the location of the peak concentration and the magnitude of the slowly decaying background counts were almost identical for the mass 12 and mass 28 data. Also, there were no differences in the SIMS data for Si between the annealed and unannealed samples, despite the obvious source of Si for the annealed sample. Thus, it was concluded that the formation of carbon monoxide from the sputtering of the implanted

carbon layer and from existing vacuum related hydrocarbons had obscured any measurement of silicon in this experiment.

The SIMS data for Cr and Mn are shown in Figure IV-52, along with the calibrated SIMS data for carbon and the single LSS Gaussian profile. Both the Cr and Mn have accumulated under the implant profile. The Cr concentration increases towards the surface by nearly a factor of 1000, compared to the background noise counts. The Mn shows a similar, though smaller, increase of a factor of 30. The Cr profile indicates a perceptible accumulation near 6000 Å.

Results of other SIMS experiments have shown that Cr will outdiffuse into VPE GaAs grown on GaAs:Cr substrates (Refs 85, 86). The data for Cr in Figure IV-52 is the only known data for Cr distribution in implanted VPE GaAs. Some of the original Cr outdiffusion experiments (Ref 85) showed that Cr would outdiffuse into VPE GaAs layers from the GaAs:Cr substrates at concentrations 10 to 100 times less than the substrate, but there was no near surface accumulation indicated. Reference 86 reports some near surface Cr accumulation in a VPE layer, but only a factor of 2 increase over the Cr concentration in the VPE layer.

A factor of 1000 increase in Cr concentration near the surface has been observed previously for implants in GaAs:Cr (Refs 87, 88). These were both experiments with control samples and Se implanted samples which were subsequently encapsulated and annealed for 15-20 minutes at 800-900° C. Some of the conclusions reached in these studies were that the interface stresses between the encapsulant and the GaAs:Cr encourages Cr migration to the surface and that implantation enhances the outdiffusion. The data for Cr in the carbon implanted VPE GaAs is in agreement with these conclusions.

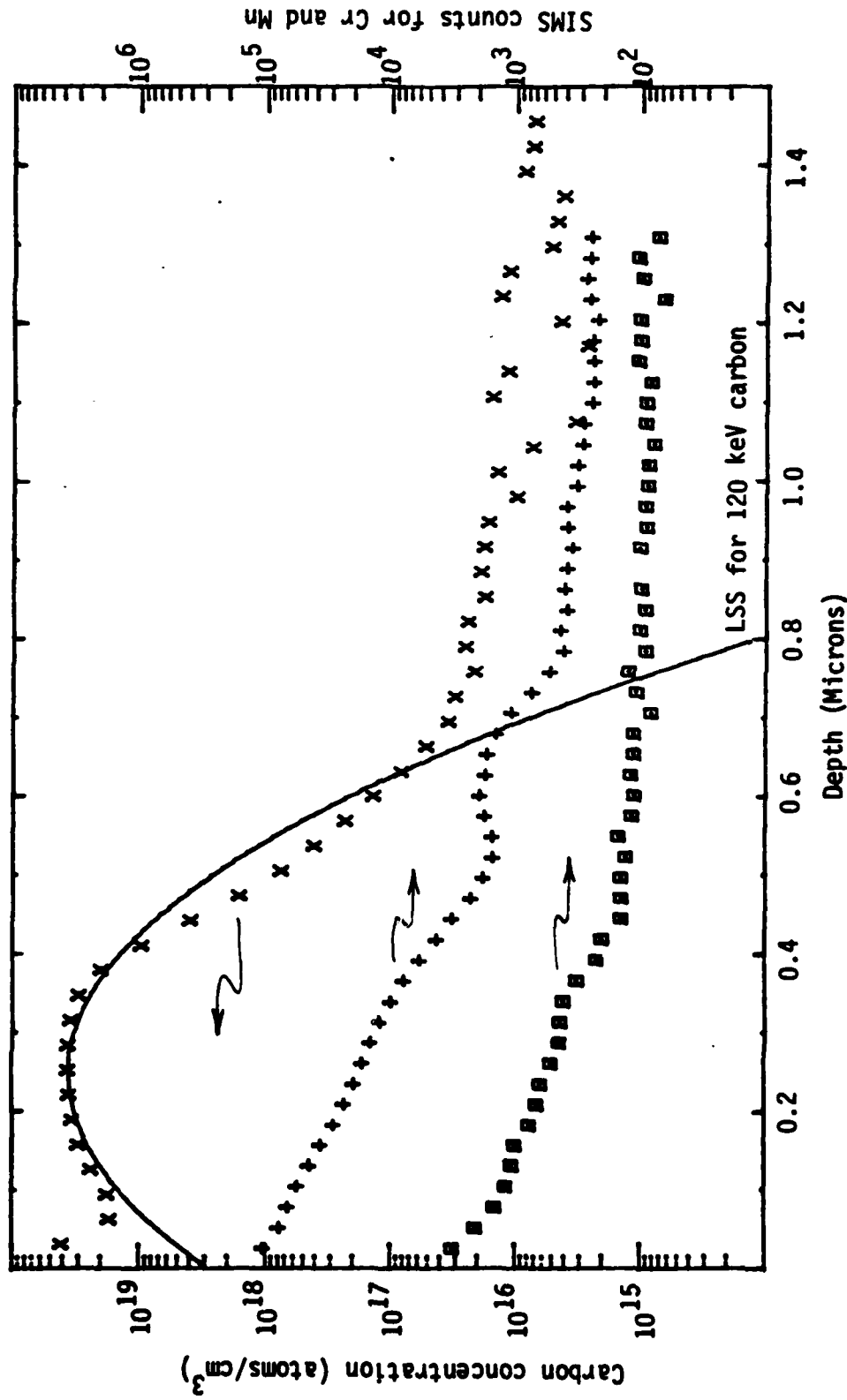


Figure IV-52. SIMS data from a 10^{15} cm^{-2} dose carbon implanted VPE GaAs sample, annealed at 850° C for 15 min. Data for carbon (X) are calibrated; data for Cr (+) and Mn (□) are uncalibrated, relative intensities only. VPE layer was 40 microns.

The slight increase of Cr at a depth of 6000 Å seen in Figure IV-52 is qualitatively similar to that observed for Se implanted GaAs:Cr (Ref 87) and Cr implanted GaAs (Ref 89). While Reference 89 offered no interpretation for the Cr accumulation, Reference 86 analyzed the accumulation as a function of post-implantation annealing and reported that Cr accumulated at a depth beyond the projected range (peak concentration) for an 800° C anneal sample, with no accumulation observed for the unannealed or 1000° C anneal sample. The interpretation for the Se implanted sample was that Cr was accumulating at a damaged region. From these other SIMS experiments, it seems reasonable to attribute the near surface accumulation of Cr to the stresses induced by the thermal expansion mismatch between the Si_3N_4 and GaAs during the thermal anneal step. The particular depth distribution of Cr observed is likely to have been influenced by the implanted carbon.

The other acceptor species analyzed by SIMS was Mn. The relationship of Mn to the p-type thermal conversion layer has been suggested before (Refs 65, 90, 91). The similarity of the Mn profile to the Cr profile in Figure IV-52 would suggest the same diffusion mechanism, i.e., outdiffusion, as discussed above for Cr. Such arguments have been presented for Mn (Ref 92) though some experiments indicated that an indiffusion of Mn from the annealing ambient was a more likely explanation (Ref 93). The limited Mn data in this experiment does not suggest a source, but its clear presence through the implanted layer suggests that Mn may contribute to the thermal conversion layer.

In summary, the limited SIMS data for two thermal conversion candidates, Cr and Mn, from a $1 \times 10^{15} \text{ cm}^{-2}$ dose carbon implanted VPE GaAs sample show that each one has accumulated near the surface. The Cr has migrated

from the GaAs:Cr substrate while the source of the Mn is unknown. The particular accumulation profiles are most likely caused by a combination of stress induced by thermal expansion mismatch of the encapsulant and the GaAs, along with the damage caused by the carbon implant. Further analysis is required to understand exactly how the Cr and Mn are contributing to the thermal conversion effect.

V. Conclusions and Recommendations

Conclusions

Prior to this experiment, it was generally known that carbon in GaAs produced p-type electrical behavior. However, quantitative results as a function of concentration were not available, due primarily to the difficulty in introducing controlled amounts of carbon into GaAs. Recent infrared absorption experiments which study localized vibrational modes (LVM) of carbon in GaAs (Ref 94) have shown that at low concentrations carbon in GaAs goes predominately to As sites, which would produce p-type behavior. Ion implantation of carbon in GaAs has been studied previously, and it was noted that increasing doses of carbon produced less electrical activation (Refs 15, 28 through 31). LVM studies of large dose carbon ion implants demonstrated that carbon appeared to leave the lattice at increased anneal temperatures (Ref 33). However, the explanations for the behavior observed in these few carbon implant studies included several possibilities. For the low electrical activation, the results could be explained by self-compensation of substitutional carbon on Ga and As sites, outdiffusion of the carbon during the post-implantation annealing step, and unannealed residual implant damage which formed compensating centers. The possibility of electrical type conversion of the GaAs substrate during the anneal step could not be ruled out completely as a partial explanation for the results also. The LVM results for annealing a high concentration implant left open the possibilities of carbon outdiffusion, carbon precipitate formation, or defect-carbon complex formation. Thus, the general body of knowledge for carbon in GaAs prior to this experiment indicated that at low concentrations carbon

was predominately a substitutional p-type dopant which could not be made to continue this behavior at high concentrations. The data left open several possible explanations for this behavior of carbon in GaAs.

As a result of this experiment, a model has been developed for the concentration dependent behavior of carbon in GaAs. Namely, there is a strong preferential As site location for carbon at low concentrations, a saturation of carbon substitutional behavior at $3 \times 10^{17} \text{ cm}^{-3}$, and a formation of carbon precipitates at higher carbon concentrations. Carbon's behavior in GaAs was observed as a function of concentration from $1 \times 10^{16} \text{ cm}^{-3}$ to $3 \times 10^{19} \text{ cm}^{-3}$ by using electrical, PL and SIMS profiling data from carbon implanted VPE GaAs. By careful use of control samples, spatial regions in the carbon implanted layers were identified where the results can clearly be attributed to the presence of carbon in GaAs. The electrical profiling measurements confirm the LVM observations of strong p-type carbon doping for low carbon concentrations, and an analysis of carbon bond strengths in GaAs shows this to be expected from minimum energy considerations (Appendix B). Both the electrical and PL etch data show a saturation of carbon substitutional behavior at $3 \times 10^{17} \text{ cm}^{-3}$, which is the first time this maximum value has been clearly observed as a function of concentration. At concentrations higher than this value, the electrical profiling data shows that carbon goes to non-substitutional sites. Both the PL profiling data and the SIMS data demonstrate that precipitate formation of carbon clusters in GaAs is the most likely explanation. Electrical compensation and carbon outdiffusion are eliminated as possible mechanisms for low electrical activation. This experiment has, therefore, provided an expanded data base for examining carbon's behavior in GaAs as a function of concentration and, by analysis of the

data, created one most likely explanation for the observed electrical, PL and SIMS data.

This experiment was the first to use electrical and PL etch measurements on carbon implanted VPE GaAs, and it is the only reported PL etch experiment on carbon implanted GaAs. The use of VPE GaAs provided sharp line structure not obtained with bulk grown GaAs and allowed clear detection of the 1.4935 eV carbon acceptor line. This allowed correlation of optical, electrical and SIMS data for carbon over the implant profiles. The range of carbon concentrations for which valid data was obtained for carbon doping ranged from approximately $1 \times 10^{16} \text{ cm}^{-3}$ to $3 \times 10^{19} \text{ cm}^{-3}$. This extended the range of concentrations for electrical profiles by an order of magnitude at each end for previous carbon implants (Refs 21, 31) and careful use of control samples isolated thermal conversion effects that may have been present in those previous measurements. The analysis of both capped and annealed controls and neon implanted controls allowed processing effects, such as implant damage and thermal conversion (electrical type conversion), to be isolated and separated from the effects which were due to the presence of carbon in GaAs. Also, a refined technique was applied to the electrical profiling data which (1) determined the implanted regions where it was reasonable to assume only ionized impurity and lattice scattering mechanisms predominated, and (2) determined the best value to assume for the lattice limited mobility. This technique allowed a higher confidence calculation of ionized donors and acceptors versus depth for an implanted sample.

The following enumerated conclusions result from a comparative analysis of the electrical, luminescence and SIMS data from carbon implanted VPE GaAs and the associated control samples. Some of the results are original

contributions in themselves, but, in general, when they are taken together they support the overall conclusion stated above for carbon's concentration dependent behavior in GaAs.

(1) This experiment has shown that carbon in GaAs at concentrations less than $3 \times 10^{17} \text{ cm}^{-3}$ tends to go strongly to As sites and act as an acceptor, while for concentrations greater than $3 \times 10^{17} \text{ cm}^{-3}$ the carbon begins to form precipitated clusters. While other experiments have shown the tendency for carbon to act as an acceptor, this experiment has tracked this behavior as a function of concentration from $1 \times 10^{16} \text{ cm}^{-3}$ to $3 \times 10^{19} \text{ cm}^{-3}$ and has determined the saturation concentration of $3 \times 10^{17} \text{ cm}^{-3}$. The experiment has produced evidence for carbon precipitation in GaAs, as opposed to outdiffusion or interstitial carbon, for the location of excess carbon above the saturation concentration. The electrical measurements and luminescence measurements which support this conclusion are shown in Figures IV-28 and IV-52, respectively. Each of these measurements independently identifies a saturation effect at a carbon concentration of approximately $3 \times 10^{17} \text{ cm}^{-3}$. A logical explanation for the preference of carbon to occupy As sites is the fact that carbon-gallium bonds are stronger than the carbon-arsenic bonds (Appendix B). The formation of precipitated clusters is suggested by the strong tendency for carbon to form bonds with itself (Appendix B) and is supported by the PL etch data which shows the carbon acceptor line at 1.4935 eV which is unshifted in energy, but only reduced in intensity at higher concentrations (Figures IV-40, IV-42, IV-45, IV-46). This fact, along with the fact that all exciton and shallow acceptor PL lines are unshifted and reduced in intensity, not just the carbon acceptor line, is the indication that excess carbon is precipitating into non-radiative clusters rather than

uniformly doping the GaAs on the lattice or interstitially. Outdiffusion of the implanted carbon has also been ruled out by the SIMS data on unannealed and annealed implants (Figure IV-50). Thus, the conclusion is that the excess carbon above the saturation concentration, determined to be $3 \times 10^{17} \text{ cm}^{-3}$, is most likely precipitating into clusters which act as non-radiative recombination centers.

(2) A minimum was observed in the electrical carrier concentration profiles which is very similar to that observed for equivalent dose silicon implants (Ref 84). However, this experiment leads to the conclusion that this dip in the electrical carrier concentration profile is due to a combination of precipitated carbon and implant damage, rather than electrical self-compensation, as was proposed for the silicon implants. There are two main arguments against electrical self-compensation of the carbon. The first is the fact that the maximum values of bulk resistivity calculated through the implant are approximately 7 orders of magnitude less than those expected in closely compensated material (Appendix A) which would exhibit mixed conduction effects. The second argument against self-compensation relates to the ionized impurity concentration calculations. While the electrical profiling data through the dip were not valid for calculating the donor and acceptor concentrations (and hence the electrical compensation) in the region of the dip, a clear trend is shown in Figure IV-28 for high carbon concentrations. This trend shows that the low values of electrical carrier concentration, $(N_a - N_d)$, are not due to close compensation of largely substitutional carbon, but are rather due to the fact that the carbon is not going substitutional at all. The correlation of the dip in electrical carrier concentration to implant damage includes the location of the dip near the expected depth

of maximum damage as well as the fact that the mobility and carrier concentration recover slightly upon higher temperature anneals (Figures IV-25, IV-26). The tendency for the formation of carbon clusters, discussed above, at the concentrations where the dip begins to form, also argues for a correlation to precipitate formation, as well as a correlation to residual implant damage. Therefore, for the carbon implants examined, the dip in the electrical carrier concentration is related both to implant damage and precipitate formation, but is definitely not self-compensation.

(3) This experiment demonstrates that useful electrical and PL etch data can be obtained from implants into VPE GaAs, despite the fact that thermal conversion may occur. Conventional experimental practices would have ruled out the VPE GaAs samples used in this experiment for electrical measurements. Surface electrical screening procedures would have revealed a relatively large p-type carrier concentration that seemingly would mask all effects due to the implant. However, this experiment demonstrates that if care is taken to characterize the thermal conversion layer and if the implanted region extends beyond the conversion layer, then useful etch profiling data may still be obtained. In this method, data from the thermal conversion layer is omitted from the electrical measurement calculations, insofar as they relate to the electrical activation of the implanted atom. Knowledge that the thermal conversion layer in VPE GaAs may not totally obscure implanted dopant activation should encourage other experimenters to pursue similar implant studies with VPE GaAs and thus gain the benefits that experiments with high purity GaAs samples can provide.

(4) This experiment has demonstrated the feasibility and utility of PL etch profiling of carbon implanted VPE GaAs in those cases where the profiling data follows relatively rapid variations in dopant concentrations. This result is due primarily to a much shorter minority carrier diffusion length than is commonly assumed for GaAs. Previous PL experiments have usually assumed a minority carrier diffusion length on the order of one micron or greater. For example, Reference 30 performed multiple energy carbon implants to achieve nearly uniform doping over a depth of one micron. This experiment has shown that the 1.4935 eV carbon acceptor line still correlates with the relatively rapid changes in carbon concentration on the back side of the Gaussian implant profile in exactly the same manner as reported in Reference 30 for several uniformly doped samples. The implication of this is a much shorter effective diffusion length than is usually assumed. This result is in agreement with the results of Reference 53 which show that cathodoluminescence depth profiling of Mg implanted GaAs samples would produce results that could be fit assuming a minority carrier diffusion length of 0.2μ . Thus, we conclude that PL etch experiments on implanted GaAs which etch off layers on the order of 0.2μ while using illuminating sources which penetrate approximately the same depth or less will produce useful luminescence data on implants with rapid concentration changes.

(5) The 1.4935 eV carbon acceptor line was found to increase in strength proportional to the $1/3$ power of the carbon concentration at moderate (1 W/cm^2) illumination intensities over a concentration range of $1 \times 10^{16} \text{ cm}^{-3}$ to $3 \times 10^{17} \text{ cm}^{-3}$, in agreement with the results in Reference 30. This experiment extended the measurements to concen-

trations of $3 \times 10^{19} \text{ cm}^{-3}$ and found that the line intensity decreases inversely proportional to the 1/2 power of the carbon concentration. This quenching effect was observed in general for all luminescence line and is believed to be an effect due to carbon precipitation at these higher concentrations, such as non-radiative recombination occurring at the precipitates.

(6) Relatively strong defect related exciton lines are reported at 1.5102, 1.5083 and 1.5020 eV for carbon implanted VPE GaAs. These peaks were also seen in the processed control samples and could be increased in strength by simply annealing unimplanted VPE GaAs at higher temperatures, which indicates the introduction of point defects by annealing. However, these peaks increased most dramatically in the high dose, high temperature anneal carbon implant (Figure IV-48), showing that the presence of both point defects and carbon are required to produce the strongest lines. The relationship of these particular exciton lines to carbon has not been reported before.

(7) The SIMS data on the carbon implants in this experiment demonstrate a dose dependent asymmetric behavior not previously reported (Figure IV-50). The high dose implant has the qualitative features of the LSS theoretical profile which includes higher order moments (Figure II-1), while the low dose implant shows a different asymmetric behavior, and the medium dose implant is approximately the symmetric Gaussian often assumed for implants. LSS theory does not predict any dependence of the shape of the profile on the total implanted dose. In the one previous publication for SIMS on carbon implanted GaAs (Ref 15), no asymmetry was reported. Knowledge of this unpredictable nature of carbon implants in GaAs is important. In this experiment, it was

essential to know the actual implant distribution (provided by SIMS in this case) in order to correlate the carbon concentration with electrical and PL etch data. In this experiment, much of the valid data on carbon was in regions where the LSS profiles were not adequately describing the location of the carbon. For example, all the implant profiles tended to overlap for depths greater than 5500 Å. The conclusion is that present LSS theory is not adequate to describe carbon implant profiles and that a technique such as SIMS is required to determine the actual concentration profile before electrical or PL etch measurements can be correlated to carbon concentration.

(8) This experiment has shown that the observed surface thermal conversion phenomena for capped and annealed VPE GaAs is not due to carbon. Though carbon has been postulated as a thermal conversion mechanism, the electrical and PL etch data on the capped and annealed and the neon implanted control samples show clearly that the thermal conversion layer occurs independently of the presence of carbon. The candidate acceptors which may contribute to the thermal conversion which were identified with PL etch and SIMS data are indiffused Si and outdiffused Cr, as well as residual Zn in the VPE GaAs and Mn from an unknown source. All of these acceptors demonstrated some degree of near surface accumulation.

(9) A new luminescence line is reported at 1.384 eV. The tentative identification is a vacancy complex similar to that which causes the "copper" complex line at 1.358 eV. While the particular impurity atom associated with the vacancy cannot be uniquely identified, silicon is a likely candidate. Silicon was observed in the PL etch data to rapidly indiffuse from the encapsulant, usually at uniform

concentrations, in all processed samples. This line is not present in unprocessed VPE GaAs (Figure IV-4) and is, therefore, related to the capping and annealing process. The Mn contamination in the VPE GaAs samples used in this experiment was low enough that the 1.384 eV line could be clearly separated from the phonon replicas of the 1.407 eV Mn acceptor line (Figures IV-35, IV-47) for those samples where implant effects had gettered the Mn at the surface. The high quality of the VPE GaAs material used in this experiment contributed identification of this new line, which was most likely obscured in previously reported PL spectra by the relatively high impurity levels in the GaAs used for those experiments.

(10) This experiment verifies that thermal diffusion of carbon in GaAs is not due to a single, simple mechanism. This is indicated by the fact that trace amounts of carbon diffused rapidly (PL etch data), while large concentrations of carbon do not diffuse discernibly during 15 minute, 850° C anneals (SIMS data). The most plausible explanation of this behavior is the tendency for carbon to form clusters at high concentrations (described above in other conclusions) which are unlikely to diffuse due to their relatively large size, while at lower concentrations the relatively small and light individual carbon atoms diffuse rapidly through the GaAs lattice.

(11) As a final conclusion, these results taken together indicate that it will be difficult, if not impossible to (i) achieve high doping efficiencies by simply increasing the carbon concentration in GaAs, or (ii) to steer carbon to Ga sites in GaAs. Thus, even though carbon is a Group IVA "amphoteric" dopant in GaAs, it is unlikely that n-type carbon doping behavior will be observed. Hence, carbon will

most likely not exhibit the electrical type conversion seen for other group IVA dopants such as Si, Ge and Sn when parameters such as dopant concentration and anneal temperature are varied.

Recommendations

(1) More work needs to be done to directly verify the precipitate formation of carbon clusters as a function of carbon concentration. One candidate technique would be transmission electron microscopy (TEM) performed on a series of carbon implanted samples of varying concentrations.

(2) Further experimental and theoretical work needs to be done to explain and predict the dose dependent asymmetric behavior of carbon implanted GaAs. A good predictive model is required because it is impractical to perform concentration profile determination experiments such as SIMS for all carbon implant experiments which require accurate knowledge of the carbon implant profile.

(3) Future SIMS data collection for carbon implants should be performed in a SIMS system with a vacuum system designed to reduce residual hydrocarbons, particularly if sensitivities are required for carbon concentrations less than $1 \times 10^{16} \text{ cm}^{-3}$.

(4) Further studies are required to determine if the carbon solubility in GaAs can be increased or if n-type carbon doping behavior (i.e., carbon on Ga sites) can be increased. Candidate techniques would include dual implantation with Ga or As, along with different annealing conditions.

(5) Investigation of the thermal conversion phenomenon in GaAs with high purity VPE GaAs may make it easier to isolate thermal

BIBLIOGRAPHY

1. Watson, H.A., Ed. Microwave Semiconductor Devices and Their Circuit Applications. New York: McGraw-Hill, 1969, p. 172.
2. Mills, T.G. Quest. Redondo Beach CA: TRW Defense and Space Systems Group, 1980, p. 22.
3. Prince, J.L., J.A. Hutchby, R.A. Donovan. Gallium Arsenide Technology, Vol. III: Device Theory and Performance. Technical Report AFAL-TR-72-3T2, Vol. III, Dec 1972, p. 9.
4. Dearnaley, G., J.H. Freeman, R.S. Nelson, J. Stephen. Ion Implantation. Amsterdam: North-Holland Publishing Co., 1973, p. 646.
5. Edmond, J.T. J. Appl. Phys. 31, 1428 (1960).
6. Wysocki, J.J. J. Appl. Phys. 31, 1686 (1960).
7. C.J. Hwang. J. Appl. Phys. 39, 5347 (1968).
8. Zucca, R. Gallium Arsenide and Related Compounds (St. Louis) 1976. Inst. Phys. Conf. Ser. No. 33b, Chapter 4.
9. Koshel, W.H., S.G. Bishop, B.D. McCombe, W.Y. Lum, H.H. Wieder. Gallium Arsenide and Related Compounds, Inst. Phys. Conf. Ser. No. 33a (1977), Chapter 2.
10. Ahn, B.H., C.W. Trussel, R.R. Shurtz. Appl. Phys. Lett., 19(408) (1971).
11. Jastrzebski, L. and H.C. Gatos. Fifth Intl. Conf. on Crystal Growth (July 1977).
12. Yeo, Y.K., J. E. Ehret, F.L. Pedrotti, Y.S. Park, W.M. Theis. Appl. Phys. Lett. 35, 197 (1979).
13. Park, Y.S., Y.K. Yeo, F.L. Pedrotti. Nucl. Instrum. and Methods, 182/183, Part II, 617 (1981).
14. Chan, S.S. Unpublished Thesis, University of Illinois. "Electrical Properties and Photoluminescence of Germanium Implanted Gallium Arsenide," 1980. (Available through DTIC, ADA085891).
15. Krautle, H. Nucl. Instrum. and Methods, 182/183, Part II, 625 (1981).
16. Wolfe, C.M., G.E. Stillman, D.M. Korn. "Gallium Arsenide and Related Compounds (St. Louis) 1976," Inst. Phys. Conf. Ser. No. 33b, p. 120.
17. Ashen, D.K., P.J. Dean, D.T.J. Hurle, J.B. Mullin, A.M. White, P.D. Greene. J. Phys. Chem. Solids 36, 1041 (1975).

18. Ozeki, M., K. Nakai, K. Dazai, O. Ryuzan. Jap. J. Appl. Phys. 13, 1121 (1974).
19. Lum, W.Y. and H.H. Wieder. Appl. Phys. Lett. 31, 213 (1977).
20. Holmes, D.E., R.T. Chen, K.R. Elliot and C.G. Kirkpatrick. Appl. Phys. Lett. 40, 46 (1982).
21. Shin, B.K. Appl. Phys. Lett. 29, 438 (1976).
22. Schokley, W. "Forming Semiconductive Devices by Ionic Bombardment of Germanium," U.S. Patent 2 787 564. Quoted by J.F. Gibbons in Proceedings of the IEEE, 56(3) (March 1968).
23. Lindhard, J., M. Scharff and H. Schiott. Matt. Fys. Medd. Kgl. Danske Videnskab Selskab, 33, 1 (1963).
24. Gibbons, J.E., W.S. Johnson, S.W. Mylorie. Projected Range Statistics, Semiconductors and Related Materials, 2nd Ed., (Dowden, Hutchinson and Ross, Inc., 1975).
25. Sanders, J.B. Can. J. Phys., 46, 445 (1968).
26. Gibbons, J.F. and S. Mylorie. Appl. Phys. Lett., 22, (1973).
27. Carger, G. and W.A. Grant. Ion Implantation of Semiconductors, (Edward Arnold Publishers, Ltd., 1976).
28. Harris, J.S. in II. International Conference on Ion Implantation in Semiconductors, I. Ruge and J. Gaul, Eds. (Springer-Verlag, Berlin, 1971), p. III.4-157.
29. Sansbury, J.D. and J.F. Gibbons. Radiation Effects 6, 269 (1970).
30. Stringfellow, G.B., W. Koschel, F. Briones, J. Gladstone, G. Patterson. Appl. Phys. Lett. 39, 581 (1981).
31. Shin, B.K., J.E. Eheret, Y.S. Park, M. Stefiniw. J. Appl. Phys. 49, 2988 (1978).
32. Krietman, M.M., J.W. Farmer, K.K. Bajaj and C.W. Litton. Solid State Comm., 32, 553 (1979).
33. Theis, W.M., C.W. Litton and K.K. Bajaj. "Optical Characterization Techniques for Semiconductor Technology," SPIE 276, 109 (1981).
34. Wang, S. Solid State Electronics. (McGraw Hill Book Co., NY, 1966).
35. McKelvey, J.P. Solid State and Semiconductor Physics. (Harper and Row, NY, 1966).
36. Blakemore, J.S. Semiconductor Statistics. (Pergamon Press, NY, 1962).

37. Spenke, E. Electronic Semiconductors. (McGraw-Hill Book Co., NY, 1958).

38. Rode, D.L. "Low-Field Electron Transport," in Semiconductors and Semimetals, Vol. 10, R.K. Willardson and A.C. Beer, Eds. (Academic Press, NY, 1975).

39. Wiley. "Mobility of Holes in III-V Compounds," Semiconductors and Semimetals, Vol. 10, R.K. Willardson and A.C. Beer, Eds. (Academic Press, NY, 1975).

40. Putley, E. The Hall Effect and Related Phenomena. (Dover Publications, NY, 1968).

41. Smith, R.A. Wave Mechanics of Crystalline Solids. (Chapman and Hall, Ltd., London, 1969).

42. Baron, R., G.A. Shifrin and O.J. Marsh. J. Appl. Phys., 40, 3702 (1969).

43. van der Pauw, L.J. Philips Research Reports, 13, 1 (1958).

44. van der Pauw, L.J. Philips Technical Review, 20, 220 (1958/59).

45. Chwang, R., B.J. Smith and C.R. Crowell. Solid State Elec. 17, 1217 (1974).

46. Petritz, R.L. Phys. Rev. 110, 1254 (1959).

47. Bebb, H.B. and E.W. Williams. "Photoluminescence I: Theory," Semiconductors and Semimetals, Vol VIII (Academic Press, NY, 1972).

48. Gershezon, M. "Radiative Recombination in the III-V Compounds," Chapter 13, Semiconductors and Semimetals, Vol. 2, R.K. Willardson and A.C. Beer, Eds., (Academic Press, NY, 1967).

49. Williams, E.W. and H.B. Bebb. "Photoluminescence II: Gallium Arsenide," Semiconductors and Semimetals, Vol. 8, R.K. Willardson and A.C. Beer, Eds. (Academic Press, NY, 1972).

50. Jastrzebski, L., J. Lagowski, H.C. Gatos, W. Walukeiwicz. Gallium Arsenide and Related Compounds, 1978. Inst. Phys. Conf. Ser. No. 45, Chap. 5.

51. Seraphin, B.O. and H.E. Bennet. "Optical Constants," Semiconductors and Semimetals, Vol. 3 (Academic Press, NY, p. 499).

52. Nelson, R.J. "Measurement of 100 Micron Minority Carrier Lengths," Gallium Arsenide and Related Compounds, 1978. Inst. Phys. Conf. Ser. No. 45, Chap. 3.

53. Cone, M.L. Unpublished Dissertation, AFIT, WPAFB OH: "Cathodoluminescence Characterization of Ion Implanted GaAs," March 1980. (Available through DTIC, AD A090302)

54. Gilleo, M.A., P.T. Bailey and D.E. Hill. Phys. Rev. 174, 898 (1968).
55. Sturge, M.D. Phys. Rev. 127, 768 (1962).
56. Heim, U. and P. Hiesinger. Phys. Stat. Sol. (b), 66, 461 (1974).
57. Reynolds, D.C., C.W. Litton, F.B. Smith, P.W. Yu and K.K. Bajaj. Solid State Comm., 42, 827 (1982).
58. Covington, D.W., C.W. Litton, D.C. Reynolds, R.J. Almassy and G.L. McCoy. Gallium Arsenide and Related Compounds, 1978, Inst. Phys. Conf. Ser. No. 45, Chap. 3, p. 171.
59. Reynolds, D.C., R.J. Almassy, C.W. Litton, S.B. Nam and G.L. McCoy. J. Appl. Phys. 49, 5336 (1978).
60. Kunzel, H., and K. Ploog. Appl. Phys. Lett. 37, 416 (1980).
61. Rossi, J.A., C.M. Wolfe and J.O. Dimmock. Phys. Rev. Lett. 25, 1614 (1970).
62. Nakamura, T. and T. Katoda. J. Appl. Phys. 53, 5870 (1982).
63. Yu, P.W. and Y.S. Park. J. Appl. Phys. 50, 1097 (1979).
64. Ilegems, M. and R. Dingle. Gallium Arsenide and Related Compounds, 1974, Inst. Phys. Conf. Ser. No. 24, 1975; Chap. 1.
65. Lee, T.C. and W.W. Anderson. Solid State Comm. 2, 265 (1964).
66. Hwang, C.J. J. Appl. Phys. 39, 5347 (1968).
67. Guislain, H.J., L. DeWolf and P. Clauws. J. Elec. Mtls., 7, 83 (1978).
68. Bogardus, E.H. and H.B. Bebb. Phys. Rev. 176, 993 (1968).
69. Ozeki, M., J. Komeno, A. Shibatomi and S. Ohkawa. Gallium Arsenide and Related Compounds, 1978, Inst. Phys. Conf. Ser. No. 45: Chap. 3, p. 225.
70. Cusano, D.A. Solid State Comm. 2, 353 (1964).
71. Tuck, B. J. Phys. Chem. Solids, 28, 2161 (1967).
72. Alferov, Z.I., V.M. Andreev, D.Z. Garberzov, M.K. Trukan. Sov. Phys. Semic. 6, 1718 (1973).
73. Bonch-Bruzevich, V.L. The Electronic Theory of Heavily Doped Semiconductors (American Elsevier Pub. Co., Inc., 1966).
74. Woodcock, J.M., J. M. Shannon and D.J. Clark. Solid State Elec. 18, 267 (1975).
75. Walter, M.J. Unpublished Thesis, Wright-Patterson AFB OH: Air Force Institute of Technology (Dec 1977).

76. Parzianello, L.V. Unpublished Thesis. Wright-Patterson AFB OH: Air Force Institute of Technology (Dec 1978).

77. Ahearn, A.J. Trace Analysis by Mass Spectroscopy (Academic Press, NY, 1972).

78. Ahearn, A.J. Mass Spectrometric Analysis of Solids (Elsevier Pub. Co., Amsterdam, 1966).

79. Runyan, W.R. Semiconductor Measurements and Instrumentation (McGraw-Hill Book Co., 1975), p. 137.

80. Hemenger, P.M. Rev. Sci. Instrum. 44, 698 (1973).

81. Evans, C.A. Private Communication given at a talk to the Electronic Research Branch, Wright-Patterson AFB OH, 6 Jun 80.

82. Blakemore, J.S. "Semiconducting and Other Major Properties of Gallium Arsenide," J. Appl. Phys. 53(10), R123 (1982).

83. Spitzer, W.G. "Multiphonon Lattice Absorption," Semiconductors and Semimetals, Vol. 3 (Academic Press, NY).

84. Antell, G.R. Appl. Phys. Lett. 30, 432 (1977).

85. Tuck, B., G.A. Adeboyeja, P.R. Jay, M.J. Cardwell. Gallium Arsenide and Related Compounds, 1978, Inst. Phys. Conf. Ser. No. 45: Chap. 2, p. 144.

86. Magee, T.J., J. Peng, J.D. Hong, C.A. Evans, Jr., V.R. Deline, R.M. Malbon. Appl. Phys. Lett. 35, 277 (1979).

87. Evans, Jr., C.A., V.R. Deline, T.W. Sigmon, A. Lidow. Appl. Phys. Lett. 35, 291 (1979).

88. Huber, A.M., G. Morillot, N.T. Linh, P.N. Favennec, B. Deveaud, B. Toulouse. Appl. Phys. Lett. 34, 858 (1979).

89. Deveaud, B. and P.N. Favennec. Solid State Comm. 24, 473 (1977).

90. Zucca, R. Gallium Arsenide and Related Compounds (St. Louis), 1976, Inst. Phys. Conf. Ser. No. 33b: Chap. 4.

91. Hallais, J., A. Mircea-Roussel, J.P. Farges, G. Poiblaud. Gallium Arsenide and Related Compounds (St. Louis), 1976. Inst. Phys. Conf. Ser. No. 33b: Chap. 4.

92. Klein, P.B., P.E.R. Nordquist, P.G. Siebenmann. J. Appl. Phys. 51, 4861 (1980).

93. Clegg, J.B., G.B. Scott, J. Hallais, M. Mircea-Roussel. J. Appl. Phys. 52, 2 (1981).

94. Theis, W.M., K.K. Bajaj, C.W. Litton, W.G. Spitzer. Appl. Phys. Lett. 41, 70 (1982).

95. Handbook of Chemistry and Physics. Robert C. Weast, Ed. (The Chemical Rubber Co., Cleveland OH, 1969), p. F-159.

APPENDIX A

Sheet Resistivity Plateau

The goal of this appendix is to derive a relation of the measured sheet resistivity as a function of depth (i.e., $\rho_s(x)$) to the bulk resistivity as a function of depth (i.e., $\rho(x)$) and apply that relation to the analysis of the observed sheet resistivity plateau.

From the definition of sheet resistivity, we have

$$\rho_s = \rho / t$$

where t is the layer thickness of the measured sheet and ρ is the bulk resistivity of the layer. To generalize to the case where the bulk resistivity is a function of depth x measured from the original surface (i.e., before etching layers away), we first define

$$x = T - t, \text{ or } t = T - x$$

where T is the original layer thickness. Also, the bulk resistivity to use is really an average of the remaining resistivity in the sample layer which we can write as

$$\langle \rho(x) \rangle = \frac{\int_x^T \rho(u) du}{\int_x^T du} = \frac{\int_x^T \rho(u) du}{(T - x)}$$

Our original sheet resistivity formula is now

$$\rho_s(x) = \frac{\langle \rho(x) \rangle}{(T - x)} = \frac{\int_x^T \rho(u) du}{(T - x)^2}$$

which implies

$$\int_x^T \rho(u) du = \rho_s(x) (T - x)^2$$

To find the bulk resistivity as a function of depth, we use the formula

$$\frac{d}{dx} \left[\int_x^T \rho(u) du \right] = -\rho(x)$$

and find

$$\rho(x) = -\frac{d}{dx} [\rho_s(x) (T - x)^2] \quad (A-1)$$

The derivative of the above expression yields

$$\rho'(x) = -\rho_s''(x)(T - x)^2 + 4\rho_s'(x)(T - x) - 2\rho_s(x)$$

For the plateau region seen in the data, the sheet resistivity is characterized by a very small slope (less than 0.3% increase between data points for the $1 \times 10^{15} \text{ cm}^{-2}$ dose carbon implant) and, hence, we have, approximately

$$\rho_s''(x) = \rho_s'(x) = 0$$

leaving

$$\rho'(x) = -2\rho_s(x)$$

Thus, in the plateau region of the sheet resistivity data, the bulk resistivity is decreasing in magnitude, as shown by the negative sign, implying a relative maximum before the plateau region.

If the bulk resistivity were a constant, the sheet resistivity takes the form

$$\rho_s(x) = \frac{\rho}{(T - x)}$$

which would demonstrate a hyperbolic behavior with an asymptote at $x = T$. Such behavior is seen for the profiles of the n-type VPE GaAs samples and for the sheet resistivity data beyond the plateau region of the high dose implants.

The differential etch data were used to calculate $\rho(x)$ from the approximate form of Eq (A-1)

$$\rho(x) = \Delta[\rho_s(x)(T - x)^2] / \Delta x$$

where $\rho_s(x)$ was measured directly, Δx is the removed layer thickness and T is inferred from the asymptotic behavior of $\rho_s(x)$. The results are shown in Figure A-1, which plots both the measured sheet resistivity and calculated bulk resistivity for the two highest dose carbon implants. The relative maximum in the bulk resistivity near the surface is observed,

and the slope of the plateau region is also seen to correspond to the relative amplitude of the maximum

The largest value of calculated bulk resistivity is approximately 30 $\Omega\text{-cm}$ which is much less than the $3 \times 10^8 \Omega\text{-cm}$ (Section II.B.2) required before mixed conduction effects are present in GaAs. Thus, the plateau region in the sheet resistivity data is not due to close compensation or conversion to n-type material, but is instead a result of decreasing values of bulk resistivity.

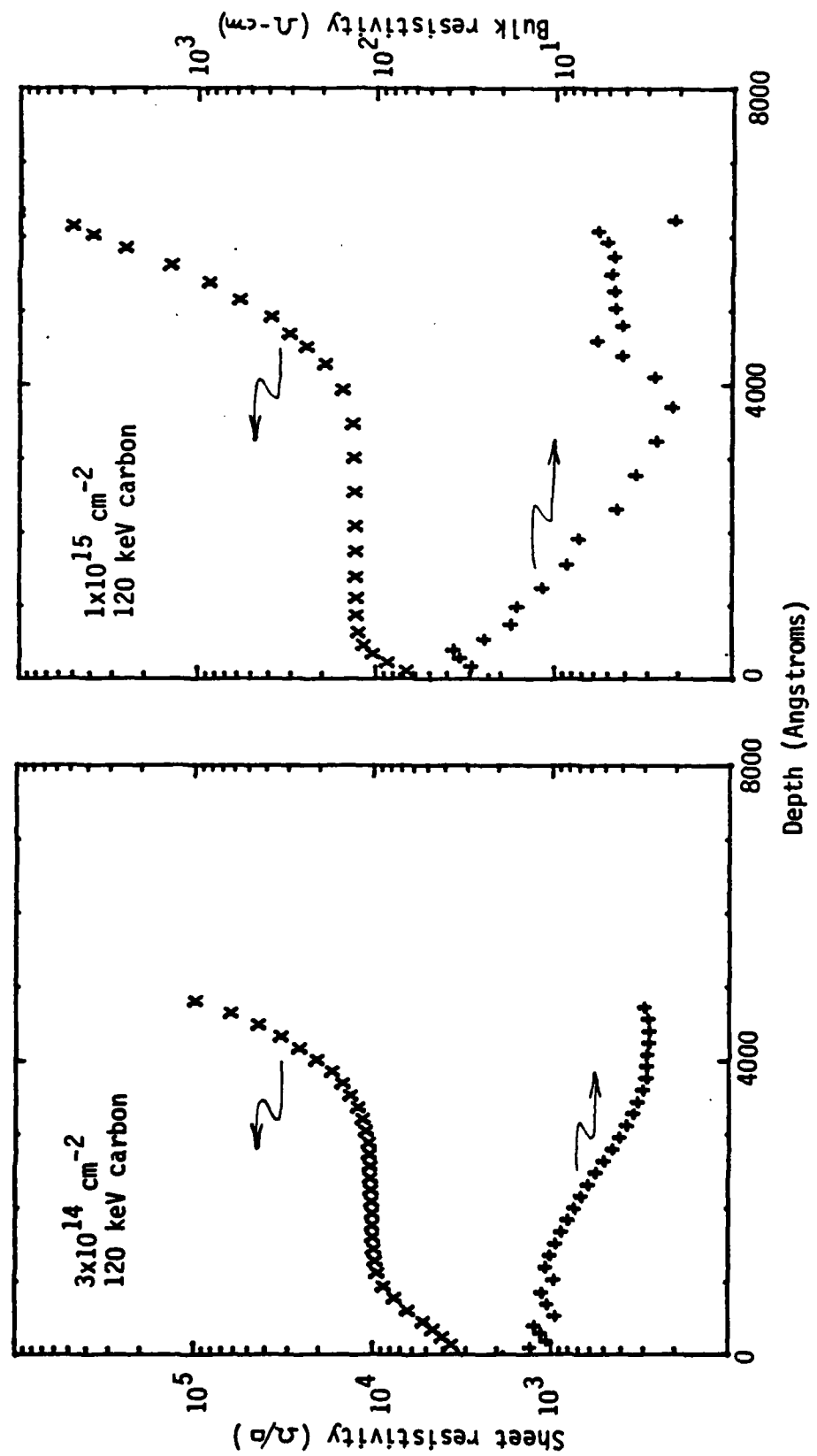


Figure A-1. Results of bulk resistivity calculations for $3 \times 10^{14} \text{ cm}^{-2}$ and $1 \times 10^{15} \text{ cm}^{-2}$ doses of 120 keV carbon in VPE GaAs, annealed at 850°C . (X=sheet resistivity, +=calculated bulk resistivity). Layer depth estimate used in calculation was $T=5500 \text{ \AA}$ for the $3 \times 10^{14} \text{ cm}^{-2}$ implant and $T=6500 \text{ \AA}$ for the $1 \times 10^{15} \text{ cm}^{-2}$ implant.

APPENDIX B

Carbon Bonding in GaAs

It is often assumed that any Group IVA element in a III-V compound, such as GaAs, can be an amphoteric impurity. That is, the impurity Group IVA element has the potential either to reside on the Ga lattice sites and act as donors, or to reside on the As lattice sites and act as acceptors. Empirical observations have shown that this is not always true. However, there are usually no simple arguments presented to explain why a Group IVA element should preferentially be a donor or acceptor in GaAs.

In this discussion, we show from simple arguments that the bond strength of carbon with Ga or As is not equal. This leads to the conclusions that carbon in GaAs will preferentially reside at As sites, and thus tend to act as an acceptor in GaAs. A second part of the discussion reviews results of measured diatomic bond strength and discusses self-bonding of Group IVA atoms in GaAs.

The principle applied is that of Pauling's description of the partial ionic character of covalent bonds and the relative electronegativity of atoms. Pauling devised a method of quantifying the electronegativity of each element, where electronegativity is defined as the power of an atom to attract electrons to itself. From the electronegativity values of two atoms, one can calculate the percent ionic character of the bond. This ionic character of the bond is the additional energy beyond that of a normal covalent bond between the two atoms. Thus, a higher percentage of ionic character indicates a stronger bond over that of the normal covalent bond.

Pauling's electronegativity values for Ga, As and the Group IVA atoms are:

Ga, 1.6 C, 2.5 Ge, 1.8 Pb, 1.8

As, 2.0 Si, 1.8 Sn, 1.8

The calculated values for the various bonds are

| <u>Bond</u> | <u>Difference of Electronegativity</u> | <u>% Ionic</u> |
|-------------|--|----------------|
| Ga-As | 0.4 | 4 |
| Ga-C | 0.9 | 19 |
| As-C | 0.5 | 6 |

All other combinations of Ga or As with the remaining Group IVA atoms give the same differences in electronegativity (0.2) and the same percent ionic character (1%). Therefore, all Group IVA atoms, except carbon, when introduced into GaAs can form bonds of comparable strength with either Ga or As, and the minimum energy for such a system would be achieved with the Group IVA atom on either Ga or As lattice sites.

For carbon, however, the percent ionic character indicates that the Ga-C bond is stronger than the As-C bond. Thus, as equilibrium is achieved in a process such as thermal annealing, the minimum energy of the system is achieved by carbon forming more bonds with Ga than with As. The resulting configuration would then have more carbon atoms on the As sites where the carbon atoms would act as acceptors.

The preceding analysis neglected the possibility of carbon forming bonds with other carbon atoms, and is therefore most applicable to relatively low concentrations of carbon in GaAs where the likelihood of two carbon atoms encountering each other is small. For high concentrations, carbon-carbon bonding can compete with carbon bonding to the GaAs lattice. The following table lists the spectroscopically determined bond strengths (in Kcal/mole) for Group IVA diatomic molecules and for Ga and As bonds (Ref 95).

| <u>Bond</u> | <u>Strength</u> | <u>Bond</u> | <u>Strength</u> |
|-------------|-----------------|-------------|-----------------|
| C-C | 144 | GA-AS | 110 |
| Si-Si | 76 | AS-AS | 92 |
| Ge-Ge | 65 | Ga-Ga | 33 |
| Sn-Sn | 47 | | |
| Pb-Pb | 20 | | |

(Specific entries for the Group IVA atoms to Ga and As were not listed). From these values we see that the carbon-carbon bonds are 2 to 7 times stronger than other Group IVA diatomic molecules, from which we infer that carbon in GaAs would be more likely to form bonds with itself than other Group IVA dopants introduced at the same concentration. However, it cannot be answered, from these data, whether carbon is more likely to bond with itself than with the GaAs lattice.

The only common bond in the electronegativity discussion and the bond strength data is the GaAs bond, which had a 4% ionic character and a strength of 110 Kcal/mole. The carbon-carbon bond is 31% stronger than the Ga-As bond, while the electronegativity results show the Ga-C and As-C bond to be 375% and 50% stronger, respectively, in ionic character

than the Ga-As bond. However, the percent ionic character alone does not give the magnitude of the bond strength. Thus, we can only say that carbon will form stronger bonds with itself than other Group IVA atoms, but cannot say with certainty that this bonding is stronger than carbon bonding to the GaAs lattice.

In summary, an examination of the interatomic bond strengths for Group IVA elements in GaAs shows that only carbon is expected to have a preferential lattice location and this location would enhance carbon's acceptor-like behavior. Also, carbon forms stronger bonds with itself than does any other Group IVA atom and is therefore more likely to form clusters at a given concentration than the other Group IVA atoms.

APPENDIX C

Si_3N_4 Edge Accumulation

A problem was encountered in performing the chemical etch for the electrical profiles. The symptom was an invariance in the voltage readings after the first few etches. When examined under a microscope (10X to 40X), samples which exhibited this behavior were found to have one or more unetched ridges along the sides of the square VPE GaAs samples. These ridges connected the indium dot contacts on the corners of the samples and were leaving a more conductive layer between contacts as the differential etch proceeded. There was no consistent occurrence of the ridges with as many as three of the four sides showing these ridges, or as little as trace amounts on one side only.

Several candidate causes were analyzed and eliminated before residual Si_3N_4 was considered. The normal procedure for removing the Si_3N_4 cap consists of soaking in HF acid for three to four minutes while monitoring the color change as the Si_3N_4 layer is removed. Various HF soak times were tried, followed by the $\text{H}_2\text{SO}_4:\text{H}_2\text{O}_2:\text{H}_2\text{O}$ etching solution. Up to 25 minutes of HF soak was required before the unetched ridges disappeared.

Subsequent examination of a pyrolytically encapsulated sample under a 40X microscope revealed that the majority of the surface had the pale blue color characteristic of 1000 \AA of Si_3N_4 . However, near the edges of the sample the color cycled through at least one color change, indicating that on the edges the Si_3N_4 was at least 2000 \AA thick. The width of this extra thick layer corresponded to the unetched ridge dimensions. Since the extra HF soak time required to suppress the unetched ridge problem was five to six times as long as the time required to remove the

majority of the Si_3N_4 , this indicates that, in addition to being at least twice as thick, the Si_3N_4 on the edges was more resistant to removal by HF.

It was somewhat of a surprise that this problem had not been encountered by previous experimenters at the Avionics Laboratory using the same differential Hall measurement procedures. The key seems to be sample geometry. Almost all previous implants were into semi-insulating GaAs:Cr which were heavily etched (more than one micron) just prior to implantation. This procedure rounds off the sharp edges of the square samples cleaved from the GaAs:Cr wafer. The edge accumulation of Si_3N_4 would then occur at a point beyond the implanted layer. Microscopic examination of several implanted GaAs:Cr samples processed for differential Hall measurements revealed the unetched ridge occurring, but at a depth that did not interfere with the electrical profiling.

The exact reason for the extra Si_3N_4 accumulation is not known. However, it is suspected to be related to spatial variations in the GaAs sample temperature or to the gas flow turbulence that occurs at the edges of the GaAs samples as they sit on the carbon strip heater in the pyrolytic chamber. The samples are often abutted (e.g., a 2 x 3 array) which keeps some edges protected from gas turbulence that probably occurs at the exposed edges. Also, when viewed during encapsulation, the exposed sample edges appear to glow brighter, indicating a slightly higher temperature. No further investigation was pursued to verify these ideas as the causes of the edge accumulation.

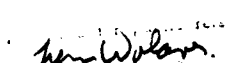
Whatever the reason for the accumulation, care should be taken when removing the Si_3N_4 encapsulant prior to chemical etch electrical profiling measurements. This is especially true for samples with sharp edges, such as cleaved VPE GaAs samples. HF soak times should be 15 to 20 minutes for

1000 Å layers, initially, followed by examination under a microscope to detect the color patterns at the edges indicative of remaining Si_3N_4 . Further soaking in HF should then be repeated until all traces are removed.

Vita

Robert M. Sydenstricker was born 4 February 1948 in Parkersburg, West Virginia. He graduated in 1966 from Annandale High School in Annandale, Virginia, and subsequently entered West Virginia University in Morgantown, West Virginia, where he graduated cum laude in 1970 with a Bachelor of Science degree in Physics. At the same time, he was commissioned as an officer in the United States Air Force through the Reserve Officer Training Corps Program. He then pursued graduate studies in physics at Ohio University in Athens, Ohio, where he graduated in 1972 with a Master of Science degree and subsequently entered active duty in the Air Force. His Air Force career has included assignments as a space systems analyst at Ent Air Force Base, Colorado (1972-1973), as a SPACE-TRACK radar controller at Diyarbakir, Turkey (1973-1974), and as a project officer for a prototype space-based infrared surveillance system at Los Angeles Air Force Station, California (1974-1977). In 1977 he entered the Air Force Institute of Technology at Wright-Patterson Air Force Base, Ohio, to pursue the doctoral degree in an engineering physics program. He is presently assigned to the Avionics Laboratory, Air Force Wright Aeronautical Laboratories, Wright-Patterson Air Force Base, Ohio.

Permanent Address: Rural Route 1
Mineral Wells, West Virginia

| | | | | | | |
|--|--|--|---|-----------------------|-------------|--|
| 8a. NAME OF FUNDING/SPONSORING ORGANIZATION | | 8b. OFFICE SYMBOL (if applicable) | 9. PROCUREMENT INSTRUMENT IDENTIFICATION NUMBER | | | |
| 8c. ADDRESS (City, State and ZIP Code) | | 10. SOURCE OF FUNDING NOS. | | | | |
| | | PROGRAM ELEMENT NO. | PROJECT NO. | TASK NO. | WORK UN NO. | |
| 11. TITLE (Include Security Classification) See Box 19 | | | | | | |
| 12. PERSONAL AUTHOR(S) Robert M. Sydenstricker, B.S., M.S., Major, USAF | | | | | | |
| 13a. TYPE OF REPORT PhD Dissertation | 13b. TIME COVERED FROM _____ TO _____ | 14. DATE OF REPORT (Yr., Mo., Day) 1983 December | | 15. PAGE COUNT 226 | | |
| 16. SUPPLEMENTARY NOTATION | | | | | | |
| 17. COSATI CODES | | 18. SUBJECT TERMS (Continue on reverse if necessary and identify by block number) Gallium Arsenide, Ion Implantation, Carbon, Luminescence, Hall measurements, Electrical Profiles, Photoluminescence Profiles, Secondary Ion Mass Spectrometry | | | | |
| 19. ABSTRACT (Continue on reverse if necessary and identify by block number) | | | | | | |
| <p>Title: ELECTRICAL, LUMINESCENCE AND SIMS CHARACTERIZATION OF CARBON IMPLANTED VAPOR PHASE EPITAXIAL GALLIUM ARSENIDE</p> <p>Committee Chairman: Dr. R. L. Hengehold</p> <p>  7 Feb 84 Dr. R. L. Hengehold Dean for Education and Professional Development Air Force Institute of Technology (AFTC) Wright-Patterson AFB, OH 45433 </p> | | | | | | |

UNCLASSIFIED

SECURITY CLASSIFICATION OF THIS PAGE

BLOCK 19 CONTINUED

The electrical, luminescence and mass distribution properties of carbon implanted VPE GaAs have been analyzed. Room temperature Hall measurements and low temperature photoluminescence (PL), each combined with chemical etching, and SIMS experiments were performed on VPE GaAs which had been implanted with 120 keV carbon atoms in doses ranging from $1 \times 10^{13} \text{ cm}^{-2}$ to $1 \times 10^{15} \text{ cm}^{-2}$. Useful data was obtained for carbon concentrations of $1 \times 10^{16} \text{ cm}^{-3}$ to $3 \times 10^{19} \text{ cm}^{-3}$. The electrical and PL etch data independently identify a saturation effect for substitutional carbon acceptors at a concentration of approximately $3 \times 10^{17} \text{ cm}^{-3}$. For lower concentrations, the carbon goes strongly to As sites and acts as an acceptor, while for higher concentrations the carbon goes to electrically and optically inactive sites, identified as precipitated carbon clusters. The PL etch data show the effect of carbon concentration on the 1.4935 eV carbon acceptor line above and below the saturation concentration of $3 \times 10^{17} \text{ cm}^{-3}$. Several new luminescence lines are also reported. Defect related excitons appear at 1.5102, 1.5083 and 1.5020 eV and their intensities are strongly enhanced by the presence of carbon. A new vacancy complex has been identified at 1.384 eV which has tentatively been associated with Si acceptors. The overall conclusion is that, for carbon concentrations above approximately $3 \times 10^{17} \text{ cm}^{-3}$, the excess carbon will not go substitutional and that for carbon concentrations less than $3 \times 10^{17} \text{ cm}^{-3}$, the carbon will reside predominately on As sites as an acceptor, unlike the amphoteric behavior of other Group IVA impurities in GaAs.

UNCLASSIFIED

SECURITY CLASSIFICATION OF THIS PAGE

END

FILED

A-84

DTIC



RD-A138 094

ELECTRICAL LUMINESCENCE AND SIMS (SECONDARY ION MASS
SPECTROSCOPY) CHARAC. (U) AIR FORCE INST OF TECH
WRIGHT-PATTERSON AFB OH SCHOOL OF ENGI.

UNCLASSIFIED

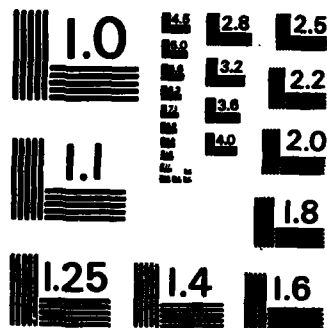
R M SYDENSTRICKER DEC 83 AFIT/DS/PH/83-4

F/G 20/12

44

NL





MICROCOPY RESOLUTION TEST CHART
NATIONAL BUREAU OF STANDARDS - 1963 - A

SUPPLEMENTARY

INFORMATION

Errata

AD-A13809X

Page IV-7 not available

17 Jul 85

END

FILMED

10-85

DTIC